Coupled Topology Optimization and Process Simulation System for Laser Powder-bed Fusion Additive Manufacturing

by

Zhidong Zhang

A thesis

presented to the University of Waterloo

in fulfillment of the

thesis requirement for the degree of

Doctor of Philosophy

in

Mechanical and Mechatronics Engineering

Waterloo, Ontario, Canada, 2019

Examining Committee Membership

The following served on the Examining Committee for this thesis. The decision of the Examining Committee is by majority vote.

External Examiner: Prof. Javad Mostaghimi

Dept. of Mechanical & Industrial Engineering

University of Toronto

Supervisor: Prof. Ehsan Toyserkani

Dept. of Mechanical and Mechatronics Engineering

University of Waterloo

Internal Member: Prof. Mustafa Yavuz

Dept. of Mechanical and Mechatronics Engineering

University of Waterloo

Internal Member: Assoc. Prof. Kaan Inal

Dept. of Mechanical and Mechatronics Engineering

University of Waterloo

Internal-External Member: Assoc. Prof. Adil Al-Mayah

Dept. of Civil and Environmental Engineering

University of Waterloo

Author's Declaration

This thesis consists of material all of which I authored or co-authored: see Statement of Contributions included in the thesis. This is a true copy of the thesis, including any required final revisions, as accepted by my examiners.

I understand that my thesis may be made electronically available to the public.

Statement of Contributions

I want to acknowledge my co-authors who contributed to the research described in this thesis:

Prof. Ehsan Toyserkani: Supervising the research, providing the initial idea for the current thesis, editing papers, and providing lab facilities.

Dr. Ali Bonakdar: Managing the research project, providing valuable discussions, and editing the papers.

Dr. Yuze Huang: Co-designing the LPBF experiments with stainless steel 17-4PH powder, and providing valuable discussions.

Dr. Usman Ali: Providing valuable discussions and helping in revising the papers.

Dr. Yahya Mahmoodkhani: Providing valuable discussions and helping in revising the papers.

Shahriar Imani Shahabad: Helping in measuring the melt pool geometries and providing valuable discussions.

Adhitan Rani Kasinathan: Helping in measuring the melt pool geometries and providing valuable discussions.

Osezua Ibhadode: Helping in measuring the part profiles by CMM, processing data, and providing valuable discussions.

Chinedu Francis Dibia: Organizing the project, helping in EDM cutting, and providing valuable discussions.

Pouyan Rahnama: Helping in measuring the part profiles by CMM and providing valuable discussions.

Abstract

Additive Manufacturing (AM), widely known as 3D printing, is a transformative method to industrial manufacturing, helping in creating lighter, stronger, smarter parts and systems. As one of the most important and commercially available AM processes, Laser Powder-bed Fusion (LPBF) can realize geometrically complex metallic parts by selectively melting layers of metallic powders. It is being used extensively in many fields, such as medical, aeronautical, etc..

As AM provides new design opportunities, topology optimization is ideal for AM, specifically LPBF, because it can be deployed to design high-performance structures and fully exploit the fabrication freedom provided by AM. However, there are still some challenges of printing parts in LPBF, such as porosity creation, low surface quality, residual stress, and deformation, which impede its widespread use in industrial applications. These challenges can be controlled by better understanding the influence of the process parameters used in the LPBF process. Nevertheless, relying exclusively on experimental efforts is expensive and time-consuming. Therefore, the LPBF process modeling can help in understanding the effects of the process parameters on the printed part quality. Furthermore, LPBF modeling can be coupled with topology optimization to produce parts with lower as-built deformation.

In this work, a coupled topology optimization and process simulation system is proposed to deal with the challenges and utilize the opportunities of the LPBF process. This system involves two major aspects: Firstly, a 3-dimensional heat transfer model is developed to study the effect of process parameters on printed LPBF parts. The simulation results show good agreement with experimental measurements. The averaged error of melt pool width and depth are 2.9% and 7.3%, respectively. Secondly, an Inherent Strain Method (ISM)-based topology optimization model is proposed to reduce the deformation in LPBF parts. A parallel-computing framework of this model is used to optimize the support structures to reduce the as-built and after-cut deflections of printed parts. Experimental results show the framework can reduce the part deformation of over 60% and

also material usage of over 50% compared to commercial support structures. Besides, the ISM model has also been employed in predicting the deflections of printed parts, and when compared to experimental results, excellent agreement is observed (average 6% error). Lastly, the parallel-computing framework can achieve considerable simulation acceleration.

Acknowledgements

Along the journey of my PhD studies as well as many years of studies, I have met many people without whom I would not be here now.

First and foremost, I thank greatly my supervisor Prof. Toyserkani, who gave me inspiring guidance, generous help, and endless encouragement. Under his mentorship, I had the opportunity to truly improve my engineering skills and scientific knowledge.

I also acknowledge my committee members, Prof. Javad Mostaghimi, Prof. Mustafa Yavuz, Prof. Kaan Inal, and Prof. Adil Al-Mayah, for taking the time to review my thesis and to provide their valuable advice.

I sincerely thank all my colleagues at MSAM. I want to thank Prof. Mihaela Vlasea for providing help and valuable discussions. I want to thank Dr. Yahya Mohamookani, Dr. Usman Ali, and Dr. Yuze Sam Huang, who provided tons of discussion and help during the research. I thank Dr. Esmat Sheydaeian, Dr. Farzad Liravi, and Evan Wheat for providing valuable assistance during the earlier days of my PhD. I thank my colleges in the Siemens project for their support and advice, Osezua, Francis, Pouyan, Shahriar, Reza, Ali, Katayoon, Ken, Dr. Ehsan Marzbanrad, and Dr. Ali Bonakdar. I also thank Dr. Dyuti Sarker, Henry Ma, Yanli Zhu, and Sera Ertay for providing help during the experiments. I appreciate the help and advice from Jerry Ratthapakdee for the machine setup and post-processing. I thank Karl Rautenberg for helping in cutting the samples. I thank Laurie Wilfong and Meghan Schmuck for the help in financial management.

I would also like to thank people in and out of the MME department at UW. I thank Prof. Ali Ghodsi for providing the HPC resources on SharcNet. I thank all the specialists from SharcNet for providing valuable tutorials and assistance. I thank Mark Griffett and Yuquan Ding for guidance in metallurgy experiments. I thank all the course lecturers who inspired me a lot for their guidance

and help, Prof. Robert Gracie, Prof. Adrian Gerlich, Prof. Grzegorz Glinka, Prof. Kaan Erkorkmaz, Nancy Oczkowski, and Dr. Stefan Rehm.

I thank my new friends met in Waterloo, Jie Wang, Yu Wang, Xiaodong Zhang, Hen Zhang, Dou Zhao, Serena Zhao, YQY, Yuting Sun, Yue Pan, Meng Wu, and many others. I thank my old friends for their company and encouragement, Yuecheng Jiao, Ye Zhang, Yicong He, Fanyi Meng, Gen Li, Axiang Zhao, Zhongheng Yin, Rui Zhang, Huijun Xia, Kun Wang, Liang Xin, Hao Cheng, Xuhui Su, Kaichao Zhang, Yawen Luo, Xiaofan Zhang, Shuang Gao, Pengqiu He, Meng Zhao, Junteng Wang, Cao Niu, Qing Li, Yahui Zhang, Jian Liu, Dan Wang, Xinggang Tang, Jungang Yang, Liang Xia, Jin Zhang, Shouyu Cai, Yun Yang, Aurore Guglielmetti, Yu Li, and many many other friends, who are so important to me. Especially, I greatly appreciate the guidance and encouragement from Cheng Chen and Qiang Xiao, without whom I definitely cannot go abroad and either see the big world. Furthermore, I thank all my teachers who gave me so much enlightenment and wisdom along my years of studies, Yehong Xu, Tanpan Han, Li Yang, Bo Liu, Jianguo Huang, Ming Wu, Jianling Liu, Xiaohong Quan, Hongshe Chen, Yonggang Chen, Xi'an Wang, Jian Cen, Gangming Che, Lanping Hang, Genjiu Xu, Genzheng Sun, Yongshou Liu, Lehua Qi, Anqiang Wang, Linke Deng, Weihong Zhang, and many many other kindly teachers.

Most importantly, the most profound appreciation is given to my family for their help, encouragement, and love, especially to my parents-Yanli and Changsheng, my aunt-Aiqin, my wife-Yuna, and our newborn boy-Hanwen.

To my family

Table of Contents

List of Figures

List of Tables

Chapter 1. Introduction

1.1. Motivations

Additive manufacturing (AM), also known as 3D printing, rapid prototyping, and rapid manufacturing [1], is a class of advanced manufacturing. AM has several unique capabilities (free-form fabrication, multi-scale design, multi-material manufacturing, and functional structures) that enable designers to maximize product performance through size, shape, and topology optimizations subject to the capabilities of AM technologies [2]. As one of the most important AM processes, Laser Powder-bed Fusion (LPBF) is widely used to produce geometrically complex metallic parts [3]. There is a growing number of applications in many different areas, especially medical [4] and aeronautical [5,6] industries for reducing weight and improving performance.

Moreover, in recent years, a wide range of alloys has been employed in manufacturing various components through the LPBF process. In LPBF, a three-dimensional model is manufactured by selectively melting layers of metallic powder. Each layer consists of line tracks deposited tightly contiguous to each other. The shape of each layer is the cross-section of the original CAD model. Thus, unlike traditional manufacturing processes, LPBF makes products directly from the digital models without the need to determine the sequence and the tools of fabrication.

As LPBF provides new design opportunities, topology optimization is ideal for LPBF because it can be used to design high-performance structures and can fully exploit the fabrication freedom provided by AM. Moreover, topology optimization can reversely help to mitigate the limitations of the AM process by considering manufacturing constraints in the structural-design stage, such as compensating the deformation of final AM parts and trimming down the residual stress. Also, not only can the product structure be optimized, but also the support structures can be topologically optimized. LPBF parts are usually printed with a support structure that connects the part to the substrate. Support structure plays a critical role in three aspects: First, supporting the weight of the

overhang features; second, dissipating the laser heat to prevent overheating; third, anchoring the printing part on the substrate to prevent unexpected deflections due to the residual stresses induced by the laser scanning [7–10]. Thus, by optimizing the topologies of the support structures, the residual stresses and deformations can be reduced.

Even though LPBF has many advantages, its widespread industrial applications and its adoption to serial production are impeded by several limitations, such as lack of fusion, keyhole collapse, porosity [11], balling [12], and low surface quality [13], which can cause failure in printed parts. Moreover, residual stress is another critical barrier leading to the failure of the final products due to high thermal gradients and cooling rate [14–16]. Besides, many process parameters, such as laser power, scanning speed, exposure time, layer thickness, hatch distance, scanning pattern, and powder properties, are involved in LPBF [17] and can influence the quality of printed parts [9,18,19]. The uncertainty of the quality of the final product has been regarded as an obstacle to LPBF applications. Therefore, better understanding the effects of the process parameters in the LPBF process is critical [20].

The main motivations of this work are as follows,

1. The first motivation for this work is to build numerical models of LPBF. For addressing the challenges, properly selecting process parameters is necessary since these defects are significantly influenced by the process parameters. The sole deployment of trial-and-error experiments to determine the process parameters is very costly and time-consuming [21]. There will be a large number of coupon samples with different combinations of process parameters, such as laser power, scanning speed, powder layer thickness, hatch spacing, preheating temperature, and scanning patterns. Therefore, numerical models of the LPBF process are to be developed and investigated.
2. The second motivation for this work is to investigate the new design opportunities provided by combining topology optimization with LPBF. Combining topology optimization with

LPBF can have multiple advantages, e.g. reducing the volume of support structures needed, compensating for the deformation of final AM parts, and so on. As an example, support topology optimization for LPBF is proposed for reducing deformations of LPBF parts.

3. The third motivation for this work is to propose a system to integrate the first and second motivation seamlessly. To date, most commercial software of structural design is yet fully considering the LPBF process. Therefore, a coupled topology optimization and process simulation system is beneficial for combining topology optimization with LPBF.

1.2. Objectives

The main aim of this research is to build up a preliminary system of design and optimization for LPBF. This system can help structural designers take full advantage of LPBF by providing information about melt-pool behavior, residual stresses, deformations, and structural topology optimization.

In order to achieve this goal, the objectives of this work are:

1. Build up a preliminary system of design and optimization for AM.
2. Develop a computationally efficient heat-source model for predicting the geometries of melt pools in LPBF and validate with experimental results.
3. Investigate the computational approaches for accelerating the part-level simulation to predict deformation and residual stresses in LPBF parts and validate with experimental results.
4. Propose a high-performance topology optimization framework for support structures in order to reduce deformations of LPBF parts and validate them with experiments.

1.3. Outline

The organization of the thesis is as follows: Chapter 2 is the literature review of LPBF process simulation, topology optimization, and attempts to couple them together. Chapter 3 illustrates modules of a design and optimization system, including the mathematical model of topology optimization, mesh-smoothing techniques, performance simulation, and the LPBF process simulation. Chapter 4 explains the fundamentals of the LPBF process simulation. Chapter 5 presents a 3-dimensional heat-transfer finite element model for LPBF, while Chapter 6 uses the proposed model to study the effect of layer thickness in LPBF. Chapter 7 presents the LPBF process simulation, including melt-pool modeling, actual-laser-scan simulation, and two accelerated simulation approaches (domain-activation and inherent-strain methods). In Chapter 8, a topology optimization parallel-computing framework is developed for designing support structures in order to minimize the deformation of LPBF parts. Chapter 9 presents conclusions and the future work.

A graphical summary of the thesis is shown in Figure 1.1.

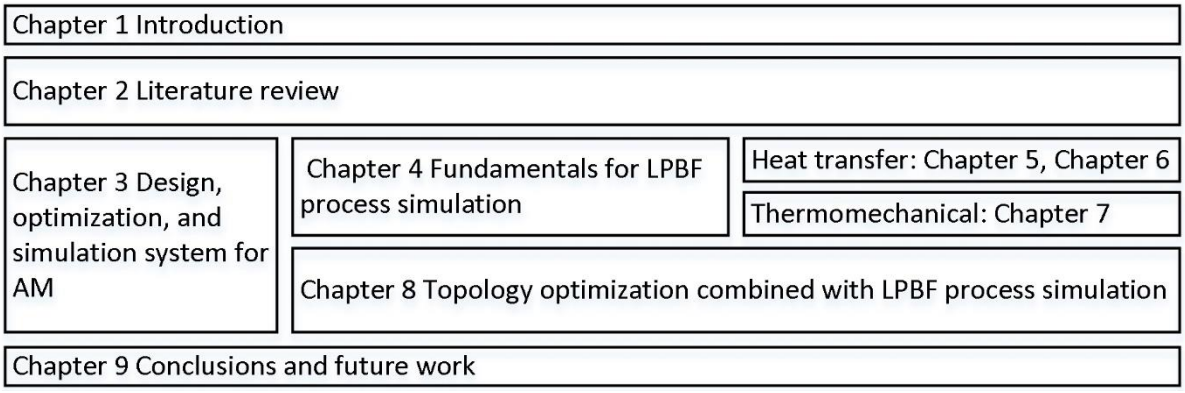

Figure 1.1. The graphical view of the thesis organization.

Chapter 2. Literature Review

This chapter presents the literature review of LPBF. In addition, the numerical modeling of LPBF has been reviewed. Furthermore, topology optimization and the advantages of combining topology optimization with LPBF have also been investigated.

2.1. LPBF

LPBF is able to fabricate geometrically complex, fully functional metallic structures typically without any pre or post-processing steps [1,22–24]. Figure 2.1 shows a schematic of a classical LPBF AM process. The system typically includes a fabrication platform, a laser system, and a powder delivery platform.

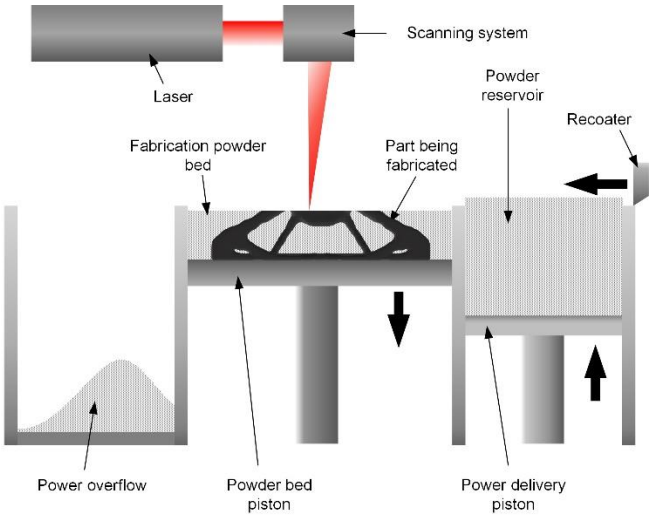

Figure 2.1. Schematic of the LPBF additive manufacturing.

During LPBF, a high-power laser selectively scans over metal powder to form a solidified metal layer while fusing it with the previously built layers. This process is repeated to create the final part. LPBF has been investigated since the 1980s and has become commercialized by many companies, such as EOS GmbH (Germany), Renishaw (British), Concept Laser GmbH (Germany), SLM Solutions (Germany), Phenix System (France), and so on.

Many innovative structures are now achievable through LPBF, such as sensor holders in commercial jet engines [5], and the hinge bracket. In the medical field, because of its manufacturing flexibility, customized bone reparations, joint implants, and dental crowns have been realized [25–27]. Figure 2.2 provides several representative parts made by LPBF.

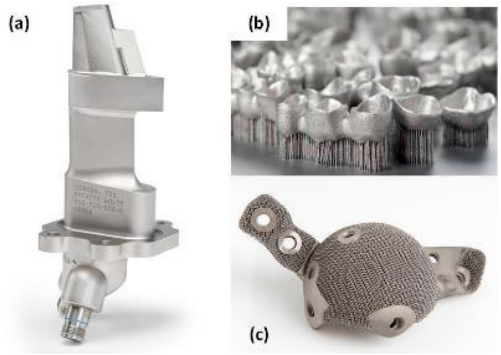

Figure 2.2. Several complex parts made by LPBF, (a) a sensor holder in a commercial jet engine [5], (b) dental crowns [25], (c) a hip implant in titanium [27].

2.2. LPBF's challenges and opportunities

2.2.1. Challenges: printed part defects, residual stress, and deformation

Although LPBF seems a free-form manufacturing technique, it still has several limitations that prevent it from widely industrial applications [22].

2.2.1.1. Defects

Porosity in LPBF is mainly caused by three reasons, as shown in Figure 2.3: a) an over large energy input may incur keyhole mode melting, and an unstable keyhole may collapse and trap vapor to form voids [28]. b) an over low energy input may lead to a lack of fusion, leaving the particle-by-particle gap voids in a printed part [29]. c) the balling effect may also induce porosities [30]. Second, high surface roughness is another defect in LPBF. Process parameters influence the surface roughness of an LPBF part, and the surface roughness could be improved by optimizing process parameters [31]. Third, overheating in the overhang geometries may lead to the failure of printing [32], as shown in Figure 2.4. Fourth, delamination and cracks, caused by high thermal

stresses, deteriorate the fatigue performance and fracture resistance of a printed part [33,34], as depicted in Figure 2.5.

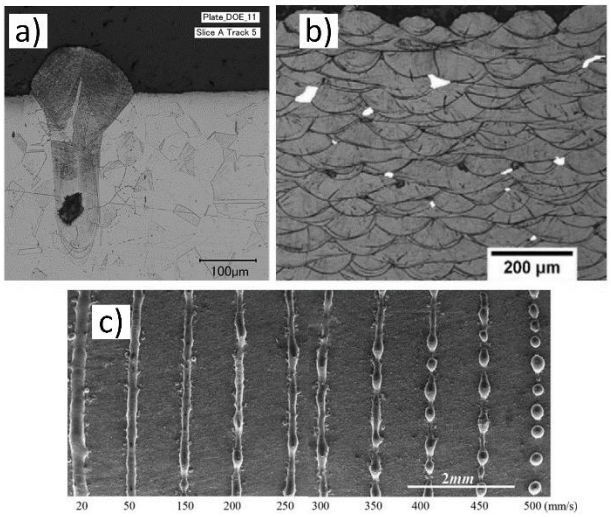

Figure 2.3. Porosity defects in LPBF, a) keyhole porosity [28], b) lack of fusion porosity [29], c) the balling effect [30].

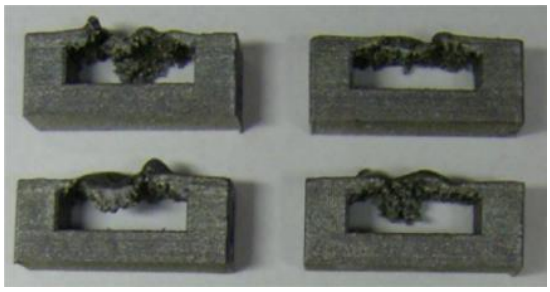

Figure 2.4. Failure of LPBF parts with down-face areas [32].

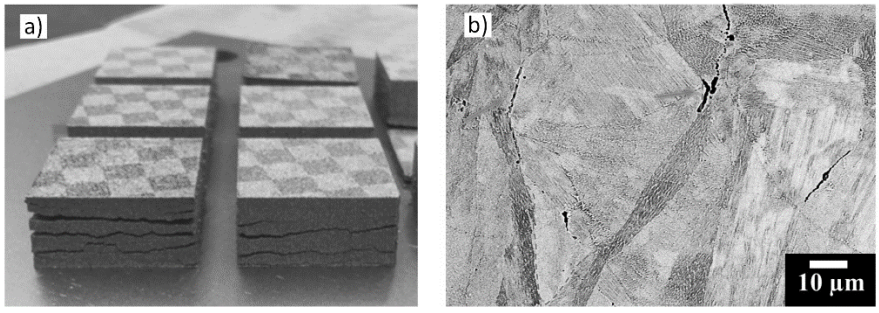

Figure 2.5. Delamination and cracks in LPBF parts, a) delamination [33], b) crack from the substrate [34].

2.2.1.2. Residual stresses and deformation in LPBF

Origin of residual stresses in LPBF

Residual stresses are defined as stresses which remain in material and at equilibrium with its surroundings after manufacturing, heat treatment, and other alterations whenever a material undergoes non-uniform plastic deformation within one part [35].

Residual stresses in LPBF are frequently built up in LPBF components [22,36]. They are caused by rapid laser scanning due to the thermal-stress-induced plastic deformation and the thermal shrinkage of the solidified melt pool [37]. The residual stresses in LPBF can be very complicated, e.g. oscillating residual stresses [38].

Influence of residual stresses

Residual stresses can lead to severely geometrical deformation, the formation of cracks, or even failure of the printing parts [14], as shown in Figure 2.6. In addition, residual stresses can cause fatigue properties of LPBF parts dramatically lower [39,40]. Therefore, residual stresses can significantly hamper the industrial applications of LPBF [9].

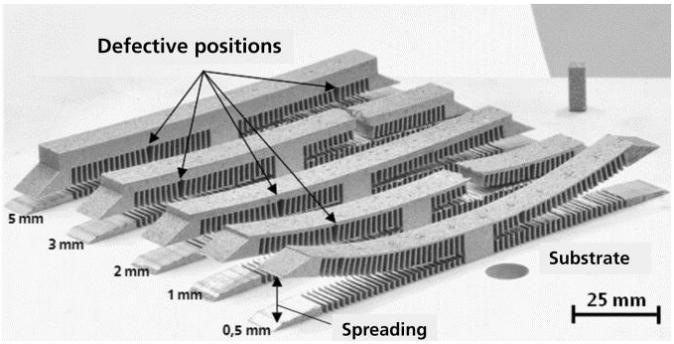

Figure 2.6. Distortion and failure of twin cantilevers made by LPBF [14].

Measurement of residual stresses and deformation

The residual stresses are locked in a material, so its measurements are indirect. Measuring residual stresses is more complicated than measuring stresses induced by external loads. For deriving the externally induced stress, the strains are first derived, and stresses are calculated based on the strains. The strains are measured by comparing the loading and unloading situations. However, for residual stresses, they cannot be removed and then loaded so that the strains are more difficult to be obtained. Typically, there are two categories for measuring residual stresses,

destructive and non-destructive methods. Destructive methods include the splitting method, sectioning method, layer removal method, the hole-drilling method, the deep-hole method, the slitting method, and the contour method [41]. They have also named relaxation measurement methods, whose basic idea is to remove away a portion of material containing residual stresses and then to derive the strains by comparing geometry before and after the removal. On the other hand, the non-destructive methods mainly consist of diffraction methods (X-ray diffraction, synchrotron X-ray, neutron diffraction), and other methods (magnetic, ultrasonic, thermoelastic, photoelastic, and indentation) [41].

For LPBF, several destructive methods that have been used are the hole-drilling method [38,42], the slitting method [38], and the contour method [42,43]. The non-destructive methods employed for LPBF includes, X-ray diffraction [42,44], synchrotron X-ray [45], neutron diffraction [46,47]. Figure 2.7 depicts an experiment of residual stress measuring for an LPBF part by using synchrotron X-ray diffraction. As for the deformation measurement, coordinate measuring machines (CMM) have been widely used [47].

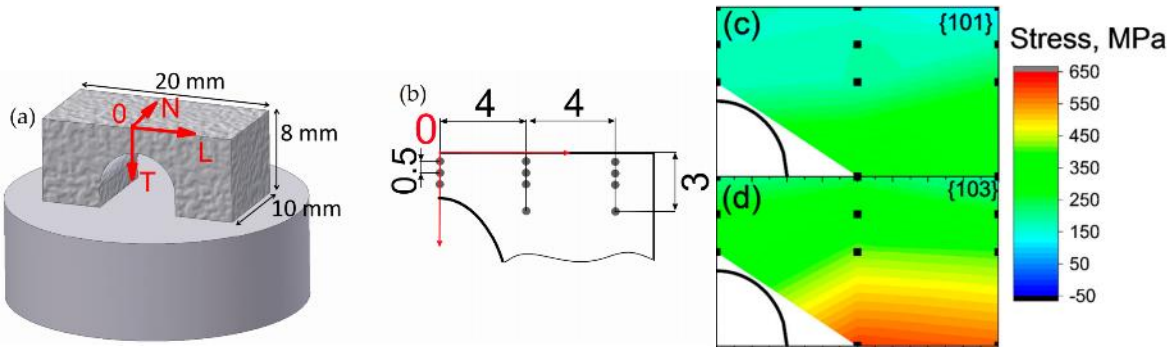

Figure 2.7. Residual stress measuring experiment, (a) schematic representation of a bridge-shaped sample made by LPBF additive manufacturing, (b) specification of the mapped area by a synchrotron, (c) and (d) residual stress maps for different crystallographic planes [45].

Reduction of residual stresses and deformation

Many other factors have influences on residual stresses in LPBF, including substrate geometry, build orientation, preheating of the substrate [9,19]. Preheating substrate was found one of the

most effective methods to reduce the residual stresses [9]. Furthermore, the process parameters (power, speed, layer thickness, scanning pattern, scanning sequence) are indicated to impact on the residual stresses and deformation significantly [9,19]. Therefore, process parameter optimization should be critical. Moreover, post-heat treatment can relieve residual stresses, which decreases the crack growth rate and improves the fatigue life of the printed parts [48]. Even though heat treatment was reported helpful in reducing the residual stress, it can decrease the mechanical properties of the printed parts, e.g. the ductility and strength [49,50].

Last but not least, support structures and part geometries can also influence the residual stresses and deformation [9,10]. Thus, by optimizing the topologies of the support structures and printed parts, the residual stresses and deformations can be reduced.

2.2.2. Opportunities: new design flexibilities

With AM, new design opportunities have been realized. As Rosen [2] indicated that AM has several unique capabilities (free-form fabrication, multi-scale design, multi-material manufacturing, and functional structures) that enable designers to maximize product performance through size, shape, and topology optimization subject to the capabilities of AM technologies.

2.2.2.1. Topology optimization of product structures

Topology optimization is a mathematical optimization process to find the optimal distribution of material in a given design domain under a couple of constraints. With topology optimization, a designer can derive high-performance structures, which may have lower weight, higher strength, increased stability, and other improvements impossible to be achieved in traditional ways.

The principles of topology optimization were first proposed around the beginning of the twentieth century by Michell, who studied the trusses design [51]. In the 1970s, Prager and Rozvany [52] formulated the basic principles of optimal layout theory. Finite-Element based topology optimization was proposed by Bendsøe in 1989 [53]. With many subsequent developments, it is now well established and has been used in many applications [54], such as

acoustics, cloaking, small antennas, energy harvesting mechanism, nano-photonics, fluids, and structural design. Figure 2.8a shows the topologically optimized ribs along the leading edge of A380 [55], and Figure 2.8b displays a topologically optimized bracket that is 64% lighter than the original design while reducing the maximum stress over 50% [56]. In the structural design field, lightweight designs are beneficial. For example, reducing one-kilogram flight mass airbus of A330 class is estimated to save 5000L of fuel during its lifetime [57].

(a)

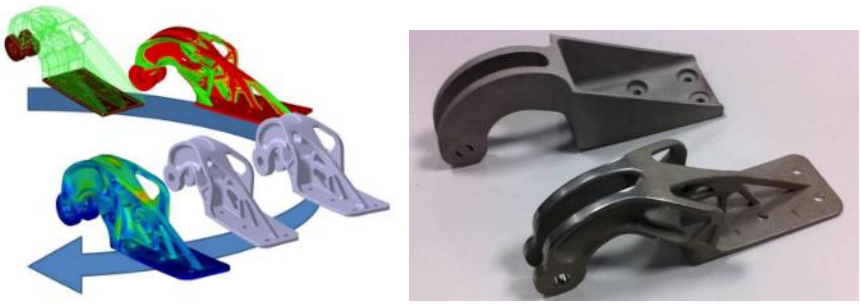

(b)

Figure 2.8. Examples of topology optimization, (a) optimized ribs in the wing of Airbus A380, (b) nacelle hinge bracket of Airbus A320.

2.2.2.2. Topology optimization of support structures

LPBF parts are usually printed with support structures that connect the part to the substrate. Support structure plays a critical role in three aspects, first supporting the weight of the overhang features, second, dissipating the laser heat to prevent overheating, and third, anchoring the printing part on the substrate to prevent unexpected deflections due to the residual stresses induced by the laser scanning [7,8]. However, support structures could cause additional cost due to longer

manufacturing time and substantial material waste caused by (a) volume of support structure (b) powder trapped inside the support structure that is wasted during part cleanup. Therefore, it is necessary to design cost-effective support structures that reduce either the manufacturing time or powder waste.

2.3. LPBF process modeling (coping with the challenges)

For addressing the challenges, process parameter optimization is necessary, but relying exclusively on experimental efforts to investigate melt-pool behaviors is expensive and time-consuming. Therefore, LPBF process modeling has been used to investigate the LPBF process. It can be significantly helpful not only in optimizing process parameters but also in predicting the residual stresses and deformation.

2.3.1. Analytical modeling

The analytical model of a moving heat source was first developed by Rosenthal [58] for welding. Later, the point heat source model was extended to a Gaussian distributed two-dimensional heat source model [59,60]. For LPBF, Yang et al. [61,62] proposed a semi-analytical thermal model of the LPBF process, in which the innovative point is considering the influence of the finite dimensions of the powder bed and the associated boundary conditions by an extra complimentary temperature field which is solved by the finite difference method. Ning et al. [63] proposed an analytical model including the boundary conditions by using pseudo heat sinks along the boundaries of the simulated domain and got a good match to the experimental results in terms of the melt pool dimensions. Moreover, the residual stress-induced deformations have been predicted by using analytical models and FEM [64,65]. Even though these works are promising and can give good results, only the thermal simulation is analytical, and the mechanical simulation in these works still relies on FEM. In addition, as melt pools in LPBF may not be in conduction

mode only [28] and the material properties may be temperature-dependent, the analytical model may still need more validations.

2.3.2. Particle-level modeling

LPBF is rather complicated since it includes multiple physics: photon absorption by particles [66], heat (heat conduction, heat convection, and radiation with extremely high heating and cooling rates), hydrodynamics (wetting of the powders with liquid, capillary effects, and Marangoni effect) [67], powder particles dynamics [68], gasification, plasma (keyhole effect) [69], phase change dynamics [70], and solid mechanics.

Therefore, some researchers applied particle-level models for investigating the heat flow and mass flow in melt pools [21,69,71–74], which included several details, such as Computational Fluid Dynamics (CFD) model, randomly distributed particles and laser-ray transmitting in particles, to simulate the melt-pool behaviors. Korner et al. [75,76] first considered a randomly packed powder bed, which is two-dimensional. The model studied the stochastic effect of particles, the influence of relative density, wetting, and capillary in LPBF. Khairallah et al. [21] developed a multi-physics code to simulate the 3D LPBF process. They coupled thermal analysis with hydrodynamics to analyze the phenomenon of Plateau-Rayleigh instability. Xia et al. [77] investigated the porosity evolution during LPBF by considering a randomly packed powder bed, thermodynamics, phase transition, and interfacial force. Recently, Panwisawas et al. [69] established a model including almost all interfacial phenomena and derived the temperature distribution of single-track molten zones. They found that with laser-scan speed increasing, the single tracks become increasingly irregular, which is shown in Figure 2.9. Furthermore, a CFD model was built to investigate the influence of the shield gas on the microstructures of the LPBF parts [78].

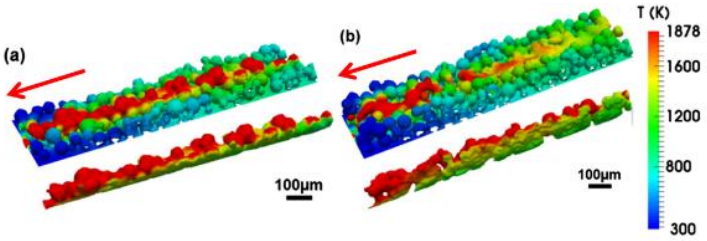

Figure 2.9. The temperature distribution of single track molten zones of (a) 20 μm layer thickness, and (b) 100 μm layer thickness [69].

In addition, for calculating the absorption of a laser beam by powders, Boley et al. [79] used ray-trace simulations. The relationships between absorption and powder content (material, size, distribution, and geometry) have been investigated. Absorption value can be affected by the size distribution and geometrical arrangement of powder spheres.

However, the computational cost for such simulations is exceptionally high. For example, the work done in [74] employed ALE3D (developed in Lawrence Liverpool National Laboratory) massively-parallel code, which consumes on the order 100,000 CPU-h [21], and the work in [73] took 140 h for only 4 ms simulation of the process. Moreover, because of the high computational cost, they cannot be directly implemented for thermo-mechanical simulation models for calculating the residual stresses and deformations. Furthermore, few particle-level models have been used in multi-layer simulations because of its complexity.

Therefore, the effective models, which will be discussed in the next section, are still efficiently used in the thermo-mechanical simulations.

2.3.3. Effective modeling

Effective models that employ several approximations and assumptions may be more effective and efficient but still accurate to predict the dimensions of melt pools (e.g., melt pool width and depth), which can be guaranteed by validating against the particle-level modeling or experiments. For simplification, instead of employing a laser-ray tracing method in randomly distributed particles, the heat source has been usually assumed as volumetric heat source models, and the

powder layer is presumed as homogeneous bulk materials with effective powder-layer material properties. Moreover, a valuable summary has been made that the primary modeling considerations may be heat source models, model dimension, material addition techniques, thermal-mechanical coupling techniques, and boundary conditions [80]. Moreover, the heat source modeling is the critical point for the prediction of microstructures in LPBF. In order to get well predictions of microstructures in LPBF, heat source models should be fundamental because it provides the thermal history which directly decides the microstructure formations [81,82].

2.3.3.1. Heat source modeling

In literature, researchers have employed various heat sources. They can be categorized into two groups based on their characteristics, namely (a) Geometrically Modified Group (GMG) and (b) Absorptivity Profile Group (APG). In GMG, different geometries are used to mimic the actual shape of the heat source, such as cylinder shape [83], semi-sphere [84], semi-ellipsoid [84,85], and conical shape [86]. For example, the work, in [83], built up a volumetric heat source model with the consideration of the optical-penetration depth (OPD) of the laser beam into the powder bed, where the shape of the heat source is a cylinder. Bruna-Rosso et al. [85] implemented the semi-ellipsoid heat source model, which was proposed firstly by Goldak et al. [84], in the LPBF simulation. The model showed good agreement with the experimental results. Wu et al. [86] proposed a conical shape of the heat source for arc welding, which is comparable to the LPBF process, and derived good accordance with experimental results.

On the other hand, in APG, the powder-bed of LPBF is viewed as an optical medium, and the laser beam is assumed to be absorbed gradually along the depth of the powder layer. Therefore, several absorptivity profiles have been proposed, such as the radiation transfer equation [66], absorptivity derived by the Monte Carlo method [87], linearly decaying equation [88], and exponentially decaying equation [89]. In APG, the heat source models are not constrained in specific geometries, and their general form is that two-dimensional Gaussian distribution is on the top surface while the laser beam is absorbed along the depth of the powder bed based on the

absorptivity functions. Gusarov et al. [66] presented a mathematical approach for effectively estimating the laser radiation scattering and absorption in powder layers and developed a volumetric heat source based on the radiation transfer. Liu, et al. [89] proposed a heat source model, which consists of a Gaussian profile on the *x* and *y* plane, and an exponentially decaying profile along the *z*-direction. The effective heat source models presented in the literature are computationally efficient and accurate while being compared to the corresponding experimental results. However, there is a lack of summary and comparison of them. Heat source modeling is regarded as one of the key factors that influence not only the melt pool dimensions but also thermal variables [89], e.g., the cooling rate, etc. Therefore, a summary and comparisons of heat sources used in the simulations of the LPBF process are necessary.

In addition to computation acceleration, thermal fluid dynamics, such as mass convection in the melt pool during LPBF, can be approximated effectively by the anisotropically enhanced thermal conductivity method [90]. The anisotropically enhanced thermal conductivity method could effectively improve the prediction precision of melt pool dimensions. However, its further investigation is still critical since it may be changed from one set of process parameters to others. Lastly, laser absorptivity is one of the most uncertain parameters during the numerical modeling, as discussed in [21,66]. All the simulation models mentioned in the above literature employed constant absorptivity, which may not be the case in reality. The laser absorption factor is influenced not only by the powder particle size and distribution but also the angle of incidence that varies due to the dynamic melt pool surface [91]. Trapp et al. [91] and Matthews et al. [92] have studied the absorptivity in LPBF using experimental approaches. The variation of absorptivity was observed very large from 0.3 up to near 0.7, corresponding to different process parameters. It seems that in some range of process parameters, the absorptivity was directly proportional to the laser power. However, there is still a lack of explicit expressions between the absorptivity and the process parameters. Besides, investigations on more different kinds of materials are still needed.

Bruna-Rosso et al. [93] proposed a global-sensitivity-analysis scheme to investigate the most influential parameters in the numerical model of LPBF and found that the emissivity coefficient significantly influences the simulation output besides LPBF process parameters. This method gives further developments of LPBF simulation models some guidance on which parameters should be paid more attention.

2.3.3.2. Powder layer thickness

Layer thickness is regarded as one of the most important parameters [31,94,95] since it can help to eliminate the process defects. Li, et al. [30] investigated the influence of layer thickness on the process defects, namely, pores and the balling phenomenon, was studied qualitatively. They found that incompatible layer thicknesses lead to excessive balling and high porosity in printed parts. Similarly, [96] proposed an analytical model to predict the surface roughness of final products and found that minimizing the layer thickness reduces the surface roughness of printed parts.

Layer thickness can also influence the build rate in the LPBF process since a smaller layer thickness relates to more printed layers, leading to more laser scanning [97]. In other words, larger layer thicknesses are very beneficial and can significantly accelerate the manufacturing process [98,99]. However, a larger layer thickness usually leads to higher surface roughness, especially on overhanging and sloped surfaces [100]. Therefore, optimizing the layer thickness corresponding to specific materials and required part performance is essential for manufacturing LPBF parts.

2.3.3.3. Thermo-mechanical modeling

An effective model can help to predict and understand the residual stresses and deformations in LPBF.

Cao et al. [101] built up a fully coupled thermo-mechanical model for predicting deformation and residual stresses in electron beam additive manufactured parts. On the contrary, the one-way coupled thermo-mechanical model was also built to investigate the residual stresses[102].

Other properties have also be included in thermo-mechanical modeling. Li et al. [103] considered the shrinkage of the powder layer after melting in a model predicting the temperature and residual stress fields in LPBF. Tan et al. [104] considered a solid-state phase transformation (SSPT) model and showed that SSPT may improve the accuracy of the residual stress prediction.

Importantly, studies have shown that scanning strategies influence the residual stresses in the LPBF parts [105,106]. Therefore, many researchers have paid attention to studying scanning strategies for the sake of reducing residual stresses. Mugwagwa et al. [107] found that by changing the scanning sequence of islands in the chessboard scanning pattern, the residual stresses and deformation were significantly reduced. Bhardwaj et al. [108] found the laser scanning strategies influence the texture, physical, and mechanical properties of the laser-sintered parts. The rotational scanning strategy helped to form preferential microstructure due to the heat flux becoming uniform. Ramos et al. [109] proposed an interesting scanning method by using a distance function, whose main idea is to spread the heat throughout the region so that a lower gradient temperature and deformation could be expected. Ali et al. [50] found that rescanning is not feasible for LPBF parts, due to the increased build time and the detrimental effect on residual stresses build-up and as well as mechanical properties of the printed parts.

Advanced computing techniques have employed in the LPBF process modeling. Denlinger et al. [110] proposed a three-dimensional non-linear thermo-elasto-plastic finite element model for LPBF, where adaptive mesh was employed. The model has been validated by comparing with the experimental deformations. Neiva et al.[111] developed a parallel finite element framework, named FEMPAR-AM, for metal additive manufacturing at the part scale. The adaptive mesh was incorporated into the framework, as well. A maximum of 19 times speedup was achieved.

In the future, numerical models could use the following experimental data as validating references. Brown et al. [46] investigated the residual stresses in additive manufactured samples by using the neutron diffraction method. They found that the stresses before and after support removal are considerably different, which indicates the cutting sequence of the support structure

could lead to different deflections. Levkulich et al. [42] investigated the influence of process parameters and substrate conditions on the evolution of residual stresses in LPBF through three different measurement techniques, X-ray diffraction, hole-drilling, and contour-method. The findings are interesting that the residual stresses were reduced by increasing laser power, decreasing scan speed, and heat treating the substrate before printing. Phan et al. [47] provided a benchmark geometry for residual stress measurements through three different methods, neutron diffraction, synchronized XRD, and contour method. The residual stress measurements by synchronized XRD and contour method matched well.

2.3.4. Part-level modeling

Even though understanding physics in melt pools should be necessary and essential, the dimensions of the models in the above studies are small (1 mm), compared to an AM part (10^1 cm). The part-level simulation should include the deposition process of multiple layers. Thus, it may be unmanageable to use those methods to deal with a part-level simulation. Therefore, fast computation methods for part-level analysis are still critical, especially for topology optimization because of its inherently iterative character.

For acceleration, an analytical model was proposed by Mercelis et al. [33] for studying the residual stresses in LPBF, which had a good qualitative coherence with the experiments. Moreover, researchers have been trying to accelerate the simulation by using a larger heat source, e.g. a vector, a layer, or a domain of melting material is deposited at a time. This method is named as the equivalent heat flux domain method. On the other hand, an equivalent mechanical method has also been proposed, in which a whole layer of material with some specified inherent strains is added each time. This method does not need a heat transfer simulation so that the simulation can be further accelerated. Besides, several other techniques and methods are employed, such as the birth and death method, and the adaptive mesh technique.

2.3.4.1. Equivalent heat flux domain method

The technique of birth and death is suitable for describing AM's material adding procedure, in which new elements are activated at the desired time. Matsumoto et al. [112,113] may be the first researchers to calculate the distribution of temperature and stress in one single layer in LPBF. Robert et al. [114] may be the first researchers to propose a multi-layer simulation model of LPBF using the element birth and death method. Lei et al. [115] employed the birth-and-death technique to simulate the temperature distribution during cladding composite coatings. Zhao et al. [116] investigated the thermal behavior of a single-pass multi-layer rapid prototyping by FEM and experiments. Kolossov et al. [117] developed a thermal model of selective laser sintering, which was comparable with experimental results. Zhang et al. [118] investigated the influence of the different dimensions of the activated domains in a domain-by-domain activation method.

Computational efficiency may be improved by using the adaptive-mesh technique, in which mesh is automatically adjusted during the simulation process. Zeng et al. [119] researched the adaptive-mesh method for LPBF, which enabled the mesh in melt pools and heat-affected zones to be refined while the remaining part of being coarser. Thus, they reduced the computational cost and derived acceptable accuracy compared with a uniform fine mesh model. Moreover, further accelerated modeling could owe to further assumptions and numerical techniques. Keller et al. [120] built a part-level simulation for LPBF by implementing the heat flux on a slice of a part at once instead of the actual-scan process, which could decrease the calculation time, as illustrated in Figure 2.10. In Seidel et al.'s work [121,122], four heat-input models for calculation temperature distribution in the LPBF process have been explained separately. Papadakis et al. [123,124] compared computational reduction models for thermal and mechanical analysis of the LPBF process, which were laser-heat input volume-by-volume, layer-by-layer, and vector-by-vector.

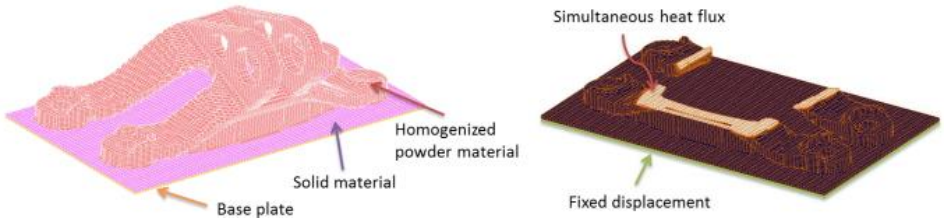

Figure 2.10. Boundary conditions and thermal loads of layer-by-layer heat input model [120].

Chiumenti et al. [125] employed the element birth-and-death technique to simulate the temperature distributions in LPBF. Three different sizes of the domain for activating are used, and they are hatch-by-hatch, layer-by-layer, and reduced hatch-by-hatch. Thermal couples were embedded in the printed part when the printing was stopped halfway in order to validate the temperature distribution. The temperature from simulated results and experiments have a good agreement. However, the residual stress distribution should be further validated.

2.3.4.2. Equivalent mechanical layer method

Similar to the equivalent heat flux domain method, researchers also investigated using an equivalent mechanical layer method to achieve the part level simulation of LPBF, in which a whole layer of material with some specified inherent strains or initial stresses is added at each time. The initial residual stress method and the inherent strain method can accelerate part-level modeling because only elastic modeling is needed to estimate deformation and residual stresses given the initial local stress or inherent strain. Their similar ideology is that mechanical results of a mesoscale analysis are imported into a macro-scale part due to the comparable mechanical history in melt pools. Li et al. [126] built a multiscale model with the idea of initial residual stress, in order to fast predict part deformation in LPBF, which included microscale, mesoscale, and macroscale simulation. Keller et al. [127] used the concept of inherent strain to build a fast simulation model for predicting deformation and residual stresses of AM parts, which may have been used in a commercial software-Simufact additive® and Additive Works®. A part-level simulation proved a similar trend of deformation as the experiments did, which is presented in Figure 2.11.

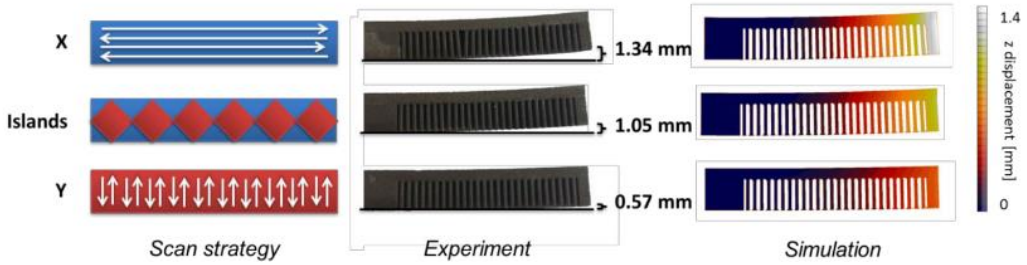

Figure 2.11. Comparison of the deformation of a cantilever specimen between the results of simulation and those of experiments [127].

Most recently, Siewert et al. [128] did a comprehensive validation for the inherent strain method, in which both the residual stresses and deformation are validated by experiments. They found that even though the inherent strain method has some simplifications, reliable prediction of residual stresses and deformations can still be achieved.

2.3.4.3. Other methods

Besides the above method, Peng et al. [129] proposed an innovative method that is a thermal circuit network model. In that model, the part and support structures were divided into the so-called thermal circuit element. The conductive heat transfer is interpreted by layer-by-layer addition of thermal circuit elements, so that the FEM thermal modeling can be replaced. This method results in two orders of magnitude acceleration compared to the FEM thermal modeling while sacrificing less than 15% accuracy.

2.3.5. Software and parallel computing

Several computational software and codes have been used in the numerical modeling of the LPBF process. They are summarized in Table 2.1.

Table 2.1. Available software for the LPBF process simulation.

Name	Description	References
3DSim®	One of the first software for LPBF. Developed by the group of Prof. Stucker. Acquired by Ansys in 2017.	https://www.ansys.com/products/structures/additive-manufacturing
Simufact Additive®	MSC software. Mainly based on the inherent strain method.	https://www.mscsoftware.com/product/simufact-additive
ESI®	France based company. Particle-level simulation.	https://www.esi-group.com/software-solutions/virtual-manufacturing/additive-manufacturing
Additive Works®	CEO Keller is the first to propose to use the inherent strain method in LPBF.	https://additive.works
Netfabb®	Strong mesh operation ability. Acquired by Autodesk®	https://www.autodesk.com/products/netfabb/overview
Ansys®	APDL. Before acquiring 3DSim, users built the LPBF models by themselves. High-Performance Computing (HPC) enabled.	[103,104,130]
Abaqus®	Strong mechanical analysis ability. Users built the LPBF models by themselves.	[19,101,102,131–133]
Comsol®	Strong multi-physics simulation ability. Particle-level and part-level are also enabled. Users built the LPBF models by themselves. High-Performance Computing (HPC) enabled.	[78,134]
MSC®	Commercial software. The most cited paper from the journal Additive Manufacturing used this software.	[37,110]
ALE3D	Particle-level model by Lawrence Livermore National Laboratory. Fluid dynamics. High-Performance Computing (HPC) enabled.	[21,74]
Diablo	Thermo-mechanical simulation for LPBF by Lawrence Livermore National Laboratory. Fluid dynamics.	[135]
Comet	FE software developed at the International Center for Numerical Methods in Engineering (CIMNE). Need an exclusive agreement to use.	[136]. http://www.cimne.upc.edu
CUBES®	Developed by Pan Computing LLC. Then it is now acquired by Autodesk®.	[137]
Deal.II	Open-source code. Strong ability in the adaptive mesh that is necessary for the LPBF process simulation. High-Performance Computing (HPC) enabled.	[85,93,138,139]

2.4. Topology optimization for LPBF (embracing the opportunities)

LPBF enables new design flexibilities, among which topology optimization is an important one. In this literature review, two aspects will be paid attention to, the topology optimization for LPBF product structures and topology optimization for LPBF support structures.

2.4.1. Topology optimization for LPBF product structures

AM can make the complex geometries obtained through topology optimization. Topologically optimized structures such as the nacelle hinge bracket mentioned above, bridges, aerospace components, have been achieved by AM [140–142]. Moreover, an optimized heat sink or internal cooling channels have been fabricated [143,144]. Compliant mechanisms with multiple materials designed by topology optimization can be obtained by AM [145,146]. In the medical field, continuous advances in both topology optimization and AM make it possible to create scaffolds, which can balance mechanical function with mass transport to aid biological delivery and tissue regeneration [147–149], as shown in Figure 2.12a and b. Furthermore, with AM, many innovative structures, such as structures with negative Poisson's ratio [150], has been realized, as shown in Figure 2.12c.

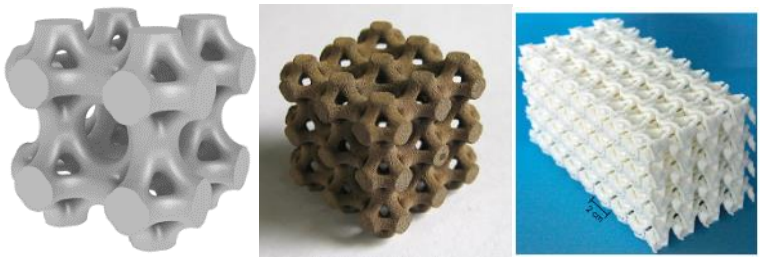

(a) (b) (c)

Figure 2.12. Innovative structures, (a) (b) scaffold lattice structure [149], (c) negative Poisson's ratio structure [150].

In addition, topology optimization can reversely help to mitigate the limitations of the AM process by considering manufacturing constraints in the structural-design stage. Those constraints

can be expressed by penalty functions and can be combined with the structural response into a single objective function. With the objective function, topology optimization can be carried out.

2.4.1.1. Minimum feature size control

For AM technologies, the minimum feature size control is dependent on the printing methods. For LPBF, there is usually a limitation of the minimum feature size. For instance, if a printed part is too small, it will be broken by the recoater. In addition, the LPBF minimum feature size is also determined by the melt pool size. The successful method is the so-called robust formulation [151,152] for warranting minimum feature size in density-based topology optimization. This method is based on implicit geometric constraints. Another method based on geometric constraints was proposed by Zhou et al. [153], which explicitly added constraint of minimum feature size to the original design problem. These two approaches can guarantee a minimum length scale for both the solid and the void phase, and the minimum feature size can be different for the two phases, which is beneficial for LPBF.

2.4.1.2. Cavity constraint

For LPBF, enclosed voids in a design should be carefully avoided; otherwise, powder material will be trapped in the enclosed voids. The approach for excluding the internal voids has been achieved by a cavity constraint. A “virtual temperature method” has been proposed for interpreting this cavity constraint [154,155], where a virtual heat source is set up within the void field, and a restriction is enforced on the maximum temperature. Isolated voids would consequently lead to heat accumulation and increasing maximum temperature, and therefore, voids are punished and eliminated by the added constraint.

2.4.1.3. Overhang constraints

For reducing the volume of support structures, maximum self-support angle (maximum overhang angle) can be regarded as the manufacturing constraint. Violation of such constraint is quantified through the use of a penalty function, which is combined with the original objective

functions in a single-new objective function; therefore, the problem can be solved as a common topology optimization problem [146,156]. The result of a beam-design problem with 45 deg overhang constraint is depicted in Figure 2.13, which does not need support structures during manufacturing.

Figure 2.13. Topology optimization result of the MBB beam problem with 45 deg overhang constraint [146].

2.4.1.4. Deformation compensation

Topology optimization can be used to consider the deformation during the LPBF manufacturing process. Allaire et al. [157] developed a layer by layer thermo-elastic model for AM and incorporated it into topology optimization in order to minimize the deformation and stress caused by the laser heat during the LPBF process. The optimization begins with an initial design that is obtained from a compliance-minimization problem. Compared to the initial design, the optimized result has less stress and deformation.

2.4.2. Topology optimization for LPBF support structures

LPBF parts are usually printed with a support structure that connects the part to the substrate. Support structures play a critical role in three aspects, first supporting the weight of the overhang features, second, dissipating the laser heat to prevent overheating, and third, anchoring the printing part on the substrate to prevent unexpected deflections due to residual stresses induced by the laser energy [7,8]. However, support structures could cause additional cost due to longer manufacturing time and substantial material waste caused by (a) volume of support structure (b) powder trapped inside the support structure that is wasted during part cleanup. Therefore, it is necessary to design cost-effective support structures that reduce either the manufacturing time or powder waste.

Most of the current LPBF manufacturing is conducted by using the support structures available in the current commercial LPBF software. However, the types of available supports are limited and rely on technicians' experience. Moreover, the functionalities of these support structures, e.g., dissipating heat and anchoring parts to prevent unexpected deflections, are still not available. The support structures need to consider these aspects during design as it might fail printing.

Design of an effective support structure depends on its ability to produce parts without any in-process errors while also using the least amount of powder to produce those supports. Topology optimization is commonly used as an effective approach to design high-performance structures for various objectives such as minimum compliance, reducing stresses, material usage, etc. [158–163]. Topology optimization usually generates geometrically complex parts, which makes topology optimization an ideal approach for the design of AM parts and support structures. [140,164–166]. In this regard, researchers have used topology optimization to reduce support structures in LPBF for producing self-supporting parts by using overhang constraints. Several approaches have been proposed in the literature to employ overhang constraints to print self-supported parts [156,167,168].

It is not possible to completely remove support structures for all geometries e.g. cantilevers. In addition, as mentioned previously, the functionalities of these supports should be included in the support structure design. Topology optimization for optimizing the support structure has been used in designing these types of supports. For the heat dissipation functionality, Zhou et al. [169] proposed a transient heat transfer based support structure optimization technique for LPBF for improving the heat dissipation performance of support structures. On the other hand, for reducing the part deflections and residual stresses through the support topology optimization, the topology optimization for the LPBF supports design requires not only the topology optimization framework but also a modeling approach that simulates the response of optimized parts. For this purpose, a fast computational technique called the Inherent Strain Method (ISM) [170] has been used for the fast prediction of deformations and residual stresses in LPBF parts [126,127,171]. A few

researchers have proposed ISM models for the optimization of support structures by using in-house and commercial software [172–174]. Cheng et al. [173] proposed a stress-based approach to reduce the maximum residual stresses caused during LPBF printing. Bartsch et al. [174] developed a two-step approach for support structure design in LPBF by linking the ISM simulation in Amphyon® with topology optimization in Comsol®.

Besides incorporating the required functionalities into the support topology optimization, a high resolution of design domains is required to avoid erroneous results [175]. In this regard, employing high-performance parallel computing provides the most efficient solution. Aage et al. [176] first developed a parallel and easy-to-use platform for large-scale topology optimization based on the solid isotropic material with penalization (SIMP) method and successfully implemented it into a giga-voxel structural design [177]. Liu et al. [175] realized a fully parallel parametrized level set method and applied it for up to 7 million elements. Mezzadri et al. [178] first proposed a high-resolution gravity-based topology optimization of AM support structures.

Despite the prospect shown in the above topology optimization for LPBF product and support structures, topology optimization for LPBF is yet fully mature. Work presented in the literature provides insight into solutions for topology optimization, ISM, and parallel computing. However, there is still a major gap between the high-performance computing topology optimization framework and support structure design in consideration of mechanical loads induced by the residual stresses produced during LPBF. Moreover, because of the character of optimization algorithms, optimization may not converge to a clear geometry with manufacturing constraints. Therefore, efficient and intelligent software is essential to extract the results of topology optimization; otherwise, post-processing may cost much time [1,179]. Secondly, structural performance may be very sensitive to the dimensional accuracy of the finished part [180]. Thus an active area of research is reducing the sensitivity of topologically optimized structures to manufacturing defects [181]. Thirdly, mathematically expressing manufacturing constraints would be challenging, since that requires a comprehensive understanding of the AM process. For example,

for the LPBF process, melt-pool behavior, residual stress, and deformation are still under investigation, since LPBF has some very complicated physical phenomena [9,20,21,182,183]. Most importantly, fast simulation of the AM process, especially part-level simulation, should be critical, because topology optimization requires many times of such simulation. If it is not fast enough, topology optimization will become extremely time-consuming.

2.5. Summary

In this chapter, several aspects of design for LPBF have reviewed, including LPBF and its challenges and opportunities. The challenges include defects in LPBF parts, residual stress, and deformation in LPBF. The LPBF process modeling, which is for dealing with the challenges, has been reviewed. The opportunities include mainly the free-form fabrication, which can be achieved by topology optimization. Topology optimization for LPBF, which utilizes the opportunities provided by LPBF, has also been reviewed.

Chapter 3. Design, Optimization, and Simulation System for AM

3.1. Introduction

In this chapter, a system of design, optimization, and simulation for AM will be illustrated. Under the background of industry 4.0, automation and data exchange will be pervasive in the manufacturing industry. AM as one of the most automatic manufacturing methods will play an increasingly significant role. Smooth workflow for AM from design to manufacturing should be beneficial, which has drawn many giant companies' attention, such as Siemens ®, and Altair ® [184,185], since it can realize high-performance products, accelerate the upgrading of products, and reduce R&D expenses. The workflow of this design-to-manufacturing process will be investigated, which includes topology optimization, post-processing, performance simulation, and manufacturing process simulation. The focus will be on the first three steps and leave the last one to the next chapters.

3.2. The system

A design, optimization, and simulation system, consisting of topology optimization, post-processing, performance test, and manufacturing simulation, has been developed, as shown in Figure 3.1. At the beginning, one defines a design domain with several boundary conditions. Then one can start to do topology optimization with defined objective and constraint functions. After multiple iterations, a converged structure can be obtained. As shown in Figure 3.1, the results of topology optimization are very rough, full of small blocks due to the inherent characteristic of topology optimization. Thus, post-processing to extract and refine the results should be essential. The results directly can be modified through several enhanced CAD modules [186]. Also, during an optimization, one may only consider a portion of the original part for efficiency based on

symmetries, so that part recovery should also be included during the post-processing. After that, it is needed to do a performance simulation to verify that the topologically optimized parts have satisfied design requirements. Before doing the performance simulation, one probably needs to convert the facet geometries obtained from the post-process into solid geometries or meshes. The last but not least, before throwing the CAD file to a printer, the manufacturing simulation should be conducted in order to check the manufacturability, including whether the part will fail during the manufacturing process because of thermal deformation and residual stresses.

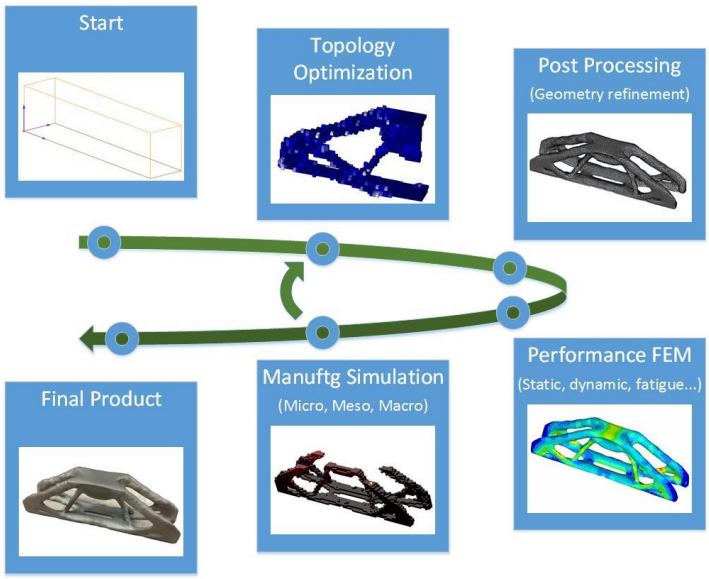

Figure 3.1. The schematic diagram of the design, optimization, and simulation workflow.

3.3. Topology optimization

Structural optimization can be divided into three levels according to the different types of design variables: size optimization, shape optimization, and topology optimization, which is demonstrated in Figure 3.2 [54]. In size optimization, designers may want to find the optimal dimensions such as thickness and cross-section area. The goal of shape optimization is to find the optimal shape of geometrical features in a design domain, such as optimizing a circular hole into an elliptical shape for the sake of lower stress concentration. On the other hand, topology

optimization will optimize the number and the locations of those geometrical features in the design domain, so that it is also called conceptual design.

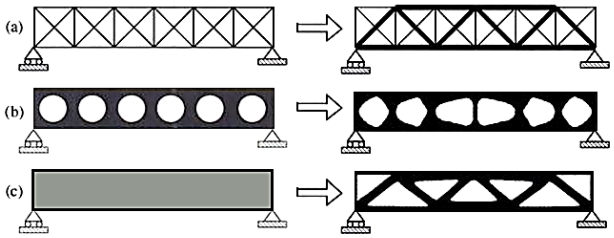

Figure 3.2. Illustration of the three levels of optimization, (a) size optimization, (b) shape optimization, and (c) topology optimization [54].

For topology optimization, a commonly used objective is to minimize the compliance, which is equal to maximizing global stiffness. Consider the elastic domain shown in Figure 3.3, in which some locations have been fixed with material and with a void. The feasible design domain is Ω. The boundary conditions are fixed displacement Γ_u, load boundary Γ_t and body force *f*. Moreover, it is assumed that the volume fraction of material in the feasible design domain is η. Topology optimization is to choose the optimal distribution of material in the feasible design domain Ω with those prescribed boundary conditions and constraints. The minimum compliance problem can be expressed mathematically in the following form.

$$\begin{aligned} &\underset{\boldsymbol{u}\in U,\boldsymbol{\varphi}}{\text{minimize}}: \quad E=\int_{\boldsymbol{\Omega}} \boldsymbol{f}\cdot\boldsymbol{u}d\boldsymbol{\Omega}+\int_{\boldsymbol{\Gamma}_t} \boldsymbol{t}\cdot\boldsymbol{u}d\boldsymbol{S} \\ &\text{subject to}: \quad \delta\Pi(\boldsymbol{u})=\delta\left(\int_{\boldsymbol{\Omega}}\frac{1}{2}\boldsymbol{D}_{ijkl}(\boldsymbol{\varphi})\boldsymbol{\varepsilon}_{ij}(\boldsymbol{u})\boldsymbol{\varepsilon}_{kl}(\boldsymbol{v})d\boldsymbol{\Omega}+\int_{\boldsymbol{\Omega}}\boldsymbol{f}\cdot\boldsymbol{v}d\boldsymbol{\Omega}+\int_{\boldsymbol{\Gamma}_t}\boldsymbol{t}\cdot\boldsymbol{v}d\boldsymbol{S}\right)=0, \\ &\quad \forall\boldsymbol{v}\in\boldsymbol{U} \\ &\quad \boldsymbol{\varphi}\in\boldsymbol{\Omega}_{sub}=\eta\cdot\boldsymbol{\Omega} \end{aligned} \tag{3.1}$$

where *E* can be regarded as the potential energy of loads. *u* is the solution for the displacement vector of the domain, while *v* is any displacement vector of the domain. *U* is the space of displacement fields. $\delta\Pi$ is the variation of the total potential energy of the whole domain. φ is the coordinates within a Cartesian reference frame. $D_{ijkl}(\varphi)$ is the tensor of elasticity constant. ε_{ij} and ε_{kl} are strain tensors. Ω_{sub} is the subdomain of the feasible domain Ω, based on the volume fraction η.

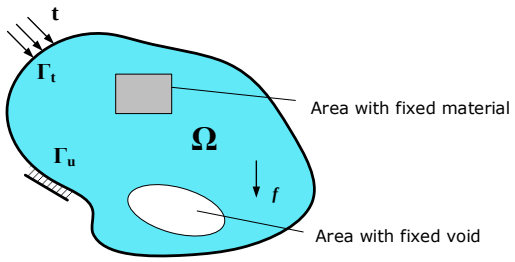

Figure 3.3. Schematic boundary conditions of topology optimization.

When employing the Finite Element Method (FEM) to solve the problem shown in Eq.(3.1), one can get the discrete form of Eq.(3.1) as follows.

$$\begin{aligned} \underset{x}{\text{minimize}}: \quad & \boldsymbol{F}^T \boldsymbol{u} \\ \text{subject to}: \quad & \boldsymbol{K}(\boldsymbol{x})\boldsymbol{u} = \boldsymbol{F} \\ & V(\boldsymbol{x}) <= \eta \cdot V_{\boldsymbol{\Omega}} \\ & \underline{x}_j \le x_j \le \overline{x}_j, \quad j = 1,\ldots,n \end{aligned} \tag{3.2}$$

where F is the load vector. u is displacement vector. $K(x)$ is the stiffness matrix. x is the vector of design variables, in which x_j represents the existence of material in the j^{th} element. x_j is 1, meaning that there is material in the element, while x_j is 0, meaning no material. In addition, $\underline{x}_j$ is set to a minimal positive number close to 0 in order to avoid numerical error, and $\overline{x}_j$ is usually 1. $V(x)$ is the volume of used material.

More generally, a structural topology optimization problem could be in the following form.

$$\begin{aligned} \underset{x}{\text{minimize}}: \quad & f_0(\boldsymbol{x}) \\ \text{subject to}: \quad & f_i(\boldsymbol{x}) \le 0, \quad i = 1,\ldots,m \\ & \underline{x}_j \le x_j \le \overline{x}_j, \quad j = 1,\ldots,n \end{aligned} \tag{3.3}$$

where $x = (x_1,\ldots,x_n)^T$ is the vector of design variables, $f_0(x)$ is the objective function, which usually is the compliance of structures. $f_i(x) \le 0$ are constraints, for example, the volume or weight limitations of structures. $\underline{x}_j$ and $\overline{x}_j$ are given lower and upper bounds of the design variables.

How to find the solution for the optimization problem in Eq.(3.3) is one of the key points. Most optimization algorithms need to do iterations before finding the optimal solution. It is necessary to

introduce a famous and widely used optimization algorithm in the field of topology optimization—Method of Moving Asymptotes (MMA) [187].

The objective and constraint functions may usually be implicit functions, so MMA uses the information of the current k^{th} iteration (k = 0, 1, 2,…) to rebuild explicit functions for approximating original functions, which is expressed in Eq.(3.4). The information includes sub-limits of the variable x_j, which are $L_j^{(k)}$ and $U_j^{(k)}$, point position $x^{(k)}$, function values $f_i(x^{(k)})$, and gradients $\partial f_i/\partial x_j$ at $x = x^{(k)}$. In addition, k is the iteration No., and when it is equal to zero, it means one uses the initial point to build explicit functions. The value of k depends on how many iterations are needed to get the optimal solution. $L_j^{(k)}$ and $U_j^{(k)}$ are known as moving asymptotes, which are normally changed between iterations.

$$f_i^{(k)}(\boldsymbol{x}) = r_i^{(k)} + \sum_{j=1}^{n}\left(\frac{p_{ij}^{(k)}}{U_j^{(k)} - x_j} + \frac{q_{ij}^{(k)}}{x_j - L_j^{(k)}}\right), \quad i = 0,1,\ldots,m$$

where

$$\begin{aligned}
p_{ij}^{(k)} &= \begin{cases} (U_j^{(k)} - x_j^{(k)})^2 \partial f_i / \partial x_j, & \text{if } \partial f_i / \partial x_j > 0 \\ 0, & \text{if } \partial f_i / \partial x_j \le 0 \end{cases} \\
q_{ij}^{(k)} &= \begin{cases} 0, & \text{if } \partial f_i / \partial x_j \ge 0 \\ -(x_j^{(k)} - L_j^{(k)})^2 \partial f_i / \partial x_j, & \text{if } \partial f_i / \partial x_j < 0 \end{cases} \\
r_i^{(k)} &= f_i(\boldsymbol{x}^{(k)}) - \sum_{j=1}^{n}\left(\frac{p_{ij}^{(k)}}{U_j^{(k)} - x_j^{(k)}} + \frac{q_{ij}^{(k)}}{x_j^{(k)} - L_j^{(k)}}\right) \\
\underline{x}_j &\le L_j^{(k)} < x_j < U_j^{(k)} \le \overline{x}_j, \quad j = 1,\ldots,n
\end{aligned} \tag{3.4}$$

Therefore, the equivalent optimization problem of Eq.(3.3) can be written as Eq.(3.5).

$$\begin{aligned}
&\underset{\boldsymbol{x}}{\text{minimize}}: \quad f_0^{(k)}(\boldsymbol{x}) = r_0^{(k)} + \sum_{j=1}^{n}\left(\frac{p_{0j}^{(k)}}{U_j^{(k)} - x_j} + \frac{q_{0j}^{(k)}}{x_j - L_j^{(k)}}\right) \\
&\text{subject to}: \quad \underline{x}_j \le L_j^{(k)} < x_j < U_j^{(k)} \le \overline{x}_j, \quad j = 1,\ldots,n \\
&\qquad\qquad f_i^{(k)}(\boldsymbol{x}) = r_i^{(k)} + \sum_{j=1}^{n}\left(\frac{p_{ij}^{(k)}}{U_j^{(k)} - x_j} + \frac{q_{ij}^{(k)}}{x_j - L_j^{(k)}}\right) \le 0, \quad i = 1,\ldots,m
\end{aligned} \tag{3.5}$$

Then, the problem can be solved by the Lagrangian multiplier method, shown in Eq.(3.6).

$$L(\boldsymbol{x}, \boldsymbol{\lambda}, \boldsymbol{\xi}, \boldsymbol{\eta}) = f_0^{(k)}(\boldsymbol{x}) + \sum_{i=1}^{m} \lambda_i f_i^{(k)}(\boldsymbol{x}) + \sum_{j=1}^{n}(\xi_j (L_j^{(k)} - x_j) + \eta_j (x_j - U_j^{(k)})) \tag{3.6}$$

where $\lambda = (\lambda_1,\ldots,\lambda_m)^T$, $\xi = (\xi_1,\ldots,\xi_n)^T$, $\eta = (\eta_1,\ldots,\eta_n)^T$ are non-negative Lagrange multipliers for the different constraints in Eq.(3.5).

As discussed above, through step-by-step iterations, the optimal solution may be found; however, this process may need many repetitions. This inherently iterative character of the topology optimization process should require fast simulation in each iteration; otherwise, the total computational time could be unacceptable. Therefore, if the AM process is taken into considerations during topology optimization, the computational time of the AM-process simulation should be fast enough. Several accelerated simulation methods for the AM process will be discussed in Chapter 7.

3.4. Mesh smoothing

During topology optimization, optimization algorithms decide the distribution of material and void. Since the design domain has been discretized into finite elements, the boundary between material and non-material may become toothed, as shown in Figure 3.4a. Thus, such a result of topology optimization with rough surfaces could not be manufactured or simulated easily. The result needs to be expressed in a more practicable CAD model.

Commonly, two methods can deal with this problem. One is to draw the result in a CAD software manually based on the topology optimization. However, the remodeling process will significantly depend on the experience of operators. Besides, it is a time-consuming process. The other method is to employ a computer to extract the result automatically based on an isosurface of the topologically optimized results. In this way, it is possible to obtain smoother surfaces compared to the original result. Thus, in this work, the second method is used to extract the results of topology optimization. The extracted isosurface of the result is depicted in Figure 3.4b.

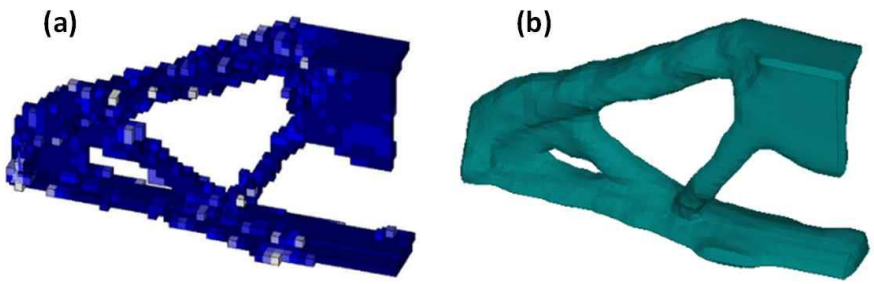

Figure 3.4. A topology optimization result, (a) original rough surface, (b) extracted-smooth isosurface.

Then, one can build the whole structure based on the one quarter obtained from topology optimization, shown in Figure 3.5a. It is necessary to mention that products of the isosurface extraction are 2D-facet meshes. From Figure 3.5b, one can see that the facet mesh includes long and thin elements, which will lead to ill 3D elements when converted to a solid mesh for the following FEM simulation.

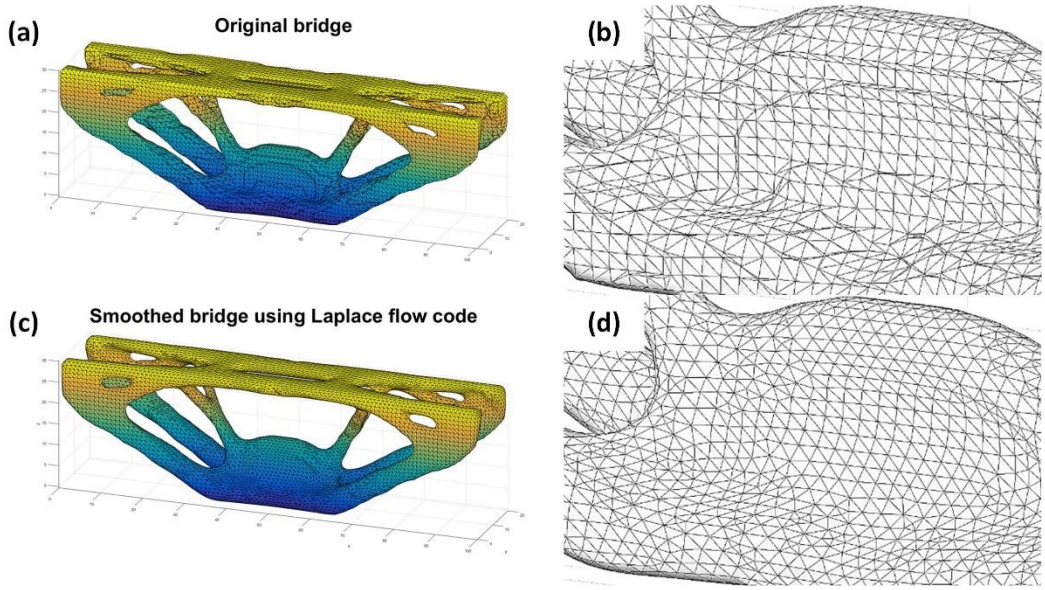

Figure 3.5. Mesh smoothing of the topologically optimized bridge, (a) and (b) original mesh, (c), and (d) smoothed mesh by Laplacian smoothing method.

Therefore, the mesh should be smoothed, and the low-quality elements should be eliminated. There are several smoothing techniques to solve this problem. Among them is the simple but famous Laplacian smoothing method. In Figure 3.6, v_i is the node needed to be adjusted, while v_j

is one of the nodes in v_i^*, which represents the set of v_i's neighbors. Thus, the new coordinates of v_i can be described as,

$$v_i' = v_i + \frac{1}{n}\sum_{v_j \in v_i^*}(v_j - v_i) \tag{3.7}$$

where, n is the number of v_i's neighbors.

The Matlab ® code provided by Kaven [188] had been employed in this work. The related smoothed result is shown in Figure 3.5c and d, where those thin and long triangular elements have disappeared. Moreover, when one uses the refined mesh to generate a solid mesh, less modification is needed compared with the original one. However, this uniform-weight method shown in Eq.(3.7) may cause shrinkage and results' dependency on triangle sizes [189], which has been exemplified in Figure 3.6b. Therefore, in future work, non-shrinking methods, such as the scale-dependent umbrella operator, should be considered.

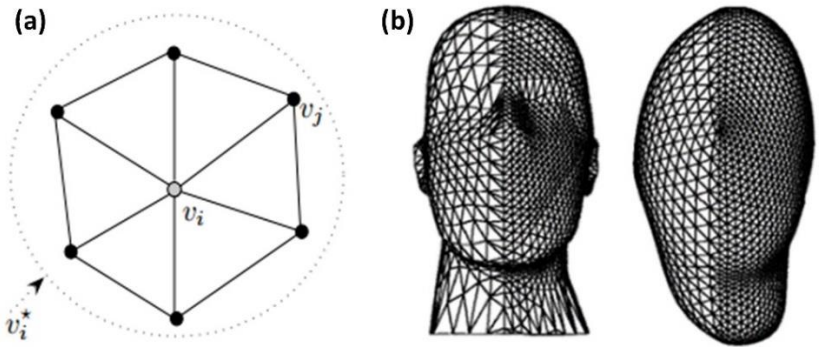

Figure 3.6. Laplacian smoothing, (a) vertex neighborhood v_i^*, (b) illustration of shrinking and mesh size dependency.

3.5. Performance simulation

With the smoothed mesh of the bridge structure with volume fraction 0.2 shown in the last section, now one can convert it to solid mesh in HyperWorks ®, shown in Figure 3.7. Then static simulation of the topologically optimized bridge was executed under the boundary conditions the same as a three-point bending test. Since the material of the parts that were printed for the

mechanical test is Acrylonitrile Butadiene Styrene (ABS), the material properties of ABS [190] were used in the simulation as shown in Table 3.1, while Poisson's ratio was assumed to be 0.3. The load applied on the bridge was 1 kN.

Table 3.1. Material properties of ABS material used in the simulation.

Young's Modulus	Poisson's Ratio	Tensile Strength
2.25 – 2.28 Gpa	0.3	34.1 – 51.2 MPa

Figure 3.8 depicts the simulation results of the bridge structure. It should be mentioned that some stress singularities have been filtered out, which may exist in the sharp corners of the small holes near the bottom of the bridge, in the load applying area, and in the fixation area. Therefore, only the central portion (colored area) of the bridge was selected, as shown in Figure 3.8a. Mesh independency verification has been executed with mesh sizes of 0.5 and 0.25 mm. The difference of maximum stress between the two models with different mesh sizes is 6.6%, which should be able to verify the mesh independency for the simulation.

Figure 3.7. The solid mesh of the topologically optimized bridge

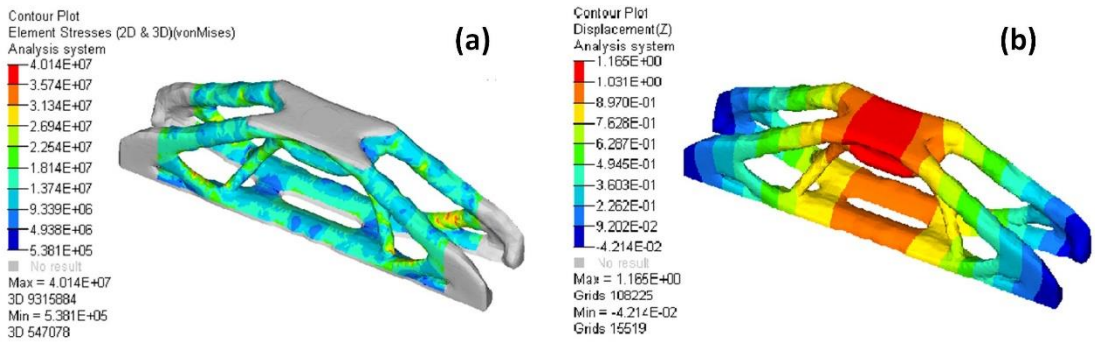

Figure 3.8. The static simulation results of the topologically optimized bridge, (a) stress distribution, (b) z-displacement.

Performance simulation should be necessary due to the reason that it can conveniently help designers to check the validity of structure before experiments and to adjust designs based on the simulation results. However, this process still needs much manual work, including mesh smoothing, conversion from 2D mesh to 3D mesh, and refinement of 3D mesh. Besides, from the simulation result of the bridge depicted in Figure 3.8a, one can see that some of the stress are not smoothly distributed due to the concave-convex surface of the bridge. So remodeling may be essential for some applications, which may also involve a significant amount of manual work. Thus, future effort on the geometrical processing may be requisite.

3.6. Experimental validation

Topologically optimized bridge structures with different material volume fractions, which are 0.2, 0.5, 0.8, and 1.0, had been printed by uPrint Stratasys ® with the material of Acrylonitrile butadiene styrene (ABS), as shown in Figure 3.9, in which the black parts are support structures removed after printing. The structure with volume fraction 1 is a block fully filled with material in the design domain.

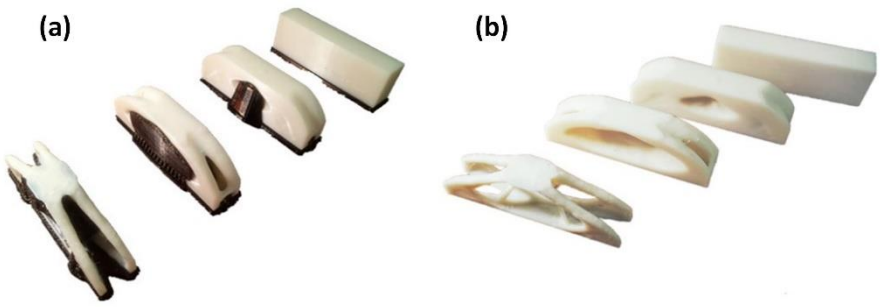

Figure 3.9. Bridge structures with different volume fractions, (a) with support structures, (b) after the removal of support structures.

Experiments of static three-point bending had been set up on the Instron ® test machine, as shown in Figure 3.10a. The bridge in the figure contacted on two cylindrical support structures and was under the compression force from the pin.

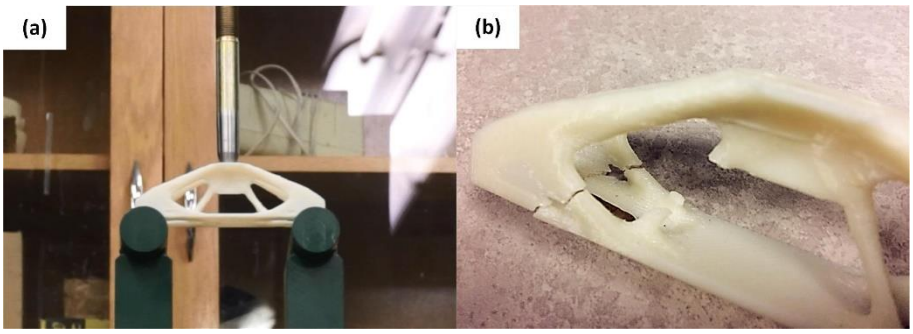

Figure 3.10. Experimental procedure and result, (a) setup of the three-point bending mechanical test, (b) the part after the mechanical test.

Figure 3.11a displays the force-deformation profiles of bridge structures with four different volume fraction, 0.2, 0.5, 0.8, 1.0, whose maximum bearing force are 1.1 kN, 4.4 kN, 5.8 kN, and 6.3 kN respectively. From Figure 3.11 (a), one can observe that the bridge with volume fraction 0.5 is the stiffest one within a range of deformation from 0 to 3 mm. Besides, within a specific-displacement range, each optimized structure can withstand bigger loads than the full block can for the same deformation, as shown in Figure 3.11 (a), representing that topology optimization can make structures stronger with less material to some degree.

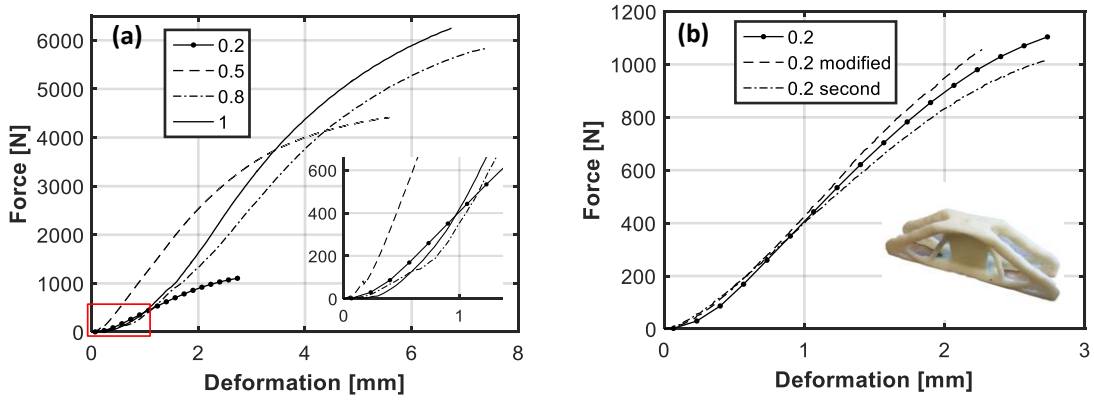

Figure 3.11. Force-deformation profile of (a) the bridge structures with the four different volume fraction (0.2, 0.5, 0.8, 1.0) and (b) a manually modified structure.

Furthermore, in order to verify the effectiveness of topology optimization, a wall structure was manually added to the center of the volume-fraction-0.2 bridge, as displayed in Figure 3.11b. It can be seen that the difference between the original structure and the modified structure could be ignored, since the deviation from another original design is even bigger than that difference, as

plotted in Figure 3.11b. Hence, the wall structure may be redundant, which implies that topology optimization has derived an effective result.

This experiment validates the performance simulation discussed previously. The simulation result in Figure 3.8a shows that under a load of 1kN, the 0.2-volume-fraction bridge tends to break since the maximum stress is within the range of tensile strength of ABS shown in Table 3.1. The areas with stress higher than 35MPa are on the upper surfaces of the four corner beams and the roots of the four middle beams, which agrees well with the experimental results shown in Figure 3.10a and Figure 3.10b, from which it can be seen that the bridge broke at the locations predicted under a load around 1kN. Nevertheless, the maximum z-displacement in the simulation shown in Figure 3.8b is 1.2 mm, which is much smaller than the 3.4 mm from the experiment. The reason for this discrepancy may be that the anisotropy of the ABS material was ignored in the simulation.

3.7. Summary

A system of design, optimization, and simulation for AM has been presented in this chapter. It includes topology optimization, post-processing, performance simulation, and manufacturing process. This end-to-end system may help to realize high-performance products, to accelerate the upgrading of products, and to reduce R&D expenses at the same time. Topology optimization can make structures stronger with less material, of which the mathematical model has been discussed in order to understand this potent designing tool better. In addition, the mesh smoothing technique may help improve the mesh quality of results obtained by topology optimization.

Moreover, performance simulation through FEM may conveniently help designers to derive better design and to understand the performance of the design before doing experiments. Furthermore, experiments had been done to verify the simulation, and to confirm the effectiveness of topology optimization in structural design. The structural breakage predicted by simulation agrees well with that from the experiment.

Chapter 4. Fundamentals of FEM Modeling for LPBF

4.1. Introduction

Finite Element Method (FEM) has been widely used by academics, researchers, and industries. It is employed extensively in the analysis of heat transfer and fluids and solids and structures. LPBF is a complex manufacturing process, which includes multiple physics, e.g. heat transfer, fluid dynamics, and elasto-plastic mechanics. The development of FEM for simulating the LPBF process is attracting more and more attention because FEM can not only reduce the development cost but also provide much valuable information that may be difficultly derived from experiments, such as the temperature gradient and cooling rate. In this chapter, the fundamentals of FEM modeling for LPBF are discussed, and they are separated into three categories, heat transfer FEM, elasto-plastic FEM, and thermo-elasto-plastic FEM. In addition, the fast simulation method—ISM will be briefly discussed.

4.2. Fundamentals of elasto-plasticity FEM

4.2.1. Linear elasticity

The equilibrium equations, which are the governing equations for a three-dimensional solid domain Ω with the surface of Γ, are described as,

$$\begin{aligned}
\frac{\partial \sigma_{xx}}{\partial x}+\frac{\partial \tau_{yx}}{\partial y}+\frac{\partial \tau_{zx}}{\partial z}+b_x=0\\
\frac{\partial \tau_{xy}}{\partial x}+\frac{\partial \sigma_{yy}}{\partial y}+\frac{\partial \tau_{zy}}{\partial z}+b_y=0\\
\frac{\partial \tau_{xz}}{\partial x}+\frac{\partial \tau_{yz}}{\partial y}+\frac{\partial \sigma_{zz}}{\partial z}+b_z=0
\end{aligned} \tag{4.1}$$

where b_x, b_y, and b_z are components of the body force in the x-, y-, and z-directions, respectively. In addition, according to the symmetry of the Cauchy stress, $\tau_{ij} = \tau_{ji}$, ($i, j = x, y, z$).

These governing equations can be expressed in a compact form,

$$\boldsymbol{S}^T\boldsymbol{\sigma}+\boldsymbol{b}=\boldsymbol{0} \tag{4.2}$$

where $\boldsymbol{S}^T$ is the differential operator,

$$\boldsymbol{S}^T=\begin{Bmatrix} \frac{\partial}{\partial x} & 0 & 0 & \frac{\partial}{\partial y} & 0 & \frac{\partial}{\partial z} \\ 0 & \frac{\partial}{\partial y} & 0 & \frac{\partial}{\partial x} & \frac{\partial}{\partial z} & 0 \\ 0 & 0 & \frac{\partial}{\partial z} & 0 & \frac{\partial}{\partial y} & \frac{\partial}{\partial x} \end{Bmatrix} \tag{4.3}$$

$\boldsymbol{\sigma} = \{\sigma_{xx}, \sigma_{yy}, \sigma_{zz}, \tau_{xy}, \tau_{yz}, \tau_{zx}\}^{\mathrm{T}}$ is the matrix form of the stress tensor, and $\boldsymbol{b}$ is the vector of the body load $\boldsymbol{b} = \{b_x, b_y, b_z\}^{\mathrm{T}}$.

For the boundary conditions, stress boundary conditions are given by the traction condition,

$$\begin{aligned} t_x &= \sigma_{xx}n_x + \tau_{yx}n_y + \tau_{zx}n_z \\ t_y &= \tau_{xy}n_x + \sigma_{yy}n_y + \tau_{zy}n_z \\ t_z &= \tau_{xz}n_x + \tau_{yz}n_y + \sigma_{zz}n_z \end{aligned} \tag{4.4}$$

where $\boldsymbol{t} = \{t_x, t_y, t_z\}^{\mathrm{T}}$ is a vector of surface tractions that act over the part of the boundary surface denoted as Γ_t (Neumann boundary). Similarly, displacement boundary conditions are presented by,

$$\mathrm{u}_i = \bar{\mathrm{u}}_i \tag{4.5}$$

and apply for all points which are on the part of the boundary surface denoted as Γ_u. (Dirichlet boundary). $\bar{\mathrm{u}}_i$ denotes the prescribed displacement on the boundary.

All of the above equations are not specified to a material. The specific behavior of a material is defined by constitutive equations that govern the stress-strain relations of the material. As for the material constitutive relations,

$$\boldsymbol{\sigma} = \boldsymbol{D}\left(\boldsymbol{\varepsilon} - \boldsymbol{\varepsilon}_0\right) + \boldsymbol{\sigma}_0 \tag{4.6}$$

where $\boldsymbol{D}$ is the elastic stress-strain matrix, $\boldsymbol{\sigma}_0$ is the initial stress vector before applying any loads, and $\boldsymbol{\varepsilon} = \{\varepsilon_{xx}, \varepsilon_{yy}, \varepsilon_{zz}, \gamma_{xy}, \gamma_{yz}, \gamma_{zx}\}^{\mathrm{T}}$ is the strain vector, $\boldsymbol{\varepsilon}_0 = \{\varepsilon_{0xx}, \varepsilon_{0yy}, \varepsilon_{0zz}, \gamma_{0xy}, \gamma_{0yz}, \gamma_{0zx}\}^{\mathrm{T}}$ is the strain vector that arises from sources other than displacement. Moreover, for linear isotropic materials, the relations are expressed as,

$$\begin{bmatrix} \sigma_{xx} \\ \sigma_{yy} \\ \sigma_{zz} \\ \tau_{xy} \\ \tau_{yz} \\ \tau_{zx} \end{bmatrix} = \begin{bmatrix} \lambda+2\mu & \lambda & \lambda & & & \\ & \lambda+2\mu & \lambda & & & \\ & & \lambda+2\mu & & & \\ & & & u & 0 & 0 \\ & symm & & & u & 0 \\ & & & & & u \end{bmatrix} \begin{bmatrix} \varepsilon_{xx}-\varepsilon_{0xx} \\ \varepsilon_{yy}-\varepsilon_{0yy} \\ \varepsilon_{zz}-\varepsilon_{0zz} \\ \gamma_{xy}-\gamma_{0xy} \\ \gamma_{yz}-\gamma_{0yz} \\ \gamma_{zx}-\gamma_{0yz} \end{bmatrix} + \begin{bmatrix} \sigma_{0xx} \\ \sigma_{0yy} \\ \sigma_{0zz} \\ \tau_{0xy} \\ \tau_{0yz} \\ \tau_{0zx} \end{bmatrix} \tag{4.7}$$

The differential operator matrix $\boldsymbol{S}$ can also be used for describing the relationship between strain $\boldsymbol{\varepsilon}$ and displacement $\mathbf{u} = \{u_x, u_y, u_z\}$,

$$\boldsymbol{\varepsilon} = \boldsymbol{S}\mathbf{u} \tag{4.8}$$

A variational (weak) form for the governing equation (Eq.(4.2)) can be constructed by multiplying the equation set by a proper arbitrary function, integrating over the domain of the problem, and set the result to zero [191]. Virtual work is a weak form where the arbitrary function is a virtual displacement vector $\delta\boldsymbol{u}$. Therefore, the weak form of the governing equation can be expressed as follows,

$$\delta\prod\nolimits_{eq} = \int_{\Omega} \delta\mathbf{u}^{T} \left(\boldsymbol{S}^{T}\boldsymbol{\sigma} + \boldsymbol{b} \right) d\Omega = 0 \tag{4.9}$$

Integrating the above equation by parts using the Green's theorem,

$$\delta\prod\nolimits_{eq} = -\int_{\Omega} \delta\left(\boldsymbol{S}\mathbf{u}\right)^{T} \boldsymbol{\sigma} d\Omega + \int_{\Gamma} \delta\mathbf{u}^{T}\boldsymbol{t} d\Gamma + \int_{\Omega} \delta\mathbf{u}^{T}\boldsymbol{b} d\Omega = 0 \tag{4.10}$$

If all the displacement boundary conditions are imposed, so that $\delta\boldsymbol{u}$ vanishes on Γ_u, the final result can be derived,

$$\delta\prod\nolimits_{eq} = -\int_{\Omega} \delta\left(\boldsymbol{S}\mathbf{u}\right)^{T} \boldsymbol{\sigma} d\Omega + \int_{\Gamma_t} \delta\mathbf{u}^{T}\boldsymbol{t} d\Gamma + \int_{\Omega} \delta\mathbf{u}^{T}\boldsymbol{b} d\Omega = 0 \tag{4.11}$$

4.2.2. FEM of Linear elasticity

The Galerkin method is employed to approximate the linear elastic problem (Eq.(4.2)) by dividing the domain of interest, Ω, into a set of subdomains (so-called elements), Ω_e, which can be expressed as,

$$\Omega \approx \sum_e \Omega_e \tag{4.12}$$

Correspondingly, the boundary is also divided into sub-surfaces as,

$$\Gamma \approx \sum_e \Gamma_e = \sum_{e_t} \Gamma_{e_t} + \sum_{e_u} \Gamma_{e_u} \tag{4.13}$$

where Γ_{e_t} and Γ_{e_u} are the boundary segments where tractions and displacements are applied respectively.

Therefore, the weak form (Eq.(4.11)) of the governing equations can be expressed as,

$$\delta \prod_{eq} \approx \sum_e \left(-\int_{\Omega_e} \delta (\boldsymbol{S}\mathbf{u})^T \boldsymbol{\sigma} d\Omega + \int_{\Gamma_{e_t}} \delta \mathbf{u}^T \boldsymbol{t} d\Gamma + \int_{\Omega_e} \delta \mathbf{u}^T \boldsymbol{b} d\Omega \right) = 0 \tag{4.14}$$

Now displacement $\boldsymbol{u}$ will be expressed by a finite element approximation,

$$\mathbf{u}(x, y, z) \approx \boldsymbol{N}(x, y, z)\hat{\mathbf{u}} \tag{4.15}$$

where $\hat{\mathbf{u}}$ is the node-displacement vector of an element, and $\boldsymbol{N}$ is a matrix of shape functions for an element with *n* nodes.

$$\boldsymbol{N} = \begin{bmatrix} N_1 & 0 & 0 & N_2 & 0 & 0 & \cdots & N_n & 0 & 0 \\ 0 & N_1 & 0 & 0 & N_2 & 0 & \cdots & 0 & N_n & 0 \\ 0 & 0 & N_1 & 0 & 0 & N_2 & \cdots & 0 & 0 & N_n \end{bmatrix} \tag{4.16}$$

In real implementations of FEM, the isoparametric form is generally used. In isoparametric form, the interpolation functions of displacement and that of geometry are the same, which can be illustrated by the following equations,

$$\begin{aligned} \mathbf{u}(\varepsilon, \eta, \zeta) &\approx \boldsymbol{N}(\varepsilon, \eta, \zeta)\hat{\mathbf{u}} \\ \mathbf{x}(\varepsilon, \eta, \zeta) &\approx \boldsymbol{N}(\varepsilon, \eta, \zeta)\hat{\mathbf{x}} \end{aligned} \tag{4.17}$$

where ε, η, ζ are the parametric (natural) coordinates for each element and $\hat{\mathbf{x}} = \{x_1, y_1, z_1; \ldots; x_n, y_n, z_n\}$ represents nodal coordinate parameters in the Cartesian coordinate system.

By using the isoparametric form, the integration in the weak form (Eq.(4.14)) is transformed from the element region) Ω_e to the Gaussian range $-1 \le \varepsilon, \eta, \zeta \le 1$. The transformation of the volume element from the Cartesian coordinates to the natural coordinates can be derived as,

$$dxdydz = \det \boldsymbol{J} \cdot d\varepsilon d\eta d\zeta \tag{4.18}$$

where $\boldsymbol{J}$ is the Jacobian transformation between x, y, z and ε, η, ζ and is presented as follows,

$$\boldsymbol{J} = \frac{\partial(x, y, z)}{\partial(\varepsilon, \eta, \zeta)} = \begin{bmatrix} \frac{\partial N_1}{\partial \varepsilon} & \frac{\partial N_2}{\partial \varepsilon} \cdots \frac{\partial N_n}{\partial \varepsilon} \\ \frac{\partial N_1}{\partial \eta} & \frac{\partial N_2}{\partial \eta} \cdots \frac{\partial N_n}{\partial \eta} \\ \frac{\partial N_1}{\partial \zeta} & \frac{\partial N_2}{\partial \zeta} \cdots \frac{\partial N_n}{\partial \zeta} \end{bmatrix} \begin{bmatrix} x_1 & y_1 & z_1 \\ x_2 & y_2 & z_2 \\ \vdots & \vdots & \vdots \\ x_n & y_n & z_n \end{bmatrix} \tag{4.19}$$

For the strain-displacement relations, the strain-displacement equations (Eq.(4.8)) can be expressed as,

$$\boldsymbol{\varepsilon} = \boldsymbol{S}\mathbf{u} \approx \boldsymbol{SN}\hat{\mathbf{u}} = \boldsymbol{B}\hat{\mathbf{u}} \tag{4.20}$$

where $\boldsymbol{B}$ is the strain matrix. Substituting into Eq.(4.14) and as well as combining material constitutive relations (Eq.(4.6)), the weak form equation can be formed into,

$$\begin{aligned} \delta \prod\nolimits_{eq} \approx \sum_e \delta \hat{\mathbf{u}}^T \Big(& -\int_{\Omega_e} \boldsymbol{B}^T \boldsymbol{D}\boldsymbol{B}\hat{\mathbf{u}} d\Omega + \int_{\Omega_e} \boldsymbol{B}^T \boldsymbol{D}\boldsymbol{\varepsilon}_0 d\Omega \\ & - \int_{\Omega_e} \boldsymbol{B}^T \boldsymbol{\sigma}_0 d\Omega + \int_{\Gamma_{e_t}} \boldsymbol{N}^T \boldsymbol{t} d\Gamma + \int_{\Omega_e} \boldsymbol{N}^T \boldsymbol{b} d\Omega \Big) = 0 \end{aligned} \tag{4.21}$$

Since the virtual displacement vector $\delta\hat{\mathbf{u}}$ is arbitrary, the expression within the brackets in the above equation should equal to zero. Besides, after summing up over all elements, the weak form expression can finally generate the following equation,

$$\boldsymbol{KU} = \boldsymbol{F} \tag{4.22}$$

where $\boldsymbol{U} = \hat{\mathbf{u}}$, $\boldsymbol{K}$ is called the stiffness matrix, and its expression is as follows,

$$\boldsymbol{K} = \sum_e \int_{\Omega_e} \boldsymbol{B}^T \boldsymbol{D}\boldsymbol{B} d\Omega \tag{4.23}$$

and $\boldsymbol{F}$ is the external load vector, and its expression is as follows,

$$\boldsymbol{F} = \sum_e \int_{\Omega_e} \boldsymbol{B}^T \boldsymbol{D}\boldsymbol{\varepsilon}_0 d\Omega - \int_{\Omega_e} \boldsymbol{B}^T \boldsymbol{\sigma}_0 d\Omega + \int_{\Gamma_{e_t}} \boldsymbol{N}^T \boldsymbol{t} d\Gamma + \int_{\Omega_e} \boldsymbol{N}^T \boldsymbol{b} d\Omega \tag{4.24}$$

Finally, Eq.(4.22) is the FEM formulation of the linear elastic problem shown in Eq.(4.2). By solving Eq.(4.22), the unknown displacement $\boldsymbol{U}$ can be derived. The other results, e.g. stress and strain, are interpreted based on the displacement results.

4.2.3. Elastoplasticity

The fundamentals of the plasticity theory mainly include: 1. the yielding criterion that defines the limit where plastic deformation first appears; 2. the flow rule that describes the relationship between stresses and strains during the plastic deformation; 3. the consistency condition that restricts the stresses from exceeding the yield limit.

4.2.3.1. Stress-strain behavior

For plastic deformation, the plastic strain ε_p should be included, and therefore the stress-strain behavior shown in Eq.(4.6) becomes,

$$\boldsymbol{\sigma} = \boldsymbol{D}\left(\boldsymbol{\varepsilon} - \boldsymbol{\varepsilon}_0 - \boldsymbol{\varepsilon}_p\right) + \boldsymbol{\sigma}_0 \tag{4.25}$$

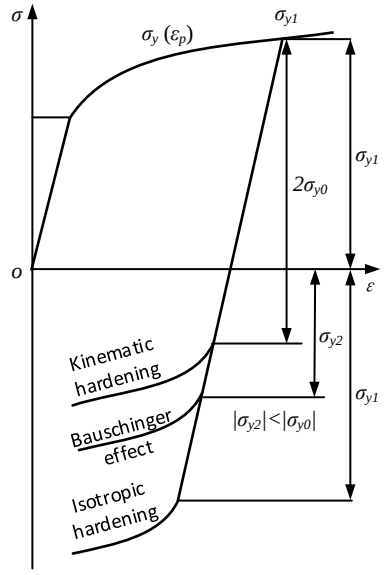

Figure 4.1. Strain hardening type and Bauschinger effect.

The stress-strain curves are usually derived by tensile tests, as shown in Figure 4.1. The Bauschinger effect is describing the reduction of compressive yield stress after cold tensile working [192]. In other words, the Bauschinger effect shows an increase in tensile yield stress occurs at the expense of compressive yield stress.

Moreover, for the stress-strain behavior, there are four basic and simple models, (a) linear elasto-plastic model, (b) elastic perfectly plastic model, (c) rigid linear hardening model, and (d) rigid perfectly plastic model, as shown in Figure 4.2. *H* is the tangent modulus, which is calculated based on the tangent modulus *K* and Young's modulus *E* and, therefore, is equal to (1/*K*-1/*E*). The corresponding friction block models are also shown in Figure 4.2 for the corresponding elasto-plastic models.

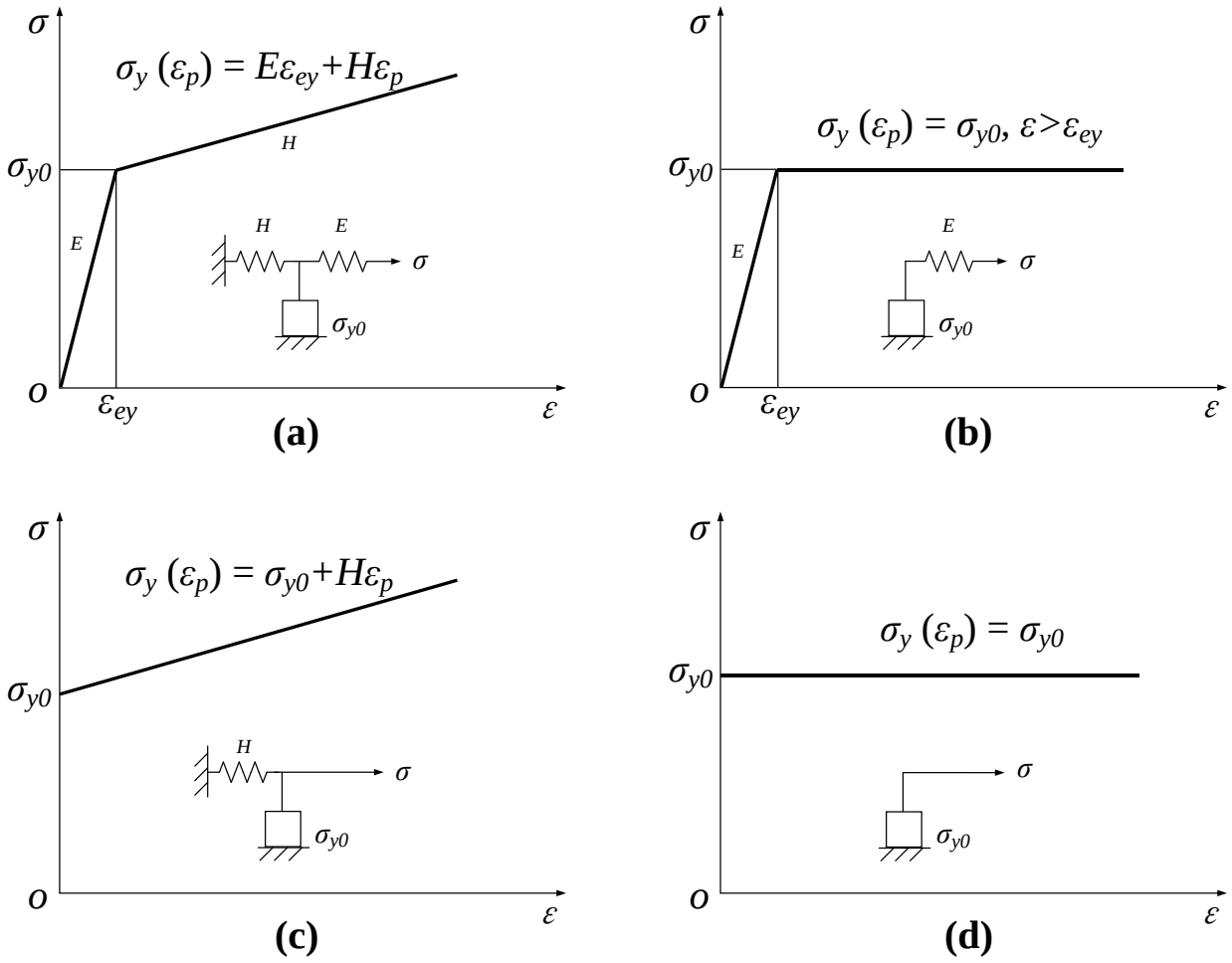

Figure 4.2. Simple models of elastic and plastic deformation, (a) linear elasto-plastic model, (b) elastic perfectly plastic model, (c) rigid linear hardening model, (d) rigid perfectly plastic model.

4.2.3.2. Deviatoric stress

From experiments, researchers found the yielding of a metal is often independent of hydrostatic stress because of the assumption of nearly incompressible materials [191], and therefore, the deviatoric stress can be produced by excluding the hydrostatic stress from the total stress, as shown in the following expression,

$$\begin{bmatrix} \sigma_{xx} & \tau_{yx} & \tau_{zx} \\ \tau_{xy} & \sigma_{yy} & \tau_{zy} \\ \tau_{xz} & \tau_{yz} & \sigma_{yy} \end{bmatrix} = \begin{bmatrix} \sigma_m & 0 & 0 \\ 0 & \sigma_m & 0 \\ 0 & 0 & \sigma_m \end{bmatrix} + \begin{bmatrix} S_{xx} & S_{yx} & S_{zx} \\ S_{xy} & S_{yy} & S_{zy} \\ S_{xz} & S_{yz} & S_{zz} \end{bmatrix} \tag{4.26}$$

where $\sigma_m = (\sigma_{xx+} \sigma_{yy} + \sigma_{zz})/3$ is the hydrostatic stress and the second matrix on the right-hand side is the deviatoric stress matrix. Its characteristic equation is as follows,

$$S^3 - J_1 S^2 - J_2 S - J_3 = 0 \tag{4.27}$$

where J_1, J_2, J_3 are called deviatoric invariants, and they are presented as follows,

$$\begin{aligned} J_1 &= S_{xx} + S_{yy} + S_{zz} \\ J_2 &= \frac{1}{6}\left[\left(S_{xx} - S_{yy}\right)^2 + \left(S_{yy} - S_{zz}\right)^2 + \left(S_{zz} - S_{xx}\right)^2\right] + 6\left(S_{xy}^2 + S_{yz}^2 + S_{zx}^2\right) \\ J_3 &= S_{xx}S_{yy}S_{zz} - S_{xx}S_{yz}^2 - S_{yy}S_{zx}^2 - S_{zz}S_{xy}^2 + 2S_{xy}S_{yz}S_{zx} \end{aligned} \tag{4.28}$$

Moreover, J_2 is most important because the von Mises stress (or equivalent stress), which is important in the von Mises yielding criterion, is defined as,

$$\sigma_e = \sqrt{\frac{3}{2} S_{ij} S_{ji}} = \sqrt{3J_2} \tag{4.29}$$

4.2.3.3. The criterion of yielding

The von Mises yielding criterion is generally used, which is expressed as follows [191],

$$\begin{aligned} f &= \sigma_e - \sigma_y \\ &= \sqrt{\frac{1}{2}\left[\left(\sigma_{xx} - \sigma_{yy}\right)^2 + \left(\sigma_{yy} - \sigma_{zz}\right)^2 + \left(\sigma_{zz} - \sigma_{xx}\right)^2 + 6\left(\tau_{xy}^2 + \tau_{yz}^2 + \tau_{zx}^2\right)\right]} - \sigma_y = 0 \end{aligned} \tag{4.30}$$

von Mises yielding criterion is elegant and effective because it has physical meaning that is the strain energy equivalence. Total strain energy before the yield point can be expressed as,

$$E = E_h + E_d = \frac{1}{2}\boldsymbol{\sigma\varepsilon} \tag{4.31}$$

where E_h is the energy due to volume change, and E_d is the energy due to deformation. E_h is derived as follows,

$$E_h = \frac{3(1-2\nu)}{2E}\left[\frac{\sigma_{xx} + \sigma_{yy} + \sigma_{zz}}{3}\right]^2 \tag{4.32}$$

where v is Poisson's ratio, and E is Young's modulus. Therefore, E_d is expressed as,

$$\begin{aligned} E_d &= E - E_h \\ &= \frac{1+v}{3E}\left(\frac{1}{2}\left[\left(\sigma_{xx}-\sigma_{yy}\right)^2+\left(\sigma_{yy}-\sigma_{zz}\right)^2+\left(\sigma_{zz}-\sigma_{xx}\right)^2+6\left(\tau_{xy}^2+\tau_{yz}^2+\tau_{zx}^2\right)\right]\right) \end{aligned} \tag{4.33}$$

Moreover, the "theory" behind the various yielding criteria is that whatever is responsible for failure in the standard tensile test will also be responsible for failure under other complex loading conditions. Therefore, in uniaxial stress-state at yield, $\sigma_1 = \sigma_y$, $\sigma_2 = \sigma_3 = 0$, and the deformation energy E_d in uniaxial stress state,

$$E_d = \frac{1+v}{3E}\sigma_y^2 \tag{4.34}$$

where σ_y is the yield stress. Therefore, by comparing Eq.(4.33) and Eq.(4.34), Eq.(4.30) is derived.

4.2.3.4. The rule of plastic flow

The normality hypothesis of plasticity enables one to determine the "direction" of flow,

$$d\boldsymbol{\varepsilon}^p = d\lambda \frac{\partial f}{\partial \boldsymbol{\sigma}} \tag{4.35}$$

This equation is called the associated flow rule. The equivalent plastic strain is defined as,

$$d\bar{\varepsilon}^p = \sqrt{\frac{2}{3}\left[\left(d\varepsilon_1^p\right)^2+\left(d\varepsilon_2^p\right)^2+\left(d\varepsilon_3^p\right)^2\right]} \tag{4.36}$$

Moreover, for von Mises yielding criterion, this equivalent plastic strain can be shown equal to the plastic multiplier, $d\bar{\varepsilon}_p = d\lambda$.

4.2.3.5. The consistency condition

Once yielding occurs, $f(\boldsymbol{\sigma},\ \bar{\varepsilon}_p) = 0$ and the stresses should remain on the yield surface during the plastic deformation. This constraint is expressed by the consistency condition as follows,

$$f(\boldsymbol{\sigma}+d\boldsymbol{\sigma},\bar{\varepsilon}_p+d\bar{\varepsilon}_p) = f(\boldsymbol{\sigma},\bar{\varepsilon}_p)+\left(\frac{\partial f}{\partial \boldsymbol{\sigma}}\right)^T d\boldsymbol{\sigma}+\frac{\partial f}{\partial \bar{\varepsilon}_p}d\bar{\varepsilon}_p = 0 \tag{4.37}$$

Moreover, due to $f(\boldsymbol{\sigma}, \bar{\varepsilon}_p) = 0$, the above consistency condition can be further simplified into the following form,

$$\left(\frac{\partial f}{\partial \boldsymbol{\sigma}}\right)^T d\boldsymbol{\sigma} + \frac{\partial f}{\partial \bar{\varepsilon}_p} d\bar{\varepsilon}_p = 0 \tag{4.38}$$

4.2.4. FEM of elasto-plasticity

Elastoplastic analyses are the fundamentals of the LPBF process modeling. The elasto-plastic Finite Element Method (FEM) problems consist of the solutions of two levels, a) the global level—global load-deflection equations, b) the material level —the incremental stress-strain relations. On the global level, equilibrium must be satisfied no matter in the linear or nonlinear FEM, whereas on the material level, the plasticity stress-strain relations must be satisfied.

In the computational elasto-plastic analysis, a load increment is usually employed, producing a displacement increment, a strain increment, and a stress increment [193]. Therefore, this requires an incremental stress-strain relation that is derived based on Eq.(4.25),

$$d\boldsymbol{\sigma} = \boldsymbol{D}\left(d\boldsymbol{\varepsilon} - d\boldsymbol{\varepsilon}_p\right) \tag{4.39}$$

where the plastic strain increment $d\varepsilon_p$ is determined by the associated flow rule (Eq.(4.35)). Thus, the above equation is changed into,

$$d\boldsymbol{\sigma} = \boldsymbol{D}\left(d\boldsymbol{\varepsilon} - d\lambda \frac{\partial f}{\partial \boldsymbol{\sigma}}\right) \tag{4.40}$$

substituting Eq.(4.40) into the consistency condition (Eq.(4.38)) and also remembering $d\bar{\varepsilon}_p = d\lambda$,

$$d\bar{\varepsilon}_p = \frac{\left(\frac{\partial f}{\partial \boldsymbol{\sigma}}\right)^T \boldsymbol{D} d\boldsymbol{\varepsilon}}{-\frac{\partial f}{\partial \bar{\varepsilon}_p} + \left(\frac{\partial f}{\partial \boldsymbol{\sigma}}\right)^T \boldsymbol{D}\left(\frac{\partial f}{\partial \boldsymbol{\sigma}}\right)} \tag{4.41}$$

substituting the above equation back into Eq.(4.40), the elasto-plastic constitutive relation can be derived as follows,

$$\begin{aligned} d\boldsymbol{\sigma} &= \boldsymbol{D}_{ep} d\boldsymbol{\varepsilon} \\ &= \left[\boldsymbol{D} - \frac{\boldsymbol{D}\left(\frac{\partial f}{\partial \boldsymbol{\sigma}}\right)\left(\frac{\partial f}{\partial \boldsymbol{\sigma}}\right)^T \boldsymbol{D}}{-\frac{\partial f}{\partial \bar{\varepsilon}_p} + \left(\frac{\partial f}{\partial \boldsymbol{\sigma}}\right)^T \boldsymbol{D}\left(\frac{\partial f}{\partial \boldsymbol{\sigma}}\right)} \right] d\boldsymbol{\varepsilon} \end{aligned} \tag{4.42}$$

where $\boldsymbol{D}_{ep}$ is the elasto-plastic constitutive matrix.

The global level

For the global level—global load-deflection equations, recalling the FEM equation (Eq.(4.22)) for the linear system

$$\boldsymbol{KU} = \boldsymbol{F} \tag{4.43}$$

where $\boldsymbol{F}$ is the applied load and $\boldsymbol{K}$ is the stiffness matrix given by (similar to but slightly different from Eq.(4.23)),

$$\boldsymbol{K} = \sum_e \int_{\Omega_e} \boldsymbol{B}^T \boldsymbol{D}_{ep} \boldsymbol{B} d\Omega \tag{4.44}$$

Because the constitutive matrix $\boldsymbol{D}_{ep}$ is dependent on the current state of stress, the stiffness matrix $\boldsymbol{K}$ is nonlinear. Furthermore, since the analysis is under the path-dependent nonlinear material condition, equilibrium relations in Eq.(4.43) need to be solved by using a step-by-step incremental solution with several load steps to finally reach the total applied load, which reduces to a one-step analysis if in a static situation. A symbol "*t*" is used for describing the number of steps, even in a situation that is time-independent, which is a general method to deal with nonlinear problems [194]. An incremental relationship between displacement and force is expressed as follows,

$$\begin{aligned} {}^t\boldsymbol{K}\Delta\boldsymbol{U} &= {}^{t+\Delta t}\Delta\boldsymbol{F} \\ &= {}^{t+\Delta t}\boldsymbol{R} - {}^{t+\Delta t}\boldsymbol{F} \end{aligned} \tag{4.45}$$

where ${}^{t}\boldsymbol{K}$ is the stiffness matrix (also named the tangent stiffness matrix) at time t. ${}^{t+\Delta t}\boldsymbol{R}$ lists the externally applied nodal point forces in the configuration at time $t+\Delta t$. ${}^{t+\Delta t}\boldsymbol{F}$ lists the nodal point forces that correspond to the element stresses in this configuration at time t. ΔU is the displacement increment and ${}^{t+\Delta t}U = {}^{t}U + \Delta U$.

Having estimated the displacements related to time $t+\Delta t$, the strains ${}^{t+\Delta t}\boldsymbol{\varepsilon}$, stresses ${}^{t+\Delta t}\boldsymbol{\sigma}$ and nodal point forces ${}^{t+\Delta t}\boldsymbol{F}$ at time $t+\Delta t$ can be calculated, and then proceed to the next time increment calculations. However, since ${}^{t}\boldsymbol{K}$ is the stiffness matrix only at time t, the stiffness matrix can be changed during t to $t+\Delta t$, leading to significant errors. In practice, it is, therefore, necessary to do iteration until ${}^{t+\Delta t}\boldsymbol{F}$ is sufficiently close to ${}^{t+\Delta t}\boldsymbol{R}$. The widely used iteration methods in finite element analysis are based on the classical Newton-Raphson technique [191,194], as shown in Figure 4.3a, where ϵ is the convergence criterion. The modified Newton-Raphson method is shown in Figure 4.3b, where the stiffness matrix is computed only once at the beginning of each load step.

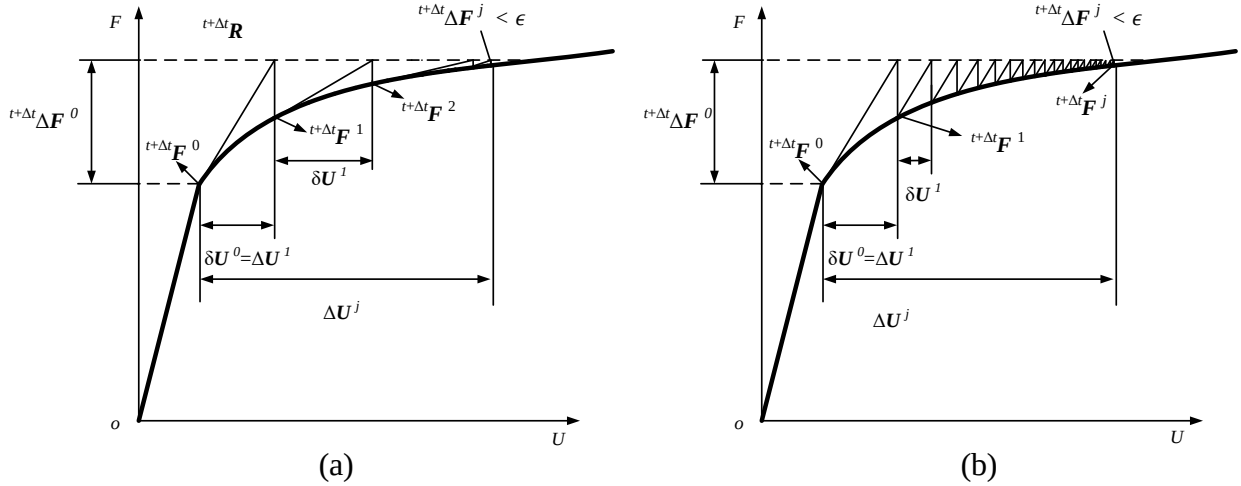

Figure 4.3. Graphical interpretation of the iterative solving method of a nonlinear system with a one-dimensional displacement variable, (a) Newton-Raphson method, and (b) Modified Newton-Raphson method.

The material level

For the material level —the incremental stress-strain relations, it is necessary because every iteration shown in Figure 4.3a and b requires accurate ${}^{t+\Delta t}\boldsymbol{F}^{j}$, which is just lying on the load-

displacement curve. In other words, the stresses should return to the yielding surface without violating the consistency requirement shown in e.g. (4.38) because accurate stresses determine accurate ${}^{t+\Delta t}\boldsymbol{F}^{j}$.

There are generally two methods to calculate the stress increment given a specific strain increment, a) explicit method, b) implicit method.

The explicit method basically is integrating the infinitesimal constitutive relation (Eq.(4.42)) to get the increment $\Delta\boldsymbol{\sigma}$. The integration can be achieved as,

$$\Delta\boldsymbol{\sigma} = \int_{\boldsymbol{\sigma}_j}^{\boldsymbol{\sigma}_j+\Delta\boldsymbol{\sigma}} d\boldsymbol{\sigma} = \int_{\boldsymbol{\varepsilon}_j}^{\boldsymbol{\varepsilon}_j+\Delta\boldsymbol{\varepsilon}} \boldsymbol{D}_{ep} d\boldsymbol{\varepsilon} \tag{4.46}$$

This integral can be calculated by splitting the range ($\boldsymbol{\sigma}_j$, $\boldsymbol{\sigma}_j + \Delta\boldsymbol{\sigma}$) into several sub increments, say N sub increments, and increasing N would lead to more accurate results. However, the $\boldsymbol{D}_{ep}$ should be calculated many times, and there is still a chance that errors may accumulate, making the stresses drift away from the yield surface.

On the other hand, the implicit method uses the process of conducting $\boldsymbol{D}_{ep}$ but does not explicitly calculate it. Instead, it solves a set of equations by using the Newton-Raphson method as well. The two equations it tries to solve are based on Eq.(4.40) and Eq.(4.37), and they are summarized as follows,

$$\begin{aligned} \boldsymbol{p} &= \Delta\boldsymbol{\sigma} - \boldsymbol{D}d\boldsymbol{\varepsilon} + \boldsymbol{D}d\lambda \left.\frac{\partial f}{\partial \boldsymbol{\sigma}}\right|_{\sigma=\sigma_A+\Delta\sigma} = \boldsymbol{0} \\ q &= f(\boldsymbol{\sigma} + d\boldsymbol{\sigma}, \bar{\varepsilon}_p + d\bar{\varepsilon}_p) = 0 \end{aligned} \tag{4.47}$$

Using Newton-Raphson method, one can get the following equations,

$$\begin{bmatrix} \boldsymbol{I} + \boldsymbol{D}d\lambda \dfrac{\partial^2 f}{\partial \boldsymbol{\sigma}^2} & \boldsymbol{D}\dfrac{\partial f}{\partial \boldsymbol{\sigma}} \\ \left(\dfrac{\partial f}{\partial \boldsymbol{\sigma}}\right)^T & \dfrac{\partial f}{\partial \lambda} \end{bmatrix} \begin{bmatrix} \delta\boldsymbol{\sigma}^k \\ \delta\lambda^k \end{bmatrix} = \begin{bmatrix} -\boldsymbol{p}^k \\ -q^k \end{bmatrix} \tag{4.48}$$

And the unknown increments of the variables are updated as follows after each sub increment,

$$
\begin{aligned}
{}^{t+\Delta t}\Delta\boldsymbol{\sigma}^{k+1} &= \Delta\boldsymbol{\sigma}^{k} + \delta\boldsymbol{\sigma}^{k} \\
{}^{t+\Delta t}\Delta\lambda^{k+1} &= \Delta\lambda^{k} + \delta\lambda^{k}
\end{aligned}
\tag{4.49}
$$

Furthermore, the stress can be updated as follows,

$$
{}^{t+\Delta t}\boldsymbol{\sigma} = {}^{t}\boldsymbol{\sigma} + {}^{t+\Delta t}\Delta\boldsymbol{\sigma} \tag{4.50}
$$

Then, by using the following equation to derive the nodal point forces at time $t+\Delta t$,

$$
{}^{t+\Delta t}\boldsymbol{F} = \sum_{e}\int_{\Omega_e} \boldsymbol{B}^{T}\, {}^{t+\Delta t}\boldsymbol{\sigma}\, d\Omega \tag{4.51}
$$

4.3. Fundamentals of heat transfer FEM

This section provides the basic FEM formulation for heat transfer analysis of AM. The fundamental theories are similar to the discussions made in previous sections because FEM is a general method for solving partial differential equations (PDF) no matter whether the PDF is from mechanics or heat transfer. First, the weak form of the PDF will be derived. Then the weak form will be discretized in space and time dimension, respectively. For the space discretization, where the whole domain is separated into finite elements based on the Galerkin method, and for the time discretization, the finite difference method is employed. Last, the Gauss quadrature and time integration techniques will be used for solving the global system equations assembled from the local elements.

The governing equations for 3D heat transfer processes can generally be as follows

$$
\rho c \frac{\partial T}{\partial t} = \nabla \cdot \left(\boldsymbol{k} \nabla T \right) + Q(x, y, z, t) \tag{4.52}
$$

where ρ is the material density, c is the specific heat. T is the current temperature. $\nabla T = \{\partial T/\partial x, \partial T/\partial y, \partial T/\partial z\}^{T}$. t is the time. x, y, and z are the coordinates in the reference system, $\boldsymbol{k} = \{k_x, 0, 0; 0, k_y, 0; 0, 0, k_z\}$ are the thermal conductivity of x, y, and z-axis direction, and $Q(x,y,z,t)$ is the internal

heat generation per unit volume at specific heat-input domain Ω_Q. The following boundary conditions are considered,

$$T = T_{base}(x, y, z) \text{ on } \Gamma_1 \tag{4.53}$$

$$q_s = -q_2 \text{ on } \Gamma_2 \tag{4.54}$$

$$q_c = -h_c(T_{\text{sur}} - T_0) \text{ on } \Gamma_3 \tag{4.55}$$

$$q_r = -\varepsilon\sigma(T_{\text{sur}}^4 - T_0^4) \text{ on } \Gamma_4 \tag{4.56}$$

where T_{base} is the preheating of the substrate, and the first boundary condition is the Dirichlet boundary (Γ_1) condition. q_s is the heat flux on a surface (Neumann boundary Γ_2). h_c is the convective heat transfer coefficient, and T_{sur} is the surface temperature; q_c is on the convection boundary Γ_3. The last boundary (Γ_4) condition is due to the radiative heat losses q_r; ε is the emissivity of the powder bed, and σ is Stefan-Boltzmann constant for radiation.

Similar to the process shown in Eq.(4.9), Eq.(4.10), and Eq.(4.11), a virtual temperature vector δT is chosen, and the weak form of the governing equation (Eq.(4.52)) can be expressed as follows,

$$\delta\prod_{eq} = \int_\Omega \delta T\left(-\rho c\frac{\partial T}{\partial t} + \nabla\cdot(\boldsymbol{k}\nabla T) + Q(x, y, z, t)\right)d\Omega = 0 \tag{4.57}$$

Integrating the above equation by parts using the Green's theorem,

$$\begin{aligned}\delta\prod_{eq} = &-\int_\Omega \delta T\rho c\frac{\partial T}{\partial t}d\Omega - \int_\Omega \delta(\nabla T)^T\boldsymbol{k}\nabla T d\Omega + \int_{\Omega_Q}\delta T Q d\Omega \\ &+ \int_\Gamma \delta T\boldsymbol{k}\nabla T d\Gamma = 0\end{aligned} \tag{4.58}$$

If all the boundary conditions are imposed so that δT vanishes on Γ_1 and the other boundary conditions can be substituted into the above equation, the final result can be derived,

$$\delta\prod_{eq} = -\int_{\Omega}\delta T\rho c\frac{\partial T}{\partial t}d\Omega - \int_{\Omega}\delta(\nabla T)^{T}\boldsymbol{k}(\nabla T)d\Omega + \int_{\Omega_Q}\delta TQd\Omega$$
$$+\int_{\Gamma_2}\delta T(-q_2)d\Gamma + \int_{\Gamma_3}\delta T\left(-h_c(T_{\text{sur}}-T_0)\right)d\Gamma + \int_{\Gamma_4}\delta T\left(-\varepsilon\sigma(T_{\text{sur}}^4 - T_0^4)\right)d\Gamma = 0 \tag{4.59}$$

Similar to the FEM of linear elasticity, the Galerkin method can also be used for the heat transfer problem, and δT will be expressed by a finite element approximation,

$$T(x,y,z) \approx \boldsymbol{N}(x,y,z)\hat{\boldsymbol{T}} \tag{4.60}$$

where $\hat{\boldsymbol{T}}$ is the node-temperature vector of an element, and $\boldsymbol{N}$ is a matrix of shape functions for an element with n nodes.

$$\boldsymbol{N} = \begin{bmatrix} N_1 & N_2 & \cdots & N_n \end{bmatrix} \tag{4.61}$$

where $\boldsymbol{N}$ is the shape matrix. Therefore, the discretized weak form equation can be as follows,

$$\delta\prod_{eq} \approx \sum_{e}\delta\hat{\boldsymbol{T}}^{T}\left(-\int_{\Omega_e}\rho_e c_e\boldsymbol{N}^{T}\boldsymbol{N}d\Omega\frac{\partial\hat{\boldsymbol{T}}}{\partial t} - \int_{\Omega_e}\boldsymbol{B}^{T}\boldsymbol{k}_e\boldsymbol{B}d\Omega\,\hat{\boldsymbol{T}} + \int_{\Omega_{eQ}}\boldsymbol{N}^{T}Q(x,y,z,t)d\Omega\right.$$
$$\left.+\int_{\Gamma_{e2}} -\boldsymbol{N}^{T}q_2 d\Gamma + \int_{\Gamma_{e3}} -h_c\boldsymbol{N}^{T}\left(\boldsymbol{N}\hat{\boldsymbol{T}} - \boldsymbol{T}_0\right)d\Gamma + \int_{\Gamma_{e4}} -\varepsilon\sigma\boldsymbol{N}^{T}\left(\left(\boldsymbol{N}\hat{\boldsymbol{T}}\right)^{\circ 4} - \boldsymbol{T}_0^{\circ 4}\right)d\Gamma\right) = 0 \tag{4.62}$$

where $^{\circ}$ is the element-wise power operation. $\boldsymbol{B}$ is the differential matrix of temperature expressed as follows,

$$\boldsymbol{B} = \boldsymbol{S}\boldsymbol{N} = \begin{bmatrix} \frac{\partial}{\partial x} \\ \frac{\partial}{\partial y} \\ \frac{\partial}{\partial z} \end{bmatrix}\begin{bmatrix} N_1 & N_2 & \cdots & N_n \end{bmatrix} = \begin{bmatrix} \frac{\partial N_1}{\partial x} & \frac{\partial N_2}{\partial x} & \cdots & \frac{\partial N_n}{\partial x} \\ \frac{\partial N_1}{\partial y} & \frac{\partial N_2}{\partial y} & \cdots & \frac{\partial N_n}{\partial y} \\ \frac{\partial N_1}{\partial z} & \frac{\partial N_2}{\partial z} & \cdots & \frac{\partial N_n}{\partial z} \end{bmatrix} \tag{4.63}$$

Since the virtual temperature vector $\delta\hat{\boldsymbol{T}}$ is arbitrary, the expression within the most-outside brackets in Eq.(4.62) should equal to zero. Therefore, after summing up over all elements, the weak form expression can finally generate the following equations,

$$\boldsymbol{M}\frac{\partial\hat{\boldsymbol{T}}}{\partial t} + \boldsymbol{K}\hat{\boldsymbol{T}} = \boldsymbol{R}_Q + \boldsymbol{R}_s + \boldsymbol{R}_c + \boldsymbol{R}_r \tag{4.64}$$

where $\boldsymbol{M}$ is the capacitance matrix, $\boldsymbol{K}$ is the conduction matrix, $\boldsymbol{R}_Q$ is the internal heat vector, $\boldsymbol{R}_s$ is the external surface flux vector, $\boldsymbol{R}_c$ is the convection vector, and $\boldsymbol{R}_r$ is the radiation vector. Their expressions are as follows,

$$\begin{aligned}
\boldsymbol{M} &= \sum_e \int_{\Omega_e} \rho_e c_e \boldsymbol{N}^T \boldsymbol{N} d\Omega \\
\boldsymbol{K} &= \sum_e \int_{\Omega_e} \boldsymbol{B}^T \boldsymbol{k}_e \boldsymbol{B} d\Omega \\
\boldsymbol{R}_Q &= \sum_e \int_{\Omega_{eQ}} \boldsymbol{N}^T Q(x,y,z,t)\, d\Omega \\
\boldsymbol{R}_s &= \sum_e \int_{\Gamma_{e2}} -\boldsymbol{N}^T q_2 d\Gamma \\
\boldsymbol{R}_c &= \sum_e \int_{\Gamma_{e3}} -h_c \boldsymbol{N}^T \left(\boldsymbol{N}\hat{\boldsymbol{T}} - \boldsymbol{T}_0 \right) d\Gamma \\
\boldsymbol{R}_r &= \sum_e \int_{\Gamma_{e4}} -\varepsilon\sigma \boldsymbol{N}^T \left(\left(\boldsymbol{N}\hat{\boldsymbol{T}} \right)^{\circ 4} - \boldsymbol{T}_0^{\circ 4} \right) d\Gamma
\end{aligned} \tag{4.65}$$

As mentioned earlier, the weak form should also be discretized in the time dimension. For the time dimension, the α-method of time integration is used [195], by which Eq.(4.64) can be changed into,

$$\begin{aligned}
\boldsymbol{M} \frac{\left({}^{t+\Delta t}\hat{\boldsymbol{T}} - {}^{t}\hat{\boldsymbol{T}} \right)}{\Delta t} = {} & (1-\alpha)^{t} \left(-\boldsymbol{K}\hat{\boldsymbol{T}} + \boldsymbol{R}_Q + \boldsymbol{R}_s + \boldsymbol{R}_c + \boldsymbol{R}_r \right) \\
& + \alpha^{t+\Delta t} \left(-\boldsymbol{K}\hat{\boldsymbol{T}} + \boldsymbol{R}_Q + \boldsymbol{R}_s + \boldsymbol{R}_c + \boldsymbol{R}_r \right)
\end{aligned} \tag{4.66}$$

where α is a constant that is selected to harvest optimum stability and accuracy properties. The properties of the integration process rest on the value of α that is chosen. The following procedures are in common use [194],

α = 0, explicit Euler forward method, conditionally stable;

α = 1/2, implicit trapezoidal rule, unconditionally stable;

α = 1, implicit Euler forward method, unconditionally stable;

After obtaining the temperature distribution, the temperature gradient can be calculated as follows,

$$\nabla T \approx \begin{pmatrix} \dfrac{T(x+\Delta x,y,z)-T(x-\Delta x,y,z)}{2\Delta x} \\ \dfrac{T(x,y+\Delta y,z)-T(x,y-\Delta y,z)}{2\Delta y} \\ \dfrac{T(x,y,z+\Delta z)-T(x,y,z-\Delta z)}{2\Delta z} \end{pmatrix} \tag{4.67}$$

Besides, the cooling rate can be approximated by the following equation,

$$\frac{\partial T}{\partial t} \approx \frac{T(x,y,z,t+\Delta t)-T(x,y,z,t)}{\Delta t} \tag{4.68}$$

4.4. Fundamentals of thermo-elasto-plasticity FEM

LPBF includes the heat transfer because of the laser heating and the elasto-plasticity because of the high thermal stresses induced by the laser heating. Thus, FEM for simulating the LPBF process should consider themo-elasto-plasticity. Since the elasto-plastic and heat transfer models have been introduced separately in the previous sections, they will be considered together in this section for the sake of simulating LPBF.

4.4.1. Basic equations

Almost all the basic equations necessary for thermo-elasto-plastic simulations have been discussed previously. The only difference between elasto-plasticity (Eq.(4.39)) and thermo-elasto-plasticity is in the strain term as shown in the following equation,

$$\boldsymbol{\sigma} = \boldsymbol{D}\left(\boldsymbol{\varepsilon} - \boldsymbol{\varepsilon}_p - \boldsymbol{\varepsilon}_T\right) \tag{4.69}$$

where ε_T is the thermal strain which can be calculated as,

$$\boldsymbol{\varepsilon}_T = \alpha_{CTE}\left(T - T_0\right)\boldsymbol{I} \tag{4.70}$$

where α_{CTE} is the coefficient of thermal expansion. T is the current temperature that is derived from the nonlinear transient heat transfer discussed in the previous section, and T_0 is the reference temperature that usually is the room temperature.

The remaining mechanical calculation is the same as in Section 4.2.4.

4.4.2. The workflow of thermo-elasto-plastic FEM

The LPBF process simulation is a multi-physics problem, which consists of heat transfer physics and solid mechanics. The two physics can interact with each other to make the problem fully coupled, as shown in Figure 4.4a. For example, the heat transfer may produce thermal strains that lead to the elasto-plastic deformations in the printed part, and on the other side, the deformations may also change the heat transfer configurations. Thus, the equilibrium equations of the two physics should be merged into an integrated system of multi-physics equations, and therefore, for both each Newton-Raphson iteration and each time step, the two physics are solved together in order to achieve the highest accuracy. After the computation, the temperature and displacement results can be generated simultaneously.

However, the fully coupled method may be very resource-consuming because the combined multi-physics system equations are bigger than those of the included individual physics. In LPBF, the thermal strains caused by the heat transfer are generally small and will not influence the heat transfer significantly. Therefore, the one-way coupled method can be employed, in which the two physics are solved separately, as illustrated in Figure 4.4b. First, the heat transfer problem is solved for all the time steps. Then, the temperature results are provided to the mechanical simulation that will be solved afterward. Finally, the displacement field results can be generated. For each Newton-Raphson iteration and time step, only one physics equations are solved, so the matrix is smaller than the fully coupled problem, making the solving much faster. Many works in literature used this one-way coupled method [102,104,109].

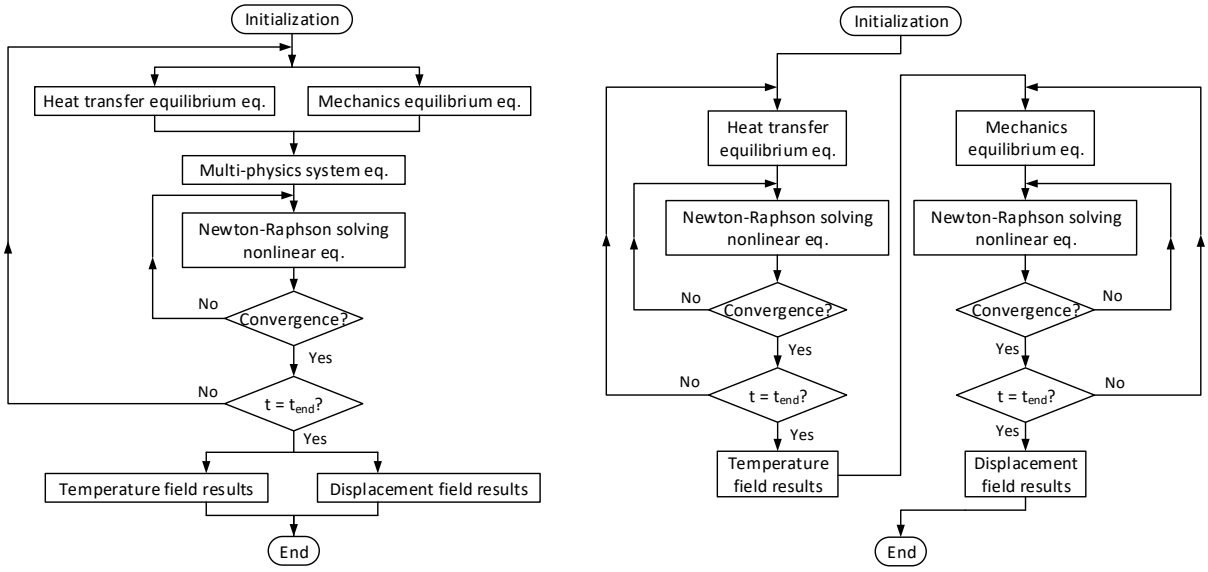

Figure 4.4. The workflow of the thermo-elasto-plastic FEM, (a) fully coupled method, (b) one-way coupled method.

4.5. Equivalent mechanical layer method - inherent strain method

In the previous sections, the thermo-elasto-plasticity FEM has been presented, which can be applied in the simulation of the LPBF process. Even though the thermo-elasto-plasticity model has been successfully used in the LPBF process simulation, it is still applied to a very small scale model, say 1 × 1 mm. There is few part level simulation of LPBF by using the themo-elasto-plasticity FEM because the simulation requires numerous computational resources and time. In LPBF, a high-power laser selectively scans over metal powder to form solidified single tracks, tracks produce a solidified metal layer, and thousands of the layers create a real part finally. Therefore, for space discretization, the mesh should be comparable to the laser beam diameter so that it should be at least as small as 1/3 of the laser beam that is usually 100 μm. For a part-level model, the number of elements would be an astronomical figure. For example, a part-level model, say 10 × 10 cm × 10 cm, requires 27 billion elements approximately. Even though some researches have employed adaptive meshes [110,111,134,139], the ability to realize fast a part-level simulation is still limited.

Therefore, for fast simulating LPBF in the part level, Keller et al. [127] first proposed a concept of “mechanical layer equivalent (MLE)”, which is also known as inherent strain method (ISM), in order to fast simulate the LPBF process and obtain the predicted stress and deformation of the printed parts. The basic idea of ISM is using an equivalent mechanical layer to replace the actual laser scanning in the layer adding process in order to derive comparable mechanical response, e.g. residual stresses and deformations. When one layer added into the solidified part, the inherent strains are applied within the newly added layer, and one solid mechanical simulation will be executed. Then, another solid mechanical simulation will be performed when adding the next layer. This process will be repeated until the last layer.

As for the fundamentals of the ISM, there are two types of mechanical models in ISM. First, a model only considers elasticity FEM, for which one can refer to Section. 4.2.2Second, a model considers elasto-plasticity FEM, which has been explained in Section. 4.2.4In this work, only the first type of ISM is considered and implemented. The second one is left for the future work.

The details of ISM will be further presented in Chapter 7 and Chapter 8.

4.6. Summary

In this chapter, the fundamentals of FEM for the LPBF process simulation has been presented, which are mainly separated into three categories, elasto-plastic FEM, heat transfer FEM, and thermo-elasto-plastic FEM. Furthermore, a fast simulation method for part-level LPBF simulations—ISM has been briefly discussed.

Chapter 5. Heat Source Modeling for LPBF*

5.1. Introduction

In this chapter, a 3-dimensional heat-transfer finite element model for LPBF was developed for accurately predicting melt pool dimensions and surface features. A literature review of heat source models was presented, where eight commonly used heat source models are evaluated and compared. A model, including expressions of varied anisotropically enhanced thermal conductivity and varied laser absorptivity has been presented in order to predict the dimensions of melt pools accurately. The validity of the proposed approach is verified by the melt pool dimensions and track surface morphology.

5.2. Governing equations

The governing expression for 3D heat transfer processes can generally be as follows

$$\rho c \frac{\partial T}{\partial t} = \frac{\partial}{\partial x}\left(k_x \frac{\partial T}{\partial x}\right) + \frac{\partial}{\partial y}\left(k_y \frac{\partial T}{\partial y}\right) + \frac{\partial}{\partial z}\left(k_z \frac{\partial T}{\partial z}\right) + Q(x, y, z, t) \tag{5.1}$$

where ρ is the material density [kg/m^3], c is the specific heat [J/kgK]. T is the current temperature [K], t is the time [s]. x, y, and z are the coordinates in the reference system [m], k_x, k_y, and k_z are the thermal conductivity [W/mK] of x, y, and z-axis direction, and Q(x,y,z,t) is the internal heat generation per unit volume [W/m^3].

Because of the preheating of the substrate, the initial temperature (T_{base}) of the substrate and the powder layer was considered as 353 [K]. The ambient temperature (T_0) distribution of the environment during LPBF can be set to 293 [K].

* The materials presented in this chapter are adapted from the author's published work [204].

Convective heat losses (q_c) were considered as follows:

$$q_c = -h_c(T_{sur} - T_0) \tag{5.2}$$

where h_c is the convective heat transfer coefficient [W/(m^{2}K)], and T_{sur} is the surface temperature [K].

Radiative heat losses (q_r) were accounted for by using Stefan-Boltzmann law:

$$q_r = -\varepsilon\sigma(T_{sur}^4 - T_0^4) \tag{5.3}$$

where ε is the emissivity of the powder bed, and σ is Stefan-Boltzmann constant for radiation.

5.3. Heat source models

It is essential to establish an appropriate heat source model of LPBF simulations since the heat source will not only influence the geometries of melt pools but also probably have an impact on the mechanical performance of final products. Heat source models used in LPBF simulations is a laser beam which is usually assumed to be two-dimensional Gaussian [114]. The beam irradiance at any point (x, y) at time t for the fundamental transverse electromagnetic mode (TEM_{00}) can be expressed as

$$I(x,y,t) = \frac{2\beta P}{\pi r_l^2}\exp\left[-2\frac{\left(x - v\cdot t\right)^2 + y^2}{r_l^2}\right] \tag{5.4}$$

where P is the power of the stationary laser source, r_l is the radius of the laser beam, (x, y) are the coordinates of the heat source, v is the scanning velocity, and β is the laser-beam absorptivity.

However, it may be improper to employ the two-dimensional heat source to simulate LPBF because the laser scanning over metal powder can penetrate the powder bed [66]. In other words, laser energy is deposited not only on the top surface of a powder bed but inside the powder bed. Thus, volumetric heat sources should be considered in order to describe the laser penetration into powders [89].

Eight heat source models will be discussed and compared to investigate which heat source model is the most suitable one for LPBF simulations, the Optical Penetration Depth (OPD) method [83], three-dimensional Gaussian distribution [84], ellipsoidal distribution [84], conical heat source [86], radiation transfer method [66,196], absorptivity function method [87], linearly decaying heat source [88], and exponentially decaying heat source [89]. They can, however, be categorized into two groups: 1) geometrically modified group including the first four heat sources; and, 2) absorptivity profile group containing the last four heat sources.

5.3.1. GMG: Geometrically Modified Group

Since the Gaussian laser beam can penetrate and reflect in the powder layers, a practical method to describe this process is to change the shape of the heat source from two-dimensional surfaces to three-dimensional geometries, which can be a cylinder, semi-spherical, semi-ellipsoidal, and conical shape.

5.3.1.1. GMG.1: Cylindrical shape heat source model

The shape of the laser beam in LPBF is usually circular so that it is relatively straightforward to employ a 3D cylindrical heat source. The authors in [83] proposed to employ a uniform energy distribution for the heat source in the cylinder volume influenced by the Optical Penetration Depth (OPD). The OPD is defined as the depth where the laser intensity drops to 1/*e* (≈36.8%) of the laser beam intensity absorbed on the top surface of the powder bed. The schematic plot of the cylindrical heat source model is plotted in Figure 5.1a. Therefore, the heat source intensity can be expressed as

$$I\left(x,y,z\right)=\beta P/V,\ \ V=S\times\alpha_{OPD}\times OPD \tag{5.5}$$

where *x*, *y*, and *z* are the variables of the three dimensions, β is the absorptivity of laser beam, *P* is the laser power (W), *V* is the volume exposed by the laser beam (m^3), *S* is the area of the laser spot (m^2), and α_{OPD} is the correction factor for the assumed OPD. In this work, the OPD is chosen to

be the layer thickness of 20 μm, and the correction factor α is assumed to be 1 because of a lack of data for stainless steel 17-4PH.

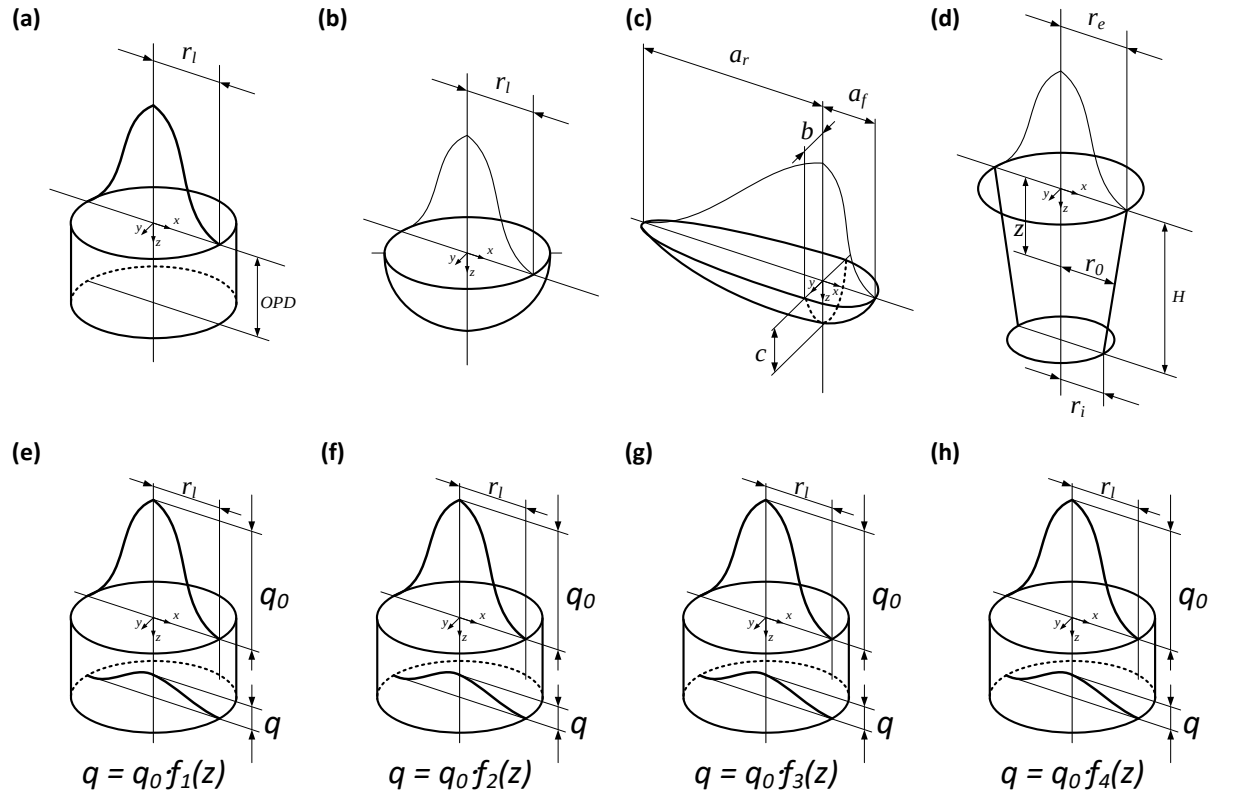

Figure 5.1. The schematic of the heat source models, (a) cylindrical shape; (b) semi-spherical shape; (c) semi-ellipsoidal shape; (d) conical shape, (e) radiation transfer method; (f) ray-tracing method; (g) linearly decaying method; (h) exponentially decaying method.

5.3.1.2. GMG.2: Semi-spherical shape heat source model

As known, the laser beam has a two-dimensional Gaussian intensity distribution [114]. In the case that a three-dimensional heat source should be considered, a semi-spherical Gaussian distribution of energy density (W/m^3) would be a step toward a more precise model [84]. The schematic plot of the conical heat source model is plotted in Figure 5.1b. As shown in [84], the expression of a 3D Gaussian distribution of the laser beam is as follows,

$$I(x,y,z) = q_0 \cdot \exp\left[-2\frac{x^2+y^2+z^2}{r_l^{\,2}}\right] \tag{5.6}$$

where q_0 is a coefficient derived by the energy balance. Based on the conservation of energy, the total energy input should be equal to the integration of intensity over the semi-infinite domain,

$$\beta \cdot P \cdot = \int_0^{\infty} \int_{-\infty}^{\infty} \int_{-\infty}^{\infty} q_0 \cdot \exp\left[-2\frac{x^2+y^2+z^2}{r_l^2}\right] dxdydz \tag{5.7}$$

Thus, the expression of q_0 should be,

$$q_0 = \frac{2^{5/2}\beta \cdot P}{\pi^{3/2} r_l^3} \tag{5.8}$$

After replacing q_0 in Eq.(5.6) by Eq.(5.8), the final expression of the intensity distribution can be obtained as,

$$I(x,y,z) = \frac{2^{5/2}\beta \cdot P}{\pi^{3/2} r_l^3} \exp\left[-2\frac{x^2+y^2+z^2}{r_l^2}\right] \tag{5.9}$$

5.3.1.3. GMG.3: Semi-ellipsoidal shape heat source model

The 3D Gaussian heat source is in semi-spherical shape; however, the melt pool in LPBF is often far from a spherical shape. In order to more accurately simulate the melt pool dimensions, the semi-ellipsoidal power distribution proposed by Goldak et al. [84] originally for the welding process has been employed and investigated, as shown in Figure 5.1c. As shown in [84], the ellipsoidal distribution is a Gaussian distribution in an ellipsoid with semi-axes *a*, *b*, and *c* and center at (0,0,0),

$$I(x,y,z) = q_0 \cdot \exp\left[-2\left(\frac{x^2}{a^2}+\frac{y^2}{b^2}+\frac{z^2}{c^2}\right)\right] \tag{5.10}$$

where *a*, *b*, *c* are semi-axes parallel to the coordinate axes *x*, *y*, *z*.

Similar to the 3D Gaussian distribution, q_0 is as follows,

$$q_0 = \frac{2^{5/2}\beta \cdot P}{\pi^{3/2} abc} \tag{5.11}$$

Thus, the final expression of the intensity distribution can be written as,

$$I(x,y,z)=\frac{2^{5/2}\beta\cdot P}{\pi^{3/2}abc}\exp\left[-2\left(\frac{x^2}{a^2}+\frac{y^2}{b^2}+\frac{z^2}{c^2}\right)\right] \tag{5.12}$$

According to the researchers [84], the front part of the ellipsoid could be different from the rear part in order to coincide with some experimental situations. Thus the double ellipsoidal power density distribution was proposed. The front part of the ellipsoid can be expressed as,

$$I_f(x,y,z)=f_f\cdot\frac{2^{5/2}\beta\cdot P}{\pi^{3/2}a_f bc}\exp\left[-2\left(\frac{x^2}{a_f^2}+\frac{y^2}{b^2}+\frac{z^2}{c^2}\right)\right] \tag{5.13}$$

while the rear part of the ellipsoid can be written as follows,

$$I_r(x,y,z)=f_r\cdot\frac{2^{5/2}\beta\cdot P}{\pi^{3/2}a_r bc}\exp\left[-2\left(\frac{x^2}{a_r^2}+\frac{y^2}{b^2}+\frac{z^2}{c^2}\right)\right] \tag{5.14}$$

where a_f and a_r are the semi-axes of the front and rear ellipsoids, respectively. It should be noted that f_f+f_r = 2, because,

$$\begin{aligned}\beta\cdot P&=\frac{1}{2}\int_0^{\infty}\int_{-\infty}^{\infty}\int_{-\infty}^{\infty}I_f(x,y,z)dxdydz+\frac{1}{2}\int_0^{\infty}\int_{-\infty}^{\infty}\int_{-\infty}^{\infty}I_r(x,y,z)dxdydz\\&=f_f\frac{\beta\cdot P}{2}+f_r\frac{\beta\cdot P}{2}\end{aligned} \tag{5.15}$$

5.3.1.4. GMG.4: Conical shape heat source model

In the welding area, researchers [86,197] have employed a conical shape heat source to simulate the welding process. Based on the inherent similarity between welding and LPBF, this model can be applied for simulating the LPBF process. The schematic plot of the conical heat source model is plotted in Figure 5.1d.

As shown in [86,197], the mathematical expression of the heat source can be written as,

$$I(x,y,z)=q_o\cdot\exp\left[-2\frac{x^2+y^2}{r_0^2}\right],\ \ r_0(z)=r_e+\frac{z}{H}\left(r_e-r_i\right) \tag{5.16}$$

where r_e and r_i are the radius at the top and bottom, respectively.

Based on the conservation of energy, the total energy input should be equal to the integration of intensity over the conical shape domain,

$$\beta \cdot P = \int_{-H}^{0} \int_{-\infty}^{\infty} \int_{-\infty}^{\infty} q_0 \cdot \exp\left[-2\frac{x^2+y^2}{r_0^2}\right] dxdydz \tag{5.17}$$

Using Eq.(5.17), an expression for q_0 can be derived,

$$q_0 = \frac{6\beta \cdot P}{\pi H\left(r_e^2 + r_e r_i + r_i^2\right)} \tag{5.18}$$

After replacing q_0 in Eq.(5.16) by Eq.(5.18), the final expression of the intensity distribution can be obtained as,

$$I(x,y,z) = \frac{6\beta \cdot P}{\pi H\left(r_e^2 + r_e r_i + r_i^2\right)} \cdot \exp\left[-2 \cdot \frac{x^2+y^2}{r_0^2}\right] \tag{5.19}$$

5.3.2. APG: Absorptivity Profile Group

During LPBF, a laser beam can penetrate a depth of a powder bed, while it is being absorbed gradually along the depth of the powder layer. Therefore, the powder bed can be viewed as an optical medium whose optical absorptivity would be described by absorptivity profiles. The heat source models in this group are not constrained in specific geometries as those in GMG, as shown in Figure 5.1(e-h). Their general form is that the two-dimensional Gaussian distribution is on the top surface while the laser beam is absorbed along the depth of the powder layer. It can be written as follows,

$$I\left(x,y,z\right) = \frac{2P}{\pi r_l^2} \exp\left[-2\frac{x^2+y^2}{r_l^2}\right] \cdot f\left(z\right) \tag{5.20}$$

where $f(z) = d\beta/dz$ is the absorptivity profile function. $\beta(z)$ is the absorptivity coefficient function.

5.3.2.1. APG.1: Radiation transfer equation method

The one-dimensional radiation transfer equation proposed by Gusarov et al. [66] is implemented and investigated. Based on the fact that laser can penetrate a depth of a powder bed, this approach resembles the powder bed with a thickness of z_{bed} with an optical media with an extinction coefficient of η. The schematic plot of this source model is plotted in Figure 5.1e.

As developed in [66], the volumetric heat source due to radiation transfer is,

$$I\left(x,y,z\right)=\frac{2P}{\pi r_l^2}\exp\left[-2\frac{x^2+y^2}{r_l^2}\right]\cdot f_1(z),\quad f_1(z)=\left(-\eta\cdot\frac{dq}{d\xi}\right) \tag{5.21}$$

where $\xi = \eta \cdot z$ is the dimensionless local depth coordinate, and q is the dimensionless form of net radiative energy flux density and is described as,

$$\begin{aligned} q=&\frac{\gamma a_s}{(4\gamma-3)D}\left\{\left(1-\gamma^2\right)\exp\left[-\lambda\right]\cdot\left[\left(1-a_s\right)\exp\left[-2a_s\xi\right]+\left(1+a_s\right)\exp\left[2a_s\xi\right]\right]-\left(3+\gamma\exp\left[-2\lambda\right]\right)\right.\\ &\left.\times\left\{\left[1+a_s-\gamma\left(1-a_s\right)\right]\exp\left[2a_s\left(\lambda-\xi\right)\right]+\left[1-a_s-\gamma\left(1+a_s\right)\right]\exp\left[2a_s\left(\xi-\lambda\right)\right]\right\}\right\}\\ &-\frac{3(1-\gamma)\left(\exp\left[-\xi\right]-\gamma\exp\left[\xi-2\lambda\right]\right)}{4\gamma-3} \end{aligned} \tag{5.22}$$

where $\lambda = \eta z_{\text{bed}}$ refers to the optical thickness for the powder bed, $a_s = \sqrt{1-\gamma}$, γ is the hemispherical reflectivity in the dense form, and D is described as,

$$\begin{aligned} D=&\left(1-a_s\right)\left[1-a_s-\gamma\left(1+a_s\right)\right]\exp\left[-2a_s\lambda\right]\\ &-\left(1+a_s\right)\left[1+a_s-\gamma\left(1-a_s\right)\right]\exp\left[2a_s\lambda\right] \end{aligned} \tag{5.23}$$

The extinction coefficient η is given as,

$$\eta = S_p / 4 \tag{5.24}$$

where S_p is the specific powder surface per unit pore volume, z_{bed} is the layer thickness. γ is 0.7 [66], S_p is regarded as π/r_{powder}, and r_{powder} is the average powder radius.

5.3.2.2. APG.2: Ray-tracing method

The above method represents an analytical way to derive the absorptivity profile function. The absorptivity profile function can also be acquired by numerical methods. Tran et al. [87] built up a powder bed model with randomly distributed particles and calculated the absorptivity profile function using Monte Carlo ray-tracing simulations. As developed in [87] and shown in Figure 5.1f, the volumetric heat source model can be formulated as,

$$I\left(x,y,z\right)=\frac{2P}{\pi r_l^2}\exp\left[-2\frac{x^2+y^2}{r_l^2}\right]\cdot f_2(z) \tag{5.25}$$

where $f_2(z)=d\beta/dz$ is the absorptivity function derived by the Monte Carlo ray-tracing simulation.

5.3.2.3. APG.3: Linearly decaying equation method

Besides the two methods presented above for deriving the absorptivity profile, Ladani et al. [88] employed a linearly decaying function (see Figure 5.1g) to describe the absorptivity profile as,

$$I(x,y,z)=\frac{2P}{\pi r_l^2}\exp\left[-2\frac{x^2+y^2}{r_l^2}\right]\cdot f_3\left(z\right),\quad f_3\left(z\right)=\frac{2\beta}{\delta}\left(1-\frac{z}{\delta}\right) \tag{5.26}$$

where δ is the beam penetration depth. In this work, the penetration depth is equal to the layer thickness.

5.3.2.4. APG.4: Exponentially decaying equation method

Similarly, an exponentially decaying heat source (see Figure 5.1h) was used by Liu et al. [89]. The specific expression is as follows,

$$I(x,y,z)=\frac{2P}{\pi r_l^2}\exp\left[-2\frac{x^2+y^2}{r_l^2}\right]\cdot f_4\left(z\right),\quad f_4\left(z\right)=\frac{\beta}{H}\cdot\exp\left[-\frac{|z|}{H}\right] \tag{5.27}$$

where H is regarded as the powder layer thickness.

5.3.3. Summary of Heat Models

The eight heat source models are summarized in Table 5.1.

Table 5.1. Summary of mathematical representations of laser-beam heat sources.

GMG1 [83]	Cylinder shape	$I(x,y,z)=\dfrac{\beta\cdot P}{S\times\alpha_{OPD}\times OPD}$
GMG2 [84]	Semi-spherical shape	$I(x,y,z)=\dfrac{2^{5/2}\beta\cdot P}{\pi^{3/2}r_l^{\,3}}\exp\left[-2\dfrac{x^2+y^2+z^2}{r_l^{\,2}}\right]$
GMG3 [84]	Semi-ellipsoidal shape	$I_f(x,y,z)=f_f\cdot\dfrac{2^{5/2}\beta\cdot P}{\pi^{3/2}a_f bc}\exp\left[-2\left(\dfrac{x^2}{a_f^{\,2}}+\dfrac{y^2}{b^2}+\dfrac{z^2}{c^2}\right)\right]$ $I_r(x,y,z)=f_r\cdot\dfrac{2^{5/2}\beta\cdot P}{\pi^{3/2}a_r bc}\exp\left[-2\left(\dfrac{x^2}{a_r^{\,2}}+\dfrac{y^2}{b^2}+\dfrac{z^2}{c^2}\right)\right]$
GMG4 [86]	Conical shape	$I(x,y,z)=\dfrac{6\beta\cdot P}{\pi H\left(r_e^2+r_e r_i+r_i^2\right)}\cdot\exp\left[-2\cdot\dfrac{x^2+y^2}{r_0^2}\right],\quad r_0=r_e+\dfrac{z}{H}\left(r_e-r_i\right)$
APG1 [66,196]	Radiation transfer equation method	$I(x,y,z)=\dfrac{2P}{\pi r_l^2}\exp\left[-2\dfrac{x^2+y^2}{r_l^2}\right]\cdot\left(-\eta\cdot\dfrac{dq}{d\xi}\right),$ $q=\dfrac{\gamma a_s}{(4\gamma-3)D}\Big\{(1-\gamma^2)\exp[-\lambda]\cdot\left[(1-a_s)\exp[-2a_s\xi]+(1+a_s)\exp[2a_s\xi]\right]$ $-(3+\gamma\exp[-2\lambda])\times\Big\{\left[1+a_s-\gamma(1-a_s)\right]\exp\left[2a_s(\lambda-\xi)\right]$ $+\left[1-a_s-\gamma(1+a_s)\right]\exp\left[2a_s(\xi-\lambda)\right]\Big\}\Big\}$ $-\dfrac{3(1-\gamma)\left(\exp[-\xi]-\gamma\exp[\xi-2\lambda]\right)}{4\gamma-3}$
APG2 [87]	Ray-tracing method	$I(x,y,z)=\dfrac{2P}{\pi r_l^2}\exp\left[-2\dfrac{x^2+y^2}{r_l^2}\right]\dfrac{d\beta}{dz}$
APG3 [88]	Linearly decaying equation	$I(x,y,z)=\dfrac{2P}{\pi r_l^2}\exp\left[-2\dfrac{x^2+y^2}{r_l^2}\right]\cdot f(z),\quad f(z)=\beta\cdot\dfrac{2}{\delta}\left(1-\dfrac{z}{\delta}\right)$
APG4 [89]	Exponentially decaying equation	$I(x,y,z)=\dfrac{2P}{\pi r_l^2}\exp\left[-2\cdot\dfrac{r^2}{r_l^2}\right]\cdot f(z),\quad f(z)=\beta\cdot\dfrac{1}{H}\exp\left[-\dfrac{\lvert z\rvert}{H}\right]$

5.4. Material properties

Two phases of Stainless Steel 17-4PH (SS17-4PH), the powder state and the solidified state, were considered in this simulation. The effective thermal conductivity of the powder bed is much smaller than that of bulk material and is typically from 0.1 to 0.2 [W/mK] at room temperature, which is around 1% of the bulk thermal conductivity (10.5 [W/mK] [198,199]). It should be noted

that the thermal conductivity of argon at room temperature is 0.017 [W/mK] at room temperature, which is still one order smaller than the effective powder conductivity. In addition, effective thermal conductivity is independent of material but depends on the size and morphology of the powders [83,114,200]. Rombouts et al. [200] have experimentally verified that there is no correlation between the conductivity of the powder bed and the material. Therefore, the effective thermal conductivity in this work is expressed as follows,

$$k_{powder} = \begin{cases} 0.01 \times k_{solid}, & T < T_m \\ k_{solid}, & T >= T_m \end{cases} \tag{5.28}$$

where T_m is the melting temperature. k_{powder} and k_{solid} are the thermal conductivity of the powder phase and solid phase, respectively.

As the powder bed is regarded as a mixture of solid powder (SS17-4PH) and gas (argon) phases, the density of SS17-4PH powder may be derived by:

$$\rho_{powder} = (1-\varphi)\rho_{solid} + \varphi \cdot \rho_{gas} \tag{5.29}$$

where φ is the porosity of SS17-4PH powder and is chosen as 0.53 based on the works by [21,201,202], ρ_{solid} is the density of the SS17-4PH bulk material, and ρ_{gas} is the density of argon gas. Since the density of argon gas is very low compared with that of SS17-4PH, it can be omitted, the density of SS17-4PH may be considered as follows,

$$\rho_{powder} = (1-\varphi)\rho_{solid} \tag{5.30}$$

The heat capacity of the powder bed may be then calculated using [83] and,

$$\rho_{powder} C_{powder} = (1-\varphi)\rho_{solid} C_{solid} + \varphi \cdot \rho_{gas} C_{gas} \tag{5.31}$$

where C_{powder}, C_{solid}, and C_{gas} are the heat capacity of the powder bed, gas phase, and solid phase, respectively. Similarly, by omitting the gas phase due to its low density, the heat capacity of the powder bed is regarded as equal to the heat capacity of the solid phase. Figure 5.2a-c show the temperature-dependent material properties of material SS17-4PH [198], and Figure 5.2d depicts

those of the base plate, material mild carbon steel [203]. It should be noted that there was a typo in the Matlab code for generating the heat capacity plot of stainless steel 17-4, which has been published in [204]. The typo is the heat capacity at room temperature, which should be 426 [J/(kg·K)], not 196. The typo has been corrected in this thesis, as shown in Figure 5.2c and later, Figure 6.1 as well. The effective capacity method [12] was employed in this work. The heat capacity due to latent heat during material phase change can be specified as

$$C = \begin{cases} C_{solid}, & T \le T_s \\ C_{solid} + 2 \cdot L_f \left(T - T_s\right) / \left(T_l - T_s\right)^2, & T_s < T \le T_l \\ C_{solid} + 2 \cdot L_v \left(T - T_l\right) / \left(T_v - T_l\right)^2, & T_l < T \le T_v \end{cases} \tag{5.32}$$

where C_{solid} is the specific heat of the material at solidus temperature, L_f and L_v are the latent heat of fusion and vaporization, T_s, T_l, and T_v are the solidus, liquidus, and vaporization temperatures.

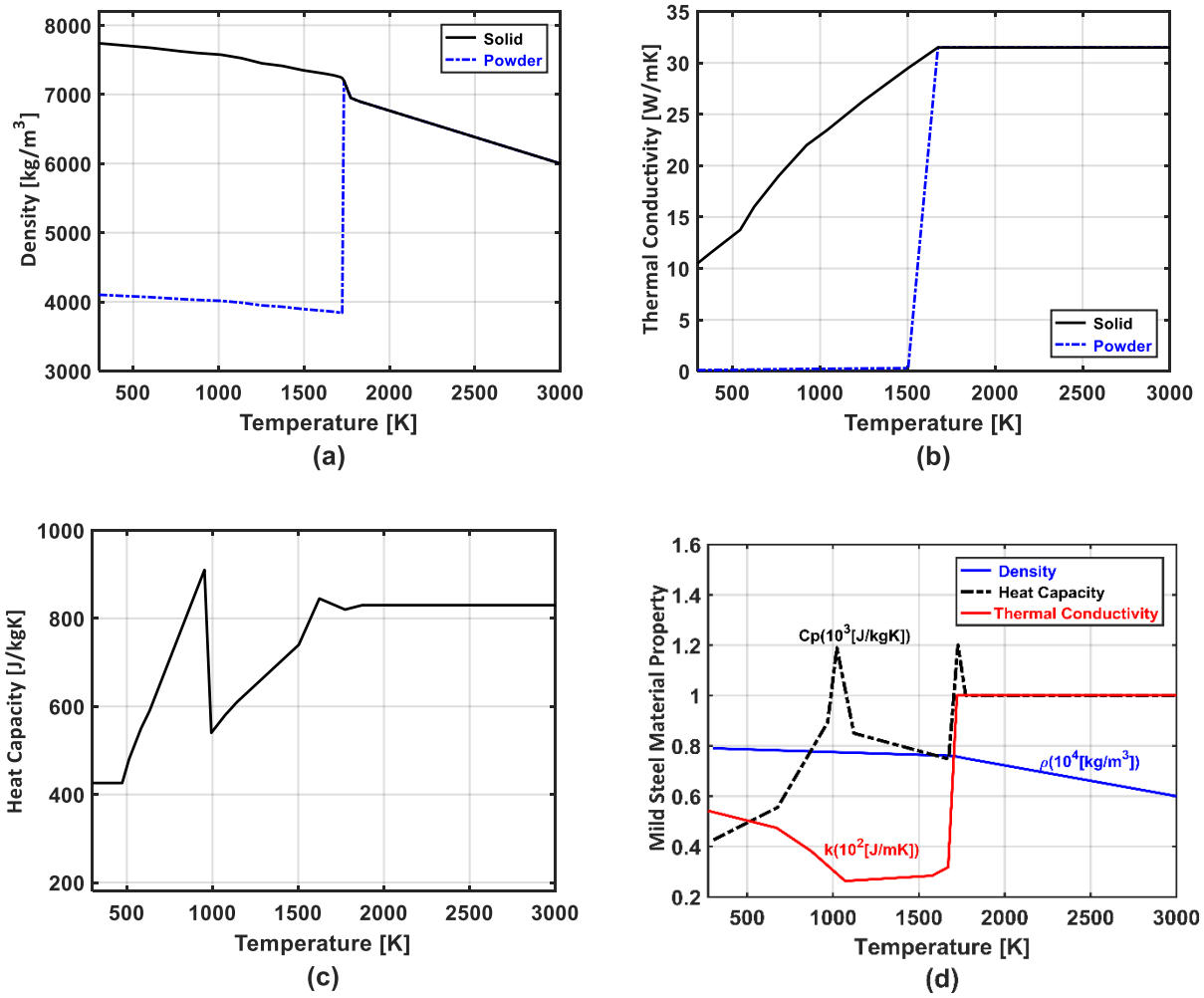

Figure 5.2. Temperature-dependent thermal material properties (a) density of SS17-4PH; (b) thermal conductivity of SS17-4PH; (c) heat capacity of SS17-4PH; (d) material properties of mild carbon steel.

Furthermore, a model related to two material properties was proposed for better predicting melt pool dimensions, anisotropically enhanced thermal conductivity k, and the effective absorptivity of continuous laser light β. To the authors' best knowledge, this is the first work that considers the varied anisotropically enhanced thermal conductivity and varied laser absorptivity in the LPBF modeling. The melt pool dimensions can be described in linear functions to the deposited energy density for several process-parameter regions, which is consistent with the findings in [28]. The deposited energy during the laser dwell time $\tau = 2r_l/v$ is $\beta P\tau$, where r_l is the laser beam radius. This energy is deposited in a volume, whose depth can be regarded as the heating depth, $HDR \cdot l_{th}$, where

$HDR=\sqrt{(4\alpha\tau)}/l_{th}$, α is the diffusivity, and l_{th} is layer thickness, according to [24]. The volume is expressed as $V=\pi r_l^2\sqrt{(\sqrt{(4\alpha\tau)})}$. Therefore, the absorbed energy density e_m is derived by dividing the deposited energy $\beta P\tau$ by V,

$$e_m = \frac{\beta}{\pi\sqrt{2\alpha r_l^3}} \cdot \frac{P}{\sqrt{v}} = C \cdot \frac{P}{\sqrt{v}} \tag{5.33}$$

where C is a coefficient, which is $\beta/(\pi\cdot\sqrt{(2\alpha r_l^3)})$. Since α during the analysis in [24] and β in [28] were regarded as constants, it can be found that the energy density is proportional to the ratio of the laser power to the root of velocity, $P/\sqrt{v}$.

Therefore, the melt pool dimensions are proportional to $P/\sqrt{v}$. However, physical explanations behind it were not fully understood, and simulation results with isotropic thermal conductivity k and constant absorptivity β are not consistent with the experimental results, which will be discussed in details in the discussion section. For improving the accuracy of simulation results, a novel model of the material properties is proposed that the absorptivity, β, and the anisotropically enhanced factors of thermal conductivity, λ_x, λ_y, and λ_z, are assumed to be simple linear algebraic equations of $P/\sqrt{v}$ based on experimental results. The anisotropically enhanced thermal conductivity discussed in [90] was employed to approximate the contribution of the melt pool convection to melt pool dimensions. During the LPBF process, an important contributory mode of heat transfer is the melt pool convection, which may change the melt pool dimensions and influence the temperature distribution in a melt pool [76,205]. Using the anisotropically enhanced thermal heat conductivity could improve the dimension accuracy of melt pool simulation results [89,90]. The anisotropically enhanced thermal conductivity can be expressed as follows,

$$k_x = \lambda_x k, \;\; k_y = \lambda_y k, \;\; k_z = \lambda_z k \tag{5.34}$$

where λ_x, λ_y, and λ_z are the anisotropically enhanced factors of thermal conductivity k. They are dependent on the temperature in the melt pool and derived based on experiments. It should be

noted that the unmelted powder bed is assumed to be isotropic, as shown by that the enhanced factors are all equal to 1.

$$\begin{cases} \lambda_x = \lambda_y = \lambda_z = 1, & T < T_{melting} \\ \lambda_x = 1,\ \lambda_y = f_y(P,v), \lambda_z = f_z(P,v), & T \geq T_{melting} \end{cases} \tag{5.35}$$

where f_y and f_z are functions of laser power P [W] and scanning speed v [mm/s].

In this work, a linear function of the enhanced factor of thermal conductivity, λ_z, is proposed to be a function of the combined process parameter $P/\sqrt{v}$ ($P/\sqrt{v}$ is originally mentioned in Eq.(5.33)), and described as,

$$\lambda_z = a_1 \frac{P}{\sqrt{v}} + b_1 \tag{5.36}$$

The enhanced factor of thermal conductivity λ_y, which influences the width of the melt pool, is formulated slightly different from λ_z since the width of melt pool is proportional only to velocity v and not globally proportional to $P/\sqrt{v}$,

$$\lambda_y = \begin{cases} a_2 v + b_2, & v \leq v_a \\ 1, & v > v_a \end{cases} \tag{5.37}$$

where v_a, a_1, b_1, a_2, and b_2 are also parameters and will be determined by experimental results. The melt pool width may be controlled by some physics in the melt pool, which causes it more sensitive to the scanning speed than the laser power. However, further investigation of the influence of melt pool dynamics on the melt pool width should be necessary.

Secondly, the effective absorptivity β of continuous laser light can also influence the melt pool dimensions significantly [91]. It typically can vary greatly based on different combinations of laser powers and scanning speeds. The recoil pressure-induced surface depression may lead to an increase in the absorption of the laser light [91].

The absorptivity β in the present work is also proposed to be a linear equation and can be written as,

$$\beta = a_3 \frac{P}{\sqrt{v}} + b_3 \tag{5.38}$$

where a_3 and b_3 are coefficients to be determined by experiment. The variation of the effective absorptivity was specified as 0.48~0.65, which is comparable with the data from [91].

5.5. Numerical model configuration

The present study is proposed to estimate the geometries of the melt pool under the substrate top surface. Using the commercial software package, COMSOL 5.2 Multiphysics, simulations were performed considering non-linear transient thermal analyses within the metal powder and the base plate. The dimensions of the solid substrate in the simulation were 2000×1000×500 μm, and those of the powder layer were appointed to be 2000×1000×20 μm. The simulation domain must be large enough for getting a stable melt pool in the simulation, because the thermal shock problem, which though has a relatively short-term effect for pure thermal analyses, may cause numerical instabilities if the melt pool is not fully developed [206,207]. The powder layer thickness was chosen as 20 μm since it is one of the commonly used layer thickness. The material of the solid substrate was mild carbon steel, and the powder layer was Stainless Steel 17-4PH. Tetrahedral elements were employed for meshing both the solid substrate and the metal powder layer. The laser beam diameter was 100 μm. The eight volumetric heat sources discussed previously were employed in the simulation, while the exponentially decaying heat source was employed in further simulations where varied anisotropically enhanced thermal conductivity and varied absorptivity were also considered. According to a series of convergence trials, the laser-beam interaction region was meshed with 20 μm elements, while the other regions were filled with coarser elements in order to improve the computational efficiency. In this study, an adaptive time step algorithm was sued with an initial time step of 7 μs. The adaptive time step allows users to give a reference time step, and the software changes the time step based on the convergence state during the simulation. The minimum and maximum value for the time step used in numerical simulations were between

0.2 μs and 6 μs. In order to accelerate the simulations, only half of the geometry was built based on symmetry, since the domain is symmetric about the vertical plane containing the laser-beam moving line, as presented in Figure 5.3. The symmetry constraint was set on the symmetric plane. In addition, radiation (Eq.(5.2)) and convection (Eq.(5.3)) heat losses at the top surface of the powder layer to the ambient air were considered. The convective heat transfer coefficient and the emissivity coefficient were chosen as 15 [W/mK] [208] and 0.5 [209], respectively. The ambient temperature was set to be 293K. The other sides of the domain were specified as a fixed preheating temperature, 353 K.

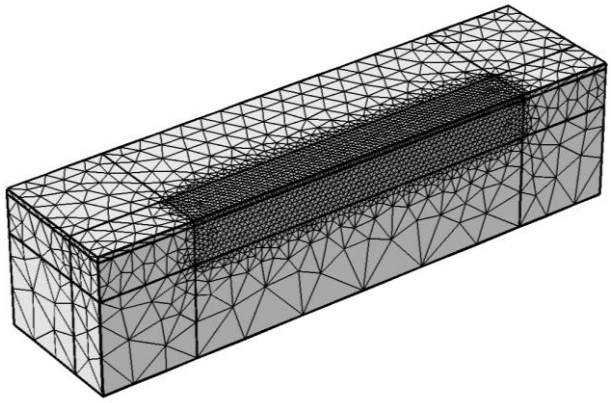

Figure 5.3. Geometry and mesh used in the finite element simulation.

5.6. Experimental procedures

Experiments were carried out on an EOS M 290 LPBF machine. Its chamber was filled with argon atmosphere during the manufacturing process. The EOS M 290 has a 400W fiber laser. The transverse electromagnetic mode of the laser beam is TEM_{00} indicating a single-mode laser, and the beam spot diameter is 100 μm. The powder used in this study is the gas atomized Stainless Steel 17-4PH powder with a particle size of 16~64 μm. The scanning electron microscopy (SEM) image (Figure 5.4) of Stainless Steel 17-4PH powder particles shows that they were almost spherical.

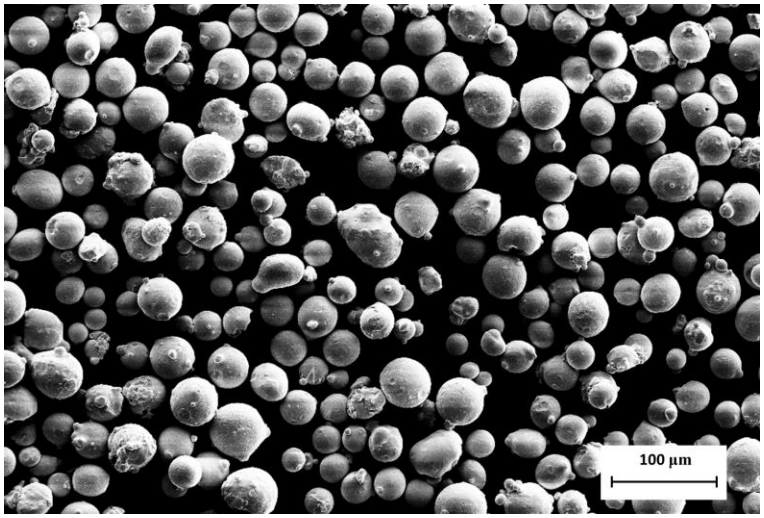

Figure 5.4. SEM image of the stating powders

In order to validate the numerical simulation results, several single-track experiments were conducted. The current design of experiment (DOE) included combinations of different process parameters, including laser power and scanning speed. According to the literature [210–216], the laser power used by other researchers is generally from 190 to 200 W, for 17-4 PH stainless steel. As such, only laser powers close to this range were studied, which were 170, 195, and 220 W. The scanning speed range was from 600 to 1300 mm/s, while two different layer thicknesses of 20 and 40 μm were employed. The corresponding selections of the processing parameters are shown in

Table 5.2. The combinations of the process parameters were categorized into 6 groups, as exhibited in Figure 5.5a. In order to avoid randomness, each set of parameters was repeated five times, as shown in Figure 5.5b.

Table 5.2. Parameters for the tests of single-line scanning

Laser power, P [W]	170	195	220					
Scanning speed, v [mm/s]	600	700	800	900	1000	1100	1200	1300
Layer thickness, lth [um]	20	40						

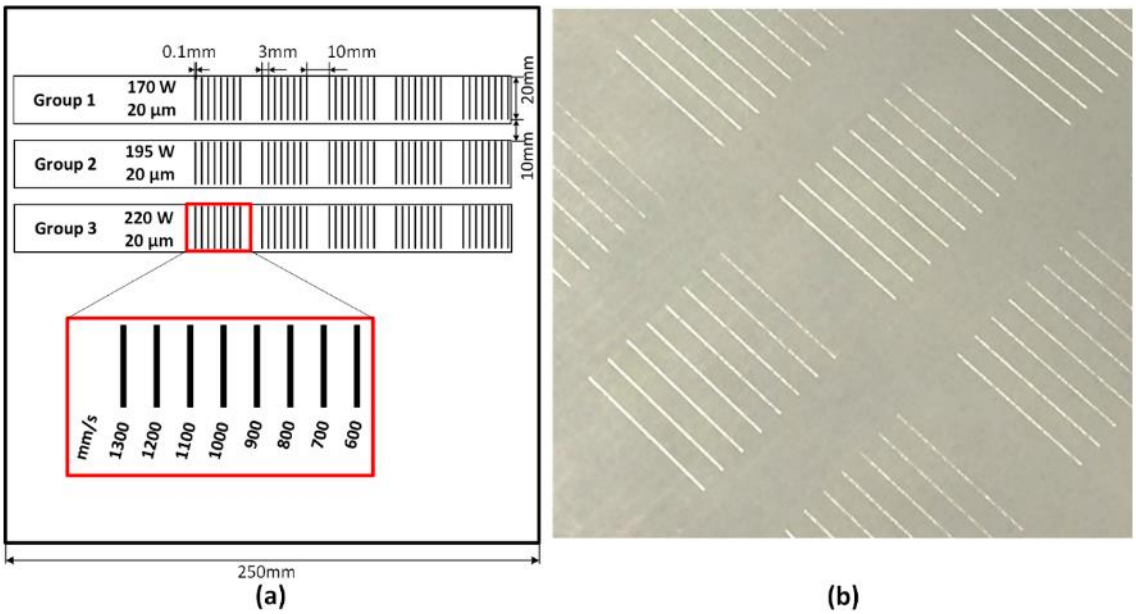

Figure 5.5. The configuration of single tracks on the substrate, (a) design of experiments, (b) the single tracks printed.

All the single tracks were cross-sectioned in the middle of the scan line perpendicular to the laser-scan direction. The samples were mounted, polished, and etched by using 5% Nital. The melt pool dimensions (width and depth) and the single-track surface profiles were measured by a laser scanning confocal microscope. For measuring the melt pool dimensions, each of the produced single tracks was mounted, cross-sectioned, and measured, as shown in Figure 5.6. It should be noted that the melt pool depth (as shown in Figure 5.6) was measured from the surface of the substrate to the bottom of the melt pool, which does not include the bead height.

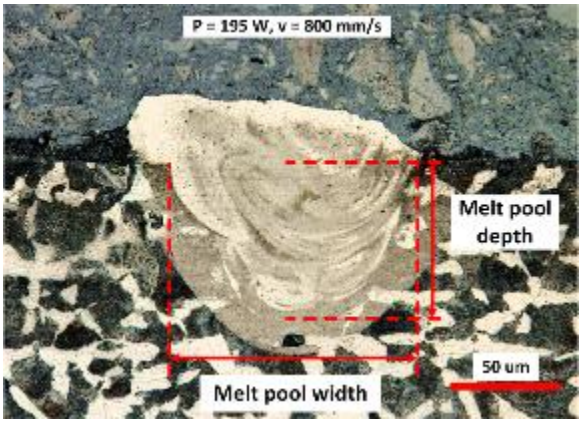

Figure 5.6. Melt pool cross-section.

5.7. Results and discussion

5.7.1. Heat source model comparisons

Heat transfer simulations with the eight heat sources (GMG1 to GMG4 and APG1 to APG4) listed in Table 5.1 were performed with laser power and scanning speed of 195 W and 800 mm/s, respectively, which were used in the literature [216,217]. The layer thickness of 20 μm was used. Figure 5.7a shows the melt pool dimensions of experimental and simulation results. The left and right show the melt pool width and depth, respectively. For the melt pool width, all the simulation results with the eight heat source models are within the experimental variation range. The maximum melt pool width error is 7.4% (GMG1). However, for the depth, all of the simulation results are over 40% smaller than the experimental results.

In GMG, GMG1 results in the largest width but the smallest depth. In contrast, GMG4 leads to the smallest width but the largest depth. The results of GMG2 and GMG3 are almost identical (0% in width, 2.5% in depth), because the semi-axes b and c, which may influence melt pool width and depth correspondingly, were chosen as the same as the radius r_l. The melt pool dimensions derived in GMG may be further improved by carefully setting the parameters of the heat source models, for example, by increasing the height of the conical shape to make the simulated melt pool deeper.

In APG, the absorptivity profile in APG2 is originally from the ray-tracing method [87], while that in APG1 is derived by mathematical analysis [66]. APG1 and APG2 have very similar melt pool dimensions (1.7% in width, 2.7% in depth). Since these two models were designed for predicting melt pools in the conduction mode [87], where the melt pool convection is not significant, the melt pool depths are near 50% smaller than the experimental result. In addition, APG4's melt pool is a little bit deeper, while the error still is very large, over 40%.

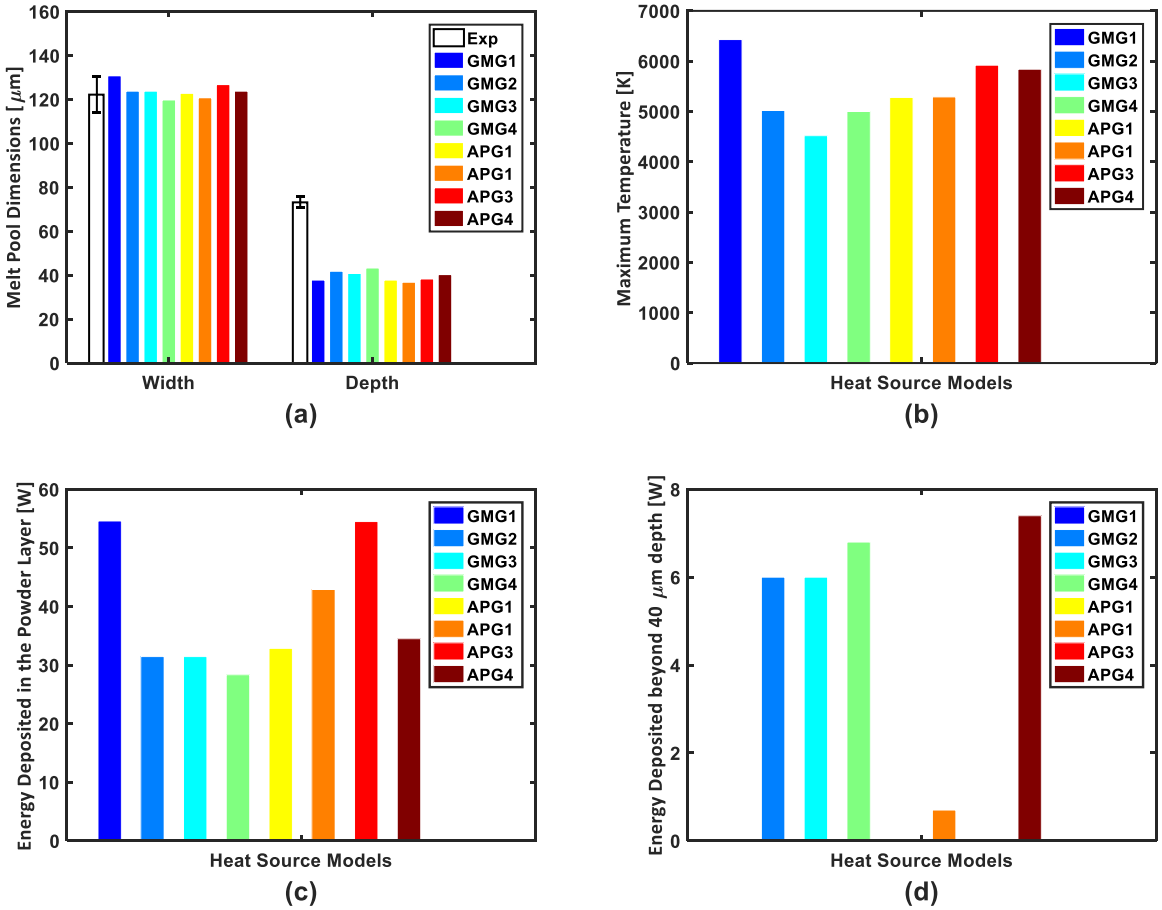

Figure 5.7. Comparisons of the heat source models, (a) melt pool dimensions, (b) maximum temperature, (c) energy deposited in the powder layer, (d) energy deposited beyond 40 μm depth.

Besides, Figure 5.7b shows the maximum temperature for the eight heat source models. The two highest maximum temperature, GMG1 and APG3, correspond to the two largest melt pool widths, respectively. Since the laser energy melted the material and formed the melt pool, the energy deposition distribution influences melt pool dimensions and as well as the maximum temperature. It should be noted that these maximum temperatures are all very high, which seems unrealistic. However, the maximum temperature becomes reasonable (Figure 5.17) when using the proposed model, which indirectly shows another strength of the proposed model. The energy deposition in the powder layer is plotted in Figure 5.7c. It can be seen that the two maximum energy deposition models are GMG1 and APG3 as well, which correspond to the trends of the maximum melt pool width and maximum temperature. In addition, the smallest energy deposition

from GMG4 results in the smallest melt pool width as well as one of the smallest maximum temperatures. Therefore, a conclusion can be derived that there is a positive correlation between either the melt pool width or the maximum temperature and the energy deposition in the powder layer. In other words, the more energy is deposited in the powder layer, the wider the melt pool and high maximum temperature are.

Furthermore, Figure 5.7d plots the energy deposition in the region beyond the melt pool depths, which is chosen as 40 μm. Comparing Figure 5.7d to Figure 5.7a manifests the heat sources GMG2 GMG3 GMG4 and APG4, which have larger energy deposition in this region than the remaining four, result in deeper melt pools. It seems that more energy is deposited in a deeper domain; the deeper melt pools are derived in the simulations. Even though it is not a restricted rule since the numerical simulations are nonlinear, the trend is obvious that there is a positive correlation between the melt pool depth and the energy deposition in the region beyond 40 μm depth.

In GMG, GMG4 may be potential to make a more accurate prediction by increasing the cone's height. However, there would be another factor, the bottom radius. To derive the optimal parameters for GMG4 may take lots of trials and errors. In addition, the energy input is constrained in the specific geometry may need further physical explanations. In APG, APG1 and APG2 are initially designed for conduction mode, and their expressions are more complex than APG3 and APG4. Besides, APG3 has a less accurate prediction than APG4. Therefore, APG4 will be chosen as the heat source for the following simulations.

It should be noted that all of the simulated depths are over 40% smaller than the experimental result, even by using APG4. The discrepancy between simulation and experimental results may even increase under some combinations of laser power and scanning speed. For example, Figure 5.8a shows the simulated and experimental depth with the same power but under different scanning speeds with APG4. The difference between the simulation and experimental results is larger with decreasing the scanning speed. All of these could be explained by the underestimation of the contribution of melt pool convection to the heat transfer model. As the discussion in [89,90] about

the anisotropically enhanced thermal conductivity, incorporating the melt pool convection effect into the analysis by choosing appropriate anisotropically enhanced thermal conductivity is helpful to describe both temperature and temperature-gradient distributions correctly. For example, Figure 5.8b shows the results derived from the model proposed in this work, and a better match between simulation and experimental results is obtained. A further detailed discussion of the melt pool prediction will be illustrated in the later sections.

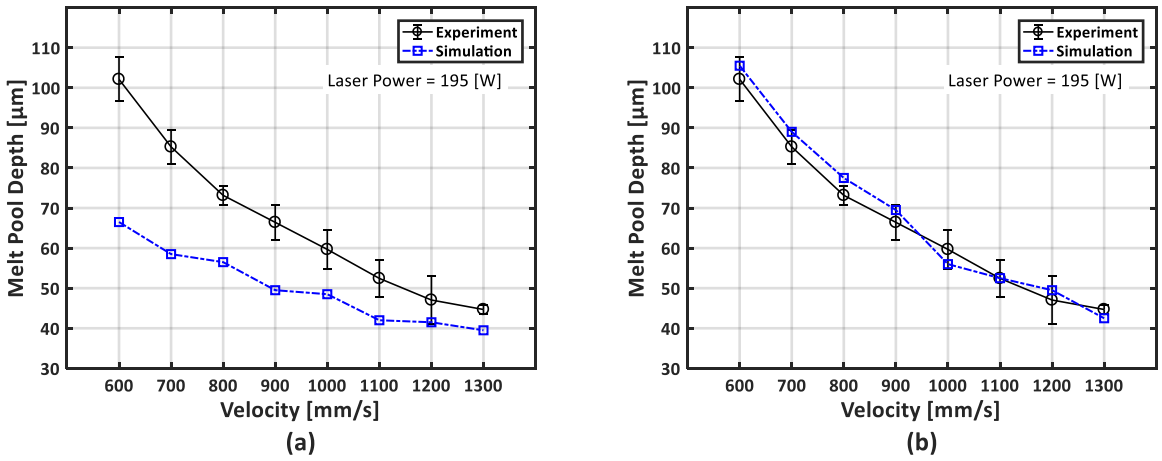

Figure 5.8. Comparison of melt pool depths between simulations by two methods, (a) the traditional method in literature, (b) the method proposed in this work considering anisotropically enhanced thermal conductivities and varied absorptivities.

5.7.2. Prediction of melt pool dimensions

In order to study the effect of the LPBF process parameters, e.g., laser power (P) and scanning velocity (v) on melt pool dimensions, experiments were carried out with the process parameters listed in

Table 5.2. The melt pool width and depth were measured through the analysis of the microscopic images, as shown in Figure 5.6. Several melt pool profiles are shown in Figure 5.9, which covers the whole range of the process parameters. The trend of melt pool dimensions with different process parameters can be observed, for example, the melt pool is the biggest with the largest power and the lowest speed, and the melt pool is the smallest with the smallest power and

the largest speed. Furthermore, the whole experimental results of the melt pool width and depth with three laser powers (170, 195, 220 W) and varied speed (600-1300 mm/s) are plotted in Figure 5.10a-b.

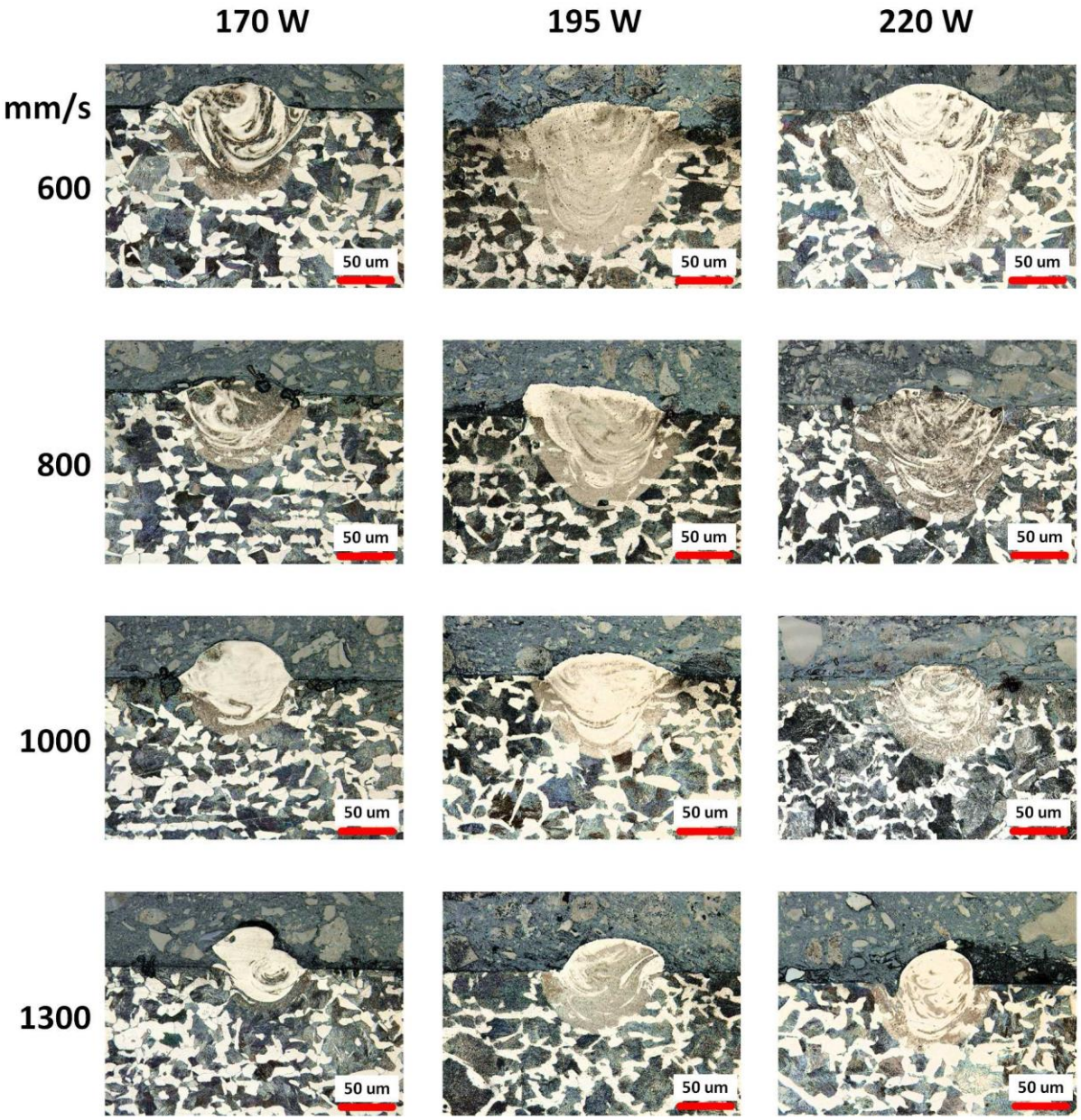

Figure 5.9. Melt pool shapes of single tracks on one layer of powder particles at different laser power and process speed combinations.

Figure 5.10 shows that the melt pool width and depth reduce with increasing scanning speeds. This trend is observed for all powers. Moreover, with higher laser power, the melt pool depths are

deeper, as shown in Figure 5.10b, where the red curve is above the others. The melt pool widths tend to increase less obviously, as shown in Figure 5.10a, where the red curve and the blue curve are relatively close for all the scanning speeds.

Figure 5.11 presents the experimental results of melt pool dimensions as functions of $P/\sqrt{v}$. Interestingly, the data of melt pool depth, which shows uncertain patterns in Figure 5.10b, collapses to a linear line, as shown in Figure 5.11b. As for the melt pool width, it is not converged into a single curve but is formed into three similar curves with close maximum and minimum value. The inability to converge to a master curve for melt pool widths could be due to other physical parameters that affect the melt pool width more than the laser power and velocity.

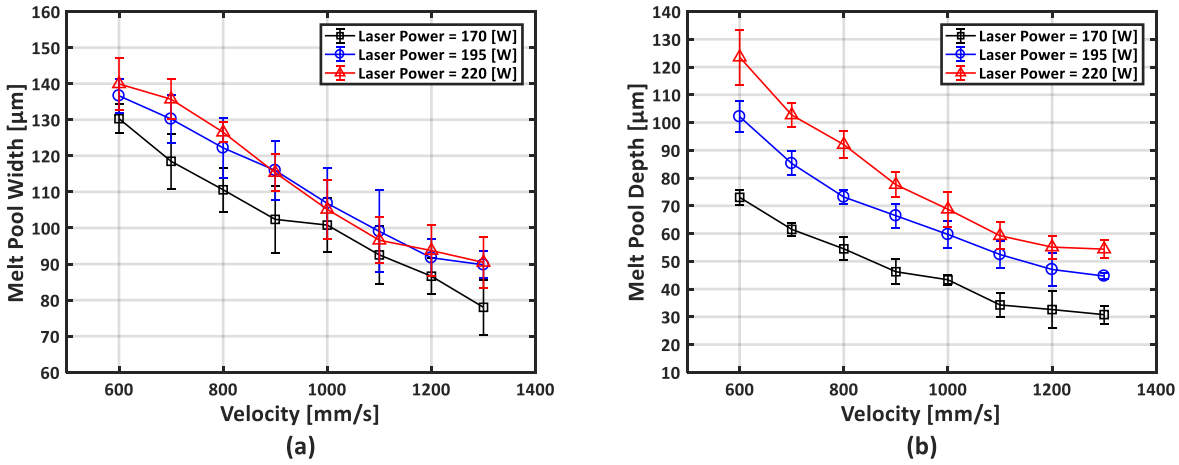

Figure 5.10. Experimental results of melt pool dimensions with different laser powers and scanning velocities, (a) melt pool width, (b) melt pool depth.

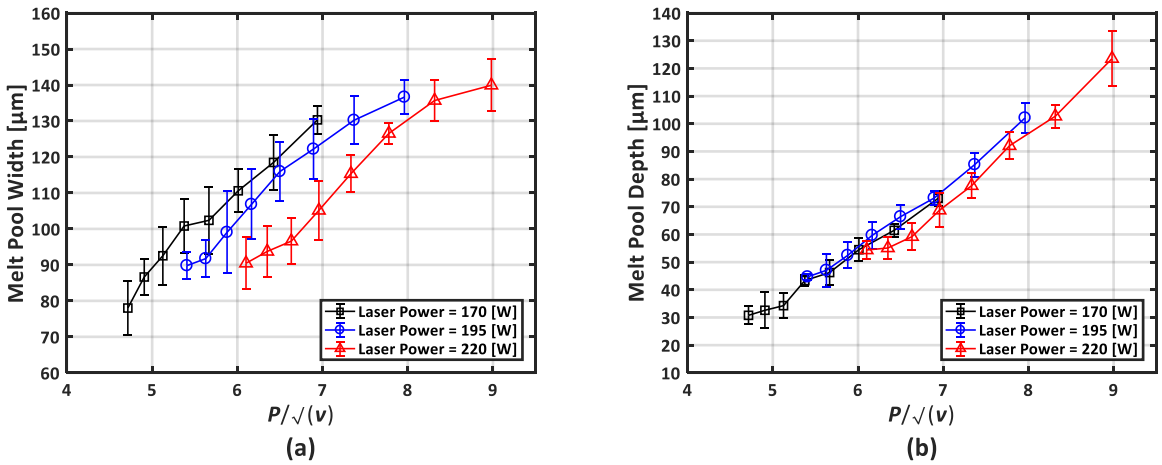

Figure 5.11. Experimental results of melt pool dimensions as functions of $P/\sqrt{v}$, (a) melt pool width, (b) melt pool depth.

Experimental melt pool width and depth results, shown in this section, were used to calibrate and validate single track LPBF simulations using heat source model APG4. As the discussion previously about Figure 5.8, a lack of considering anisotropically enhanced thermal conductivity and varied absorptivity, may cause the simulation results diverged from the experimental ones. In order to predict the melt pool dimensions more accurately as the experimental results, the model shown in Eq.(5.38), Eq.(5.36), and Eq.(5.37) was employed, in which the absorptivity β and the anisotropically enhanced factors of thermal conductivity λ_{yy} and λ_{zz} are formulated in simple linear equations of $P/\sqrt{v}$. The coefficients (Table 5.3) in these three equations are obtained by matching numerical results with experimental results. It should be noted that with the coefficients, the variation of the effective absorptivity is calculated as 0.48~0.65 by Eq.(5.37), which are comparable with the data from [91,92]. In addition, it should be pointed out that a1, a2, and a3 should have units in order to make the units of the final products correct.

Table 5.3. Coefficients in the approximation equations of anisotropically enhanced thermal conductivity and varied absorptivity.

a_1 $(\sqrt{m/s}/W)$	b_1	a_2 (s/m)	b_2	a_3 $(\sqrt{m/s}/W)$	b_3	v_a (mm/s)
2.1095	2.7241	-0.0036	4.96	0.0398	0.4748	1100

Figure 5.12a-c show the comparison of the melt pool dimensions between the simulation (sim) and experimental (exp) results at a laser power of 170 W, 195 W, and 220 W, respectively. Results from Figure 5.12 show good agreement with experimental results. The melt pool width and depth error between simulation and experimental results are listed in Table 5.4. As seen in Table 5.4, when the proposed model consisting of Eq.(5.38), Eq.(5.36), and Eq.(5.37) was included, all average error of the melt pool width is within 4%. The average error of melt pool depth is within 7% for 195 W and 220 W. The 170 W has a larger error, which may be due to measuring error. In addition, 170W resulted in the smallest melt pool depth, so the absolute error should be comparable to those of 195 W and 220 W.

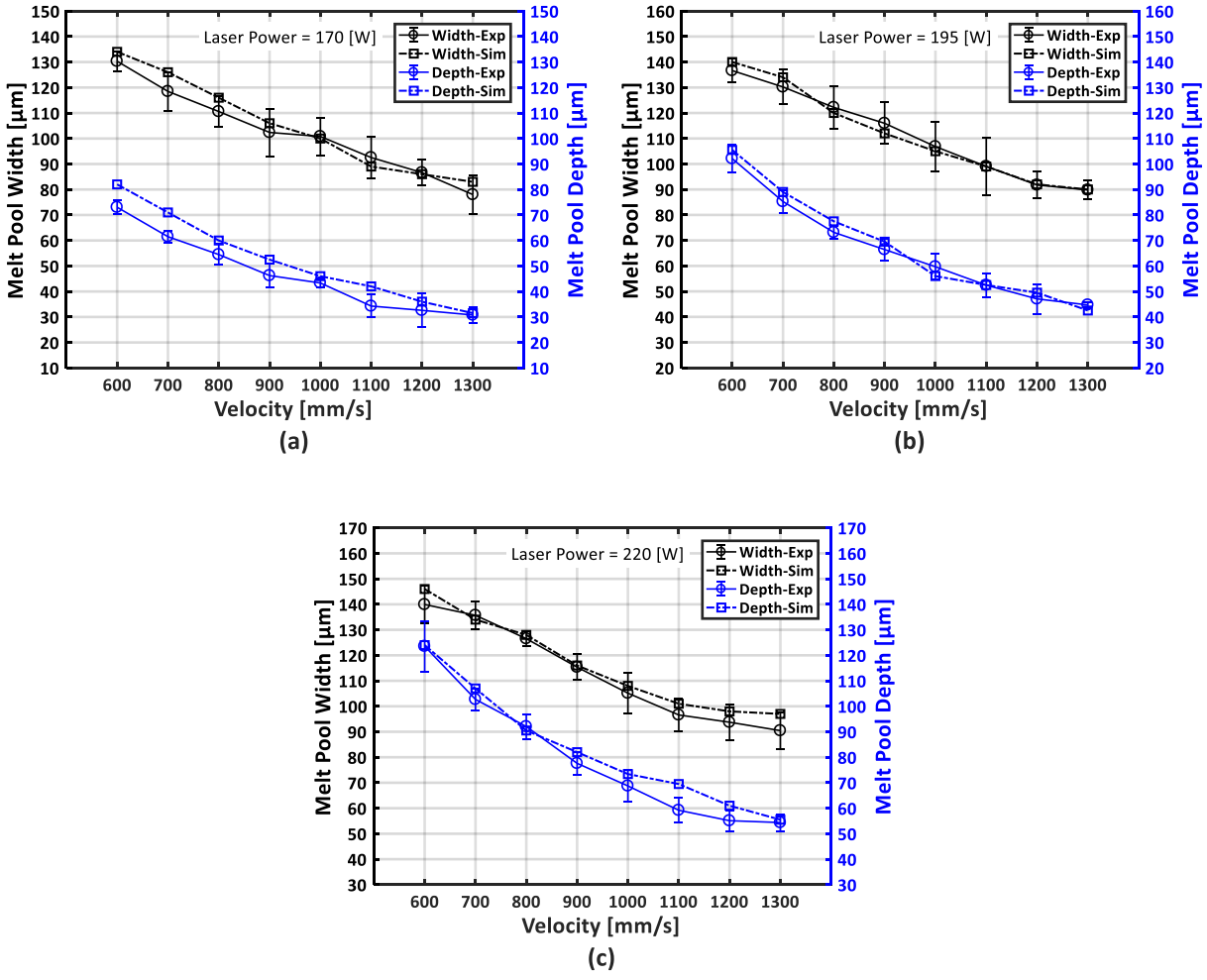

Figure 5.12. Comparisons of melt pool dimensions at different power (a) *P* = 170 W, (b) *P* = 170 W, (c) *P* = 220 W.

Table 5.4. Proposed model validation and comparison of simulation results with experimental data.

Power (W)	Min Error Width (%)	Min Error Depth (%)	Max Error Width (%)	Max Error Depth (%)	Average Error Width (%)	Average Error Depth (%)
170	0.8	2.35	6.3	22.6	3.7	11.6
195	0.22	0.11	-3.4	-5.9	1.6	4.3
220	0.57	0.37	4.5	10.7	3.3	6.1

The simulation (sim) and experimental (exp) results are also plotted together in Figure 5.13 as functions of $P/\sqrt{v}$, where it is proved that the proposed model can predict the trend of the melt pool dimensions very well. Results presented in Figure 5.13b show that the melt pool depth is proportional to $P/\sqrt{v}$. Therefore, the melt pool depth d can be approximated with the following equation,

$$d = k_d \cdot \frac{P}{\sqrt{v}} + k_i \tag{5.39}$$

where k_d is the slope, and k_i is the y-intercept. It should be noted that Eq.(5.39) is similar to the expression of the absorbed energy density shown in Eq.(5.33), which implies the melt pool depth may be a linear function of the absorbed energy density e_m. However, since the C in Eq.(5.33) consists of the absorptivity and thermal conductivity k ($\alpha=k/\rho C_p$), which are all variables in this proposed model, e_m as a function to $P/\sqrt{v}$ should be evaluated by substituting the absorptivity β (Eq.(5.38)) and the enhanced factors of thermal conductivity λ_{zz} (Eq.(5.36)) into it.

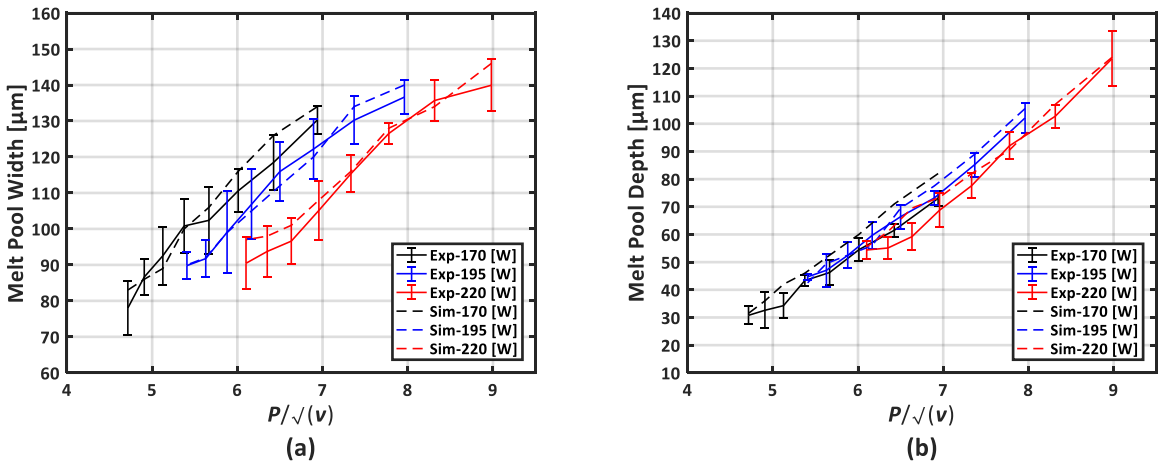

Figure 5.13. Comparison between the numerical and experimental results of melt pool dimensions as functions of $P/\sqrt{v}$, (a) melt pool width, (b) melt pool depth.

Figure 5.14 depicts the absorbed energy density e_m versus $P/\sqrt{v}$, from which the approximately linear behavior for a large portion of the range could be observed. Therefore, the conclusion can be proved, as discussed in [28,218], that melt pool depth is proportional to the absorbed energy density for a range of the input process parameters. Furthermore, since during simulation, laser absorptivity is regarded as a linear function of the parameter $P/\sqrt{v}$, as shown in Eq.(5.38), it may prove that the absorptivity in the laser scanning process may increase with larger $P/\sqrt{v}$ value, as illustrated in [91]. This phenomenon may be explained by the reason that at higher intensities, a deeper depressed surface would be formed by the vapor recoil pressure in the melt pool, so that the laser interacts with the deeper and steeper walls, leading to less reflection of the laser beam and increased energy absorption. It is necessary to note that the left end of the curve in Figure 5.14 seems to be nonlinear, which is belonged to 170 W, and this nonlinearity may be another reason why the error of 170 W shown in Table 5.4 is larger than those of 195 W and 220 W. However, further investigation on the applicable range of this proposed model should be addressed in the future work.

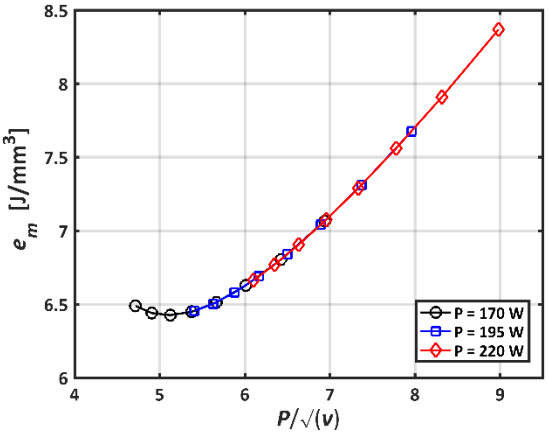

Figure 5.14. Absorbed energy density vs. $P/\sqrt{v}$.

5.7.3. Printed track surfaces

Figure 5.15 shows the 3D surfaces of experimental samples for different combinations of process parameters. The ripple, for example, in 1-1, is almost in a triangle shape, and it indicates the shape of the isotherm curves. From Figure 5.15a, it can be observed that the triangle-shaped pattern of ripple becomes not clear when the scanning speed is increased to 800 mm/s In addition, peaks and valleys are formed, not uniformed height anymore as shown by those with lower scanning speed, which may imply that the single tracks are becoming unstable. The similar phenomena happened at the laser power of 195 W (Figure 5.15b) and 220 W (Figure 5.15c), while the thresholds of the scanning speed that cause instability are around 1000mm/s, which are larger than of that with the laser power of 170 W.

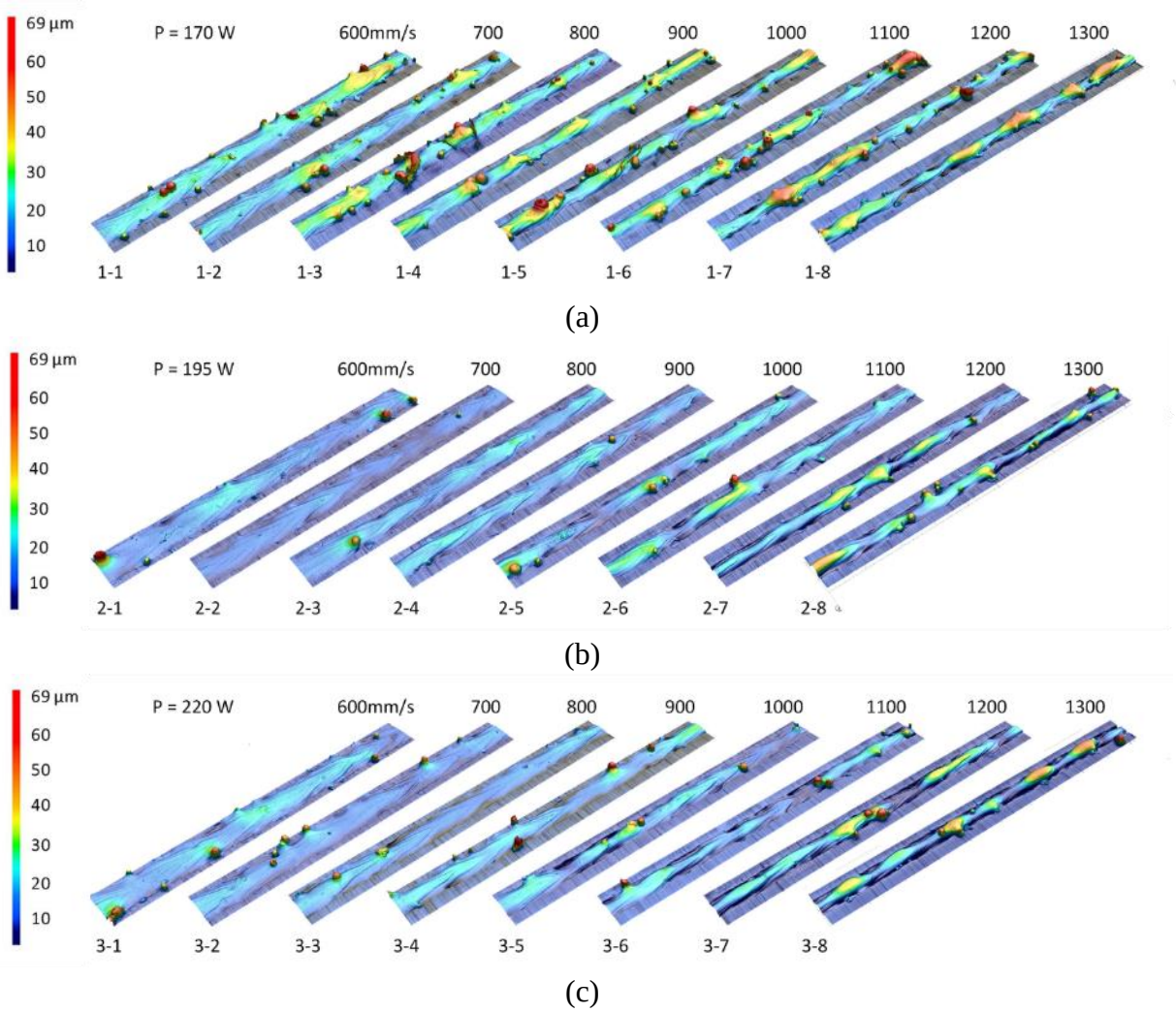

Figure 5.15. Experimental 3D surfaces of the single tracks at different laser power, (a) 170W, (b)195W, (c) P = 220W

As highlighted in [219], "*The Plateau-Rayleigh analysis of the capillary instability of a circular cylinder of a liquid points out that the cylinder is stable*" when the stability condition is satisfied [219]. The necessary and sufficient condition of stability is $\pi D/L > 1$, where D is the diameter of the cylinder, and L is the wavelength. πD represents the circumference of the cylinder cross-section. In this work, the circumference can be regarded as the perimeter of a melt pool cross-section, and the wavelength is assumed to be the length of a melt pool. Therefore, the melt pool stability can be predicted by calculating the ratio of the circumference and the length of the melt pools in numerical simulations, which is shown as follows,

$$Stability = \frac{C_{mp}}{L_{mp}} \tag{5.40}$$

where C_{mp} is the circumference of a melt pool, and L_{mp} is the length of the melt pool.

Figure 5.16 provides the numerical results of stability calculated based on Eq.(5.40). The data points above the red dash line imply stable melt tracks, while those below imply that the melt tracks may be unstable. As seen in Figure 5.16, the first several single tracks with lower scanning speed tend to be stable for all three laser powers, and melt pool stability is inclined to decrease with increasing scanning speed. Generally, the predicted results are consistent with that of the experimental results shown in Figure 5.15, except that the stability of single tracks at the laser power of 170 W seems to be a little bit overestimated.

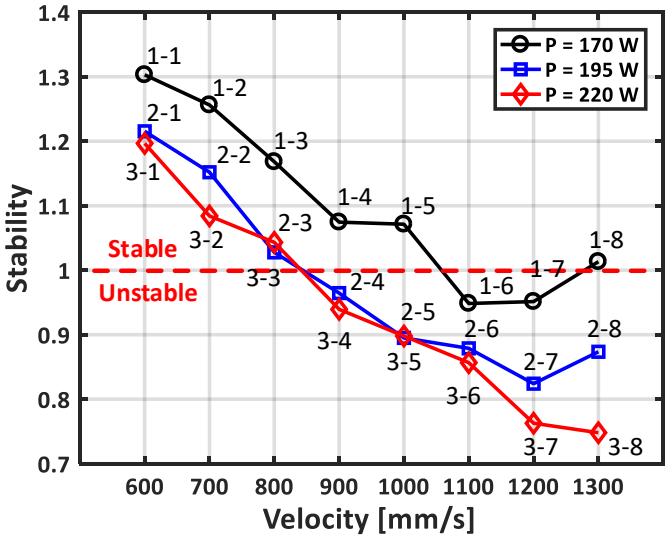

Figure 5.16. Prediction of melt-track stability based on the simulated melt pool data.

For comparing with the form of ripples and isotherm curves, an angle θ [89] is defined as depicted in Figure 5.17. θ is the tail angle of a triangle ripple. In order to reduce the randomness, five measurements on a single track were averaged. For the track with the laser power of 195W and scanning speed of 800mm/s, the experimental θ is in the range of 23° to 32°, as displayed in

Figure 5.17a. The numerical result of θ is 22°. Therefore, the simulated value is close to the experimental value, and the percentage of the difference between them is 20%.

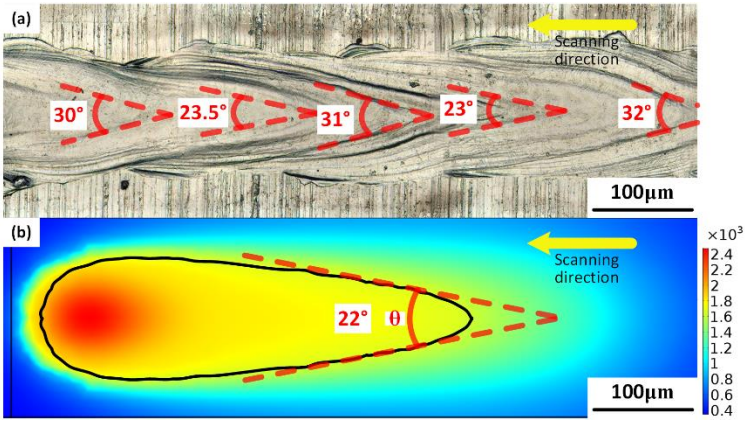

Figure 5.17. Ripple-angle θ comparison of a track with process parameter 195W and 800mm/s, (a) experimental result, (b) numerical result.

Figure 5.18 shows the ripple-angle (θ) comparison of experimental results and numerical data for all stable tracks with the numbering of 1-1, 1-2, 2-1 to 2-4, and 3-1 to 3-4. All the simulated ripple angles are smaller than those of the experiment; however, they are either within or close to the range of experimental results. For the tracks with the laser power of 195 W, the maximum difference of angles in experimental data is 17.3%, and for 220 W, it is 18.13%. The maximum error between the experimental and simulated results is 22%, which was derived from sample 1-2 with170 W and 700 mm/s. The similar trend of ripple angles θ with a specific power versus scanning speed can be observed from the experimental and simulated values; for example, θ decreases with the scanning speed. The reason can be ascribed to the fact that with the higher scanning speed, the temperature gradient could be smaller, and the isotherm curves are elongated with a smaller ripple angle θ.

Moreover, the tracks with a specific scanning speed versus power ended up with very close angles, e.g., the group of tracks 1-1, 2-1, and 3-1, and the group of tracks 1-2, 2-2, and 3-2. For the group with the scanning speed of 600 mm/s, tracks 1-1, 2-1, and 3-1, the maximum difference in the experimental data is only 4.66%. For scanning speed of 700 mm/s, tracks 1-2, 2-2, and 3-2

have a maximum difference of 5.9%. This trend is probably attributed to the reason that laser power may have less influence on the ripple angles than scanning speed.

In the future, a larger range of process parameters such as laser power and scanning speed should be considered in order to validate the proposed model further. Besides, the influence of powder layer thickness on melt pool profiles and track morphology would be investigated. Then the proposed 3D FEM model can be implemented for multiple-track and even multiple-layer situations of the LPBF process.

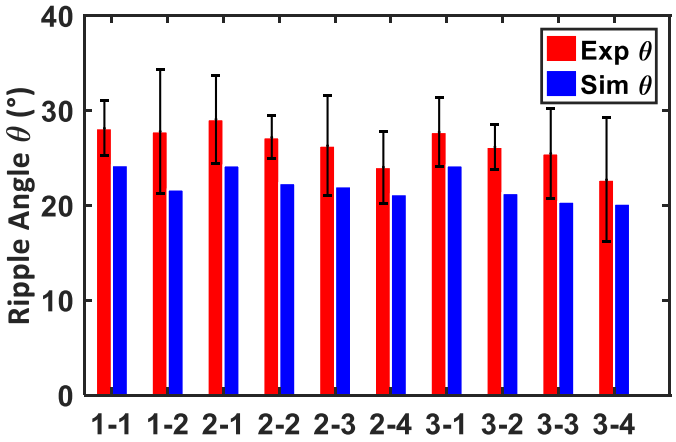

Figure 5.18. Ripple angles θ comparison between the experimental results and simulated data for all the stable tracks.

5.8. Summary

A 3D heat-transfer finite element model for LPBF was developed for accurately predicting melt pool dimensions and surface features. Based on the literature review, eight heat source models are used for the numerical modeling of LPBF and can be categorized as 1) geometrically modified group (GMG); and, 2) absorptivity profile group (APG). Experiments were carried out to validate the simulation results. All the eight heat source models lead to over 40% shallower melt pools compared with the experiments. In order to improve the model performance, a novel mathematical model with varied anisotropically enhanced thermal conductivity and varied absorptivity was

proposed and applied to the heat transfer simulation with the exponentially decaying heat source (APG4). The main conclusions are listed as follows:

1. The expressions of varied anisotropically enhanced thermal conductivity and varied absorptivity were linear algebraic equations. Good agreement between the simulation and the experimental results was derived. The averaged error of melt pool width and depth are 2.9% and 7.3%, respectively.
2. The proposed heat transfer model has been further validated by the surface features—track stability and ripple angle. For track stability, the predicted results are in good agreement with the experimental results. In addition, the simulated ripple angles are within the range of experimental results.

Chapter 6. Heat Source Modeling Application – Investigation on the Influence of Layer Thickness in LPBF*

6.1. Introduction

Layer thickness is one of the most important input process parameters in LPBF since it directly affects the defects found in the printed products, such as porosity, cracks, and manufacturing rate. In this work, a three-dimensional finite element heat transfer model was employed to compare and evaluate two different powder layer thicknesses (20 μm and 40 μm) at varying laser power and scanning speeds. A layer-thickness dependent laser absorptivity approach was considered to improve the prediction accuracy of the proposed model. Single-track experiments with stainless steel 17-4PH were conducted to validate the simulation model.

6.2. Background of heat transfer modeling

6.2.1. Governing equations

The thermal equilibrium governing equation for three-dimensional heat transfer in LPBF can be stated as,

$$\rho c \frac{\partial T}{\partial t} = Q + \frac{\partial}{\partial x}\left(k_x \frac{\partial T}{\partial x} \right) + \frac{\partial}{\partial y}\left(k_y \frac{\partial T}{\partial y} \right) + \frac{\partial}{\partial z}\left(k_z \frac{\partial T}{\partial z} \right) \tag{6.1}$$

where T is the current temperature [K], ρ is the material density [kg/m^3], c is the specific heat [J/kgK], t is the time [s], x, y, and z are the coordinates in the reference system [m], k_x, k_y, and k_z are the thermal conductivity [W/mK] in the three directions and Q represents the heat source in

* The materials presented in this chapter are adapted from the author's published work [95].

LPBF [W/m^3]. [66] have shown that the laser not only scans over the powder-bed but can also penetrate the build area powder-bed, and thus, heat is absorbed not only on the top surface but is also absorbed into the powder-bed. Therefore, an exponentially decaying 3D heat source has been used [89],

$$Q(x,y,z) = \frac{2P}{\pi r_l^2}\exp\left[-2\frac{x^2+y^2}{r_l^2}\right]\cdot f(z), \quad f(z) = \frac{\beta}{H}\cdot\exp\left[-\frac{|z|}{H}\right] \tag{6.2}$$

where P is the laser power [W], r_l is the laser beam radius [μm], and β is the laser-beam absorptivity, H [μm] is assumed to be the powder layer thickness.

The boundary conditions for the LPBF simulations are as follows: the initial temperature (T_{base}) and the ambient temperature (T_0) were chosen as 353 K and 293 K, respectively. Heat convection (q_c) on the outer surface was considered as follows:

$$q_c = -h_c(T_{sur} - T_0) \tag{6.3}$$

where h_c is the convective heat transfer coefficient [W/(m^{2}K)], and T_{sur} represents the surface temperature [K]. Radiation heat transfer (q_r) were described by using Stefan-Boltzmann law:

$$q_r = -\varepsilon\sigma(T_{sur}^4 - T_0^4) \tag{6.4}$$

where ε is the powder-bed emissivity, and σ is Stefan-Boltzmann radiation constant[W·m^{-2}·K^{-4}].

6.2.2. Material properties

The effective thermal conductivity of the Stainless Steel 17-4PH (SS17-4PH) powder used in this study is considered to be 1% of the bulk-material thermal conductivity, as reported by [83,220].

$$k_{powder} = \begin{cases} 0.01\times k_{bulk}, & T < T_m \\ k_{bulk}, & T >= T_m \end{cases} \tag{6.5}$$

where T_m is the melting temperature. k_{powder} and k_{bulk} are the thermal conductivity of the powder phase and solid phase, respectively. The powder density can be deliberated as follows,

$$\rho_{powder} = (1-\varphi)\rho_{bulk} \tag{6.6}$$

where φ is the powder-bed porosity and is picked as 0.53 [21,201]. The latent heat was considered as the heat absorbed during the phase transformation of material. The effective capacity method [12] was used in this study. The latent heat during material phase change was considered in the heat capacity and was specified as:

$$C = \begin{cases} C_{bulk}, & T \le T_s \\ C_{bulk} + 2 \cdot L_f \left(T - T_s\right) / \left(T_l - T_s\right)^2, & T_s < T \le T_l \\ C_{bulk} + 2 \cdot L_v \left(T - T_l\right) / \left(T_v - T_l\right)^2, & T_l < T \le T_v \end{cases} \tag{6.7}$$

where C_{bulk} denotes the bulk-material heat capacity, L_f and L_v are the latent heat of fusion and vaporization respectively, T_s is the solidus, T_l is the liquidus, and T_v is the vaporization temperature. In this study, the powder particles of SS17-4PH were directly deposited on the substrate, which is mild steel. Figure 6.1a shows the SS17-4PH temperature-dependent bulk material properties [198], and Figure 6.1b portrays those of the substrate (mild carbon steel) [203].

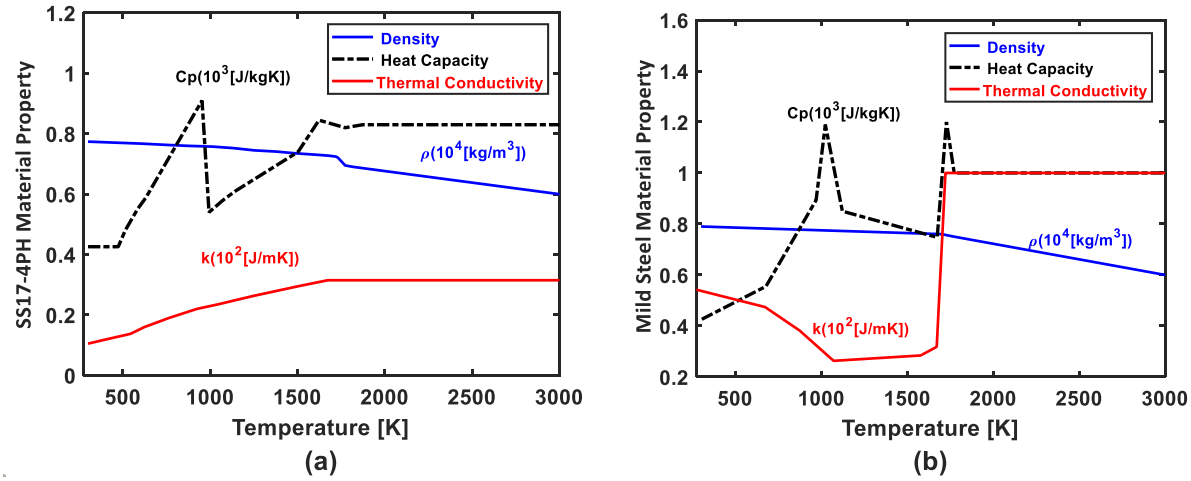

Figure 6.1. Temperature-dependent material properties (a) SS17-4PH [198]; (b) mild carbon steel [203].

In the LPBF process, it is also important to consider the melt pool convection, which may cause deeper melt pools due to the Marangoni effect [74,205]. The Marangoni effect is faster than the solidification, as indicated by [74]. Using the anisotropic thermal heat conductivity could increase the melt-pool dimensional accuracy [90]. Therefore, the enhanced thermal conductivity can be stated as,

$$k_x = \lambda_x k, \;\; k_y = \lambda_y k, \;\; k_z = \lambda_z k \tag{6.8}$$

where λ_x, λ_y, and λ_z are the enhanced factors of thermal conductivity k. However, the enhanced factor can be dependent on the process parameters in order to obtain more close predictions of the melt pool dimensions. They are described in linear algebraic functions of $P/\sqrt{v}$ according to experimental results, where P is laser power and v is laser scanning speed.

$$\begin{cases} \lambda_x = \lambda_y = \lambda_z = 1, \;\; T < T_{melting} \\ \lambda_x = 1, \; \lambda_y = f_y(P,v), \lambda_z = f_z(P,v), \;\; T \geq T_{melting} \end{cases} \tag{6.9}$$

where f_y and f_z can be formulated as,

$$\begin{aligned} f_z &= a_1 \frac{P}{\sqrt{v}} + b_1 \\ f_y &= \begin{cases} a_2 v + b_2, & v \leq v_a \\ 1, & v > v_a \end{cases} \end{aligned} \tag{6.10}$$

where v_a, a_1, b_1, a_2, and b_2 are also parameters and were determined by using only two extreme points from experimental data.

Furthermore, during the LPBF modeling, one of the most uncertain coefficients is the laser absorptivity. It depends on the powder morphology and on the incidence angle, which varies owing to the dynamic melt pool topologies [91]. Similar to the anisotropically enhanced thermal conductivities, the absorptivity was also regarded as a simple linear algebraic equation of $P/\sqrt{v}$,

$$\beta = a_3 \frac{P}{\sqrt{v}} + b_3 \tag{6.11}$$

where a_3 and b_3 are coefficients determined through two extreme points from the experimental data. The effective absorptivity can be calculated accordingly and was in the range of 0.48~0.7, which is comparable with the experimental data from [91].

6.3. Numerical model setup

The commercial software package, COMSOL Multiphysics 5.2, was used to perform FEM thermal analyses. The substrate dimensions were 2000×1000×500 μm, and those of the powder layer were chosen to be 2000×1000×20(40) μm. (Note that in order to investigate the influence of layer thicknesses on melt-pool dimensions, two kinds of layer thicknesses were chosen in this work (20 μm and 40 μm). Both the solid substrate and the powder layer were meshed by tetrahedral elements. Similar to experimental conditions, the laser beam diameter of 100 μm was used in the simulation. The scanning region was meshed with 20 μm elements according to mesh-convergence trials, as depicted in the blue region in Figure 6.2, while rougher elements were used in the other regions for the sake of computational efficiency. Besides, the initial time step was chosen to be 7μs with a convergence based adaptive time step. The symmetrical property of the domain was used so that only half of the domain was developed. In addition, the model considered radiation and convection cooling at the top surface. The convective heat transfer coefficient was chosen as 15 W/mK [208], and the emissivity coefficient of 0.5 [209] was used.

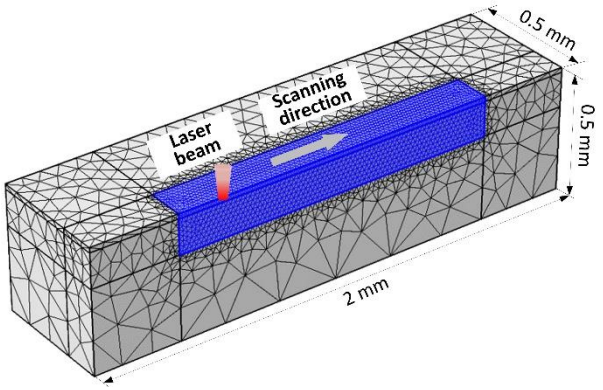

Figure 6.2. Schematic of the simulation and mesh in the FEM, the blue area represents the laser-scanned region.

6.4. Material and experiments

Single-track experiments were conducted using an EOS M 290 (EOS GmbH, Krailling, Germany) LPBF machine for validating the numerical simulation results. The EOS M 290 has a TEM_{00} transverse mode laser beam with a spot diameter of 100 μm. Stainless Steel 17-4PH gas atomized powder with a particle size range of 16~64 μm was used, and size distribution with a D10 = 30.2 μm, D50 = 42.4 μm, and D90 = 58.1 μm respectively was determined by a particle analyzer (Retsch CAMSIZER X2, Retsch Technology GmbH, Haan, Germany). Surface profiles of the single tracks were measured with a high-performance confocal laser scanning microscope (Keyence VK-X250, Keyence Corporation, Osaka, Japan).

The present design of experiment (DOE) involved combinations of different process parameters, comprising laser power, scanning speed, and layer thickness. In literature [210–214,216], the laser power is generally between 190 to 200 W, for SS 17-4PH. In this work, the laser powers were set to be 170, 195, and 220 W while the scanning speeds were from 600 to 1300 mm/s. Two different layer thicknesses (20 and 40 μm) were employed with five repetitions for each condition. In order to avoid the irregularities with printing single lines on printed substrates [221], all the single tracks were printed directly on the mild steel substrate. The corresponding combinations of the processing parameters are presented in

Table 5.2.

Table 6.1. Process parameters for the single tracks

Test #	Laser power, *P* [W]	Scanning speed, *v* [mm/s]	Layer thickness, *lth* [um]	**Test #**	Laser power, *P* [W]	Scanning speed, *v* [mm/s]	Layer thickness, *lth* [um]
1	170	600	20	**10**	170	600	40
2	170	900	20	**11**	170	900	40
3	170	1300	20	**12**	170	1300	40

4	195	600	20	**13**	195	600	40
5	195	900	20	**14**	195	900	40
6	195	1300	20	**15**	195	1300	40
7	220	600	20	**16**	220	600	40
8	220	900	20	**17**	220	900	40
9	220	1300	20	**18**	220	1300	40

All the single track samples were cross-sectioned vertical to the laser-scan direction and then were mounted, polished, and etched by using 5% Nital. The melt-pool dimensions were measured by a Keyence VK-X250 (Keyence Corporation, Osaka, Japan) laser scanning confocal microscope, as shown in Figure 6.3. It should be noted that the melt pool depth (as shown in Figure 6.3) was measured from the surface of the substrate to the bottom of the melt pool, which does not include the bead height. The bead is formed because the melted powder layer provides extra material.

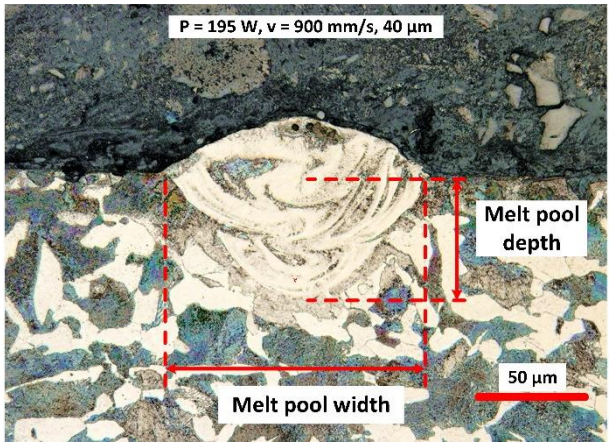

Figure 6.3. Melt pool cross-section.

6.5. Results and discussions

6.5.1. Experimental melt-pool dimensions

For validating the simulation model, experiments were carried out with the different combinations of process parameters shown in

Table 5.2. As an example, melt pool profiles with different layer thicknesses under laser power of 195 W are shown in Figure 6.4. Melt pools in Figure 6.4 show a decrease in melt pool dimensions with increasing scanning speed. For the melt pools with the same power and scanning speed, the dimensions with 20 μm layer thickness are slightly bigger than those with 40 μm.

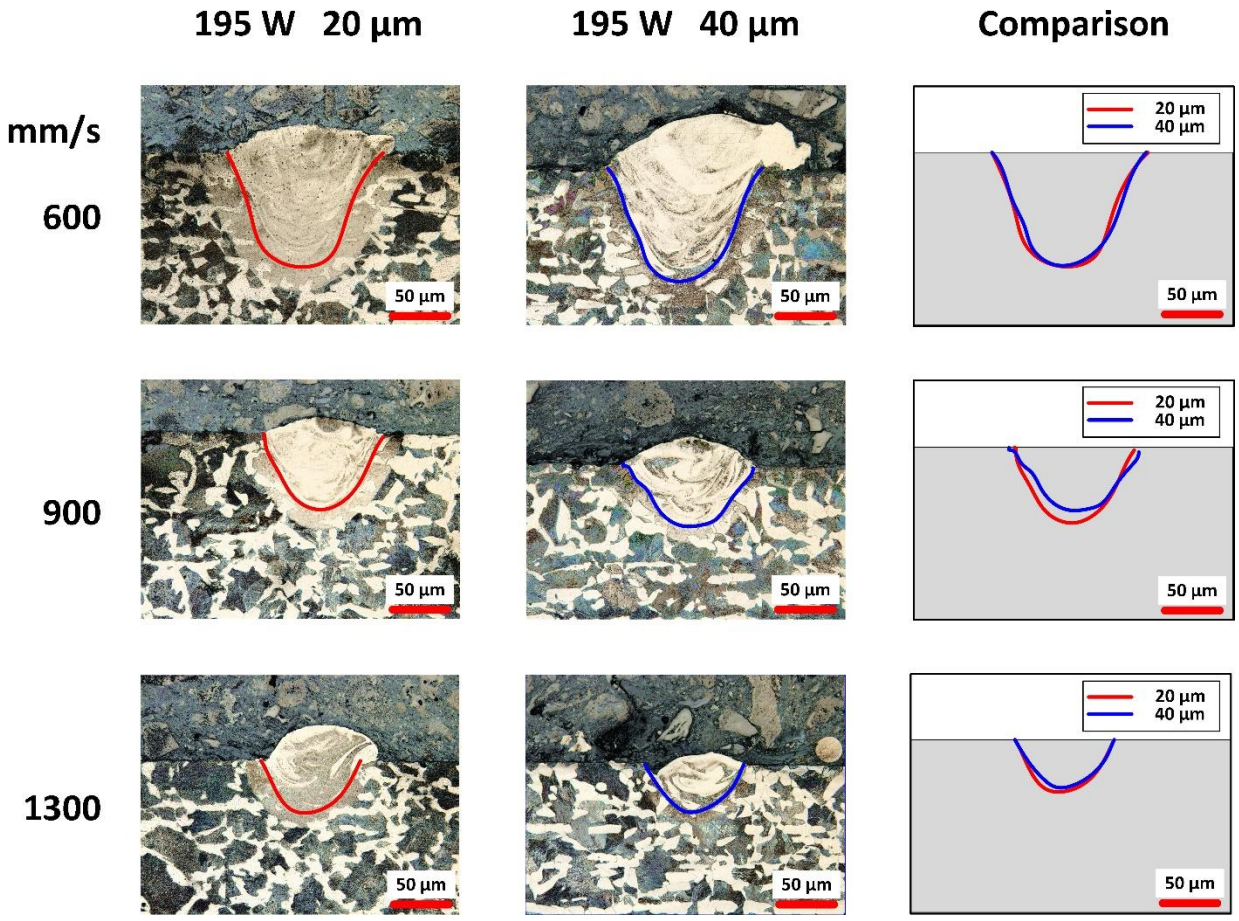

Figure 6.4. Comparison of melt pool dimensions with different layer thicknesses.

Figure 6.5a-d depict the complete experimental results. It is noticed that the melt-pool dimensions reduce with increasing scanning speeds. The trend is the same for different layer thicknesses and laser powers. In addition, with larger laser power, the melt-pool is deeper, as illustrated in Figure 6.5c and d. However, the melt-pool widths seem to be increasing less noticeably, as shown in Figure 6.5a and b.

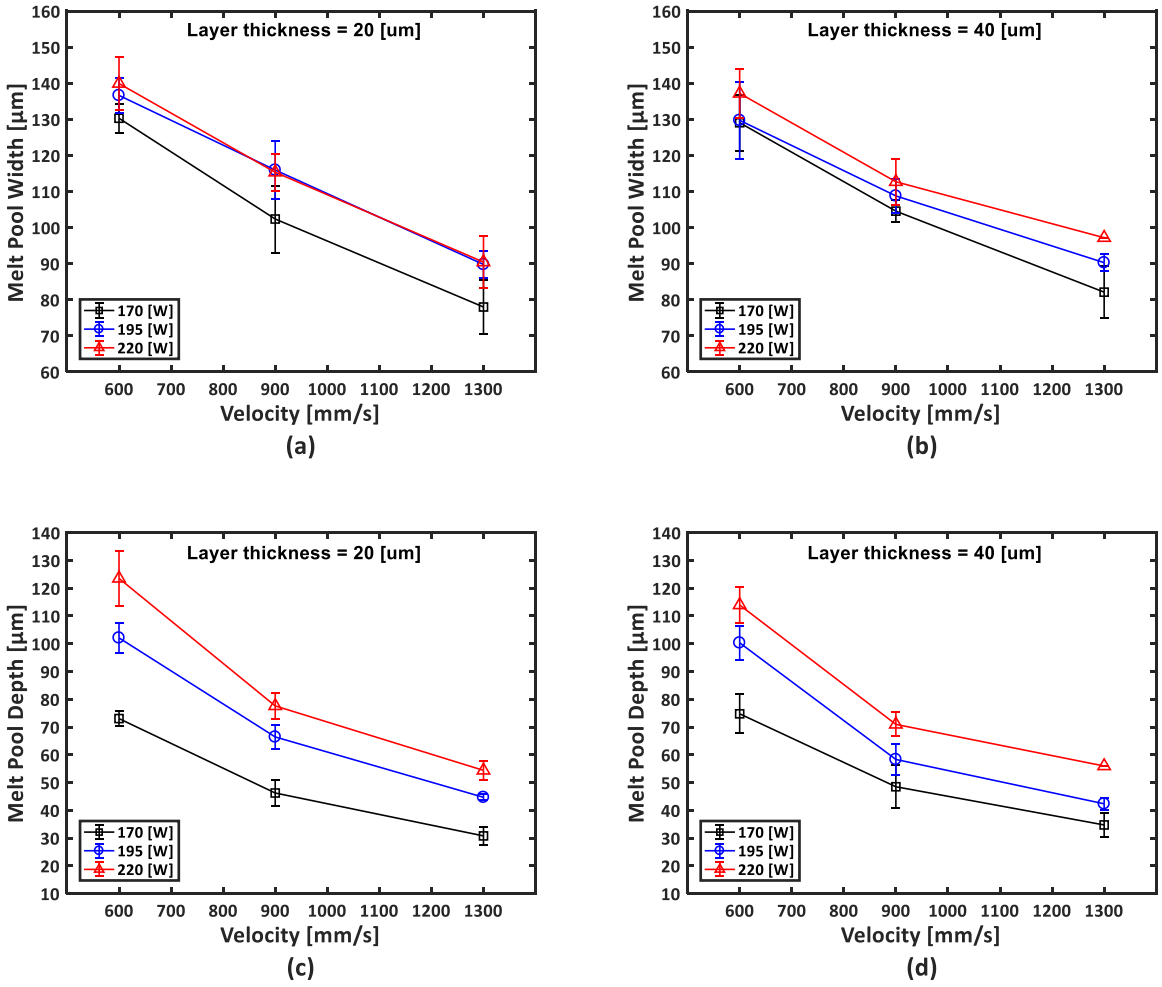

Figure 6.5. Experimental melt pool dimensions with different laser power and scanning velocities, (a, b) melt-pool width with 20 µm and 40 µm layer thicknesses, (c, d) melt-pool depth with 20 µm and 40 µm layer thicknesses.

Moreover, Figure 6.5 illustrates that the melt pool dimensions with different layer thicknesses are very similar to each other. The melt pool depth and width with a layer thickness of 40 µm are, on average, 1.45% and 1.52% less than those with 20 µm. The reason may be attributed to the thicker powder layer which requires more laser energy to melt than the thinner one, resulting in less energy penetrating to the substrate to form the melt pool; however, at the same time, the thicker powder layer may lead to a higher absorptivity [222], which may compensate for the previous effect. Thus, the melt pool dimensions with different layer thicknesses of 20 µm and 40 µm are very close to each other. It is essential to note that all the melt pool cross-sections shown in Figure

6.4 were scanned by using the medium laser power of 195 W, which is one of the reasons why the comparison does not show any major variation between melt pools. This might lead to the conclusion that melt pool dimensions are independent of the layer thickness. However, this conclusion does not apply to other laser powers. Figure 6.6 shows the melt pool morphologies with the 220 W laser power and speed of 600 mm/s with a discrepancy in melt pool dimensions of more than 15% (20 μm).

Successful printing during LPBF is not only dependent on the melt pool dimensions but also on the morphology of the track profile. A discontinuous track profile is the reason for many defects and might result in extra porosities in printed parts. Figure 6.7 shows the top view of the single tracks as $P/\sqrt{v}$ increases from 4.7 W/ √(mm/s) (left) to 8.9 W/ √(mm/s) (right) for both layer thicknesses of 20 μm and 40 μm. Results show an increase in track stability with an increase in $P/\sqrt{v}$ from 6.5-8.98 W/ √(mm/s) for both layer thicknesses. In contrast, unstable single tracks with many large peaks and valleys are observed within the $P/\sqrt{v}$ range of 4.7-6.1 W/ √(mm/s).

The effect of layer thickness on track stability is highlighted in Figure 6.8. Figure 6.8 shows the top view of the printed single tracks with $P/\sqrt{v}$ of 4.7 W/ √(mm/s) (170 W, 1300 mm/s) with 20 μm and 40 μm layer thickness. Track discontinuity is more obvious with the 40 μm layer thickness, as highlighted. The main reason for this discontinuity is thought to be due to the increasingly needed energy to melt the extra volume of powder found in the 40 μm layer. Therefore, results show that even though layer thickness does not seem to greatly affect the melt pool dimensions at certain power levels, the layer thickness should be chosen compatible with the other process parameters in order to form adequate melt pools with continuous melt tracks.

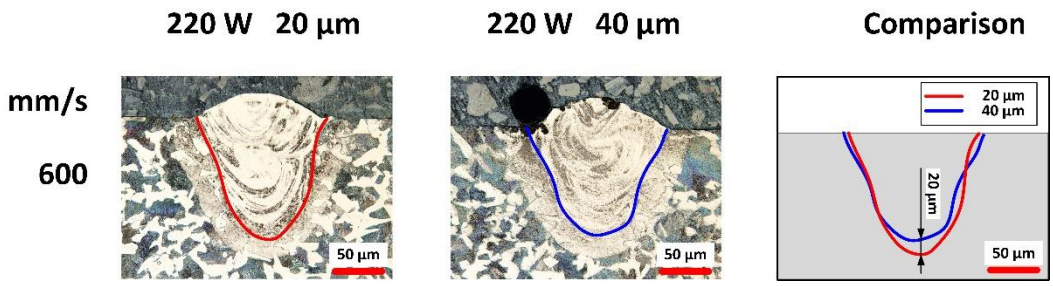

Figure 6.6. The discrepancy in melt pool dimensions with different layer thicknesses.

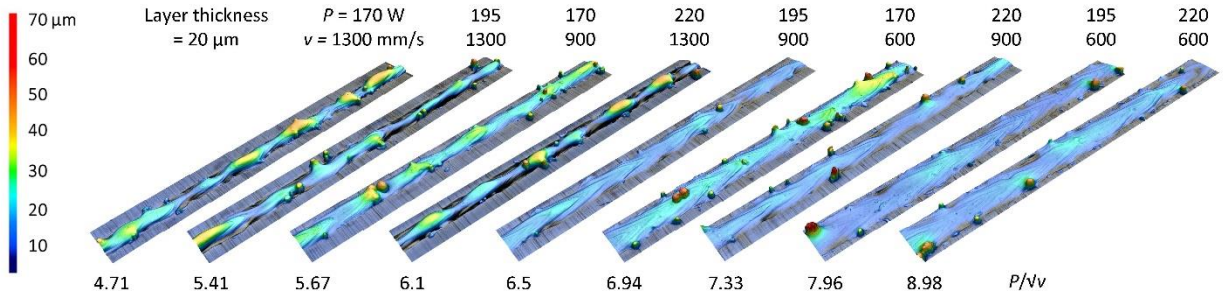

(a) 20 µm

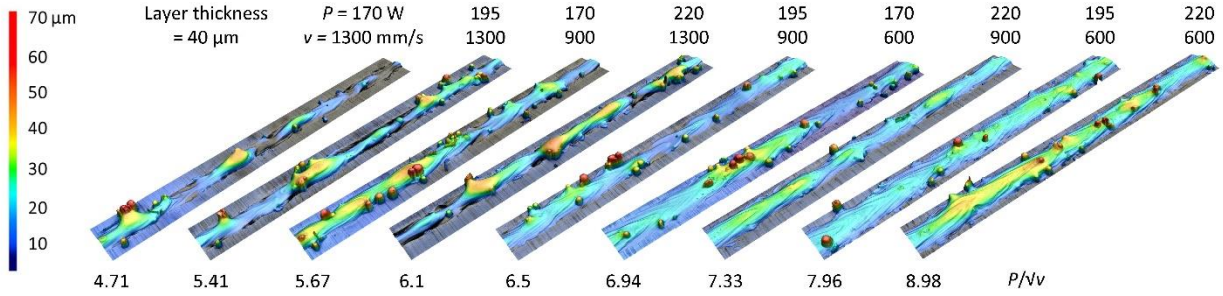

(b) 40 µm

Figure 6.7. The top view of the single tracks as $P/\sqrt{v}$ increasing for the layer thickness of (a) 20 µm, (b) 40 µm.

(a) 20 µm, 170 W, 1300 mm/s, 4.71 W/ √ (mm/s)

(b) 40 µm, 170 W, 1300mm/s, 4.71 W/ √ (mm/s)

Figure 6.8. The top view of the single tracks with layer thicknesses of (a) 20 µm, (b) 40 µm.

Figure 6.9 depicts the experimental melt-pool dimensions as functions of $P/\sqrt{v}$. Remarkably, the melt pool depth results in Figure 6.5c and d collapse to linear lines a,s shown in Figure 6.9c and d. However, melt-pool width does not converge into a single line but into three comparable lines, which may imply the melt pool width is less sensitive to the laser power than to the scanning speed. Moreover, the maximum melt pool depth with the layer thickness of 40 μm is slightly smaller than that with 20 μm. However, the minimum one is slightly bigger. A similar trend can also be observed for the melt pool width. This may be explained by the interplay among the layer thickness, the laser absorptivity, and particle dynamics [68]. With bigger layer thickness, the powder layer needs more energy to be melted resulting in a smaller melt pool; however, the thicker layer could lead to the increase of laser absorptivity [222], which could make melt pool bigger. Thus, these two phenomena interact with each other, probably causing these differences in maximum and miminum melt pool depths between 20 and 40 μm. Furthermore, the melt pool dimensions presented in this work show similar melt pools, which are within or near conduction mode, when the parameter $P/\sqrt{v}$ is within 6-8 with the different layer thicknesses, which suggests that the two layer thicknesses have almost the same effects on melt pool dimensions within this range. This trend can also be observed in Figure 6.7, where the tracks become more smooth and stable with $P/\sqrt{v}$ of 6.5-7.69 for both 20 μm and 40 μm. However, experimental results at high power and low velocity show significant differences in melt pool depths whereas experimental results at low power and high velocity show similar melt pools but discontinuous track profiles. Even though the other manufacturing objectives should be considered, like the final surface roughness which may be lower by employing smaller layer thicknesses, using the thicker layer thickness has potential to accelerate the manufacturing process, because of the fewer number of layers needed to print for final parts.

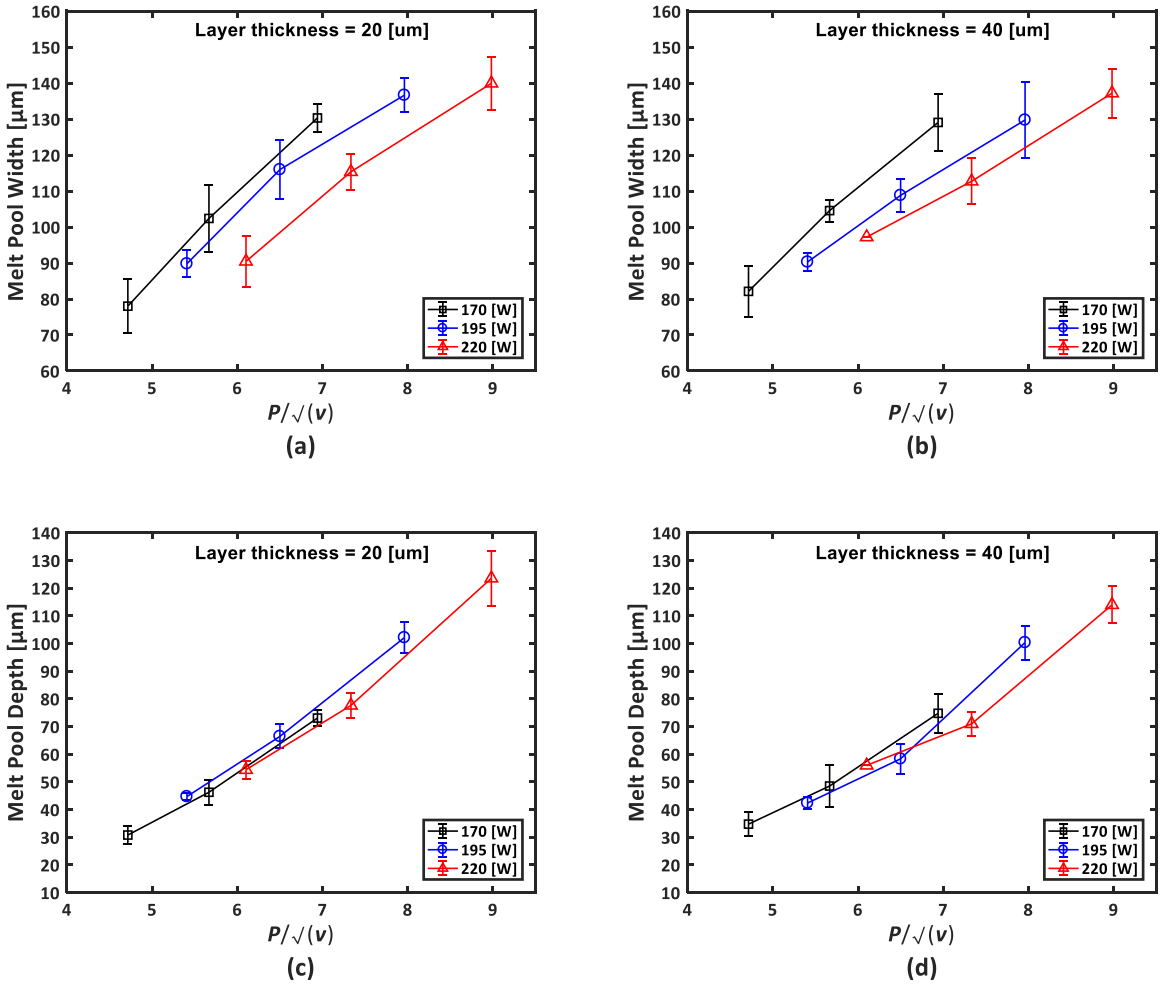

Figure 6.9. Experimental melt-pool dimensions as functions of $P/\sqrt{v}$, (a-b) melt-pool width with 20 μm and 40 μm layer thicknesses, (c-d) melt-pool depth with 20 μm and 40 μm layer thicknesses.

6.5.2. Simulation results

As discussed previously, the model in Eq.(6.10) and Eq.(5.38) was employed in the simulations to approximate the melt-pool dimensions more precisely, where the absorptivity β and the enhanced factors of thermal conductivity λ_{yy} and λ_{zz} are expressed in linear equations of $P/\sqrt{v}$. The constants of this model are listed in Table 5.3. The absorptivity range is from 0.48 to 0.65 based on different values of the combined parameter, $P/\sqrt{v}$.

Table 6.2. Coefficients in the approximating equations.

a_1	b_1	a_2	b_2	a_3	b_3	v_a (mm/s)

2.1095	-6.9460	-0.0036	4.96	0.0398	0.2921	1100

For the layer thickness of 40 μm, Figure 6.10a shows simulated and experimental melt pool depth at 170 W but with varied scanning speeds. The maximum variance between the simulation and experimental results is over 30%. The authors assume this is caused by the underestimations of the laser absorptivity because the thicker powder layers could lead to higher absorptivity [222]. Besides, The underestimation in melt pool dimensions may be due to the complex fluid and particle dynamics [68,70], which may be more obvious at high scanning speeds. According to the literature [91], the laser absorptivity of stainless steel can be as high as 0.7. Therefore, the range of the absorptivity for 40 μm in this work was adjusted from 0.48-0.65 to 0.6-0.7 based on different values of the combined parameter, $P/\sqrt{v}$, and the corresponding simulation results are shown in Figure 6.10b. The higher absorptivity results in better agreement between the simulation and experimental results with a slight underestimation at high velocity with an average error of 11%. This results in over two-time improvement in simulation results. It should be noted that this modification of absorptivity only influences the parameters a_3 and b_3 (Table 5.3). New values for a_3 and b_3 are 0.0234 and 0.4895 r,espectively.

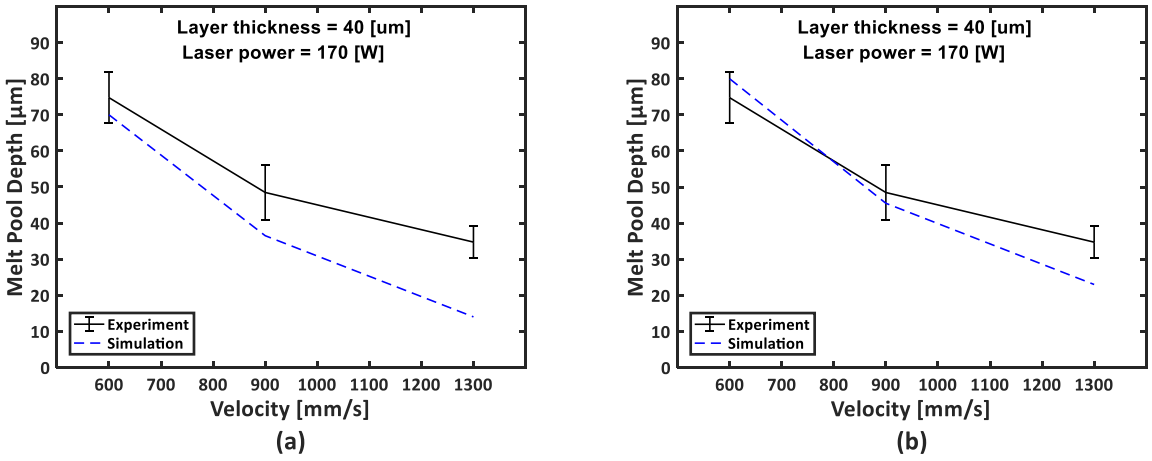

Figure 6.10. Melt pool depth comparisons at two different $P/\sqrt{v}$ dependant absorptivity equations, (a) 0.48-0.65, (b) 0.6-0.7

Figure 6.11a-d shows the comparison of the melt-pool dimensions between simulation and experimental results at different laser powers of 170 W, 195 W, and 220 W with different layer thicknesses of 20 μm and 40 μm, respectively. All the melt pool dimensions are plotted as functions of $P/\sqrt{v}$. The dash lines represent the simulation results while the solid lines denote the experimental results. The simulation results in Figure 6.11a-d match well with the experimental results, which proves the effectiveness of the stated simulation model.

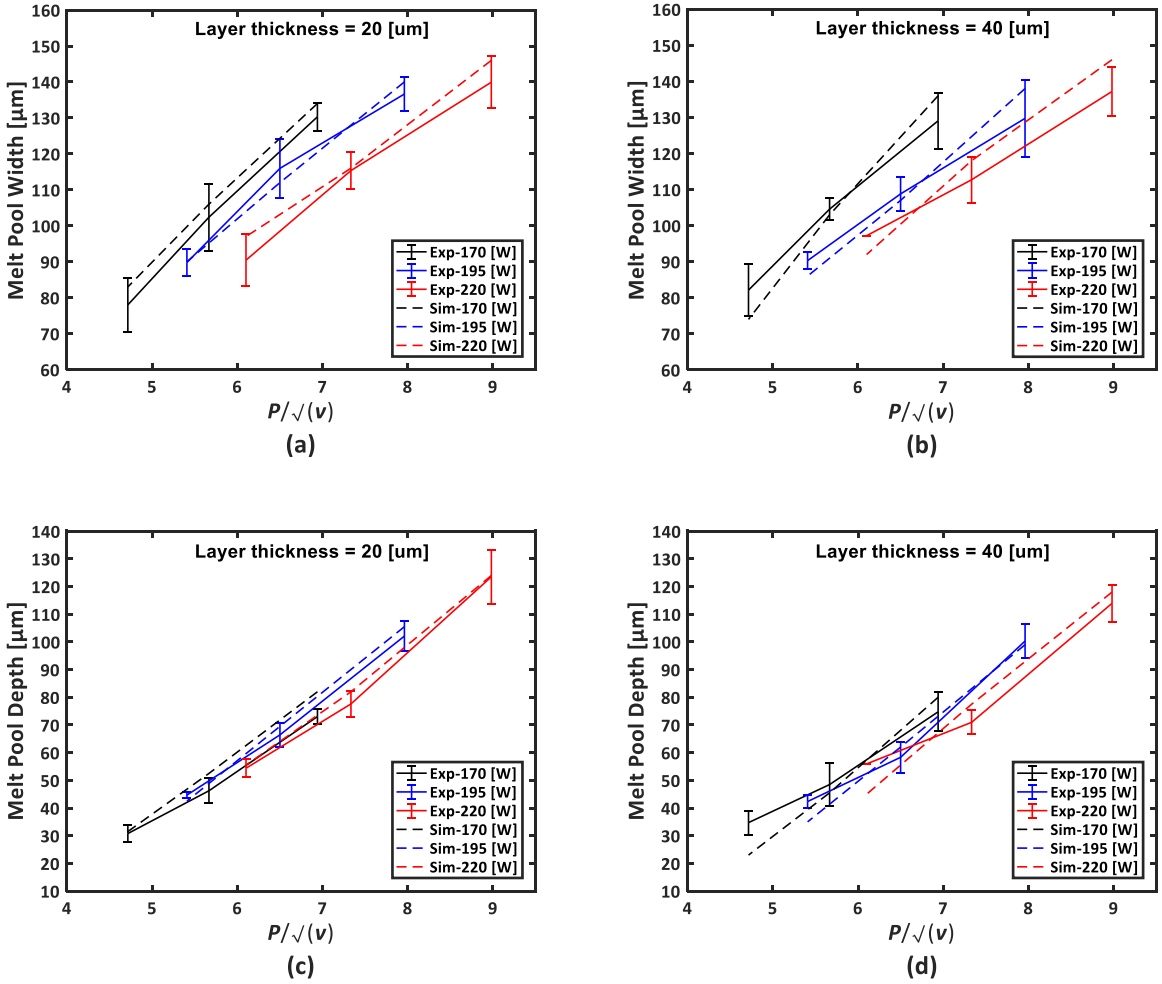

Figure 6.11. Melt-pool dimensions comparison between the simulation and experimental results as functions of $P/\sqrt{v}$ (a) melt-pool width, (b) melt-pool depth.

The corresponding errors of the melt pool width and depth for 20 μm and 40 μm layer thickness with different powers are summarized in Table 5.4. Each row in Table 5.4 corresponds to all the

scanning speeds for that layer thickness and laser power. Table 5.4 shows that for results with a layer thickness of 20 μm, the average of the width and depth are within 10%. Especially for the width, the average errors are within 5%. However, the average errors of the width and depth with 40 μm thickness are generally bigger than the corresponding results with 20 μm. Noticeably, the maximum errors of the melt depth with 40 μm are relatively large, which are 33.8%, 17.3%, and 15.1%. In Table 5.4 and Figure 6.11d, it can be found that these large errors are all with the 1300 mm/s scanning speed. In contrast, the predicted melt pool depth becomes more accurate with the 600 mm/s scanning speed, where the errors are only 6.2%, 1.3%, and 1.3%. This finding may be explained by the fact that the particle configuration is being changed by the fluid and particle dynamics in and near the melt pool [68,70]. For example, researchers [68] found that based on the process parameters, the particle can be dramatically moved by the local recoil pressure, where the speed can be as high as 20m/s, leading to the denudation or pileup effects. The denudation effect explains how the powder particles are pushed away, while the pileup effect explains how the particles are stacked up at the front of the melt pool track. As discussed previously, the large simulation errors under the speed 1300 mm/s could be attributed to the fewer particles, caused by the dominant denudation effects observed at higher scanning speed. Fewer particles mean less energy absorbed by powder, and therefore, more energy deposited downwards to form deeper melt pools. In addition, the reason why the 40 μm has the bigger errors than 20 μm may be because the 40 μm layer thickness seems to be influenced more by the fluid-particle dynamics than that with the 20 μm as more particles exist in a 40 μm layer. In other words, as more particles exist in a 40 μm layer, there occurs a higher possibility that these particles collide with each other, leading to a more remarkable denudation effect. This trend can also be observed in Figure 6.7, where the 40 μm single tracks exhibit more partially melted particles than the 20 μm single tracks

Table 6.3. Proposed model validation and errors between the simulation and experimental data.

Layer thickness (μm)	Power (W)	Min Error Width (%)	Min Error Depth (%)	Max Error Width (%)	Max Error Depth (%)	Ave. Error Width (%)	Ave. Error Depth (%)

	170	2.8	2.4	6.4	13.5	4.3	9.4
20	195	0.2	3.3	3.4	4.9	2.0	4.3
	220	0.6	0.4	7.2	5.7	4.1	8.1
	170	1.5	6.2	9.9	33.8	5.6	15.7
40	195	1.7	1.3	6.4	17.3	4.3	8.3
	220	4.7	1.3	6.4	15.1	5.4	8.5

Even though the fluid and particle dynamics are not considered in the present simulation model of LPBF, the model still gives good melt pool dimension predictions for both the 20 and 40 μm layer thicknesses. The averaged error of melt pool width and depth are 4.2% and 9.1%, correspondingly. In order to understand the effect of layer thickness comprehensively, it is important to consider a wider range of layer thicknesses, laser power, and scanning speed. Moreover, including the effect of fluid-particle dynamics would also greatly improve the predictability of the proposed model. Finally, with a validated numerical model of LPBF, the relationships between the process parameters and microstructures as well as the material properties can be investigated in future works because different process parameters, such as laser power, scanning speed, lead to different microstructures which lead to different grain sizes [18]. As grain size is directly related to material strength, this significantly affects the material properties of printed parts with different process parameters [223].

6.6. Summary

A three-dimensional heat-transfer finite element model for LPBF was employed to predict melt pool dimensions with two different layer thicknesses accurately. Varied anisotropically enhanced thermal conductivity and varied absorptivity were included in the proposed model for capturing the experimental process in more detail. The main conclusions are as follows:

1. Generally, the simulation results of the melt pool dimensions matched well with the experimental results. The averaged melt pool width and depth errors were 4.2% and 9.1%, respectively.
2. Using the combined parameter $P/\sqrt{v}$ shows that layer thickness has a minor effect on the melt pool dimensions when between 6-8 W/ √(mm/s). In other words, within this range, it is possible to use 40 μm layer thickness to accelerate the building rate while not losing quality.

Chapter 7. Multi-Scale Thermo-Mechanical Modeling for LPBF

7.1. Introduction

Previously (Chapter 5, Chapter 6), heat source modeling has been investigated, where the thermal analysis helps to understand whether a set of process parameters leads to suitable melt pool dimensions and stable melt tracks. As is discussed in Section 2.3, thermo-mechanical modeling is important because it enables to predict deformation and residual stresses in LPBF printed parts. In this chapter, multi-scale LPBF process simulation models will be investigated in order to find an effective and efficient method to simulate the LPBF process. It includes a small scale modeling—actual-scan model, a medium-scale modeling—domain activation model, and large-scale modeling—ISM. Moreover, the LPBF process modeling provides important information to the LPBF-based topology optimization that considers the LPBF process in the design process.

7.2. Small scale modeling—actual-scan model

Numerical modeling helps researchers optimize process parameters, describe the thermal history of the AM process, and predict part deformation as well as residual stresses. In order to obtain the basic knowledge of AM simulation, a simple block is chosen as the part to fabricate, as plotted in Figure 7.1a. The cross-section of the block is 2x1 mm rectangular. Besides, a one-layer (20μm) scan was taken into consideration, beneath which there is a thicker block with the two-layer thickness (40μm), representing support structures. The boundary conditions were heat flux on the top surface with the heat flux 8 W/(m^2), a constant temperature on the bottom surface with 373K, and the other thermally insulated surfaces. For the solid mechanics, the bottom surface was

completely constrained for the heating and cooling process, while it departed from a base plate at the end of the simulation.

The commercial LPBF machine—EOS M 290—uses a raster-scan pattern, which is also chosen for the simulation of AM, as shown in Figure 7.1b. It is necessary to note that the laser does not scan on the dash lines.

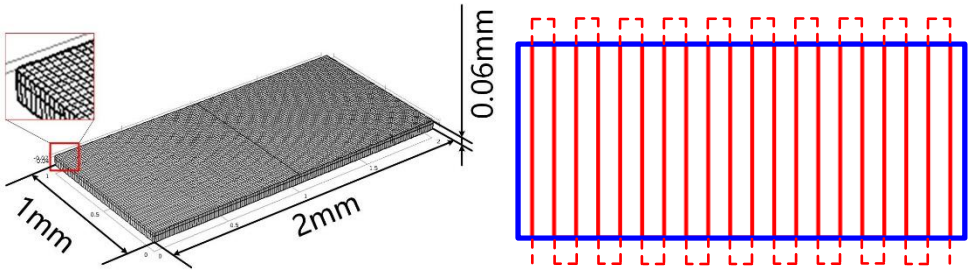

(a) (b)

Figure 7.1. The schematic of the AM simulation model, (a) geometry and mesh, (b) the scan pattern used.

For the laser heat source, 3D volumetric laser heat source—3D Gaussian distribution was chosen for simplicity. The material used in this simulation is Ti-6Al-4V, whose temperature-dependent properties are listed in Table A.3. The process parameters are summarized in Table 7.1. Moreover, latent heat correction has been considered, which is similar to the work of Ashby[224].

Table 7.1. Input-process parameters for the numerical model with the material of Ti-6Al-4V.

Laser power P	Scan speed v	Beam radius r_l	Absorptivity β	Layer thickness lth
300 [W]	1200 [mm/s]	100 [μm]	0.3	20 [μm]

Isotropic hardening model has been employed, which is indicated in Eq.(7.1).

$$\sigma_{ys} = \sigma_{ys0} + \frac{E_{Tiso}}{1-\frac{E_{Tiso}}{E}}\varepsilon_{pe} \tag{7.1}$$

where σ_{ys} and σ_{ys0} are yield stress and initial yield stress, respectively; E_{Tiso} is the isotropic tangent modulus; E is Young's modulus; ε_{pe} is the effective plastic strain.

For improving calculation efficiency, heat transfer and solid mechanics were not strongly coupled, which means that the heat transfer was simulated firstly, and then the solid-mechanical

analysis was executed using the thermal history from heat transfer analysis. The temperature distribution at one specific time point during the laser scan is displayed in Figure 7.2a. The maximum temperature was varying around 6100 K. Melt-pool dimensions are 53μm in depth, 140μm in width, and 320 μm in length. Figure 7.2b and c show the deformation of the part before and after it was removed from the substrate. The maximum deformation is 0.23 mm after it was removed from the substrate.

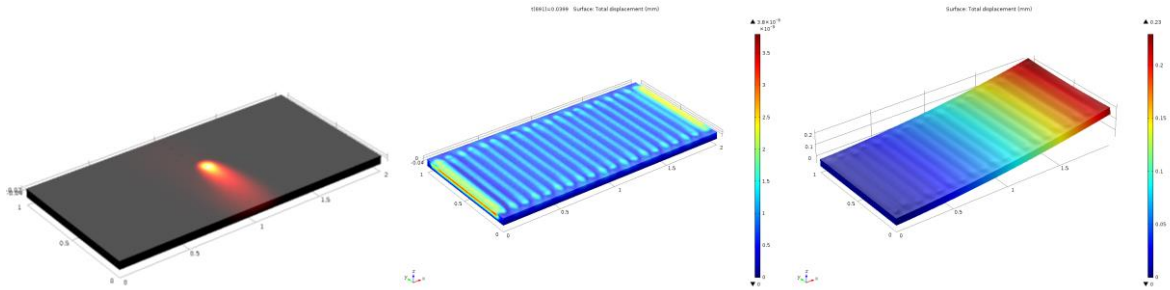

(a) (b) (c)

Figure 7.2. Simulation results of the actual laser-scan model, (a) the temperature distribution during laser scan, (b) the deformation before and (c) the deformation after the removal from the substrate.

For computational time, 3 days 16.5 hours were used on a desktop with a Core i7-6700 CPU and 16 GB RAM, for this part with dimensions of 2×1×0.3 mm. Therefore, this actual-scan method may not be applicable in part-level simulation. Accelerated methods should be developed.

7.3. Domain-by-domain heat-input method

In the actual-scan model, since the laser-beam diameter is very small (around 100 μm), compared to what people want to manufacture through LPBF, the mesh should be fine enough to capture the features of the laser beam (the heat source), making the total number of elements extremely huge. For the sake of accelerating the simulation, it may not be difficult to think of whether one can reduce the number of elements by employing an equivalent but bigger heat source. Therefore, the domain-activation method was investigated, in which the material is melted domain by domain with effective heat flux. The activated domain could be a thin line with the width of

laser-beam diameter and depth of powder-bed layer thickness, a whole layer to be deposited, or even a couple of layers together. Thus, in this way, the simulation process would be accelerated.

As for deriving an effective heat input method, there are two methods, (a) initial melting temperature; (b) equivalent-laser-exposure heat flux.

For the initial melting temperature, a bridge structure in Figure 7.3 has been used, which is the topologically optimized bridge with 0.2 volume fraction discussed in Chapter 3. The preliminary result was derived by activating voxel one by one with an initial temperature of the melting point. The whole simulation took near 30 days. This heat input model may not be accurate compared to the (b) equivalent-laser-exposure heat flux that will be discussed later because the maximum temperature of the melting material usually is much higher than the melting temperature [196].

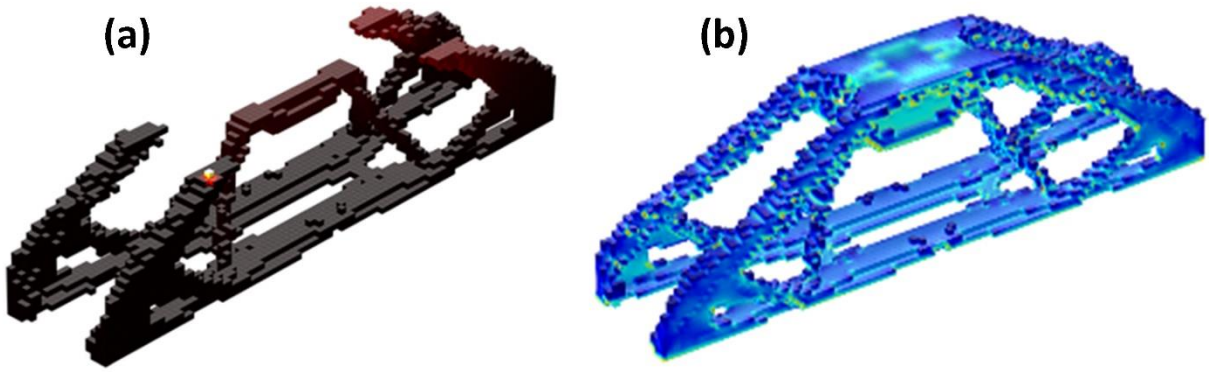

Figure 7.3. Preliminary part-level simulation for the LPBF process by domain-by-domain activation method, (a) temperature, and (b) stress distribution.

Thus, a more accurate heat input model—equivalent-laser-exposure heat flux will be discussed. As for the calculation of the equivalent-laser-exposure time, it is assumed that an evenly distributed-laser beam of the circular shape is passing through a line with a length of hatch spacing, as shown in Figure 7.4.

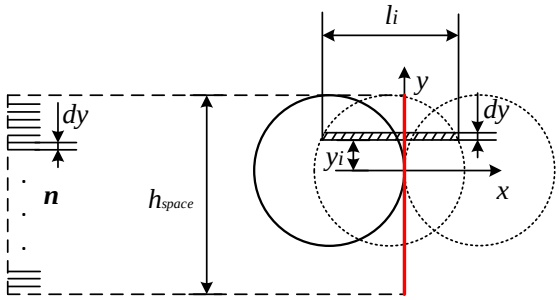

Figure 7.4. The illustrative graph of the calculation of equivalent-laser-exposure time.

The equivalent moving distance of laser beam during shining on the infinitely small segment, dy, is shown in Eq.(7.2),

$$l_i = \frac{2\sqrt{r_l^2 - y_i^2}\,dy}{dy} \tag{7.2}$$

where the r_l is the radius of the laser beam, and y is the y-coordinate of the shadow area. Then the equivalent exposure time for the i^{th} segment is derived by dividing the equivalent distance l_i with scan speed v_s, as shown below,

$$t_i = \frac{l_i}{v_s} = \frac{2\sqrt{r_l^2 - y_i^2}\,dy}{dy \cdot v_s} \tag{7.3}$$

By averaging the equivalent exposure time of the n segments, the equivalent time for a laser scan on the line is calculated as in Eq.(7.4),

$$\begin{aligned} t_{equ} &= \frac{1}{n}\sum_{i=1}^{n} t_i = \frac{1}{n \cdot dy}\sum_{i=1}^{n} \frac{2\sqrt{r_l^2 - y_i^2}\,dy + 0 + \ldots + 0}{v_s} = \frac{\int_{-r_l}^{r_l} 2\sqrt{r_l^2 - y^2}\,dy}{n \cdot dy \cdot v_s} \\ &= \frac{\int_{-r_l}^{r_l} 2\sqrt{r_l^2 - y^2}\,dy}{h_{space} \cdot v_s} = \frac{\pi r_l^2}{h_{space} \cdot v_s} \end{aligned} \tag{7.4}$$

where h_{space} is the hatch spacing of laser scan.

Similarly, for a three-dimensional heat source, one can also obtain the equivalent-laser-exposure time,

$$t_{equ} = \frac{\frac{2}{3}\pi r_l^3}{l_{thick} h_{space} \cdot v_s} \tag{7.5}$$

For comparison, the model used in the actual-scan model was also used in this model. Nevertheless, the actual laser scan was replaced by a quick exposure of laser power within a larger domain with proper exposure time. The top layer had been divided into 20 long-narrow domains, as shown in Figure 7.5. The heat source was applied to each domain successively. The total number of elements in the mesh is 10 k, 44% less than the number 17956 of the actual-scan model.

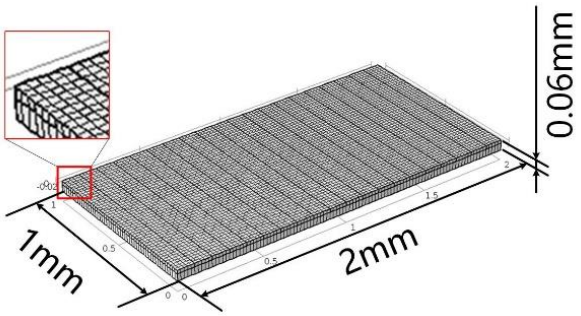

Figure 7.5. The geometry and mesh of the whole domain in the domain-by-domain method.

The total computational time is around 13 hours. The simulation results are shown in Figure 7.6. The maximum temperature and final deformation are 5930 K and 0.25 mm, similar to the 6100K and 0.23 mm of the actual-scan model.

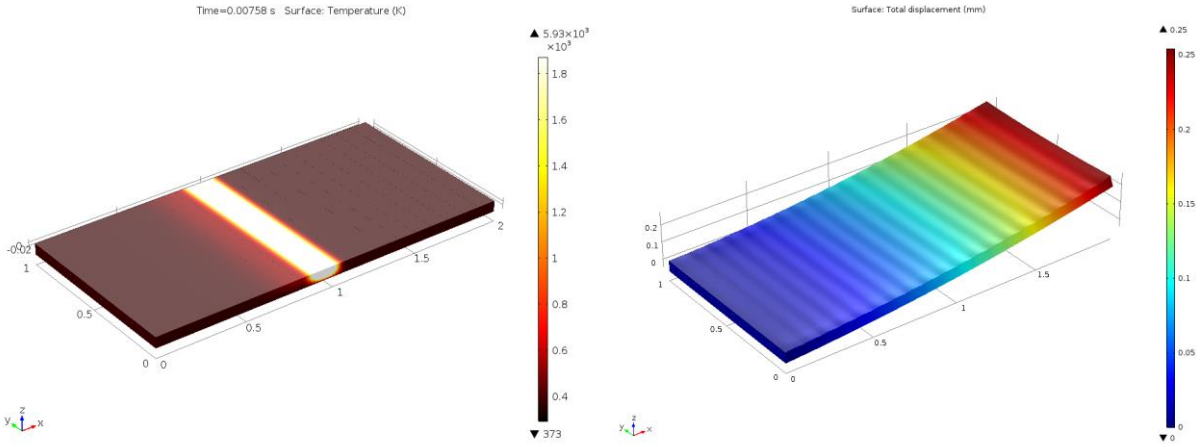

(a) (b)

Figure 7.6. Simulation results of the domain-by-domain model, (a) the temperature distribution during laser scanning, (b) the deformation after removal from the substrate.

Furthermore, Figure 7.7 plots the temperature profiles of one point on the scan path (the dot near the center), for both actual-scan model and domain-by-domain method, from which one can observe that the temperature profiles are very similar, and the maximum temperature is only 5% different. The temperature profile is not symmetric as the time of the heating region is shorter than the cooling region, as shown in Figure 7.7.

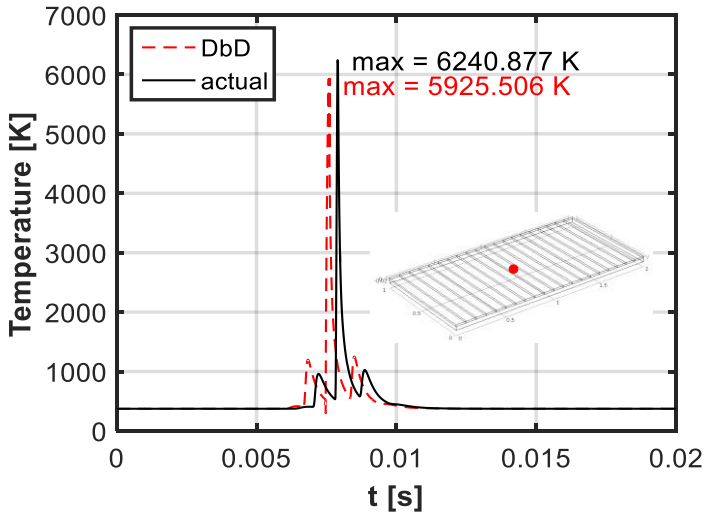

Figure 7.7. The temperature profile of one point (the dot marked on the part) on the scan path.

It should be noted that the small shift is due to the difference in heat-input mechanisms behind these two methods. In the domain-by-domain method, the heat source was applied on the sub-domain right at the time when the laser started to scan on the sub-domain, but in the actual-scan method, the laser took time to move from the side to the location of the dot position, which caused the delay. In addition, it is over 6 times faster (13 h vs. 3 d 16 h) compared to the actual-scan model. Therefore, the domain-by-domain activation model may be capable of simulating the LPBF process.

However, the simulation of a larger domain by this method still took a too long time. For example, as a bigger domain of 2×1×0.7 mm as shown in Figure 7.8, the simulation took 11 days, which makes it almost impossible to be employed for a part-level simulation that is required by topology optimization, since topology optimization may need multiple times of such simulation to

during the iterations for deriving optimal results. Therefore, further accelerated methods for the LPBF process simulation should be explored.

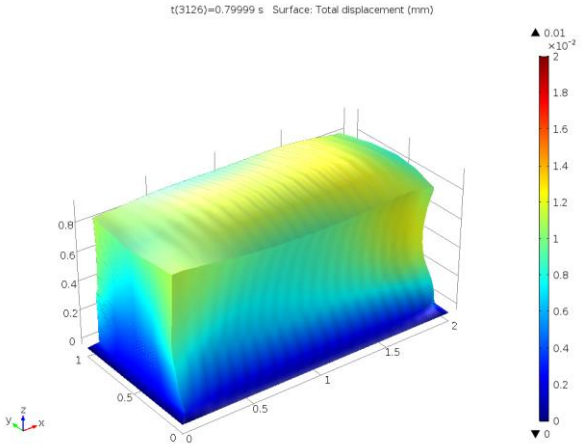

Figure 7.8. Deformation of a bigger domain with 35 layers (2×1×0.7 mm).

7.4. Inherent strain method for LPBF

The Inherent Strain Method (ISM) has been used for the fast prediction of deformation and residual stresses in the welding area [225,226]. Distortion and residual stresses in welding-like manufacturing are caused by the incompatible strains, including thermal strains and plastic strains. Such incompatible strains are a result of uneven temperature distribution during the heating process and are generally called inherent strains [225]. The inherent strains include thermal strains, plastic strains, and other types of strains except for elastic strain [227]. With inherent strains, only an elastic calculation is needed for the prediction deformation and residual stress. Since the natural similarities between welding and LPBF, this fast computational technique is also suitable for fast predicting deformation and residual stresses in LPBF [228]. The theory of such simplified elastic calculation is based on the Eshelby's inclusion [229], which will be briefly explained as follows.

7.4.1. The Eshelby's inclusion

In LPBF, the material is gradually melted and added to a solidified part that is defined as a matrix, as illustrated in Figure 7.9. The newly deposited material can be regarded as an inclusion

in the matrix. Since the newly added material may contain incompatible strain caused by uneven temperature distribution during the heating process, both the matrix and the inclusion will deform and experience an elastic stress field. The problem is to solve the stress, strain, and displacement both in the matrix and the inclusion. As for solving this problem, the analysis procedure is similar to that of the classic Eshelby's inclusion problem [229].

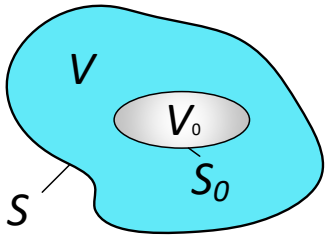

Figure 7.9. A linear elastic solid with volume *V* and surface *S*. It is called the matrix. The subvolume V_0 and subsurface S_0 are of the inclusion. The inclusion experiences an inelastic deformation.

The problem is solved by the superposition principle of linear elasticity [230], as shown in Figure 7.10. First, the inclusion is removed from the matrix, during which it may change its shape because of the inherent strains inside. Second, one should apply surface traction $\boldsymbol{T}$ on the surface of inclusion, making it changes back to its original shape. Third, one should put the inclusion back to the matrix. There is no change in the deformation fields in either the inclusion or the matrix from step 2 to step 3. Lastly, the traction $\boldsymbol{T}$ should be removed in order to resume the original inclusion, as shown in Figure 7.9, which is achieved by adding a traction $\boldsymbol{F} = -\boldsymbol{T}$ on the boundary between the inclusion and the matrix. Therefore, the stress, strain, and displacement in this two-body system can be solved by elastic analysis.

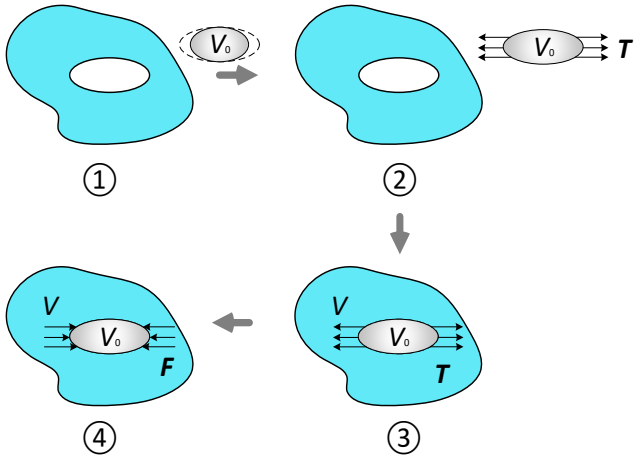

Figure 7.10. Virtual experiment for explaining the inherent strain method.

In the LPBF process, when more material is added, the above process will be repeated until the part is completely manufactured.

7.4.2. Inherent strain method

Since the natural similarities between Eshelby's inclusion and LPBF, this fast computational technique is suitable for fast predicting deformation and residual stresses in LPBF [228]. As for the derivation of the inherent strains, a small dimensional analysis with detailed heat source and physics is employed to calculate it since melt pools in LPBF experience a comparable mechanical history [126]. This inherent strain derivation and calibration will be further explained in Section 7.5. Moreover, it is necessary to mention that for one material, one set of parameters, and on the LPBF machine, such detailed analysis only needs to be executed once. An inherent strain $\boldsymbol{\varepsilon}^*$ is expressed as,

$$\boldsymbol{\varepsilon}^* = \{\varepsilon_x^*, \varepsilon_y^*, \varepsilon_z^*, \varepsilon_{xy}^*, \varepsilon_{yz}^*, \varepsilon_{xz}^*\}^T \tag{7.6}$$

where, *x*, *y*, *z* are the axes of the coordinate system, which is shown in Figure 7.11. According to Deng et al. [226] and Ueda et al. [170], those shear components can be neglected, maintaining a good prediction of deformation and residual stress. Therefore, the inherent strain can be expressed as follows,

$$\boldsymbol{\varepsilon}^* = \{\varepsilon_x^*, \varepsilon_y^*, \varepsilon_z^*, 0, 0, 0\}^T \tag{7.7}$$

Furthermore, with a detailed thermo-elastic-plastic model, the three inherent strain components in a cross-section that is perpendicular to laser scan direction are obtained using the following equations,

$$\begin{aligned} \varepsilon_x^* &= \frac{1}{V}\int_V \varepsilon_x^p dv \\ \varepsilon_y^* &= \frac{1}{V}\int_V \varepsilon_y^p dV \\ \varepsilon_z^* &= \frac{1}{V}\int_V \varepsilon_z^p dV \end{aligned} \tag{7.8}$$

where V is the volume of the heat-affected zone caused by a laser scan.

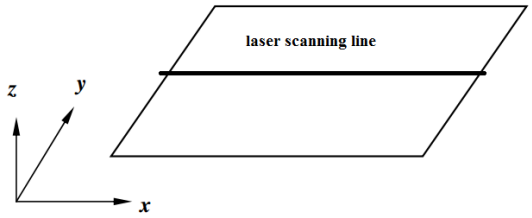

Figure 7.11. The coordinate system of the laser-scan process

With the inherent strain ε*, one then can apply it to larger domains, such as a whole slice of the part, in order to accelerate the simulation speed. For investigating the applicability of this efficient method to the LPBF process, a bridge-shape part (20×10×8 mm), which is the same as the one in the work of Mishurova et al. [45], had been employed in simulation, which is displayed in Figure 7.12a. The part connected with a substrate directly without any support structures. In order to describe the layer-wise adding process, the geometry needs to be sliced. However, when slicing such a curved-surface part, it may be better to approximate it by numbers of blocks. The reason is that when one slices the original CAD model, the derived layers may have sharp corners that probably requires a finer mesh to represent. The computational time would inevitably increase. Therefore, the final sliced geometry of the bridge-shape part consists of numbers of block-shaped

slices,, as shown in Figure 7.12b Each slice here is equal to 20 layers of actual layer thickness 20μm.

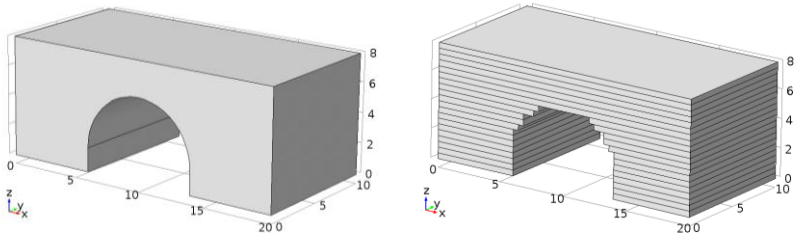

(a) (b)

Figure 7.12. Model geometry in the simulation by the inherent strain method, (a) before slicing, (b) after slicing.

The stress distributions at the as-built condition are displayed in Figure 7.13a. It can be seen that the high stresses are at the root of the part, which, to some degree, may explain the delamination between AM parts and substrates [9]. Figure 7.13b and c show the deformations of the part when it is half and completely cut off from the substrate, separately.

Figure 7.13 (d-f) display the results of the commercial software MSC Simufact Additive®, using the same inherent strain $\boldsymbol{\varepsilon}^{*}$ = {-0.005, -0.001, 0.02}. It is found that the stress distributions are very similar to the results of this work. Since the range of the legends in Figure 7.13 (a-c) and (d-f) are similar, the quantities of the stresses are close in most locations except for the stress concentration locations.

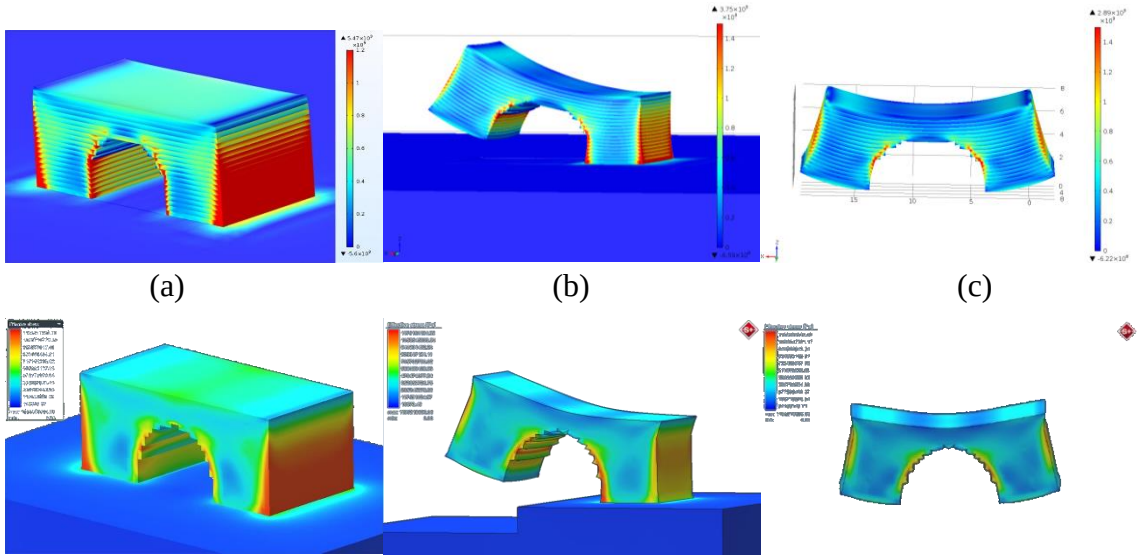

(a) (b) (c)

(d) (e) (f)

Figure 7.13. The stress distribution and deformation of the bridge-shape part by in-house model based on COMSOL Multiphysics software ®, (a) as-built condition, (b) half-cut off from the substrate, (c) complete removal from the substrate; related results from MSC Simufact Additive ®, (d) as-built condition, (e) half-cut off from the substrate, (f) complete removal from the substrate.

In Figure 7.13a and d, the maximum stresses are 5.47 GPa and 1.19 GPa, respectively. Simufact additive ® may use some filtering techniques to smooth the final stress results, so that the result of high stresses may be averaged off. There should be stress singularities in the model, for example, the area of the root of the part, since sharp reentrant corners may lead to a singularity in the derivatives of the variables of elliptic partial differential equations [231]. That is the reason why the maximum stress is extremely high. Using chamfers to round off the sharp corner may prevent those singularities from appearing; nevertheless, this may need more elements, reducing the computational efficiency. However, according to the St. Veneant's principle, one could monitor the stress of the node one element away from a singularity instead of that of the singularity node, where stresses may be fine and representative of the reality [232]. Moreover, stress is computed from the derivative of the displacement field, which may lead to singularities, but the displacement field of FEM should not have singularities.

The curvature of the upper surface of the bridge-shape part obtained by the inherent strain method looks like a parabolic curve, which is similar to the experimental result from Mishurova

et al. [45], as shown in Figure 7.14. Interestingly, the curvatures of the simulation and the experiment matched well, even though only the bulk material properties are considered in the actual laser-scan model for deriving the inherent strain. The reason may be that the powder properties do not influence the deformation prominently; however, further investigation should be carried out, and heat-source models with the existence of powder for deriving inherent strain more accurately should be developed in the future.

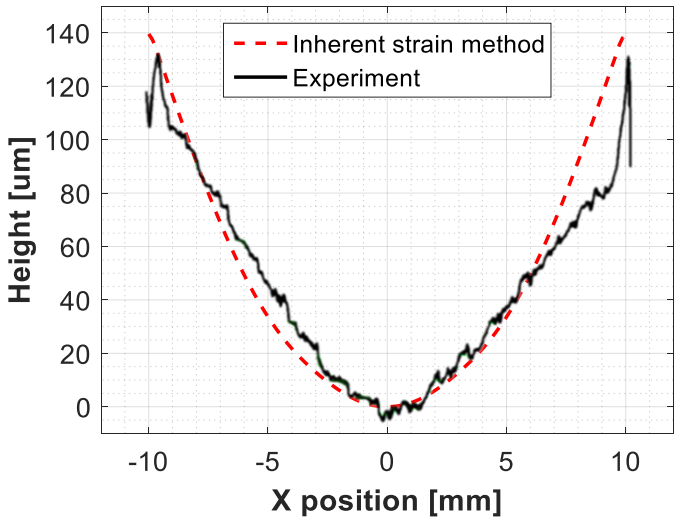

Figure 7.14. The curvatures of the upper surface of the bridge by the inherent strain method and experiment [45]**.**

It is necessary to note that the total computational time of the in-house developed ISM model is around 3 hours, which is very fast compared to the methods discussed previously. The comparison of computational time is listed in Table 7.2. It can be seen that actual-scan and domain-by-domain methods take a very long time and thus may not be suitable for a part-level simulation. Moreover, the developed ISM model can become faster, since now there are several data written and read processes, which are very time-consuming. Furthermore, the Simufact Additive® software is also very fast and probably also employs the ISM; however, computational data cannot be exported, of which the reason is unknown up to now, while topology optimization requires detailed information to build up the optimization model, such as the stiffness matrix, displacement,

strain, stress, and so on. Thus, the in-house developed ISM model is promising to be used for topology optimization.

Table 7.2. Comparison of the computational time of the discussed LPBF simulation methods.

Method	Time [hour]	Model dimensions [mm]	Possibility for part-level
Actual-scan	88.5	2×1×0.06	No
DbD	13	2×1×0.06	Probably no
Inherent strain model	3	20×10×8	Yes
Simufact ®	0.25	20×10×8	Yes

7.5. Inherent strain derivation and calibration for Hastelloy X

In previous sections in this Chapter, the background knowledge of ISM has been discussed. A computational example, which is a bridge-shape part, has been used to demonstrate the advantages of ISM and to verify the in-house develop ISM program by comparing it with the results from commercial software. ISM enables researchers to implement a part-level simulation of LPBF with good accuracy compared to experimental results in an acceptable time, compared to the other LPBF simulation methods. However, the procedure of deriving the inherent strains has not been explained in detail. In addition, the inherent strains are different for different materials. In the next Chapter, Hastelloy X will be used due to the need for the project that the author participate. Therefore, in this section, the inherent strain derivation and calibration for Hastelloy X will be used as an example showing how the inherent strains are derived and calibrated generally, and the derived value will be provided to the ISM simulation in the next Chapter.

7.5.1. Derivation

As mentioned in Section 7.4.2, the inherent strains are derived by implementing an actual-scan thermo-mechanical simulation of LPBF. The averaged plastic strains derived from the thermo-mechanical simulation are the inherent strains, according to Eq.(7.8). Therefore, a thermo-mechanical simulation of LPBF has been built by using COMSOL, whose background information

has been explained in Section 4.4. The one-way coupled method, as shown in Figure 4.4b, has been employed.

First, the heat transfer simulation is executed. The governing equations and the fundamentals of the heat transfer FEM have been explained in Section 4.3. Second, the temperature history during the real laser scanning is fed back to an elasto-plastic simulation model, whose basic equations are presented in Section. 4.2. The linear elasto-plastic model, as shown in Figure 4.2a, has been employed along with the kinematic hardening model illustrated in Figure 4.1. Lastly, the simulated plastic strains will be averaged, and therefore, the inherent strains can be obtained consequently.

First of all, for validating the heat transfer model, a single track simulation has been implemented. The simulated melt pool dimensions have been compared with and validated by the experimental ones. The heat source model—APG4 discussed in Chapter 5—has been used. The validation procedures are also similar to those in Chapter 5. Figure 7.15 shows the comparison of melt pool dimensions between the experimental and simulated results, where good agreement is achieved. Therefore, the heat source is validated and can be used for the following actual-scan simulation. For the actual-scan simulation, the heat transfer is executed first, and then the mechanical simulation is implemented.

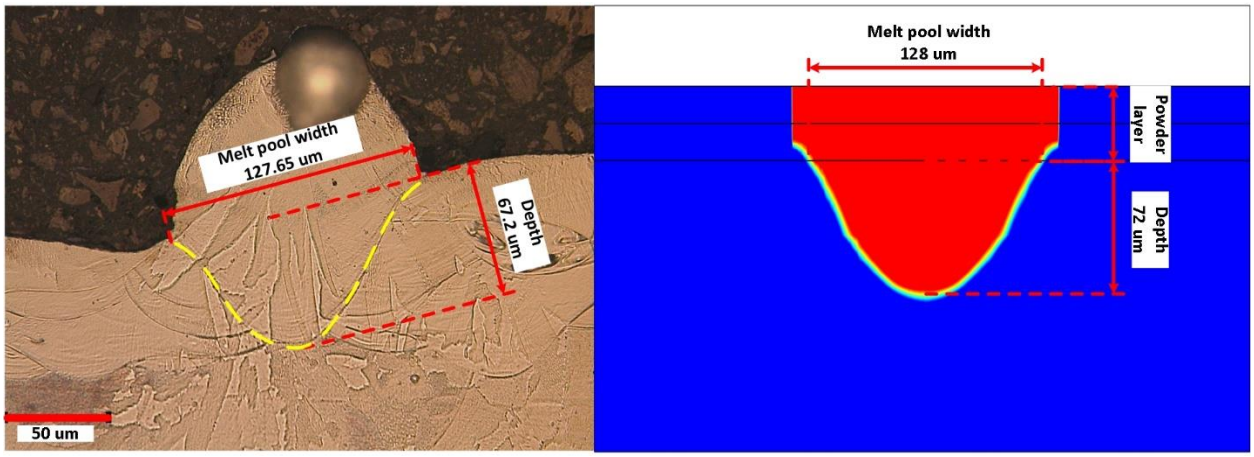

(a) (b)

Figure 7.15. Comparison of melt pool dimensions between (a) experimental (courtesy of Ali Keshavarzkemani and Reza Esmaeilizadeh) and (b) simulated results at process parameters, *P* = 200 W, *v* = 1000 mm/s.

Now actual-scan simulation should be executed, whose scan domain geometry and mesh are shown in Figure 7.16a and b, respectively. The simulation domain dimensions are 500 × 500 × (200 + 40) µm. The 40 µm is the powder layer thickness. The powder layer is assigned with powder material properties, which is similar to the model explained in Chapter 5. The boundary conditions for the heat transfer simulation are also as same as those shown in Chapter 5. For the mechanical simulation, the bottom of the block is fixed.

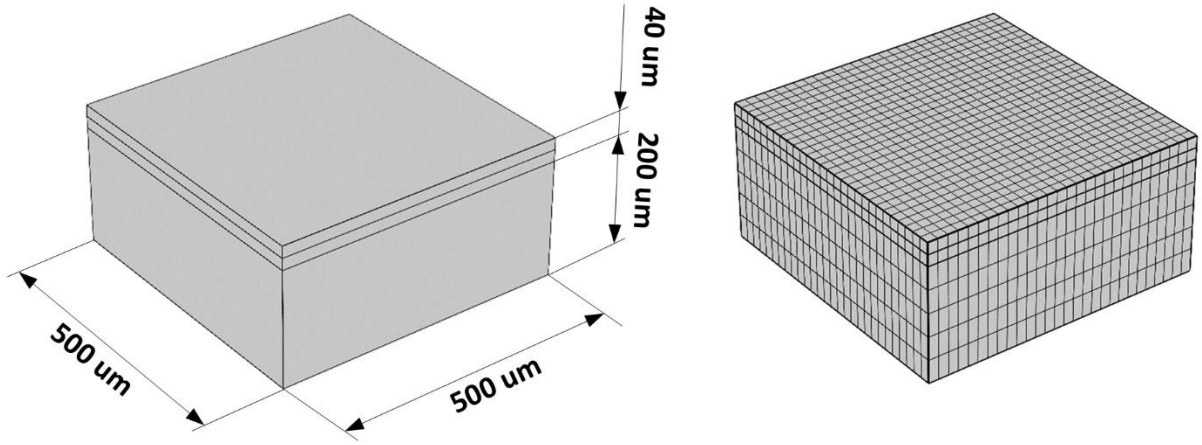

(a) (b)

Figure 7.16. The actual-scan simulation configurations, (a) geometry and (b) mesh

Figure 7.17 shows the simulation results of the one-way coupled thermo-mechanical simulation at the time of 0.0022 s. Figure 7.17a shows the temperature distribution when a laser beam is scanning. The scan pattern is the raster pattern, which is similar to the one shown in Figure 7.1b. Figure 7.17b depicts the von Mises stress at the same time. It can be observed that the area above the melting temperature (~1533K) has low stress because the melting liquid cannot bear too much mechanical stress. This characteristic was achieved by assigning very small Young's modulus to the material when it is melting.

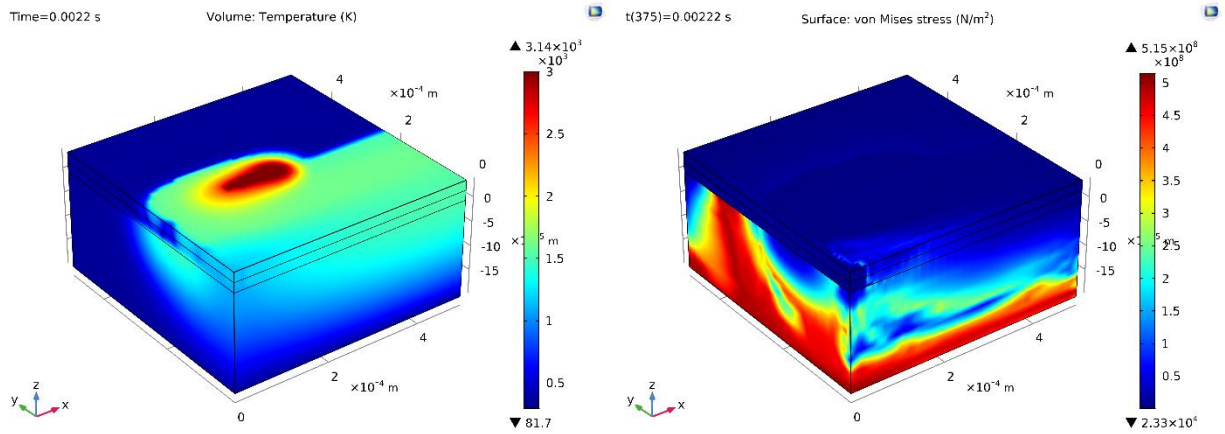

(a) (b)

Figure 7.17. The actual-scan simulation results at the time of 0.0022s, (a) heat transfer simulation, (b) mechanical simulation.

The von Mises stress after the domain is cooled down near to room temperature is presented in Figure 7.18a. It can be seen that the maximum stress is around 600 MPa, which is very close to the yield stress, which is consistent with the experimental observation that the top of an LPBF part has the large tensile stress close to the yield stress [47]. Figure 7.18b,c,d illustrate the plastic strain in the x-direction, y-direction, z-direction respectively. The averaged value of them can then be derived as $\boldsymbol{\varepsilon}^{*}$ = {-0.0115, -0.00415, 0.0157}. This value then can be used to simulate the part-level distortion and residual stresses through ISM. Moreover, the uppermost layer is not constrained from above, and a non zero contribution of strain loads in build-up direction will cause in simple shrinkage of the new layer; however, there will be no extra force acting on the solidified part. This

shrinkage of the layer itself will be refilled with the next recoating process. For this reason, ε_{zz}^* can also be set to zero [128]. So the inherent strains are $\boldsymbol{\varepsilon}^* = \{-0.0115, -0.00415, 0\}$.

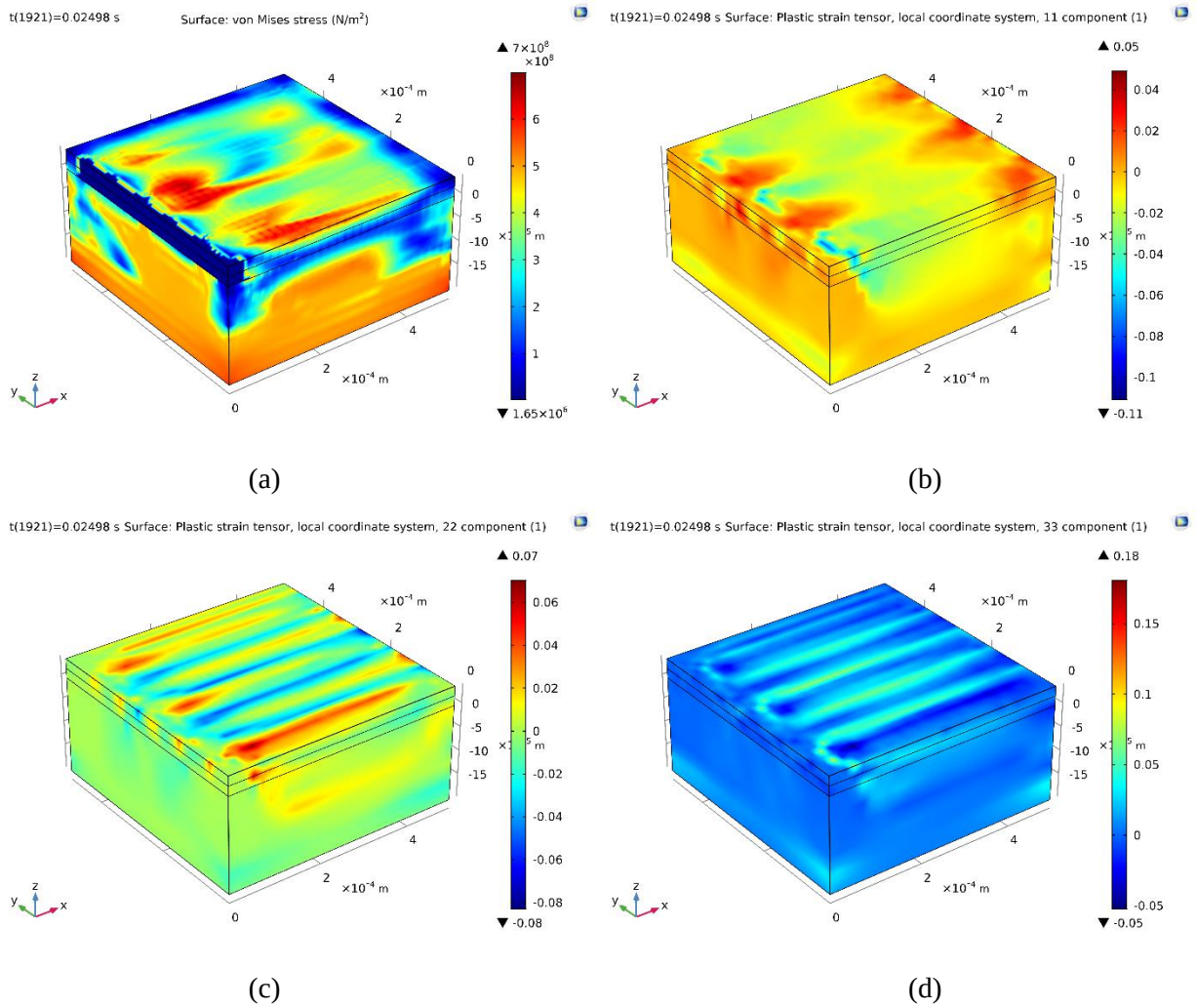

Figure 7.18. The final von Mises stress and the plastic strains, (a) von Mises stress, (b) plastic strain xx, (c) plastic strain yy, (d) plastic strain zz.

7.5.2. Calibration

In order to calibrate the derived inherent strains, twin cantilevers are printed, as shown in Figure 7.19a. The cantilever is cut, and the deformation is measured. The inherent strains derived from the previous thermo-mechanical simulation are fed into the ISM simulation model, and one of the results is presented in Figure 7.19b. The ISM simulation model is based on the in-house ISM program that will be mentioned in Section 8.2.5.

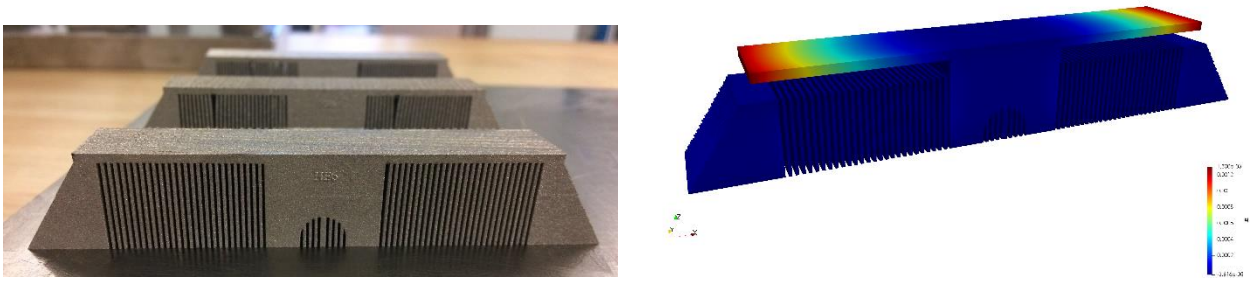

(a) (b)

Figure 7.19. Twin cantilever by LPBF for validating simulation-derived inherent strains, (a) printed cantilevers, (b) ISM simulated cantilever.

The workflow of the inherent strain calibration is depicted in Figure 7.20. The initial inherent strains $\boldsymbol{\varepsilon_0}^*$ = {-0.0115, -0.00415, 0}, which are obtained from the thermo-mechanical simulation discussed in the previous section. They will be input into the in-house ISM program (C++ code) to get the deformations of the twin cantilevers under different scan directions (uni-X, uni-Y, XY rotation). The inherent strains will be manually modified based on the comparisons with the experimental deformation values. If the simulated deformation in one direction is larger than its corresponding experimental result, then the inherent strain value corresponding to that direction is going to be reduced, and vice versa.

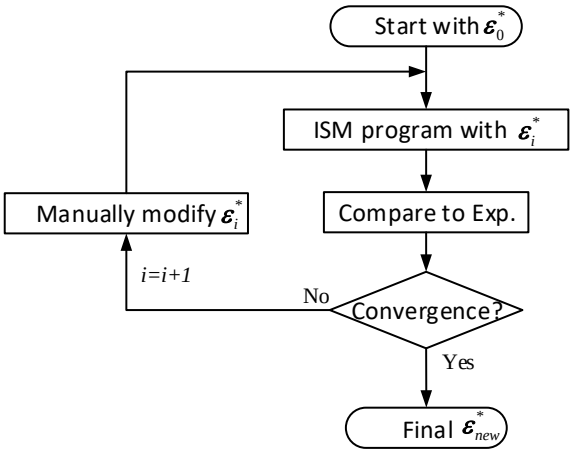

Figure 7.20. The workflow of the inherent strain calibration

After the inherent strain calibration process, the new inherent strains can be derived as $\boldsymbol{\varepsilon_{new}}^*$ = {-0.002, -0.001, 0}. The ISM simulated results with the new inherent strains are derived and

compared to the measured deformations, which are summarized in Table 7.3. Good agreement can be found.

Table 7.3. Summary of the support optimizations executed in this work.

Scan pattern	ISM sim. [mm]	Exp. [mm]
X	1.286	1.258
Y	0.9997	1.01
XY	1.139	1.11

It is necessary to mention that the initial inherent strains are $\boldsymbol{\varepsilon_0}^* = \{-0.0115, -0.00415, 0\}$, the experimentally calibrated inherent strains are $\boldsymbol{\varepsilon_{new}}^* = \{-0.002, -0.001, 0\}$. The discrepancy is around 5 times. This difference is caused by the fact that the thermo-mechanical simulation did not consider the stress and strain initialization. The stress and strain initialization are that when material experiences a temperature over the melt temperature, the stresses and strains within it will be reset to zero as mentioned in [37] because the liquid of melt pool cannot bear the mechanical load and does not have the concept of strain ether. However, to the author's best knowledge, the COMSOL Multiphysics does not have this capability to reset the strains and stresses in remelting elements. Therefore, in the future, more FEM tools will be used to fulfill this task, e.g. deal.II [138]. Even though the thermo-mechanical model needs further improvements for deriving more accurate inherent strains, the inherent strains have been experimentally calibrated, and it is valid to use them in the next chapter.

7.6. Summary

In this chapter, the multi-scale modeling of the LPBF process has been investigated in order to develop a proper AM-process-simulation method for the couple topology optimization and process simulation system for LPBF. First, a model with an actual laser scan was built. After finding that the actual laser scan is impossible for a part-level simulation, an accelerated model has been tested, in which domains were activated one by one with an equivalent heat source.

Nevertheless, it is still slow, so a further accelerated method was investigated, called the inherent strain method (ISM). Computational time is significantly reduced with reasonable accuracy. Lastly, the inherent strain derivation and calibration for Hastelloy X have been presented as an example of how generally the inherent strains are derived and calibrated. The new derived inherent strains will be used in the next Chapter.

Chapter 8. Topology Optimization Combined with LPBF Process Simulation*

8.1. Introduction

In this chapter, a topology optimization parallel-computing framework is developed to design support structures for minimizing deflections in LPBF parts. The parallel-computing framework consists of a topology optimization model and an Inherent Strain Method (ISM) model. The proposed framework is used to design stiffer support structures to reduce the before and after-cutting deflections in printed cantilevers. The performance of the optimized support structures in terms of the part deformation has been incorporated and validated by a comprehensive set of experimental results.

8.2. Topology optimization formulations

8.2.1. Statement of the problem

Support optimization for LPBF should be of importance because the printing could fail if the support is not designed well. Moreover, optimization can reduce the material usage of support structures. Thirdly, support structures could affect the residual stresses and the deflections in as-built and after support removal parts.

Support structures in LPBF are for supporting overhanging material against gravity. Thus, it is not difficult to think of implementing support topology optimization under gravity load. Moreover,

---

* A similar version of this chapter will be submitted as:
Zhidong Zhang, Osezua Ibhadode, Usman Ali, Chinedu Francis Dibia, Pouyan Rahnama, Ali Bonakdar, Ehsan Toyserkani, Topology optimization parallel-computing framework based on the inherent strain method for support structure design in laser powder-bed fusion additive manufacturing.

besides the gravity load, supports should be able to stand with the residual stress load in the printed parts. If not, the printing could fail as well. In this work, two formulations with different loading conditions have been considered: a. the gravity load only in Section 8.2.2 and b. the combined loads of gravity and residual stress in Section 8.2.3.

8.2.2. Formulation 1: Support optimization under gravity load only

The schematic of the problem has been displayed in Figure 8.1. The LPBF part is printed on top of the substrate with a support structure. $\boldsymbol{F}_1$ is the load vectors induced by the gravity of the overhanging material.

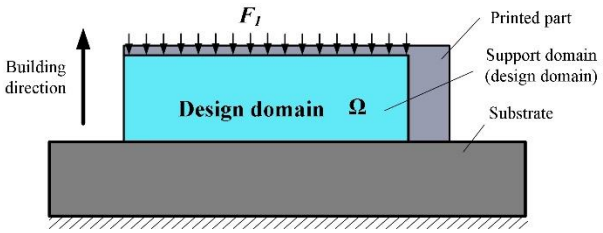

Figure 8.1. Schematic of the support topology optimization with gravity load only.

The objective of the topology optimization in this work is to minimize the compliance of the support structures (maximizing global stiffness). By employing the density-based topology optimization approach, the objective function can be expressed as,

$$\begin{aligned} &\underset{\boldsymbol{\rho}}{\text{Min.}} \quad C = \boldsymbol{F}_1^T \boldsymbol{U}_1 \\ &\text{s. t.} \quad \boldsymbol{K}(\boldsymbol{\rho})\boldsymbol{U}_1(\boldsymbol{\rho}) = \boldsymbol{F}_1 \\ &\qquad V(\boldsymbol{\rho}) = \sum_{i=1}^{n} \rho_i \le \bar{V}_{\mathrm{f}} \cdot V_0 \\ &\qquad 0 < \rho_i \le 1 \qquad\qquad i = 1, 2, \cdots, N_e \end{aligned} \tag{8.1}$$

where $\boldsymbol{U}_1$ is the displacement vector, $\boldsymbol{K}(\boldsymbol{\rho})$ is the stiffness matrix. $\boldsymbol{\rho}$ is the vector of design variables, in which ρ_i represents the density of the material in the i^{th} element where ρ_i =1 represents a solid element, while ρ_i = 0 represents an empty element. $V(\boldsymbol{\rho})$ is the volume of used material, $\bar{V}_{\mathrm{f}}$ is the volume fraction, and V_0 is the total volume of the design domain. The material properties

interpolation function of Solid Isotropic Material with Penalization (SIMP) is used in this work [233]. The Young's modulus E_i for element i is interpolated as,

$$E_i = \rho_i^p \left(E_1 - E_0\right) + E_0 \tag{8.2}$$

where E_1 is Young's modulus of the material, $E_0 > 0$ is Young's modulus of the void region (10E-9E_1), and p is the penalty factor. In this work, p is gradually increasing during topology optimization so that the penalty is weak at the beginning and gradually stronger.

8.2.3. Formulation 2: Support optimization under combined loads of gravity and residual stress

A two-loading problem is considered (a) gravity load $\boldsymbol{F_1}$ of the printed part and (b) the LPBF induced residual stresses $\boldsymbol{F_2}$ within the printed part, as shown in Figure 8.2. The residual stress $\boldsymbol{F_2}$ is only computed once at the beginning and fixed during topology optimization for simplification. In other words, the residual stress $\boldsymbol{F_2}$ is regarded as design-independent in this work.

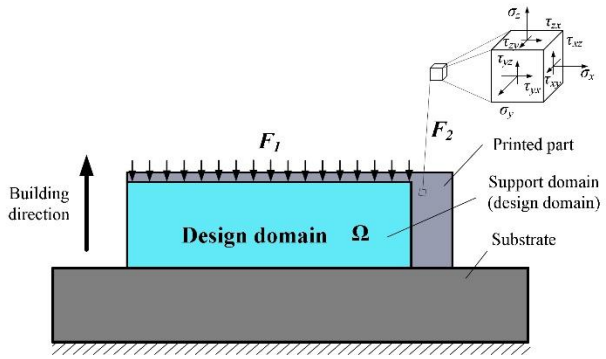

Figure 8.2. Schematic of the support topology optimization under a two-load condition.

After adding the residual stresses $\boldsymbol{F_2}$, the new formulation is expressed as:

$$\begin{aligned} \min_{\boldsymbol{\rho}} \quad & C = w_1 \boldsymbol{F}_1^T \boldsymbol{U}_1 + w_2 \boldsymbol{F}_2^T \boldsymbol{U}_2 \\ \text{s. t.} \quad & \boldsymbol{K}(\boldsymbol{\rho})\boldsymbol{U}_1(\boldsymbol{\rho}) = \boldsymbol{F}_1 \\ & \boldsymbol{K}(\boldsymbol{\rho})\boldsymbol{U}_2(\boldsymbol{\rho}) = \boldsymbol{F}_2 \\ & V(\boldsymbol{\rho}) = \sum_{i=1}^{n} \rho_i \le \overline{V}_{\mathrm{f}} \cdot V_0 \\ & 0 < \rho_i \le 1 \qquad\qquad i = 1, 2, \cdots, N_e \end{aligned} \tag{8.3}$$

where $\boldsymbol{U}_1$ and $\boldsymbol{U}_2$ are the displacement vectors under the two loading conditions. w_1 and w_2 are the weight coefficients of the two loading conditions, respectively. In this formulation, the two loading conditions are chosen to contribute to the objective function equally. In addition, their compliances are normalized by their value at the first iteration, respectively. Therefore, the weight factors w_1 and w_2 can then be calculated correspondingly.

As residual stresses $\boldsymbol{F_2}$ is required to solve the optimization problem, an efficient technique should be employed to calculate $\boldsymbol{F_2}$. The residual stresses can be calculated by a thermo-mechanical model with actual laser-scanning models. However, this approach would be extremely time-consuming [21,73,204]. Therefore, a fast-computational method is required for the prediction of residual stresses during LPBF. In this work, the Inherent Strain Method (ISM) [127,234] has been used for the fast prediction of distortions and residual stresses. In ISM, distortions and residual stresses are calculated by the incompatible strain, including thermal and plastic strain caused by the uneven temperature distribution during the LPBF process [225]. In general, an inherent strain $\boldsymbol{\varepsilon}^*$ can be expressed as $\boldsymbol{\varepsilon}^*=\{\varepsilon_x^*, \varepsilon_y^*, \varepsilon_z^*, \varepsilon_{xy}^*, \varepsilon_{yz}^*, \varepsilon_{xz}^*\}$. The ε_z^* and shear strains can be set to zero, as explained by Siewert et al. [128]. In this work, the inherent strain values of $\varepsilon_x^* = -0.002$ and $\varepsilon_y^* = -0.001$ are derived based on the method used by other researchers [128,171], which includes a small-scale thermo-elasto-plastic simulation model and experimental validations. With the inherent strains, one can implement the ISM simulation. The flowchart of the ISM simulation is drawn in Figure 8.3.

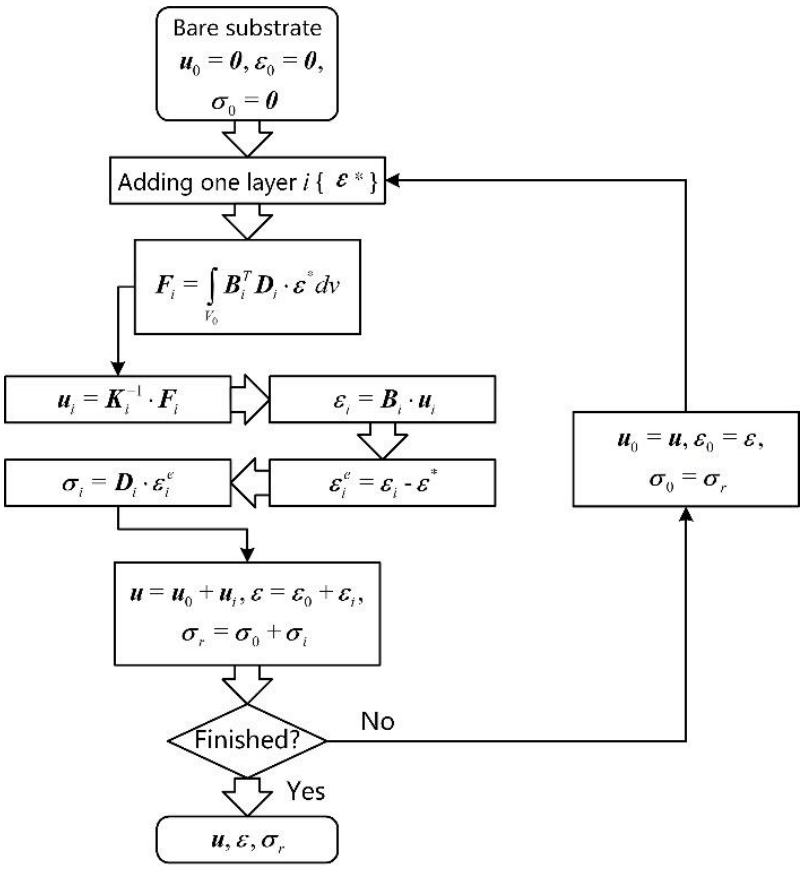

Figure 8.3. Flowchart of the LPBF process simulation through ISM.

8.2.4. Sensitivity analysis

In topology optimization problems, the gradient of the objective function is defined as the sensitivity. The sensitivity is used to find the global optimum based on the predefined objective. By comparing Eq.(8.1) and Eq.(8.3), it can be found that Eq.(8.1) is a special case of Eq.(8.3) when w_2 is equal to 0. Therefore, the following sensitivity analysis is based on Eq.(8.3). The sensitivity of the objective function in Eq.(8.3) concerning a design variable, ρ_i, is calculated by the direct method, which is as follows,

$$\frac{\partial C}{\partial \rho_i} = w_1 \frac{\partial \boldsymbol{F}_1^T \boldsymbol{U}_1}{\partial \rho_i} + w_2 \frac{\partial \boldsymbol{F}_2^T \boldsymbol{U}_2}{\partial \rho_i} \tag{8.4}$$

where,

$$w_1 \frac{\partial \boldsymbol{F}_1^T \boldsymbol{U}_1}{\partial \rho_i} = w_1 \left(\frac{\partial \boldsymbol{F}_1^T}{\partial \rho_i} \boldsymbol{U}_1 + \boldsymbol{F}_1^T \frac{\partial \boldsymbol{U}_1}{\partial \rho_i} \right) \tag{8.5}$$

According to the balance function,

$$\boldsymbol{K}(\boldsymbol{\rho})\boldsymbol{U}_1(\boldsymbol{\rho}) = \boldsymbol{F}_1(\boldsymbol{\rho}) \tag{8.6}$$

The gradient of the displacement vector can be derived from Eq. (8.6) as,

$$\frac{\partial \boldsymbol{U}_1(\boldsymbol{\rho})}{\partial \rho_i} = \boldsymbol{K}^{-1}(\boldsymbol{\rho}) \left(\frac{\partial \boldsymbol{F}_1^T(\boldsymbol{\rho})}{\partial \rho_i} - \frac{\partial \boldsymbol{K}(\boldsymbol{\rho})}{\partial \rho_i} \boldsymbol{U}_1(\boldsymbol{\rho}) \right) \tag{8.7}$$

Substitute Eq.(8.7) into Eq.(8.5), then Eq.(8.5) can be expressed as follows,

$$w_1 \frac{\partial \boldsymbol{F}_1^T \boldsymbol{U}_1}{\partial \rho_i} = -w_1 \boldsymbol{U}_1^T(\boldsymbol{\rho}) \frac{\partial \boldsymbol{K}(\boldsymbol{\rho})}{\partial \rho_i} \boldsymbol{U}_1(\boldsymbol{\rho}) \tag{8.8}$$

As mentioned in Section 8.2.3, the load vector $\boldsymbol{F}_2$ is also regarded as design-independent and therefore, is expressed in a form similar to $\boldsymbol{F}_1$. The sensitivity of the objective function to the design variables (Eq. (8.4)) can, therefore, be expressed as,

$$\frac{\partial C}{\partial \rho_i} = -w_1 \boldsymbol{U}_1^T(\boldsymbol{\rho}) \frac{\partial \boldsymbol{K}(\boldsymbol{\rho})}{\partial \rho_i} \boldsymbol{U}_1(\boldsymbol{\rho}) - w_2 \boldsymbol{U}_2^T(\boldsymbol{\rho}) \frac{\partial \boldsymbol{K}(\boldsymbol{\rho})}{\partial \rho_i} \boldsymbol{U}_2(\boldsymbol{\rho}) \tag{8.9}$$

8.2.5. Parallel-computing implementation

For LPBF, the support structures sometimes should be of fine features. A high-performance, parallel-computing platform of topology optimization proposed by Aage et al. [176] has been employed in this work. On top of that, a parallel-computing module of ISM has been incorporated, which is based on the workflow shown in Figure 8.3.

The workflow of the proposed parallel-computing topology optimization framework is presented in Figure 8.4. It can be seen from Figure 8.4 that the parallel ISM module has been used to obtain the residual stress vector $\boldsymbol{F_2}$ before the beginning of the optimization loop. $\boldsymbol{F_2}$ is then used as the second loading condition in the topology optimization problem. The sensitivity filtering

technique [235] is used to avoid the well-known check-board problems in density-based topology optimization [159]. The sensitivity filter radius r_f is characterized in terms of the element number. It is chosen to be 6 in this work to ensure the optimized support does not present features too small to be printed. The Method of Moving Asymptotes (MMA) [236] is employed to solve the topology optimization problem. The cluster graham [237] on SHARCNET was employed in this work where each compute node has 32 cores (2×Intel® E5-2683 v4 (Broadwell) @ 2.1 GHz).

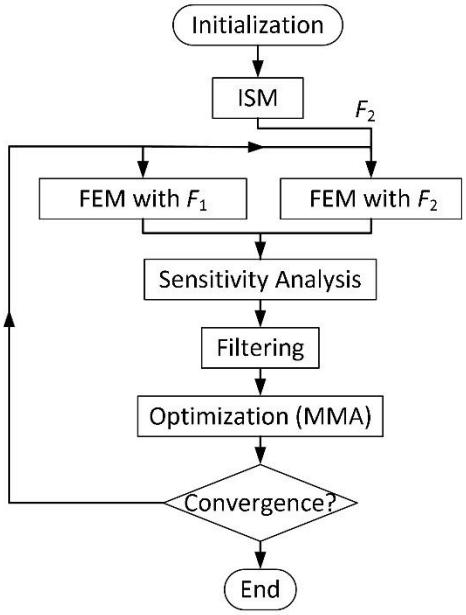

Figure 8.4. The schematic of the parallel-computing optimization framework.

8.3. Implementation of the proposed formulations

8.3.1. Implementation specifications

The support structure of the cantilevers was chosen to be optimized and printed, as shown in Figure 8.5a. The grey domain is the non-optimizable cantilever, and the blue domain represents the design domain for the support structures. The cantilever dimensions are shown in Figure 8.5a. The material properties of Hastelloy X are used: Young's modulus of 190 GPa and Poisson's ratio of 0.3 [238,239]. Because of the design-domain symmetry, only half of the domain was modeled. It should be noted that the top of the support domain is connected with the cantilever, while the

right side of the support domain has a one-element gap from the cantilever. The penalty factor p in Eq.(8.2) is starting with 2 and gradually increasing to 4.5 later, in order to generate more evenly distributed support branches at the interface between the cantilever and the support structure. As discussed previously, gravity $\boldsymbol{F}_1$and residual stress $\boldsymbol{F}_2$ within the cantilever were used as loading conditions (Figure 8.5b,c). In addition, the support domain and the cantilever were constrained at the bottom.

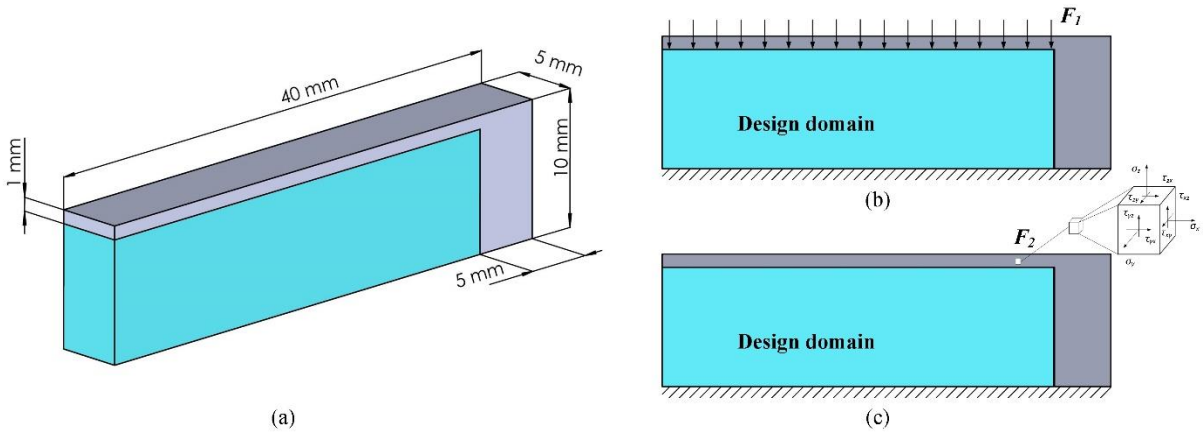

Figure 8.5. A cantilever structure (grey) with support design domain (blue) in (a), and the schematics of the two loading conditions: (b) gravity, (c) inherent strain method (ISM).

Four different volume fractions $\bar{V}_{\mathrm{f}}$-0.3, 0.4, 0.5, and 0.65 of support structures were considered. As the default OEM support structure was found to have a volume fraction of 0.65, $\bar{V}_{\mathrm{f}} = 0.65$ was also chosen for the topology optimization. As discussed in Section 8.2.2 and Section 8.2.3, two separate topology optimization formulations namely (a) topology optimizations with gravity only (GraOnly) and (b) topology optimization with gravity and residual stresses from ISM (GraAndISM) were performed in this study and are summarized in Table 8.1.

Table 8.1. Summary of the support optimizations executed in this work.

Cantilever Name	$\overline{V}_f$	Loading
GraOnly0.3	0.3	Gravity only
GraAndISM0.3	0.3	Gravity + ISM
GraOnly0.4	0.4	Gravity only
GraAndISM0.4	0.4	Gravity + ISM
GraOnly0.5	0.5	Gravity only
GraAndISM0.5	0.5	Gravity + ISM
GraOnly0.65	0.65	Gravity only
GraAndISM0.65	0.65	Gravity + ISM

8.3.2. Investigation of mesh size

It is well known that the mesh size affects the topology optimization results significantly [240]. Therefore, an investigation into the optimum mesh size was performed. Figure 8.6 shows the support topology optimization with different mesh size from 64×4×16 to 480×32×120. As is expected, the support structure is rougher when using a coarser mesh. The rough results could induce several problems: (a) the rough results cannot express small features; (b) the rough results cause uneven surfaces which are detrimental to the final printing. Therefore, a high-resolution mesh is necessary for the design of AM support structures [178]. In addition, a high-resolution mesh does not require any further mesh smoothing or reconstruction before printing. After comparison among the different mesh sizes, the results of 240×16×64 and 480×32×120 are smooth and should be acceptable to be printed. However, 480×32×120 is chosen as the mesh for topology optimization in this work because the result seems to have a few more features

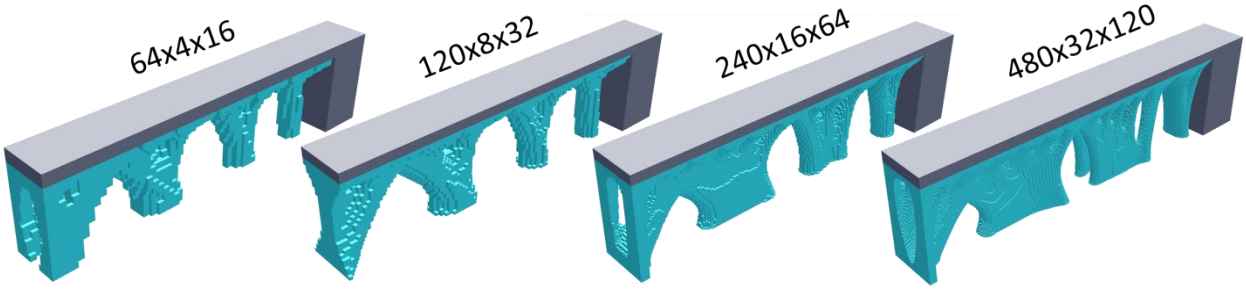

Figure 8.6. Support topology optimization with different mesh sizes.

8.3.3. Topology optimization results of the support structures

The mesh of 480×32×120 (1,843,200) eight-node hexahedron elements has been used for all the following simulations. The optimized design solutions with different support volume fractions are shown in Figure 8.7, where the first row shows the results with gravity loading (GraOnly) condition while the second row presents the results under gravity and residual stress loading (GraAndISM) conditions. For the GraOnly models, the results are symmetric along the cantilever length as a uniform gravity load is applied across the cantilever. A tree-branch structure is observed with a volume fraction of 0.3, which was also found in the literature [178]. However, with increasing volume fraction, the separated branches join together partially to form stronger support structures.

Optimized support structures from GraAndISM show slight variation from GraOnly results. The support structures tend to form stronger support near the free ends of the cantilevers and are not symmetric along the longitudinal direction of the cantilevers due to the addition of ISM loads. The occurrence of stronger support near the edge of the cantilever may be due to the occurrence of maximum deflection observed in this location after printing.

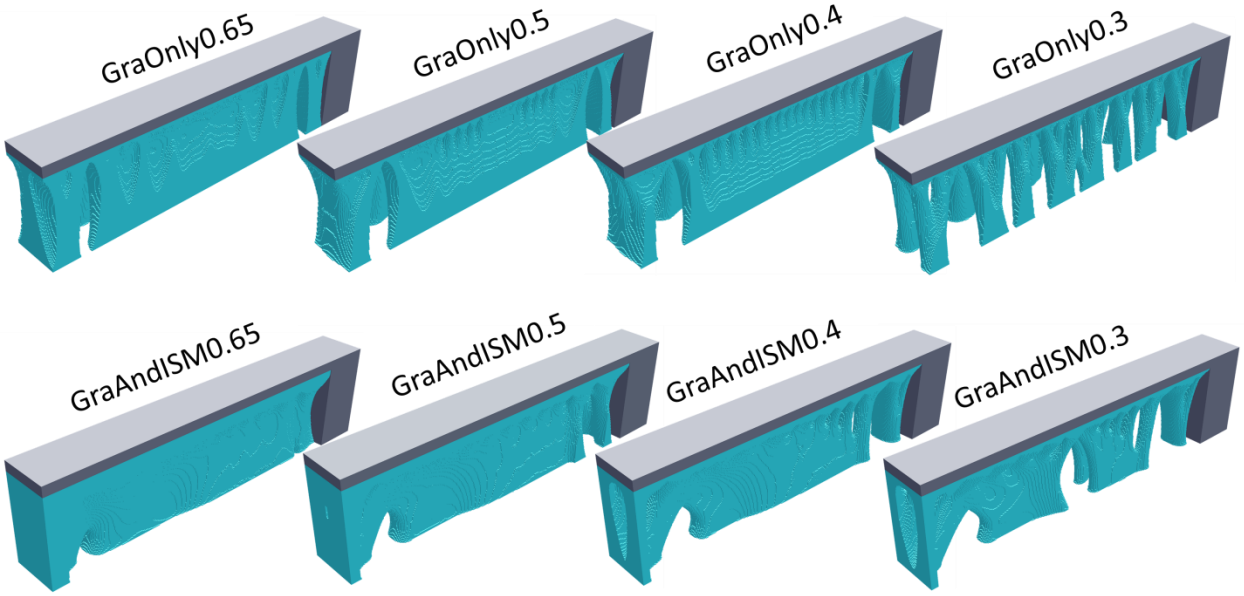

Figure 8.7. Topology optimization results of the support structures with different loading conditions and different volume fractions.

The iteration histories of compliance and volume fraction for GraOnly0.3 and GraAndISM0.3 are chosen as examples for illustration and shown in Figure 8.8a and b, respectively. Figure 8.8a shows an increase in compliance at the beginning because of the changing penalty factor *p* (Eq.(8.2)). The jump at iteration 100 is because filtering is turned off from then in order to generate clearer structures. The compliance is normalized by its value at the first iteration, which is also the implementation in literature [176]. Figure 8.8b shows two compliance curves: Compliance 1-gravity load and Compliance 2-residual stress load derived from ISM. They are all normalized by their value at the first iteration respectively, to achieve an equal contribution to the objective function (Eq.(8.3)).

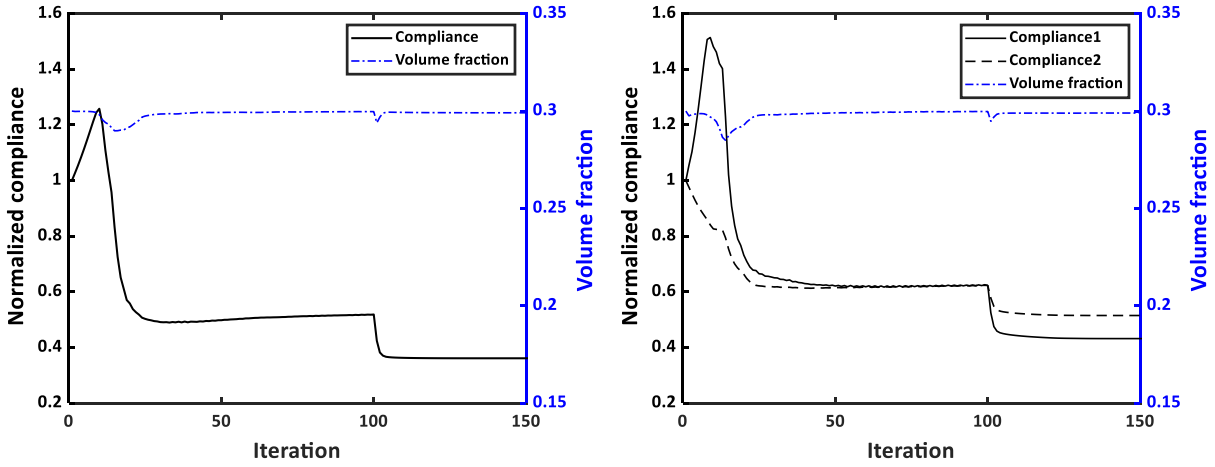

(a) (b)

Figure 8.8. Iteration histories of compliance and volume fraction, a. GraOnly0.3, b. GraAndISM0.3.

It should be noted that in this work, the easy removal [178,241] of supports is not considered for the sake of simplification, which may need to be included in the future. Moreover, Figure 8.7 manifests the support structures are self-supported even without overhang constraints, which is consistent with the findings in the work of Mezzadri et al. [178]. The characteristic of self-support could be indirectly proven by the successfully experimental printings in the next section, as well. The self-support could be explained by the existence of the gravity load, making the pillars tend to be more parallel with the gravity transmissible loads. Thus, the overhang area of the supports is reduced significantly. In the future, overhang constraints [167,168] should also be considered when dealing with more complex part geometries instead of the simple cantilevers. Furthermore, design constraints, e.g., maximum/minimum length scale control [153,242], may also need to be considered in the future in order to prevent the support structures for LPBF from being too bulky or too delicate.

8.4. Experimental procedures

The cantilevers were printed on an EOS M 290 LPBF machine. The geometry of the printed cantilevers is depicted in Figure 8.9a. It should be noted that two referencing parts, (a) default OEM support and (b) the solid support, have also been printed along with the topologically optimized parts. The performance of these support structures has been experimentally examined and compared, which will be explained in the next section.

Argon atmosphere was within the building chamber during the manufacturing process. Hastelloy X gas-atomized powder supplied by EOS GmbH was used to fabricate the cantilevers with the x unidirectional scanning pattern, which is parallel to the cantilever's longitudinal direction. All of the cantilevers were printed on a printed sub-substrate with the same set of processing parameters (laser power 200 W and scanning speed 1000 mm/s). The printed parts under the as-built condition are shown in Figure 8.9b.

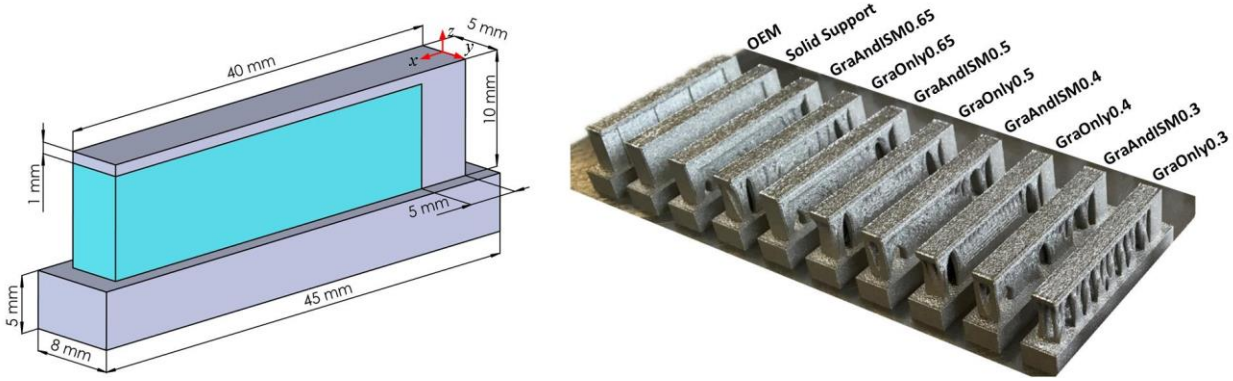

(a) (b)

Figure 8.9. The configuration of the cantilevers on the substrate, (a) the layout plan, (b) the printed parts.

Electrical Discharge Machining (EDM) was used to cut all the printed parts off from the substrate and to cut the supports off from the cantilevers such that the deflection data before and after support removal can be obtained, respectively.

A Coordinate Measuring Machine (CMM), a mobile 3D white light scanner of AICON SmartScan, HEXAGON®, was used to measure the high-precision 3D data of the printed parts in order to get the deflections of printed parts and to compare with simulated results. Moreover, point data representing the top and side surfaces of the cantilevers were extracted from the 3D scanned data with the origin placed at the center of the top right corner, as shown in Figure 8.9a.

8.5. Results and discussions

8.5.1. Experimental results

All the topology optimized support structures with cantilevers before (as-built) and after cutting are shown in Figure 8.10a,b, respectively. Quantitative measurements on samples before and after cutting were collected by CMM.

Figure 8.11a,b show the corresponding results for before and after-cutting cantilevers, respectively. It should be noted that the results in Figure 8.11 shows the deflections in the z-direction only. Figure 8.11a indicates that the two smaller edges on the top surface show high deflections than the center areas. This height variation within the top surface of the printed cantilevers is due to the laser scanning pattern. As the laser turns at the edges, it causes an increase in the energy input near the edge of the cantilever resulting in more material being melted. In addition, the left longer edges along the cantilever direction are also higher than the center area. There is available powder on both sides of the edge, which results in higher tracks [201].

Figure 8.11b shows the z-deflection after cutting where the maximum deflections are highlighted by annotation boxes. As expected, all maximum deflections were recorded at the edge of the cantilevers due to the accumulation of local deflections along the cantilevers. Results show that the default OEM support induced the largest deflection of 2.31 mm. All the cantilevers from GraAndISM show ~20% smaller deflections than their GraOnly counterparts. Especially for the situations of volume fraction 0.3 and 0.65, the deflection reductions are over 28%. Maximum

deflections provide a general trend for the support efficiency and validation of the topology optimization framework discussed in this work. A detailed analysis is presented below.

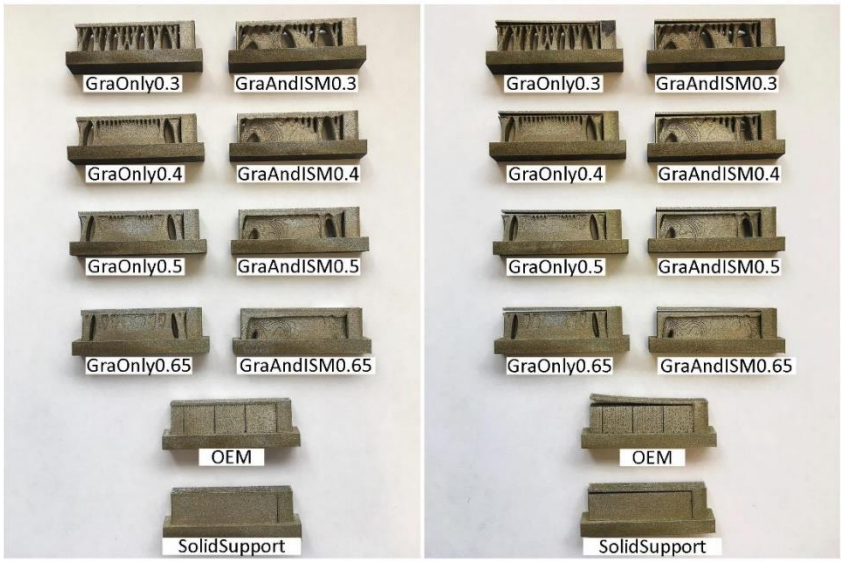

(a) (b)

Figure 8.10. 3D printed cantilevers (a) before cutting, (b) after cutting.

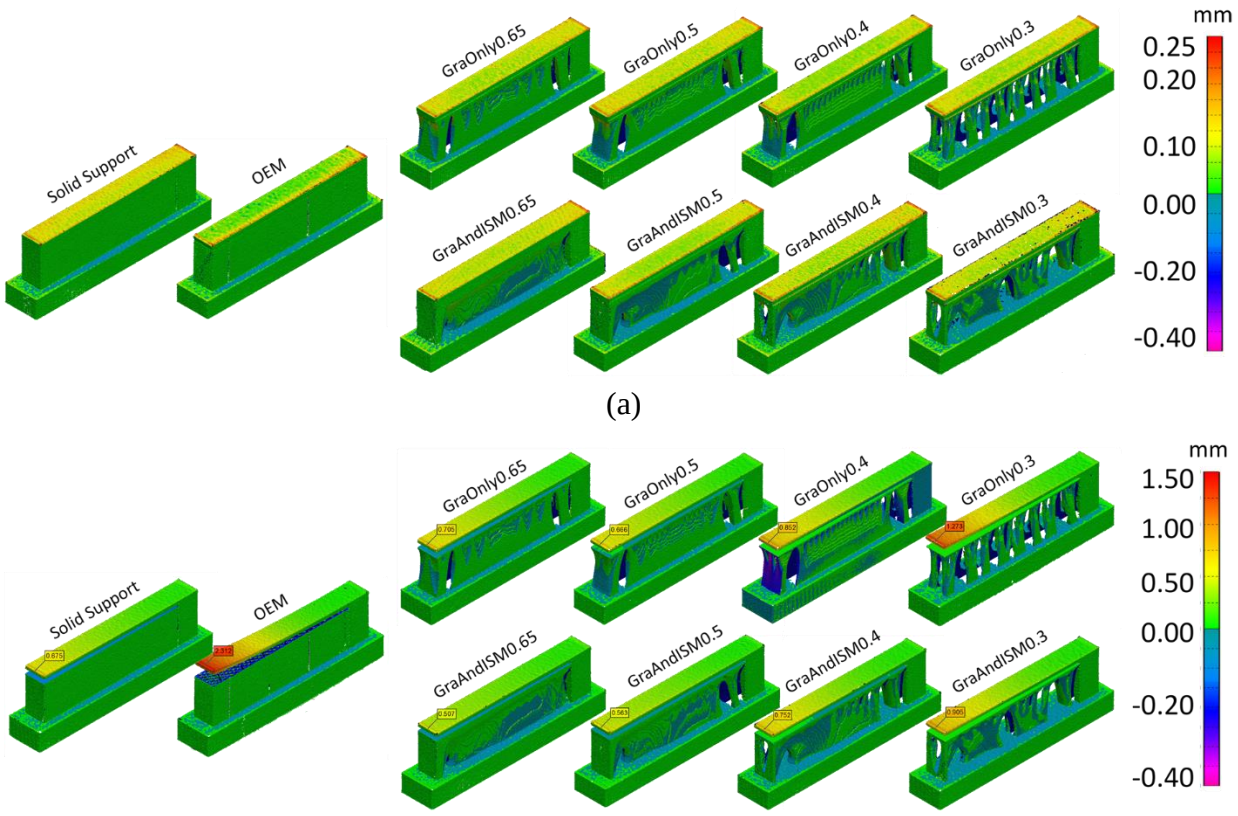

Figure 8.11. The CMM results of the printed cantilevers for the distortion in the z-direction, (a) before cutting, (b) after cutting.

Figure 8.12c,d show the before and after-cutting deflection data of the cantilevers, respectively. The deflection results are derived from the CMM point data from the top surface (red lines in Figure 8.12a,b). Results from all the cantilevers before cutting show very similar results with minor variations near the edges as having been observed in Figure 8.11a. However, results show that all cantilever structures were a little higher (~100 µm) than the CAD model (red dash line). Figure 8.12d presents the cantilever profiles after cutting. Clearly, the default OEM support produced the maximum deflection, followed by the GraOnly0.3. GraAndISM0.65 shows the least deflection along the cantilever top surface. As the dimensional accuracy (deflection) after the support removal is very important, results from optimized support structures show that the default OEM support can be replaced to improve dimensional accuracy.

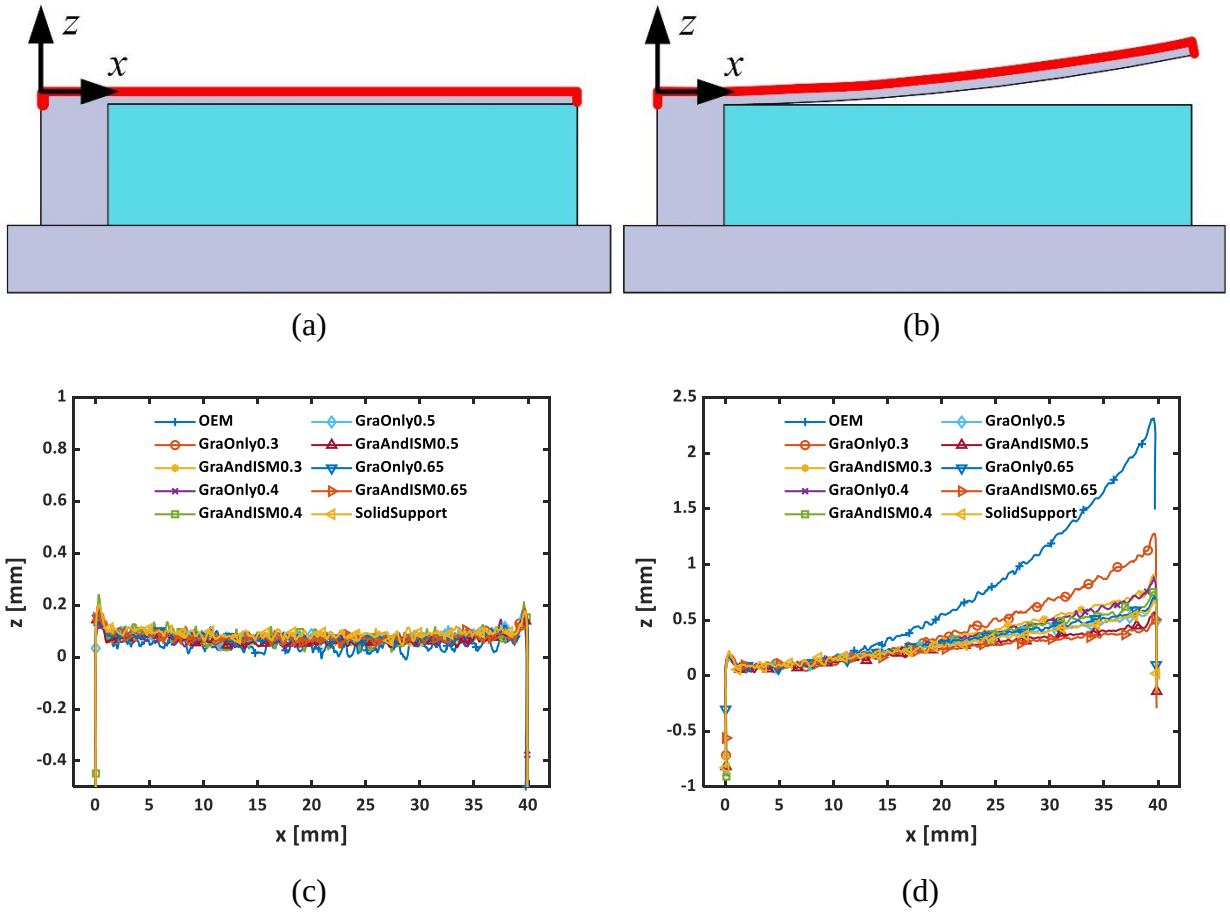

Figure 8.12. Experimental results of the cross-section profiles of all the cantilevers and the data extraction schematics, (a) (c)before cutting, (b) (d) after cutting.

Even though Figure 8.12 has given a summary of the deflections observed before and after cutting, a detailed analysis is required to analyze the deflections in the as-built and after-cutting cantilevers. Results from Figure 8.12c show no major changes on the top surface of the cantilever. However, the side surface (red line in Figure 8.13a) of the cantilevers undergoes shrinkage and has been used to analyze the deformations in the as-built parts. Figure 8.13b,c show the tip profiles (side surface) from the GraOnly and GraAndISM, respectively. Results show the higher deformation in the OEM support while GraAndISM0.65 shows the least deformation. In general, the GraAndISM is better than GraOnly, and the deflections are shown to decrease by increasing the volume fraction of support structures. Moreover, all the GraAndISM cantilevers show similar deformations (~100 µm) in the as-built profiles. This may be due to the support structures in this

group are all strengthened at the tips of the cantilevers, as displayed in Figure 8.7. In addition, the deflection profiles of all the GraAndISM overlap with the solid support profile, which means that GraAndISM leads almost to the most accurate dimensions one can get. Therefore, it can be concluded that the ISM model in the support topology optimization can significantly improve the dimensional accuracy in the x-direction. It should be noted that the deflection in the before-cutting parts also affects the accuracy of the printed parts as it changes the overall dimensions of printed parts (Figure 8.15), which could have a major effect on the performance of these parts and could affect part assemblies with additively manufactured parts.

(a)

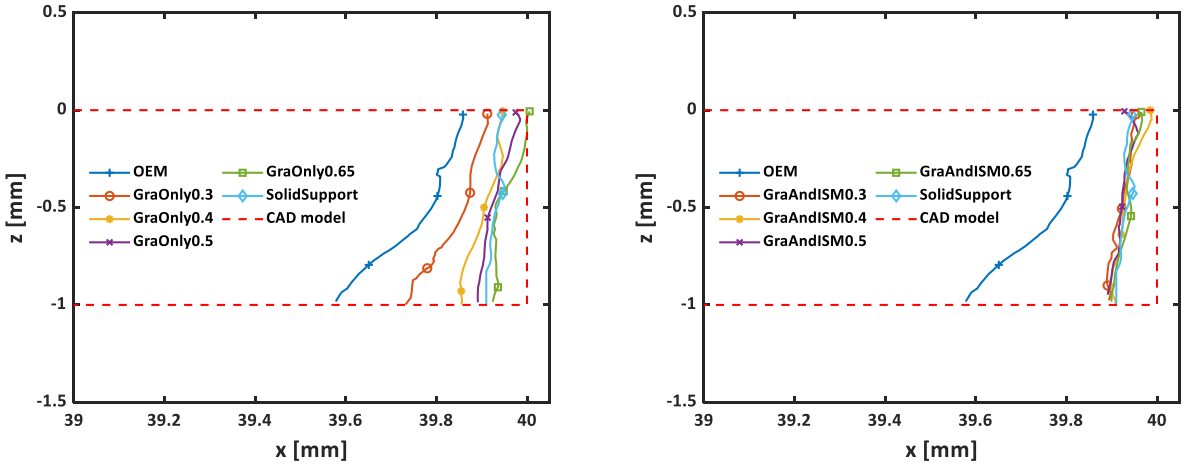

(b) (c)

Figure 8.13. Experimental results of the cross-section profiles of the cantilevers' tips before cutting, (a) GraOnly, (b) GraAndISM.

The side surface provides the perfect measure for evaluating the parts before cutting. However, top surfaces provide the best evidence of after-cutting deflections as it undergoes the most

deformation after cutting. Deflections of the cantilevers (red line in Figure 8.14a) after cutting for GraOnly and GraAndISM are plotted in Figure 8.14b,c, respectively. Results from the GraOnly group (Figure 8.14b) show less deflection than the default OEM support. In addition, the support volume fraction of 0.5 or more results in deflections similar to the full solid support. On the other hand, for the GraAndISM group, all the deflections are smaller than their counterparts with the same volume fraction in the GraOnly group. The reduction in maximum deflections for GraAndISM compared to GraOnly are 28.9%, 11.73%, 15.47%, and 28.09% for the volume fractions of 0.3, 0.4, 0.5, and 0.65 respectively. The deflections in the GraAndISM are, on average, over 20% smaller than those in the GraOnly group and over 44% smaller than the default OEM support. These improvements manifest the advantages of considering the ISM model in the topology optimization of support structures.

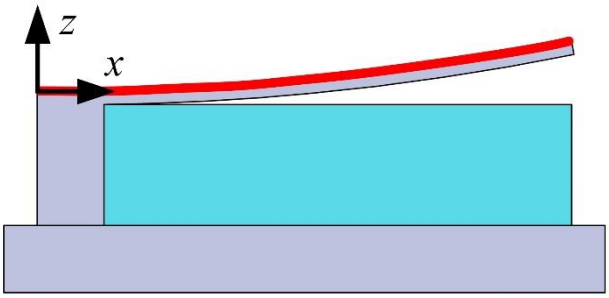

(a)

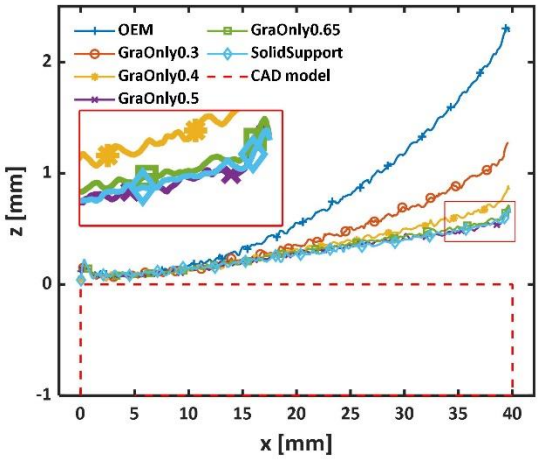

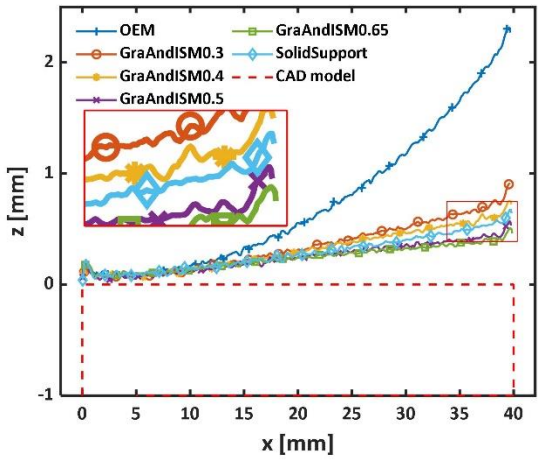

(b) (c)

Figure 8.14. Experimental results of the cross-section profiles of the cantilevers after cutting (a) GraOnly designs, (b) GraAndISM designs.

A summary of the maximum deflections before cutting (side surface) and after cutting (top surface) has been plotted in Figure 8.15a,b, respectively, where Gra and ISM represent GraOnly and GraAndISM respectively. There is a trend that a larger deformation before cutting is most likely to result in a much bigger dimensional change after cutting. The red dash lines indicate the value of the solid support. It should be noted that the reason why the solid support is not optimal could be that there are some cracks at the interface between the solid support and the sub-substrate, as shown in Figure 8.10, which may influence the deflection of the cantilever. Figure 8.15a, b show that increasing the volume fraction of support leads to smaller deflections before and after cutting. The OEM support leads to the maximum deflections. It should be noted that even though

the residual stress is regarded as design independent in Formulation 2 (Section8.2.3), the cantilevers from Formulation 2 (GraAndISM) perform much better than the GraOnly cantilevers.

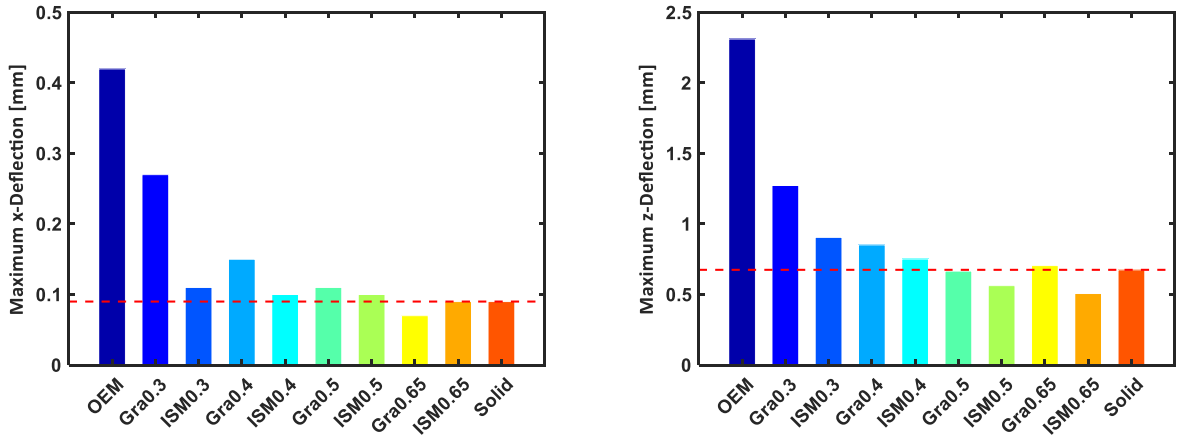

(a) (b)

Figure 8.15. The maximum deflections of different support structures, (a) x-deflections before cutting, (b) z-deflections after cutting, (Gra and ISM represent GraOnly and GraAndISM respectively).

The topologically optimized support structures show a huge reduction in the maximum deflection. However, as the expense of material is a high manufacturing cost in LPBF, a reduction in the material usage for support structures would be of great benefit. Therefore, powder savings based on the different volume fraction were calculated and are presented in Table 8.2 along with the before and after-cutting deflection reductions compared to the OEM support. Even though the GraAndISM0.65 and OEM have the same support structure volume fraction, GraAndISM0.65's deflection is ~78% less than that of the OEM support. On the other hand, GraAndISM0.3 manifests over 60% deflection reduction with over 50% material reduction compared to OEM support. Results indicate that the optimized supports lead to decreased deflections as well as considerable cost savings due to a reduction of support material usage. Therefore, it can be concluded that the experimental results presented in this section highlight the effectiveness of the proposed model.

Table 8.2. Material usage and deflections reduction of optimized supports compared to those of OEM support.

	Material reduction %	Before cut-x reduction %	After cut-z reduction %
OEM	0	0	0
GraOnly0.3	53.85	35.7143	45.8874
GraOnly0.4	38.46	64.2857	62.3377
GraOnly0.5	23.08	73.8095	70.5628
GraOnly0.65	0	83.3333	67.5325
GraAndISM0.3	53.85	73.8095	60.6061
GraAndISM0.4	38.46	76.1905	67.5325
GraAndISM0.5	23.08	76.1905	75.3247
GraAndISM0.65	0	78.5714	77.9221

8.5.2. Deformation comparisons of simulated and experimental results

Validation of the experimental results with the topology optimized support structures confirm the effectiveness of the topology optimization framework presented in this work. However, the ISM model can be further validated by comparing the before and after-cutting simulated and experimental results. Simulated results before and after cutting are shown in Figure 8.16a,b, respectively. Cantilever results before cutting represent similar results with a few hotspots in the GraOnly0.3 and OEM results. On the other hand, simulated results after cutting show the maximum displacement from the OEM support. A more detailed analysis is presented below.

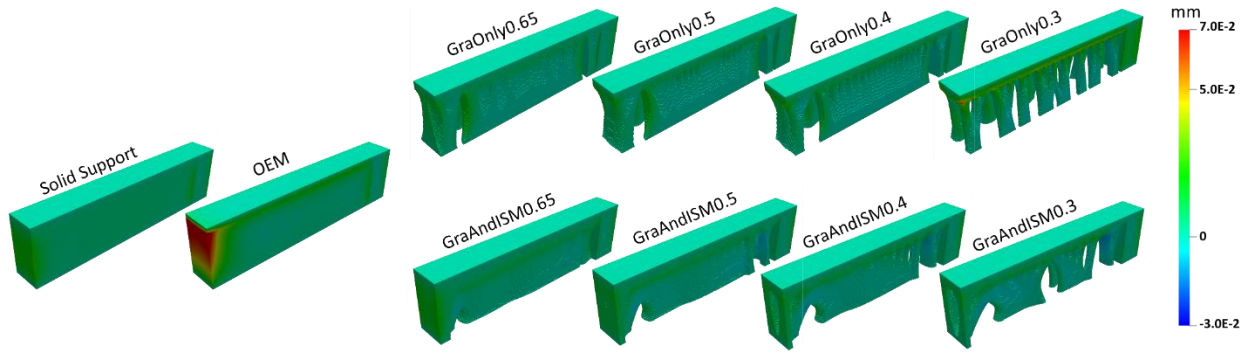

(a)

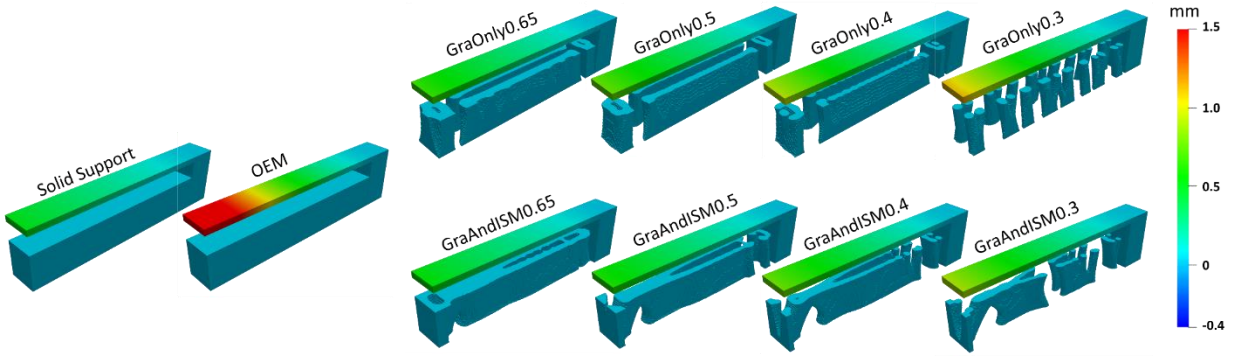

(b)

Figure 8.16. The ISM simulated results of the printed cantilevers for the distortions in the z-direction, (a) before cutting, (b) after cutting. The colors highlight the deformation in the z-direction.

The simulated deformations, as well as the experimental ones, were plotted together in Figure 8.17 and Figure 8.18. As presented previously (Section 8.5.1), since the top surfaces do not undergo major deformation before cutting, side surfaces provide the most applicable way of comparison before cutting. Therefore, Figure 8.17b,c show the before cutting cantilevers' tips (Figure 8.17a) profiles for GraOnly and GraAndISM, respectively, where the OEM support leads to the biggest deformation. Even though the simulated results illustrate a few underestimations of the tips' deformations, the trend is quite comparable. The reason for the underestimations could be that the simulation model does not include shrinkage.

(a)

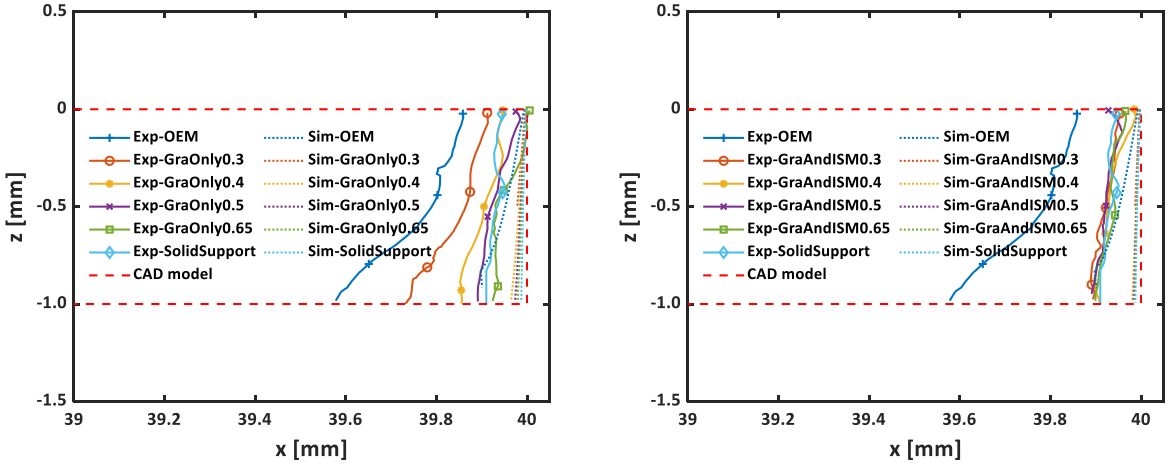

(b) (c)

Figure 8.17. Comparisons of the deformations between the simulated (ISM) and experimental results before cutting, (a) data extraction schematic, (b) GraOnly, (c) GraAndISM.

The simulated results after cutting the support structures are shown in Figure 8.18b,c from the GraOnly and GraAndISM cantilevers, respectively. Results show an excellent prediction of the z-displacement from the GraOnly and GraAndISM cantilevers with a maximum difference of 13% observed in the GraOnly0.65. In addition, an average difference of only 6% is achieved between the experimental and simulated results for the optimized structures.

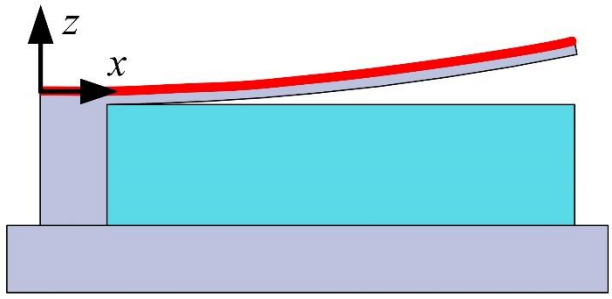

(a)

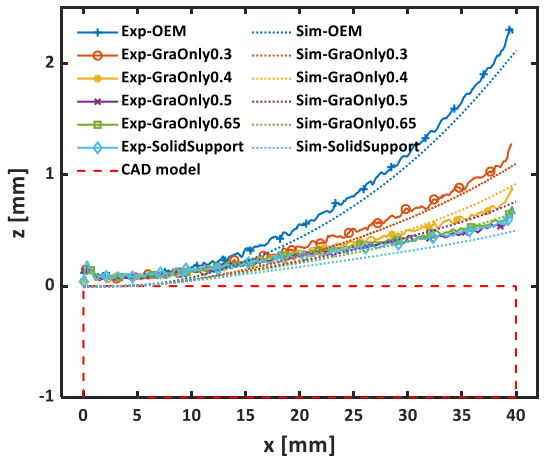

(b)

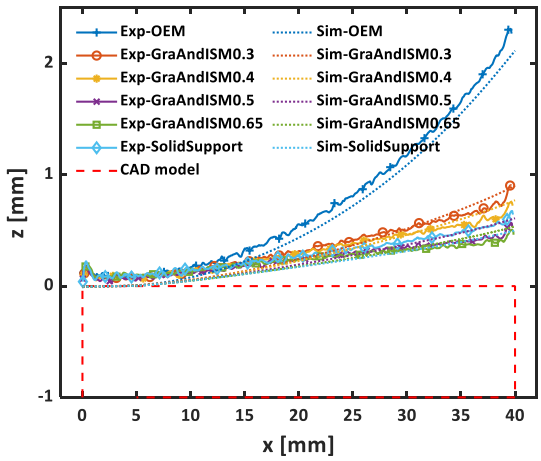

(c)

Figure 8.18. Comparisons of the deformations between the simulated (ISM) and experimental results after cutting, (a) data extraction schematic, (b) GraOnly, (c) GraAndISM.

The maximum x and z deformations from simulations and experiments are listed in Table 8.3. x-deformations are presented for the before cutting, while for the after-cutting conditions, z-direction deformations are presented. Results from the before-cutting cantilevers show a maximum error of 0.32 mm between the experimental and simulated results, while the maximum error from the after-cutting cantilevers was calculated to be 0.23 mm. In general, the top surface (z-direction) from the after-cutting simulations show a much better agreement with the experimental results. The GraOnly simulations show an average error of 9.7%, while the GraAndISM simulations show an average error of 2.57%. Therefore, generally, the ISM model can derive reasonable predictions compared to the experimental results and therefore, can be used to model the LPBF process.

Table 8.3. Comparisons of maximum deformations between simulations and experiments.

	Before cut–x Exp [mm]	Before cut–x Sim [mm]	Error [mm]	After cut–z Exp [mm]	After cut–z Sim [mm]	Error [mm]
OEM	-0.42	-0.1	0.32	2.31	2.08	0.23
GraOnly0.3	-0.27	-0.05	0.22	1.25	1.1	0.15
GraOnly0.4	-0.15	-0.04	0.11	0.87	0.9	0.03
GraOnly0.5	-0.11	-0.03	0.08	0.68	0.75	0.07
GraOnly0.65	-0.07	-0.02	0.05	0.75	0.65	0.1
GraAndISM0.3	-0.11	-0.02	0.09	0.91	0.9	0.01
GraAndISM0.4	-0.1	-0.02	0.08	0.75	0.75	0
GraAndISM0.5	-0.1	-0.02	0.08	0.57	0.6	0.03
GraAndISM0.65	-0.09	-0.01	0.08	0.51	0.53	0.02
SolidSupport	-0.09	-0.01	0.08	0.67	0.5	0.17

8.5.3. Speedup and efficiency of parallelization

The framework presented in this work was parallelized to achieve maximum speedup, as discussed in Section 8.2.5. The GraAndISM0.3 model was executed multiple times with different numbers of cores (32, 64, 128, and 256) to study the effectiveness of the proposed parallelization model. Since the one compute node on the graham (SHARCNET) has 32 cores. Thus, the computing resources for the different conditions can be written as 1 node, 2 nodes, 4 nodes, and 8 nodes. Besides, since the large number of elements (1,843,200) was used in the design domain (Section 0), a single core cannot be used as the benchmark. Therefore, the 32-core results were regarded as the reference when calculating the parallelization speedup and efficiency. The speedup factor S_N can be defined as the ratio of the 32-cores computational time (T_{32}) over the computational time (T_N) obtained with N cores, as shown in Eq.(8.10).

$$S_N = \frac{T_{32}}{T_N} \tag{8.10}$$

As speedup measures the computational gain with increasing processors, efficiency (E_p) measures the fraction of time a processor is utilized and is described as E_p,

$$E_P = \frac{S_N}{N/32} \tag{8.11}$$

Table 8.4 reports the speedup and efficiency of the parallelization module, while Figure 8.19a,b show the speedup and efficiency achieved with the parallelization. The speedup ratio increases with more cores, while the efficiency decreases with more cores used. Compared to the results from 32 cores, the 256 core results show an almost 5 times speedup resulting in 78% reduction of the computational time. However, compared to the ideal speedup ratio, the implementation performed in this work tend to be more divergent and is known as sublinear. This is due to the decreased efficiency of the parallelization (Figure 8.19b). However, efficiency from all runs was calculated to be above 50%. It should be noted that it is crucial to employ parallel computing in the support optimization problem because AM usually has complex geometries of support, which is difficult to be computed with desktops[178]

Table 8.4. Speedup and efficiency of the code parallelization.

Core number	32	64	128	256
Wall clock time (s)	13783	9203	5327	2956
Speedup (S_N)	1	1.50	2.59	4.66
Efficiency (E_P)	1	0.75	0.65	0.58

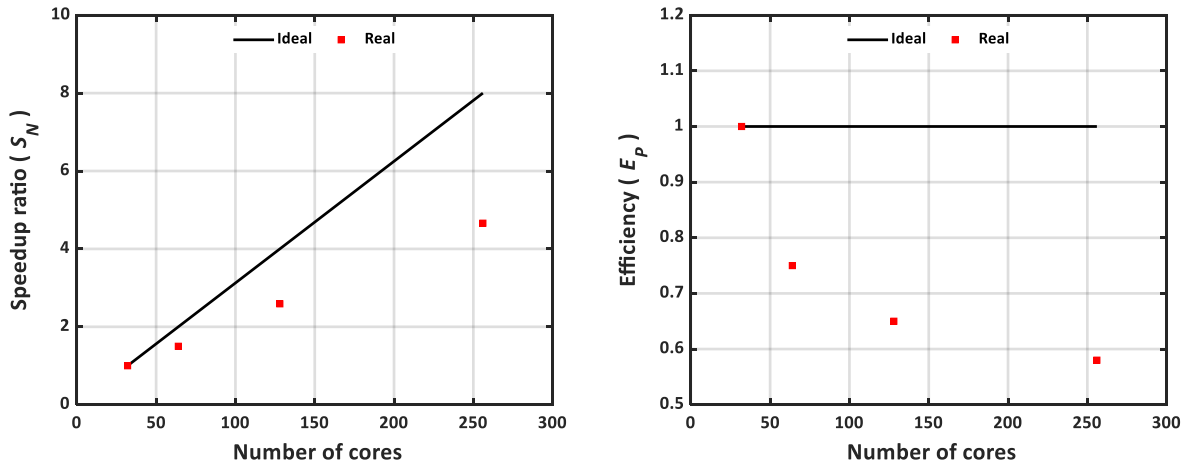

(a)

(b)

Figure 8.19. The visualization of the code parallelization (a) speedup, (b) efficiency.

8.5.4. Further discussions of the proposed formulations

The proposed formulations in Section 8.2 are with as-built conditions, while deflections after cutting are also reduced as displayed in Section 8.5.1. There seems to be a gap between the objective functions and the after-cutting deflections. However, this section will explain why the deflection after cutting can be reduced by the proposed topology optimization formulation 2 compared to formulation 1. With the following explanation, one can find that maximizing the stiffness of the support structure under as-built boundary conditions is equivalent to reducing the deflections of the cantilevers after support removal.

The deflections after cutting are determined by the residual stresses within cantilevers. LPBF is known to induce large residual stresses in printed parts due to the rapid heating and cooling processes[33,37]. Therefore, for investigating the residual stress, an analytical model adapted from the work of Mercelis et al. [33] is proposed to approximate the residual stresses within a combined equilibrated body (part, support, and substrate) as shown in Figure 8.20.

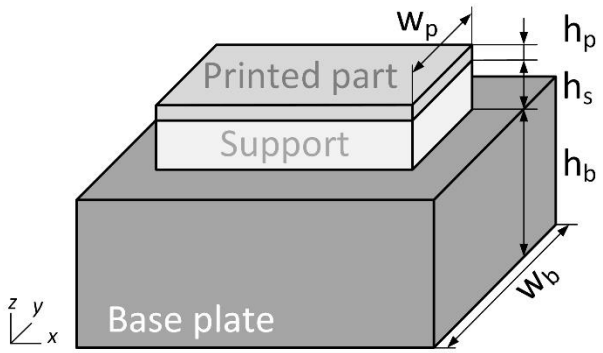

Figure 8.20. Schematic of the combined part-support-substrate equilibrated body.

The derivation of the analytical model has been presented in Appendix B. Then, the analytical model was used in analyzing the influence of the support stiffness (Young's modulus) on the printed part deflection. Figure 8.21 displays the resulting residual stress profiles in the part, support, and substrate with several assumed values of parameters: three different support Young's modulus, 30 GPa, 70 GPa, and 110 GPa; Young's modulus of the printed part is assumed to be 110 GPa,

and that of the substrate is 210 GPa; the printed part w_p is assumed to be equal to w_s and half the width of the substrate w_b; the yield stress of the printed part is 300 MPa; l is 50 μm, h_b is 20 mm, h_s is 5 mm, and h_p is 2 mm.

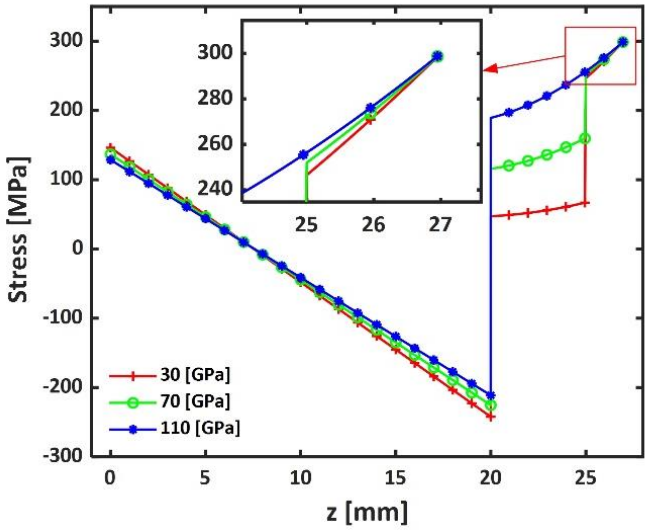

Figure 8.21. Residual stress distributions from the part-support-substrate combined bending theory.

Figure 8.22 depicts the schematic of the bending moment within the printed part. The straight lines are corresponding to the stress distributions in the zoomed-in plot of Figure 8.21. Therefore, it can be clearly seen that the stiffness of the support can determine the bending moment in the LPBF parts. The stiffer support (blue line, 110 GPa) leads to a lower bending moment than softer support (red line, 30 GPa).

Until now, the supports have not been removed yet. In other words, this is under an as-built condition. When the supports are removed, the bending moment will induce deflections of the printed part based on the analytical beam bending deflection theory [243] as follows,

$$v_{max} = \frac{M \cdot L^2}{2EI} \tag{8.12}$$

where M is the bending moment, L is the length, E is Young's modulus of the cantilever, I is the area moment of inertia, the deflection is proportional to the bending moment.

Therefore, the stiffer support (110 GPa) under the as-built condition will lead to smaller deflection after support removal than the softer support (30 GPa). In other words, the formulations mentioned in previous sections, which are at the as-built condition, can reduce the deflections of the LPBF printed parts after support removal. The gap between the target that is to reduce deflections after support removal and the optimization formulations has been fulfilled.

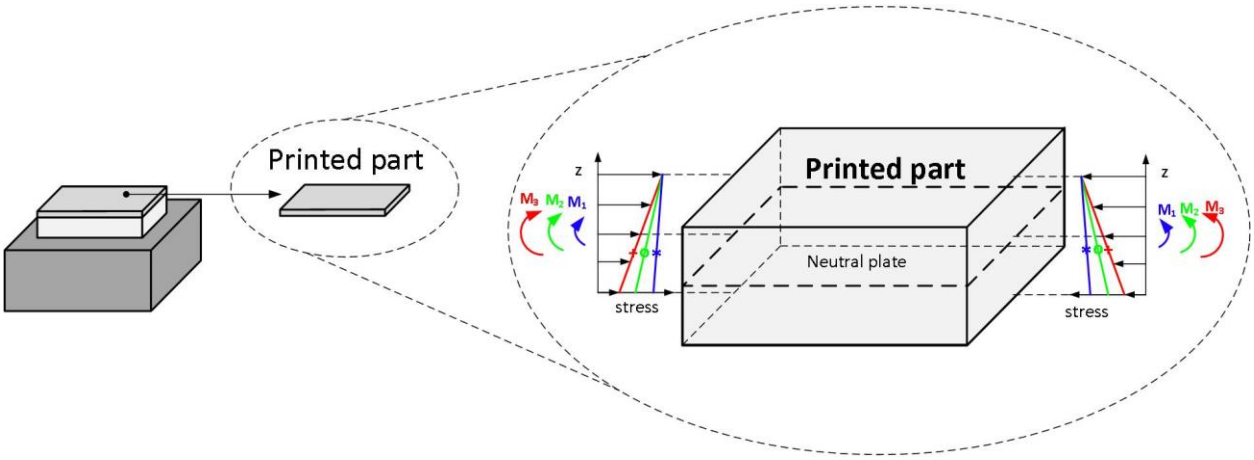

Figure 8.22. Schematic of the bending moment derived with the different support-structure stiffnesses.

In the proposed formulations, Formulation 2 (GraAndISM) considers residual stress and can generate stiffer support structures than Formulation 1 (GraOnly) does under residual stress. Therefore, Formulation 2 subsequently ends up with less bending moment as well as less after-cutting deflections based on the above discussions. Table 8.5 lists the bending moment of different support structures, which is derived from ISM. It can be found that the GraAndISM cantilevers do induce less bending moment than their counterparts of GraOnly, and thus, will have smaller deflections based on Eq. (8.12). Therefore, maximizing the stiffness of the support structure under the residual stress with the as-built boundary conditions is equivalent to reducing the deflections of the cantilevers after support removal.

Table 8.5. Summary of the bending moments on the cantilevers with different support structures.

	Bending moment-*M* [N·m]
OEM	0.2535
GraOnly0.3	0.2326
GraOnly0.4	0.0998
GraOnly0.5	0.0728
GraOnly0.65	0.0618
GraAndISM0.3	0.1215
GraAndISM0.4	0.0989
GraAndISM0.5	0.0685
GraAndISM0.65	0.0541
SolidSupport	0.0436

8.6. Summary

A density-based topology optimization model is presented to design support structures with improved mechanical performances for LPBF. The model is implemented on a parallel-computing framework and includes the Inherent Strain Method (ISM) to model the residual stresses and deflections in LPBF. The objective of this work is to design stiffer support structures to reduce the deflections in printed parts under both the gravity load and the LPBF residual stress load. The main conclusions are as follows,

1. The proposed model was used to design optimized cantilever support structures under only gravity (GraOnly) and gravity combined with residual stress (GraAndISM) loading conditions. The optimized supports were manufactured and compared to commercial OEM support structures. The optimized support structures show much smaller deflections before and after support removal. The deflections in the GraAndISM situations were, on average, 20% smaller than those in the GraOnly situations and over 44% smaller than that of OEM default support. Especially, GraAndISM0.65 has the same material usage as OEM but achieves over 78% reduction compared to OEM. On the other hand, GraAndISM0.3 leads

to over 60% deflection reduction as well as over 50% material usage reduction compared to OEM.

2. Besides generating the residual stresses for the topology optimization model, the ISM model was also employed in predicting the deflections of the printed cantilevers. The predicted deflections are comparable to the experimental results for both before and after-cutting situations. Results show an average of only 6% error between the experimental and simulated results for the after-cutting situations.
3. A semi-analytical model based on the beam bending theory is proposed for predicting the cantilever deflections. The semi-analytical model results are comparable with those from experiments but show more deviation than the ISM results.
4. The proposed parallel topology optimization model has been implemented on multiple computational nodes and shows a computational advantage of almost 5 times over a single node.

Future work is to consider the ISM into the loop of topology optimization.

Chapter 9. Conclusions and Future Work

9.1. Conclusions

In this work, a coupled topology optimization and process simulation system was proposed for dealing with the challenges and opportunities of the LPBF process. The system mainly includes a 3-dimensional heat transfer model to study the effect of process parameters on printed LPBF parts and an ISM-based topology optimization model to reduce the deformation in LPBF parts. In addition, the proposed system also includes several supplementary modules, post-processing techniques, performance simulation, and LPBF process simulation. As a demonstration, a parallel computing framework of the proposed system was used to optimize the support structures resulting in reductions of the as-built and after-cut deflections in printed parts.

According to the developed system and associated experimental results, the following conclusions can be drawn:

1. The proposed methodology is useful and valid. Experiments have verified material-usage reduction and structural design effectiveness of topology optimization.
2. In the post-processing, the mesh quality of topology optimization results can be improved by mesh smoothing, which may minimize manual work of model preparation for performance simulation.
3. The performance simulation is for predicting the behaviors of the topologically optimized under working conditions. The predicted behaviors of the topologically optimized parts are validated by the experimental results, such as correctly predicting the breakage locations.
4. The process simulation includes a 3-dimensional heat transfer model, an actual-scan model, domain-by-domain model, and ISM model. In the 3-dimensional heat transfer model, the expressions of varied anisotropically enhanced thermal conductivity and varied

absorptivity were linear algebraic equations. Good agreement between the simulation and the experimental results was derived. The averaged error of melt pool width and depth are 2.9% and 7.3%, respectively.

5. The 3-dimensional heat transfer model has been further validated by the surface features—track stability and ripple angle. For track stability, the predicted results are in good agreement with the experimental results. In addition, the simulated ripple angles are within the range of experimental results.

6. Using the combined parameter $P/\sqrt{v}$ shows that layer thickness has a minor effect on the melt pool dimensions when between 6-8 W/ √(mm/s). In other words, within this range, it is possible to use 40 μm layer thickness to accelerate the building rate while not losing quality.

7. The ISM model, which is based on elastic FEM, is one of the most suitable methods for part-level simulation because it reduces the computational time from months to minutes in comparison with the other models (actual-scan model and domain-by-domain activation model).

8. The proposed framework of parallel-computing support topology optimization was used to design optimized cantilever support structures. The optimized supports were manufactured and compared to commercial OEM support structures. The optimized support structures can lead to over 60% deflection reduction as well as over 50% material usage reduction compared to OEM.

9. The ISM model was also employed in predicting the deflections of the printed cantilevers. Results show an average of only 6% error between the experimental and simulated results for the after-cutting situations.

10. The proposed parallel topology optimization framework has been implemented on multiple computational nodes while providing a computational advantage of almost 5 times over a single node.

9.2. Future work

In the future, several extensions of this work can be done.

1. The coupled system is just at a preliminary stage, and more work may need to be done. For example, non-shrinking methods, such as the scale-dependent umbrella operator, should be considered in the future.
2. The actual-scan method and domain-by-domain heat-input method of the LPBF process modeling can be further fulfilled by including the adaptive mesh, using HPC, and comprehensively being validated by experiment.
3. ISM could be further refined by including the elasto-plastic module and considering different inherent strains for different scans, layers, or domains. In addition, further experimental validations would be helpful. Moreover, acceleration computational techniques, eg. HPC and adaptive mesh, should be considered in order to help incorporate ISM into each loop of topology optimization.
4. For topology optimization for LPBF, several manufacturing constraints mentioned in the literature can be incorporated and integrated as a combine design system, e.g. minimum feature size control, cavity constraint, overhang constraints, and so on.
5. Guidelines for structural optimization for LPBF should be developed. Structural optimization for LPBF needs a variety of different knowledge from structural design to process optimization. It should be significantly beneficial that one can generate guidelines for structural optimization for LPBF based on several trial-and-errors based on both experiments and simulations.

Letter of Copyright Permission

Title: 3-Dimensional heat transfer modeling for laser powder-bed fusion additive manufacturing with volumetric heat sources based on varied thermal conductivity and absorptivity

Author: Zhidong Zhang,Yuze Huang,Adhitan Rani Kasinathan,Shahriar Imani Shahabad,Usman Ali,Yahya Mahmoodkhani,Ehsan Toyserkani

Publication: Optics & Laser Technology

Publisher: Elsevier

Date: January 2019

Logged in as:
Zhidong Zhang
LOGOUT

Please note that, as the author of this Elsevier article, you retain the right to include it in a thesis or dissertation, provided it is not published commercially. Permission is not required, but please ensure that you reference the journal as the original source. For more information on this and on your other retained rights, please visit: https://www.elsevier.com/about/our-business/policies/copyright#Author-rights

References

[1] Gibson I, Rosen DW, Stucker B. Additive Manufacturing Technologies (Vol. 17). New York: Springer; 2014.

[2] Rosen D. Design for Additive Manufacturing: Past, Present, and Future Directions. J Mech Des 2014;136:90301. https://doi.org/10.1115/1.4028073.

[3] Wohlers T. Wohlers Report 2013: Additive Manufacturing and 3D Printing State of the Industry–Annual Worldwide Progress Report, Wohlers Associates. Fort Collins, CO 2013.

[4] Dzhendov D, Dikova T. Application of Selective Laser Melting in Manufacturing of Fixed Dental 2016;22:1414–7.

[5] GE. The FAA Cleared The First 3D Printed Part To Fly In A Commercial Jet Engine From GE n.d. http://www.gereports.com/post/116402870270/the-faa-cleared-the-first-3d-printed-part-to-fly/.

[6] EOS GmbH. EADS and EOS – Study Demonstrates Savings Potential for DMLS in the Aerospace Industry. 2015. https://www.eos.info/press/customer_case_studies/eads.

[7] Zeng K, Pal D, Teng C, Stucker BE. Evaluations of effective thermal conductivity of support structures in selective laser melting. Addit Manuf 2015;6:67–73. https://doi.org/10.1016/j.addma.2015.03.004.

[8] Hussein A, Hao L, Yan C, Everson R, Young P. Advanced lattice support structures for metal additive manufacturing. J Mater Process Technol 2013;213:1019–26. https://doi.org/10.1016/j.jmatprotec.2013.01.020.

[9] Vranchen B. Study of Residual Stresses in Selective Laser Melting. 2016.

[10] Luo Z, Zhao Y. A survey of finite element analysis of temperature and thermal stress fields in powder bed fusion Additive Manufacturing. Addit Manuf 2018;21:318–32. https://doi.org/10.1016/j.addma.2018.03.022.

[11] Aboulkhair NT, Everitt NM, Ashcroft I, Tuck C. Reducing porosity in AlSi10Mg parts processed by selective laser melting. Addit Manuf 2014;1–4:77–86. https://doi.org/10.1016/J.ADDMA.2014.08.001.

[12] Teng C, Gong H, Szabo A, Dilip JJS, Ashby K, Zhang S, et al. Simulating Melt Pool Shape and Lack of Fusion Porosity for Selective Laser Melting of Cobalt Chromium Components. J Manuf Sci Eng 2016;139:011009. https://doi.org/10.1115/1.4034137.

[13] Edwards P, Ramulu M. Fatigue performance evaluation of selective laser melted Ti–6Al–4V. Mater Sci Eng A 2014;598:327–37. https://doi.org/10.1016/J.MSEA.2014.01.041.

[14] Buchbinder D, Meiners W, Pirch N, Wissenbach K, Schrage J. Investigation on reducing distortion by preheating during manufacture of aluminum components using selective laser melting. J Laser Appl 2014;26:012004. https://doi.org/10.2351/1.4828755.

[15] Kempen K, Vrancken B, Buls S, Thijs L, Van Humbeeck J, Kruth JP. Selective Laser Melting of Crack-Free High Density M2 High Speed Steel Parts by Baseplate Preheating. J

Manuf Sci Eng Trans ASME 2014;136:61026. https://doi.org/10.1115/1.4028513.
[16] Shipley H, McDonnell D, Culleton M, Coull R, Lupoi R, O'Donnell G, et al. Optimisation of process parameters to address fundamental challenges during selective laser melting of Ti-6Al-4V: A review. Int J Mach Tools Manuf 2018;128:1–20. https://doi.org/10.1016/J.IJMACHTOOLS.2018.01.003.
[17] Tsopanos S, Mines RAW, McKown S, Shen Y, Cantwell WJ, Brooks W, et al. The Influence of Processing Parameters on the Mechanical Properties of Selectively Laser Melted Stainless Steel Microlattice Structures. J Manuf Sci Eng 2010;132:041011. https://doi.org/10.1115/1.4001743.
[18] Keshavarzkermani A, Sadowski M, Ladani L. Direct metal laser melting of Inconel 718: Process impact on grain formation and orientation. J Alloys Compd 2018;736:297–305. https://doi.org/10.1016/j.jallcom.2017.11.130.
[19] Ali H, Ghadbeigi H, Mumtaz K. Residual stress development in selective laser-melted Ti6Al4V: a parametric thermal modelling approach. Int J Adv Manuf Technol 2018;97:2621–33. https://doi.org/10.1007/s00170-018-2104-9.
[20] King WE, Anderson AT, Ferencz RM, Hodge NE, Kamath C, Khairallah SA, et al. Laser powder bed fusion additive manufacturing of metals; physics, computational, and materials challenges. Appl Phys Rev 2015;2:041304. https://doi.org/10.1063/1.4937809.
[21] Khairallah SA, Anderson A. Mesoscopic simulation model of selective laser melting of stainless steel powder. J Mater Process Tech 2014;214:2627–36. https://doi.org/10.1016/j.jmatprotec.2014.06.001.
[22] DebRoy T, Wei HL, Zuback JS, Mukherjee T, Elmer JW, Milewski JO, et al. Additive manufacturing of metallic components – Process, structure and properties. Prog Mater Sci 2018;92:112–224. https://doi.org/10.1016/j.pmatsci.2017.10.001.
[23] Plessis A du, Broeckhoven C, Yadroitsava I, Yadroitsev I, Hands CH, Kunju R, et al. Beautiful and Functional: A Review of Biomimetic Design in Additive Manufacturing. Addit Manuf 2019;27:408–27. https://doi.org/10.1016/j.addma.2019.03.033.
[24] Fayazfar H, Salarian M, Rogalsky A, Sarker D, Russo P, Paserin V, et al. A critical review of powder-based additive manufacturing of ferrous alloys: Process parameters, microstructure and mechanical properties. Mater Des 2018;144:98–128. https://doi.org/10.1016/j.matdes.2018.02.018.
[25] SLM. 3D-PRINTING TECHNOLOGY IN DENTAL INDUSTRY n.d. https://slm-solutions.com/medical-and-dental.
[26] Farinia Group. How Metal Additive Manufacturing Improves Common Types of Medical Implants n.d. http://www.farinia.com/additive-manufacturing/industrial-3d/metal-additive-manufacturing-improves-common-medical-implants.
[27] SLM. Individual hip implant in titanium n.d. https://slm-solutions.com/products/accessories-and-consumables/slm-metal-powder.
[28] King WE, Barth HD, Castillo VM, Gallegos GF, Gibbs JW, Hahn DE, et al. Observation of

keyhole-mode laser melting in laser powder-bed fusion additive manufacturing. J Mater Process Technol 2014;214:2915–25. https://doi.org/10.1016/j.jmatprotec.2014.06.005.

[29] Darvish K, Chen ZW, Pasang T. Reducing lack of fusion during selective laser melting of CoCrMo alloy: Effect of laser power on geometrical features of tracks. Mater Des 2016;112:357–66. https://doi.org/10.1016/J.MATDES.2016.09.086.

[30] Li R, Liu J, Shi Y, Wang L, Jiang W. Balling behavior of stainless steel and nickel powder during selective laser melting process. Int J Adv Manuf Technol 2012;59:1025–35. https://doi.org/10.1007/s00170-011-3566-1.

[31] Mahmoodkhani Y, Ali U, Liravi F, Esmaeilizadeh R, Marzbanrad E. Determination of the Most Contributing Laser Powder Bed Fusion Process Parameters on the Surface Roughness Quality of Hastelloy X Components. Glob. Power Propuls. Soc., Montreal: 2018, p. 1–8.

[32] Mertens R, Clijsters S, Kempen K, Kruth J-P. Optimization of Scan Strategies in Selective Laser Melting of Aluminum Parts With Downfacing Areas. J Manuf Sci Eng 2014;136:061012. https://doi.org/10.1115/1.4028620.

[33] Mercelis P, Kruth J. Residual stresses in selective laser sintering and selective laser melting. Rapid Prototyp J 2006;12:254–65. https://doi.org/10.1108/13552540610707013.

[34] Marchese G, Basile G, Bassini E, Aversa A, Lombardi M, Ugues D, et al. Study of the microstructure and cracking mechanisms of hastelloy X produced by laser powder bed fusion. Materials (Basel) 2018;11. https://doi.org/10.3390/ma11010106.

[35] Withers PJ, Bhadeshia HKDH. Residual stress. Part 2 – Nature and origins. Mater Sci Technol 2001;17:366–75. https://doi.org/10.1179/026708301101510087.

[36] Bartlett JL, Li X. An overview of residual stresses in metal powder bed fusion. Addit Manuf 2019;27:131–49. https://doi.org/10.1016/j.addma.2019.02.020.

[37] Parry L, Ashcroft IA, Wildman RD. Understanding the effect of laser scan strategy on residual stress in selective laser melting through thermo-mechanical simulation. Addit Manuf 2016;12:1–15. https://doi.org/10.1016/j.addma.2016.05.014.

[38] Strantza M, Vrancken B, Prime MB, Truman CE, Rombouts M, Brown DW, et al. Directional and oscillating residual stress on the mesoscale in additively manufactured Ti-6Al-4V. Acta Mater 2019;168:299–308. https://doi.org/10.1016/J.ACTAMAT.2019.01.050.

[39] Edwards P, Ramulu M. Fatigue performance evaluation of selective laser melted Ti–6Al–4V. Mater Sci Eng A 2014;598:327–37. https://doi.org/10.1016/J.MSEA.2014.01.041.

[40] Cain V, Thijs L, Van Humbeeck J, Van Hooreweder B, Knutsen R. Crack propagation and fracture toughness of Ti6Al4V alloy produced by selective laser melting. Addit Manuf 2015;5:68–76. https://doi.org/10.1016/J.ADDMA.2014.12.006.

[41] Schajer GS. Practical residual stress measurement methods. John Wiley & Sons; 2013.

[42] Levkulich NC, Semiatin SL, Gockel JE, Middendorf JR, DeWald AT, Klingbeil NW. The effect of process parameters on residual stress evolution and distortion in the laser powder bed fusion of Ti-6Al-4V. Addit Manuf 2019;28:475–84.

https://doi.org/10.1016/j.addma.2019.05.015.
[43] Vrancken B, Cain V, Knutsen R, Van Humbeeck J. Residual stress via the contour method in compact tension specimens produced via selective laser melting. Scr Mater 2014;87:29–32. https://doi.org/10.1016/J.SCRIPTAMAT.2014.05.016.
[44] López C, Elías-Zúñiga A, Jiménez I, Martínez-Romero O, Siller HR, Diabb JM. Experimental Determination of Residual Stresses Generated by Single Point Incremental Forming of AlSi10Mg Sheets Produced Using SLM Additive Manufacturing Process. Materials (Basel) 2018;11:2542. https://doi.org/10.3390/ma11122542.
[45] Mishurova T, Cabeza S, Artzt K, Haubrich J, Klaus M, Genzel C, et al. An assessment of subsurface residual stress analysis in SLM Ti-6Al-4V. Materials (Basel) 2017;10. https://doi.org/10.3390/ma10040348.
[46] Brown DW, Bernardin JD, Carpenter JS, Clausen B, Spernjak D, Thompson JM. Neutron diffraction measurements of residual stress in additively manufactured stainless steel. Mater Sci Eng A 2016;678:291–8. https://doi.org/10.1016/j.msea.2016.09.086.
[47] Phan TQ, Strantza M, Hill MR, Gnaupel-Herold TH, Heigel J, D'Elia CR, et al. Elastic Residual Strain and Stress Measurements and Corresponding Part Deflections of 3D Additive Manufacturing Builds of IN625 AM-Bench Artifacts Using Neutron Diffraction, Synchrotron X-Ray Diffraction, and Contour Method. Integr Mater Manuf Innov 2019. https://doi.org/10.1007/s40192-019-00149-0.
[48] Syed AK, Ahmad B, Guo H, Machry T, Eatock D, Meyer J, et al. An experimental study of residual stress and direction-dependence of fatigue crack growth behaviour in as-built and stress-relieved selective-laser-melted Ti6Al4V. Mater Sci Eng A 2019;755:246–57. https://doi.org/10.1016/j.msea.2019.04.023.
[49] Deng D, Peng RL, Brodin H, Moverare J. Microstructure and mechanical properties of Inconel 718 produced by selective laser melting: Sample orientation dependence and effects of post heat treatments. Mater Sci Eng A 2018;713:294–306. https://doi.org/10.1016/j.msea.2017.12.043.
[50] Ali H, Ghadbeigi H, Mumtaz K. Effect of scanning strategies on residual stress and mechanical properties of Selective Laser Melted Ti6Al4V. Mater Sci Eng A 2018;712:175–87. https://doi.org/10.1016/J.MSEA.2017.11.103.
[51] Rozvany GIN. Aims, scope, methods, history and unified terminology of computer-aided topology optimization in structural mechanics [J]. Struct Multidiscip Optim 2001;21:90–108. https://doi.org/10.1007/s00158-002-0245-8.
[52] Rozvany GIN, Prager W. A new class of structural optimization problems: Optimal archgrids. Comput Methods Appl Mech Eng 1979;19:127–50. https://doi.org/10.1016/0045-7825(79)90038-0.
[53] Bendsoe M. Methods for optimization of structural topology, shape and material. Springer Verlag, New York 1995.
[54] Bendsoe MP, Sigmund O. Topology optimization: theory, methods and applications.

Springer; 2003.
[55] Sigmund O. Introductory Lecture of Topology Optimization. 2011.
[56] Tomlin M, Meyer J. Topology Optimization of an Additive Layer Manufactured (ALM) Aerospace Part. 7th Altair CAE Technol Conf 2011 2011:1–9.
[57] Kaufmann M. Cost Optimization of Aircraft Structures. Royal Institute of Technology, 2009. https://doi.org/urn:nbn:se:kth:diva-11482.
[58] Rosenthal D. The Theory of Moving Source of Heat and its Application to Metal Transfer. ASME Trans 1946;43:849–66.
[59] Eagar T, TSAI N-S. Temperature Fields Produced by Traveling Distributed Heat Sources Use of a Gaussian heat distribution in dimensionless form indicates final weld pool shape can be predicted accurately for many welds and materials. Weld J (Miami, Fla) 1983;62.
[60] Huang Y, Khamesee MB, Toyserkani E. A comprehensive analytical model for laser powder-fed additive manufacturing. Addit Manuf 2016;12:90–9. https://doi.org/10.1016/j.addma.2016.07.001.
[61] Yang Y, Ayas C. Point, surface and volumetric heat sources in the thermal modelling of selective laser melting. AIP Conf Proc 2017;1896. https://doi.org/10.1063/1.5008032.
[62] Yang Y, Knol MF, van Keulen F, Ayas C. A semi-analytical thermal modelling approach for selective laser melting. Addit Manuf 2018;21:284–97. https://doi.org/10.1016/j.addma.2018.03.002.
[63] Ning J, Mirkoohi E, Dong Y, Sievers DE, Garmestani H, Liang SY. Analytical modeling of 3D temperature distribution in selective laser melting of Ti-6Al-4V considering part boundary conditions. J Manuf Process 2019;44:319–26. https://doi.org/10.1016/j.jmapro.2019.06.013.
[64] Kamat AM, Pei Y. An analytical method to predict and compensate for residual stress-induced deformation in overhanging regions of internal channels fabricated using powder bed fusion. Addit Manuf 2019;29:100796. https://doi.org/10.1016/J.ADDMA.2019.100796.
[65] Afazov S, Denmark WAD, Lazaro Toralles B, Holloway A, Yaghi A. Distortion prediction and compensation in selective laser melting. Addit Manuf 2017;17:15–22. https://doi.org/10.1016/j.addma.2017.07.005.
[66] Gusarov A V., Yadroitsev I, Bertrand P, Smurov I. Model of Radiation and Heat Transfer in Laser-Powder Interaction Zone at Selective Laser Melting. J Heat Transfer 2009;131:072101. https://doi.org/10.1115/1.3109245.
[67] Zhao C, Fezzaa K, Cunningham RW, Wen H, De Carlo F, Chen L, et al. Real-time monitoring of laser powder bed fusion process using high-speed X-ray imaging and diffraction. Sci Rep 2017;7:1–11. https://doi.org/10.1038/s41598-017-03761-2.
[68] Matthews MJ, Guss G, Khairallah SA, Rubenchik AM, Depond PJ, King WE. Denudation of metal powder layers in laser powder bed fusion processes. Acta Mater 2016;114:33–42. https://doi.org/10.1016/j.actamat.2016.05.017.

[69] Panwisawas C, Qiu C, Anderson MJ, Sovani Y, Turner RP, Attallah MM, et al. Mesoscale modelling of selective laser melting: Thermal fluid dynamics and microstructural evolution. Comput Mater Sci 2017;126:479–90. https://doi.org/10.1016/j.commatsci.2016.10.011.

[70] Bidare P, Bitharas I, Ward RM, Attallah MM, Moore AJ. Fluid and particle dynamics in laser powder bed fusion. Acta Mater 2018;142:107–20. https://doi.org/10.1016/j.actamat.2017.09.051.

[71] Bayat M, Mohanty S, Hattel JH. A systematic investigation of the effects of process parameters on heat and fluid flow and metallurgical conditions during laser-based powder bed fusion of Ti6Al4V alloy. Int J Heat Mass Transf 2019;139:213–30. https://doi.org/10.1016/J.IJHEATMASSTRANSFER.2019.05.017.

[72] Bayat M, Mohanty S, Hattel JH. Multiphysics modelling of lack-of-fusion voids formation and evolution in IN718 made by multi-track/multi-layer L-PBF. Int J Heat Mass Transf 2019;139:95–114. https://doi.org/10.1016/J.IJHEATMASSTRANSFER.2019.05.003.

[73] Yan W, Ge W, Qian Y, Lin S, Zhou B, Liu WK, et al. Multi-physics modeling of single/multiple-track defect mechanisms in electron beam selective melting. Acta Mater 2017;134:324–33. https://doi.org/10.1016/j.actamat.2017.05.061.

[74] Khairallah SA, Anderson AT, Rubenchik A, King WE. Laser powder-bed fusion additive manufacturing: Physics of complex melt flow and formation mechanisms of pores, spatter, and denudation zones. Acta Mater 2016;108:36–45. https://doi.org/10.1016/j.actamat.2016.02.014.

[75] Körner C, Attar E, Heinl P. Mesoscopic simulation of selective beam melting processes. J Mater Process Technol 2011;211:978–87. https://doi.org/10.1016/j.jmatprotec.2010.12.016.

[76] Körner C, Bauereiß A, Attar E. Fundamental consolidation mechanisms during selective beam melting of powders. Model Simul Mater Sci Eng 2013;21. https://doi.org/10.1088/0965-0393/21/8/085011.

[77] Xia M, Gu D, Yu G, Dai D, Chen H, Shi Q. Porosity evolution and its thermodynamic mechanism of randomly packed powder-bed during selective laser melting of Inconel 718 alloy. Int J Mach Tools Manuf 2017;116:96–106. https://doi.org/10.1016/j.ijmachtools.2017.01.005.

[78] Masoomi M, Pegues JW, Thompson SM, Shamsaei N. A numerical and experimental investigation of convective heat transfer during laser-powder bed fusion. Addit Manuf 2018;22:729–45. https://doi.org/10.1016/j.addma.2018.06.021.

[79] Boley CD, Khairallah SA, Rubenchik AM. Calculation of laser absorption by metal powders in additive manufacturing. Appl Opt 2015;54:2477. https://doi.org/10.1364/AO.54.002477.

[80] Bandyopadhyay A, Traxel KD. Invited review article: Metal-additive manufacturing—Modeling strategies for application-optimized designs. Addit Manuf 2018;22:758–74. https://doi.org/10.1016/j.addma.2018.06.024.

[81] Zinovieva O, Zinoviev A, Ploshikhin V. Three-dimensional modeling of the microstructure evolution during metal additive manufacturing. Comput Mater Sci 2018;141:207–20. https://doi.org/10.1016/J.COMMATSCI.2017.09.018.

[82] Koepf JA, Gotterbarm MR, Markl M, Körner C. 3D multi-layer grain structure simulation of powder bed fusion additive manufacturing. Acta Mater 2018;152:119–26. https://doi.org/10.1016/J.ACTAMAT.2018.04.030.

[83] Foroozmehr A, Badrossamay M, Foroozmehr E, Golabi S. Finite Element Simulation of Selective Laser Melting process considering Optical Penetration Depth of laser in powder bed. Mater Des 2016;89:255–63. https://doi.org/10.1016/j.matdes.2015.10.002.

[84] Goldak J, Chakravarti A, Bibby M. New Finite Element Model for Welding Heat Sources. Metall Trans B, Process Metall 1984;15 B:299–305. https://doi.org/10.1007/BF02667333.

[85] Bruna-Rosso C, Demir AG, Previtali B. Selective Laser Melting Finite Element Modeling: Validation with High-Speed Imaging and Lack of Fusion Defects Prediction. Mater Des 2018. https://doi.org/10.1016/j.matdes.2018.06.037.

[86] Wu CS, Wang HG, Zhang YM. A new heat source model for keyhole plasma arc welding in FEM analysis of the temperature profile. Weld J (Miami, Fla) 2006;85:284–91.

[87] Tran HC, Lo YL. Heat transfer simulations of selective laser melting process based on volumetric heat source with powder size consideration. J Mater Process Technol 2018;255:411–25. https://doi.org/10.1016/j.jmatprotec.2017.12.024.

[88] Ladani L, Romano J, Brindley W, Burlatsky S. Effective liquid conductivity for improved simulation of thermal transport in laser beam melting powder bed technology. Addit Manuf 2017;14:13–23. https://doi.org/10.1016/j.addma.2016.12.004.

[89] Liu S, Zhu H, Peng G, Yin J, Zeng X. Microstructure prediction of selective laser melting AlSi10Mg using finite element analysis. Mater Des 2018;142:319–28. https://doi.org/10.1016/j.matdes.2018.01.022.

[90] Kamara AM, Wang W, Marimuthu S, Li L. Modelling of the melt pool geometry in the laser deposition of nickel alloys using the anisotropic enhanced thermal conductivity approach. Proc Inst Mech Eng Part B J Eng Manuf 2011;225:87–99. https://doi.org/10.1177/09544054IEM2129.

[91] Trapp J, Rubenchik AM, Guss G, Matthews MJ. In situ absorptivity measurements of metallic powders during laser powder-bed fusion additive manufacturing. Appl Mater Today 2017;9:341–9. https://doi.org/10.1016/j.apmt.2017.08.006.

[92] Matthews M, Trapp J, Guss G, Rubenchik A. Direct measurements of laser absorptivity during metal melt pool formation associated with powder bed fusion additive manufacturing processes. J Laser Appl 2018;30:032302. https://doi.org/10.2351/1.5040636.

[93] Bruna-Rosso C, Demir AG, Vedani M, Previtali B. Global sensitivity analyses of a selective laser melting finite element model: Influential parameters identification. Int J Adv Manuf Technol 2018;99:833–43. https://doi.org/10.1007/s00170-018-2531-7.

[94] Jain PK, Taufik M. Surface roughness improvement using volumetric error control through

adaptive slicing. Int J Rapid Manuf 2017;6:279–302. https://doi.org/10.1504/IJRAPIDM.2017.10008454.

[95] Zhang Z, Huang Y, Rani Kasinathan A, Imani Shahabad S, Ali U, Mahmoodkhani Y, et al. Experimental and numerical investigation on the effect of layer thickness during laser powder-bed fusion of stainless steel 17-4PH. Int J Rapid Manuf 2019;X:xxx–xxx.

[96] Ahn D, Kim H, Lee S. Surface roughness prediction using measured data and interpolation in layered manufacturing. J Mater Process Technol 2009;209:664–71. https://doi.org/10.1016/J.JMATPROTEC.2008.02.050.

[97] Vayre B, Vignat F, Villeneuve F. Metallic additive manufacturing: State-of-the-art review and prospects. Mech Ind 2012;13:89–96. https://doi.org/10.1051/meca/2012003.

[98] Ma M, Wang Z, Gao M, Zeng X. Layer thickness dependence of performance in high-power selective laser melting of 1Cr18Ni9Ti stainless steel. J Mater Process Technol 2015;215:142–50. https://doi.org/10.1016/j.jmatprotec.2014.07.034.

[99] Partanen J, Kaivola M, Seppälä J, Korhonen H, Lehtinen P. Producing parts with multiple layer thicknesses by projection stereolithography. Int J Rapid Manuf 2017;6:235. https://doi.org/10.1504/ijrapidm.2017.10008424.

[100] Qiu C, Panwisawas C, Ward M, Basoalto HC, Brooks JW, Attallah MM. On the role of melt flow into the surface structure and porosity development during selective laser melting. Acta Mater 2015;96:72–9. https://doi.org/10.1016/j.actamat.2015.06.004.

[101] Cao J, Gharghouri MA, Nash P. Finite-element analysis and experimental validation of thermal residual stress and distortion in electron beam additive manufactured Ti-6Al-4V build plates. J Mater Process Technol 2016;237:409–19. https://doi.org/10.1016/J.JMATPROTEC.2016.06.032.

[102] Wu J, Wang L, An X. Numerical analysis of residual stress evolution of AlSi10Mg manufactured by selective laser melting. Optik (Stuttg) 2017;137:65–78. https://doi.org/10.1016/J.IJLEO.2017.02.060.

[103] Li Y, Zhou K, Tan P, Tor SB, Chua CK, Leong KF. Modeling temperature and residual stress fields in selective laser melting. Int J Mech Sci 2018;136:24–35. https://doi.org/10.1016/j.ijmecsci.2017.12.001.

[104] Tan P, Shen F, Li B, Zhou K. A thermo-metallurgical-mechanical model for selective laser melting of Ti6Al4V. Mater Des 2019;168:107642. https://doi.org/10.1016/J.MATDES.2019.107642.

[105] Wang D, Wu S, Yang Y, Dou W, Deng S, Wang Z, et al. The effect of a scanning strategy on the residual stress of 316L steel parts fabricated by selective laser melting (SLM). Materials (Basel) 2018;11. https://doi.org/10.3390/ma11101821.

[106] Song J, Wu W, Zhang L, He B, Lu L, Ni X, et al. Role of scanning strategy on residual stress distribution in Ti-6Al-4V alloy prepared by selective laser melting. Optik (Stuttg) 2018;170:342–52. https://doi.org/10.1016/J.IJLEO.2018.05.128.

[107] Mugwagwa L, Dimitrov D, Matope S, Yadroitsev I. Evaluation of the impact of scanning

strategies on residual stresses in selective laser melting. Int J Adv Manuf Technol 2019;102:2441–50. https://doi.org/10.1007/s00170-019-03396-9.
[108] Bhardwaj T, Shukla M. Effect of laser scanning strategies on texture, physical and mechanical properties of laser sintered maraging steel. Mater Sci Eng A 2018;734:102–9. https://doi.org/10.1016/J.MSEA.2018.07.089.
[109] Ramos D, Belblidia F, Sienz J. New scanning strategy to reduce warpage in additive manufacturing. Addit Manuf 2019;28:554–64. https://doi.org/10.1016/J.ADDMA.2019.05.016.
[110] Denlinger ER. Thermomechanical Model Development and In Situ Experimental Validation of the Laser Powder-Bed Fusion Process. Thermo-Mechanical Model Addit Manuf 2017;16:215–27. https://doi.org/10.1016/B978-0-12-811820-7.00016-1.
[111] Neiva E, Badia S, Martín AF, Chiumenti M. A scalable parallel finite element framework for growing geometries. Application to metal additive manufacturing 2018;6.
[112] Matsumoto M, Shiomi M, Osakada K, Abe F. Finite element analysis of single layer forming on metallic powder bed in rapid prototyping by selective laser processing. Int J Mach Tools Manuf 2002;42:61–7. https://doi.org/10.1016/S0890-6955(01)00093-1.
[113] Shiomi M, Osakada K, Nakamura K, Yamashita T, Abe F. Residual stress within metallic model made by selective laser melting process. CIRP Ann … 2004;53:195–8. https://doi.org/http://dx.doi.org/10.1016/S0007-8506(07)60677-5.
[114] Roberts IA, Wang CJ, Esterlein R, Stanford M, Mynors DJ. A three-dimensional finite element analysis of the temperature field during laser melting of metal powders in additive layer manufacturing. Int J Mach Tools Manuf 2009;49:916–23. https://doi.org/10.1016/j.ijmachtools.2009.07.004.
[115] Lei Y, Sun R, Tang Y, Niu W. Numerical simulation of temperature distribution and TiC growth kinetics for high power laser clad TiC/NiCrBSiC composite coatings. Opt Laser Technol 2012;44:1141–7. https://doi.org/10.1016/j.optlastec.2011.09.030.
[116] Zhao H, Zhang G, Yin Z, Wu L. A 3D dynamic analysis of thermal behavior during single-pass multi-layer weld-based rapid prototyping. J Mater Process Technol 2011;211:488–95. https://doi.org/10.1016/j.jmatprotec.2010.11.002.
[117] Kolossov S, Boillat E, Glardon R, Fischer P, Locher M. 3D FE simulation for temperature evolution in the selective laser sintering process. Int J Mach Tools Manuf 2004;44:117–23. https://doi.org/10.1016/j.ijmachtools.2003.10.019.
[118] Zhang W, Tong M, Harrison NM. Resolution, energy and time dependency on layer scaling in finite element modelling of laser beam powder bed fusion additive manufacturing. Addit Manuf 2019;28:610–20. https://doi.org/10.1016/J.ADDMA.2019.05.002.
[119] Zeng K, Pal D, Gong HJ, Patil N, Stucker B. Comparison of 3DSIM thermal modelling of selective laser melting using new dynamic meshing method to ANSYS. Mater Sci Technol 2015;31:945–56. https://doi.org/10.1179/1743284714Y.0000000703.
[120] Keller N, Neugebauer F, Xu H, Ploshikhin V. Thermo-mechanical Simulation of Additive

Layer Manufacturing of Titanium Aerospace structures. Light Conf 2013.
[121] Schilp J, Seidel C, Krauss H, Weirather J. Investigations on temperature fields during laser beam melting by means of process monitoring and multiscale process modelling. Adv Mech Eng 2014;2014. https://doi.org/10.1155/2014/217584.
[122] Seidel C, F. Zaeh M, Wunderer M, Weirather J, A. Krol T, Ott M. Simulation of the laser beam melting process-approaches for an efficient modelling of the beam-material interaction. Procedia CIRP 2014;25:146–53. https://doi.org/10.1016/j.procir.2014.10.023.
[123] Papadakis L, Loizou A, Risse J, Schrage J. Numerical computation of component shape distortion manufactured by Selective Laser Melting. Procedia CIRP 2014;18:90–5. https://doi.org/10.1016/j.procir.2014.06.113.
[124] Papadakis L, Loizou A, Risse J, Bremen S, Schrage J. A computational reduction model for appraising structural effects in selective laser melting manufacturing. Virtual Phys Prototyp 2014;9:17–25. https://doi.org/10.1080/17452759.2013.868005.
[125] Chiumenti M, Neiva E, Salsi E, Cervera M, Badia S, Moya J, et al. Numerical modelling and experimental validation in Selective Laser Melting. Addit Manuf 2017;18:171–85. https://doi.org/10.1016/J.ADDMA.2017.09.002.
[126] Li C, Fu CH, Guo YB, Fang FZ. A multiscale modeling approach for fast prediction of part distortion in selective laser melting. J Mater Process Technol 2015;229:703–12. https://doi.org/10.1016/j.jmatprotec.2015.10.022.
[127] Keller N, Ploshikhin V. New Method for Fast Predictions of Residual Stress and Distortions of AM Parts. Solid Free Fabr Symp 2014:1229–37. https://doi.org/10.1017/CBO9781107415324.004.
[128] Siewert M, Neugebauer F, Epp J, Ploshikhin V. Validation of Mechanical Layer Equivalent Method for simulation of residual stresses in additive manufactured components. Comput Math with Appl 2018. https://doi.org/10.1016/j.camwa.2018.08.016.
[129] Peng H, Ghasri-Khouzani M, Gong S, Attardo R, Ostiguy P, Gatrell BA, et al. Fast prediction of thermal distortion in metal powder bed fusion additive manufacturing: Part 1, a thermal circuit network model. Addit Manuf 2018;22:852–68. https://doi.org/10.1016/j.addma.2018.05.023.
[130] Liu Y, Zhang J, Pang Z. Numerical and experimental investigation into the subsequent thermal cycling during selective laser melting of multi-layer 316L stainless steel. Opt Laser Technol 2018;98:23–32. https://doi.org/10.1016/J.OPTLASTEC.2017.07.034.
[131] Xie R, Chen G, Zhao Y, Zhang S, Yan W, Lin X, et al. In-situ observation and numerical simulation on the transient strain and distortion prediction during additive manufacturing. J Manuf Process 2019;38:494–501. https://doi.org/10.1016/J.JMAPRO.2019.01.049.
[132] Liu PW, Ji YZ, Wang Z, Qiu CL, Antonysamy AA, Chen LQ, et al. Investigation on evolution mechanisms of site-specific grain structures during metal additive manufacturing. J Mater Process Technol 2018;257:191–202. https://doi.org/10.1016/j.jmatprotec.2018.02.042.

[133] Liu P, Cui X, Deng J, Li S, Li Z, Chen L. Investigation of thermal responses during metallic additive manufacturing using a “Tri-Prism” finite element method. Int J Therm Sci 2019;136:217–29. https://doi.org/10.1016/J.IJTHERMALSCI.2018.10.022.
[134] Ren K, Chew Y, Zhang YF, Bi GJ, Fuh JYH. Thermal Analyses for Optimal Scanning Pattern Evaluation in Laser Aided Additive Manufacturing. J Mater Process Technol 2019;271:178–88. https://doi.org/10.1016/j.jmatprotec.2019.03.029.
[135] Hodge NE, Ferencz RM, Solberg JM. Implementation of a thermomechanical model for the simulation of selective laser melting. Comput Mech 2014;54:33–51. https://doi.org/10.1007/s00466-014-1024-2.
[136] Lu X, Lin X, Chiumenti M, Cervera M, Li J, Ma L, et al. Finite element analysis and experimental validation of the thermomechanical behavior in laser solid forming of Ti-6Al-4V. Addit Manuf 2018;21:30–40. https://doi.org/10.1016/J.ADDMA.2018.02.003.
[137] Denlinger ER, Jagdale V, Srinivasan G V., El-Wardany T, Michaleris P. Thermal modeling of Inconel 718 processed with powder bed fusion and experimental validation using in situ measurements. Addit Manuf 2016;11:7–15. https://doi.org/10.1016/j.addma.2016.03.003.
[138] Bangerth W, Hartmann R, Kanschat G. deal.II---A general-purpose object-oriented finite element library. ACM Trans Math Softw 2007;33:24-es. https://doi.org/10.1145/1268776.1268779.
[139] Zhibo Luo;, Yaoyao Zhao. Numerical simulation of part-level temperature fields during selective laser melting of stainless steel 316L. Int J Adv Manuf Technol 2019. https://doi.org/10.1007/s00170-019-03947-0.
[140] Zegard T, Paulino GH. Bridging topology optimization and additive manufacturing. Struct Multidiscip Optim 2015. https://doi.org/10.1007/s00158-015-1274-4.
[141] Aremu a., Ashcroft I, Wildman R, Hague R, Tuck C, Brackett D. The effects of bidirectional evolutionary structural optimization parameters on an industrial designed component for additive manufacture. Proc Inst Mech Eng Part B J Eng Manuf 2013;227:794–807. https://doi.org/10.1177/0954405412463857.
[142] Sundararajan VG. Topology Optimization for Additive Manufacturing of Customized Meso-Structures using Homogenization and Parametric Smoothing Functions. The University of Texas at Austin, 2010.
[143] Sepp J, Hupfer A. Topology Optimization in Structural Design of a Lp Turbine Guide. ASME Turbo Expo 2014 Turbine Tech Conf Expo 2014:1–10.
[144] Dede EM. Topology Optimization, Additive Layer Manufacturing, and Experimental Testing of an Air-Cooled Heat Sink. J Mech Des 2015;137:1–9. https://doi.org/10.1115/1.4030989.
[145] Howell LL. Compliant mechanisms. John Wiley & Sons; 2001.
[146] Gaynor AT. Topology Optimization Algorithms for Additive Manufacturing. John Hopkins University, 2015.
[147] Sercombe TB, Xu X, Challis VJ, Green R, Yue S, Zhang Z, et al. Failure modes in high

strength and stiffness to weight scaffolds produced by Selective Laser Melting. Mater Des 2015;67:501–8. https://doi.org/10.1016/j.matdes.2014.10.063.
[148] Hollister SJ. Porous scaffold design for tissue engineering 2005;4.
[149] Challis VJ, Roberts AP, Grotowski JF, Zhang L-C, Sercombe TB. Prototypes for Bone Implant Scaffolds Designed via Topology Optimization and Manufactured by Solid Freeform Fabrication. Adv Eng Mater 2010;12:1106–10. https://doi.org/10.1002/adem.201000154.
[150] Andreassen E, Lazarov BS, Sigmund O. Mechanics of Materials Design of manufacturable 3D extremal elastic microstructure. Int J Mech Mater 2014;69:1–10. https://doi.org/10.1016/j.mechmat.2013.09.018.
[151] Sigmund O. Manufacturing tolerant topology optimization. Acta Mech Sin Xuebao 2009;25:227–39. https://doi.org/10.1007/s10409-009-0240-z.
[152] Wang F, Lazarov BS, Sigmund O. On projection methods, convergence and robust formulations in topology optimization. Struct Multidiscip Optim 2011;43:767–84. https://doi.org/10.1007/s00158-010-0602-y.
[153] Zhou M, Lazarov BS, Wang F, Sigmund O. Minimum length scale in topology optimization by geometric constraints. Comput Methods Appl Mech Eng 2015;293:266–82. https://doi.org/10.1016/j.cma.2015.05.003.
[154] Liu S, Li Q, Chen W, Tong L, Cheng G. An identification method for enclosed voids restriction in manufacturability design for additive manufacturing structures. Front Mech Eng 2015;10:126–37. https://doi.org/10.1007/s11465-015-0340-3.
[155] Li Q, Chen W, Liu S, Tong L. Structural topology optimization considering connectivity constraint. Struct Multidiscip Optim 2016;54:971–84. https://doi.org/10.1007/s00158-016-1459-5.
[156] Brackett D, Ashcroft I, Hague R. Topology optimization for additive manufacturing. Proc. solid Free. Fabr. Symp. Austin, TX, vol. 1, S; 2011, p. 348–62.
[157] Allaire G, Jakabčin L. Taking into account thermal residual stresses in topology optimization of structures built by additive manufacturing 2017:1–45.
[158] Bendsøe MP, Kikuchi N. Generating optimal topologies in structural design using a homogenization method. Comput Methods Appl Mech Eng 1988;71:197–224. https://doi.org/10.1016/0045-7825(88)90086-2.
[159] Bendsøe MP, Sigmund O. Topology optimization: theory, methods and applications. Springer, Berlin; 2003.
[160] Sigmund O, Maute K. Topology optimization approaches. Struct Multidiscip Optim 2013;48:1031–55. https://doi.org/10.1007/s00158-013-0978-6.
[161] Allaire G, Jouve F, Toader AM. Structural optimization using sensitivity analysis and a level-set method. J Comput Phys 2004;194:363–93. https://doi.org/10.1016/j.jcp.2003.09.032.
[162] Rozvany GIN. A critical review of established methods of structural topology optimization.

Struct Multidiscip Optim 2009;37:217–37. https://doi.org/10.1007/s00158-007-0217-0.
[163] Xia L, Xia Q, Huang X, Xie YM. Bi-directional Evolutionary Structural Optimization on Advanced Structures and Materials: A Comprehensive Review. Arch Comput Methods Eng 2018;25:437–78. https://doi.org/10.1007/s11831-016-9203-2.
[164] Meng L, Zhang W, Quan D, Shi G, Tang L, Hou Y, et al. From Topology Optimization Design to Additive Manufacturing: Today's Success and Tomorrow's Roadmap. Arch Comput Methods Eng 2019. https://doi.org/10.1007/s11831-019-09331-1.
[165] Liu J, Gaynor AT, Chen S, Kang Z, Suresh K, Takezawa A, et al. Current and future trends in topology optimization for additive manufacturing. Struct Multidiscip Optim 2018;57:2457–83. https://doi.org/10.1007/s00158-018-1994-3.
[166] Zhu JH, Zhang WH, Xia L. Topology Optimization in Aircraft and Aerospace Structures Design. Arch Comput Methods Eng 2016;23:595–622. https://doi.org/10.1007/s11831-015-9151-2.
[167] Langelaar M. An additive manufacturing filter for topology optimization of print-ready designs. Struct Multidiscip Optim 2017;55:871–83. https://doi.org/10.1007/s00158-016-1522-2.
[168] Gaynor AT, Guest JK. Topology optimization considering overhang constraints: Eliminating sacrificial support material in additive manufacturing through design. Struct Multidiscip Optim 2016;54:1157–72. https://doi.org/10.1007/s00158-016-1551-x.
[169] Zhou M, Liu Y, Lin Z. Topology optimization of thermal conductive support structures for laser additive manufacturing. Comput Methods Appl Mech Eng 2019;353:24–43. https://doi.org/10.1016/j.cma.2019.03.054.
[170] Ueda Y, Kim YC, Yuan MG. A predicting method of welding residual stress using source of residual stress. Q J Japan Weld Soc 1988;6:59–64. https://doi.org/10.2207/qjjws.6.59.
[171] Liang X, Cheng L, Chen Q, Yang Q, To A. A Modified Method for Estimating Inherent Strains from Detailed Process Simulation for Fast Residual Distortion Prediction of Single-Walled Structures Fabricated by Directed Energy Deposition. Addit Manuf 2018. https://doi.org/10.1016/J.ADDMA.2018.08.029.
[172] Cheng L, To A. Part-scale build orientation optimization for minimizing residual stress and support volume for metal additive manufacturing: Theory and experimental validation. Comput Des 2019. https://doi.org/10.1016/j.cad.2019.03.004.
[173] Cheng L, Liang X, Bai J, Chen Q, Lemon J, To A. On Utilizing Topology Optimization to Design Support Structure to Prevent Residual Stress Induced Build Failure in Laser Powder Bed Metal Additive Manufacturing. Addit Manuf 2019. https://doi.org/10.1016/j.addma.2019.03.001.
[174] Bartsch K, Lange F, Gralow M, Emmelmann C. Novel approach to optimized support structures in laser beam melting by combining process simulation with topology optimization. J Laser Appl 2019;31:022302. https://doi.org/10.2351/1.5096096.
[175] Liu H, Tian Y, Zong H, Ma Q, Wang MY, Zhang L. Fully parallel level set method for

large-scale structural topology optimization. Comput Struct 2019;221:13–27. https://doi.org/10.1016/j.compstruc.2019.05.010.

[176] Aage N, Andreassen E, Lazarov BS. Topology optimization using PETSc: An easy-to-use, fully parallel, open source topology optimization framework. Struct Multidiscip Optim 2015;51:565–72. https://doi.org/10.1007/s00158-014-1157-0.

[177] Aage N, Andreassen E, Lazarov BS, Sigmund O. Giga-voxel computational morphogenesis for structural design. Nature 2017;550:84–6. https://doi.org/10.1038/nature23911.

[178] Mezzadri F, Bouriakov V, Qian X. Topology optimization of self-supporting support structures for additive manufacturing. Addit Manuf 2018;21:666–82. https://doi.org/10.1016/j.addma.2018.04.016.

[179] Oropallo W, Piegl LA. Ten challenges in 3D printing. Eng Comput 2016;32:135–48. https://doi.org/10.1007/s00366-015-0407-0.

[180] Smith CJ, Derguti F, Hernandez Nava E, Thomas M, Tammas-Williams S, Gulizia S, et al. Dimensional accuracy of Electron Beam Melting (EBM) additive manufacture with regard to weight optimized truss structures. J Mater Process Technol 2016;229:128–38. https://doi.org/10.1016/j.jmatprotec.2015.08.028.

[181] Schevenels M, Lazarov BS, Sigmund O. Robust topology optimization accounting for spatially varying manufacturing errors. Comput Methods Appl Mech Eng 2011;200:3613–27. https://doi.org/10.1016/j.cma.2011.08.006.

[182] King W, Anderson AT, Ferencz RM, Hodge NE, Kamath C, Khairallah SA. Overview of modelling and simulation of metal powder bed fusion process at Lawrence Livermore National Laboratory. Mater Sci Technol 2015;31:957–68. https://doi.org/10.1179/1743284714Y.0000000728.

[183] Yadroitsev I, Yadroitsava I. Evaluation of residual stress in stainless steel 316L and Ti6Al4V samples produced by selective laser melting. Virtual Phys Prototyp 2015;10:67–76. https://doi.org/10.1080/17452759.2015.1026045.

[184] Altair. Altair to Reveal New Design Processes and Software Tools for Additive Manufacturing at formnext in Frankfurt 2016. http://www.altair.com/newsdetail.aspx?news_id=11305&news_country=en-US.

[185] SIEMENS. Siemens to revolutionize product development with end-to-end additive manufacturing solution 2016. https://www.plm.automation.siemens.com/en/about_us/newsroom/press/press_release.cfm?Component=251141&ComponentTemplate=822.

[186] SIEMENS. Siemens' NX Delivers Next Breakthrough in Product Design with Convergent Modeling 2016. https://www.plm.automation.siemens.com/en/about_us/newsroom/press/press_release.cfm?Component=250263&ComponentTemplate=822.

[187] K. S. The method of moving asymptotes - a new method for structural optimization. Int J Numer Methods Eng 1987;24:359–73.

[188] Kaven JO. Two functions for smoothing/denoising of triangular meshes 2009.
[189] Desbrun M, Meyer M, Schröder P, Barr AH. Implicit fairing of irregular meshes using diffusion and curvature flow. Proc. 26th Annu. Conf. Comput. Graph. Interact. Tech., 1999, p. 317–24.
[190] Prospector. Acrylonitrile Butadiene Styrene (ABS) Typical Properties Generic ABS. n.d.
[191] Zienkiewicz OC, Taylor RL. The finite element method for solid and structural mechanics. Elsevier; 2005.
[192] Kelly P. Mechanics Lecture Notes: Engineering Solid Mechanics. Available from http://homepages.engineering.auckland.ac.nz/~pkel015/SolidMechanicsBooks/index.html n.d.
[193] KRABBENHØFT K. BASIC COMPUTATIONAL PLASTICITY. 2002.
[194] Bathe KJ. Finite element procedures. 2006.
[195] Mozaffar M, Ndip-Agbor E, Lin S, Wagner GJ, Ehmann K, Cao J. Acceleration strategies for explicit finite element analysis of metal powder-based additive manufacturing processes using graphical processing units. Comput Mech 2019;64:879–94. https://doi.org/10.1007/s00466-019-01685-4.
[196] Verhaeghe F, Craeghs T, Heulens J, Pandelaers L. A pragmatic model for selective laser melting with evaporation. Acta Mater 2009;57:6006–12. https://doi.org/10.1016/j.actamat.2009.08.027.
[197] Bonakdar A, Molavi-Zarandi M, Chamanfar A, Jahazi M, Firoozrai A, Morin E. Finite element modeling of the electron beam welding of Inconel-713LC gas turbine blades. J Manuf Process 2017;26:339–54. https://doi.org/10.1016/j.jmapro.2017.02.011.
[198] Sabau AS, Porter WD. Alloy shrinkage factors for the investment casting of 17-4PH stainless steel parts. Metall Mater Trans B Process Metall Mater Process Sci 2008;39:317–30. https://doi.org/10.1007/s11663-007-9125-3.
[199] Taylor R. Measurement of Thermal Properties. Armour Research Foundation Chicago IL; 1995. https://doi.org/10.1201/9781420049718.ch16.
[200] Rombouts M, Froyen L, Gusarov A V., Bentefour EH, Glorieux C. Photopyroelectric measurement of thermal conductivity of metallic powders. J Appl Phys 2005;97. https://doi.org/10.1063/1.1832740.
[201] Ali U, Mahmoodkhani Y, Imani Shahabad S, Esmaeilizadeh R, Liravi F, Sheydaeian E, et al. On the measurement of relative powder-bed compaction density in powder-bed additive manufacturing processes. Mater Des 2018;155:495–501. https://doi.org/10.1016/j.matdes.2018.06.030.
[202] Lee YS, Zhang W. Mesoscopic Simulation of Heat Transfer and Fluid Flow in Laser Powder Bed Additive Manufacturing. Int Solid Free Form Fabr Symp Austin 2015:1154–65.
[203] Deng D, Murakawa H. Prediction of welding distortion and residual stress in a thin plate butt-welded joint. Comput Mater Sci 2008;43:353–65. https://doi.org/10.1016/j.commatsci.2007.12.006.

[204] Zhang Z, Huang Y, Rani Kasinathan A, Imani Shahabad S, Ali U, Mahmoodkhani Y, et al. 3-Dimensional heat transfer modeling for laser powder-bed fusion additive manufacturing with volumetric heat sources based on varied thermal conductivity and absorptivity. Opt Laser Technol 2019;109:297–312. https://doi.org/10.1016/j.optlastec.2018.08.012.

[205] Wang L, Jue J, Xia M, Guo L, Yan B, Gu D. Effect of the Thermodynamic Behavior of Selective Laser Melting on the Formation of In situ Oxide Dispersion-Strengthened Aluminum-Based Composites. Metals (Basel) 2016;6:286. https://doi.org/10.3390/met6110286.

[206] Othman MIA, Abbas IA. Generalized thermoelasticity of thermal-shock problem in a non-homogeneous isotropic hollow cylinder with energy dissipation. Int J Thermophys 2012;33:913–23. https://doi.org/10.1007/s10765-012-1202-4.

[207] Fachinotti VD, Bellet M. Linear tetrahedral finite elements for thermal shock problems. Int J Numer Methods Heat Fluid Flow 2006;16:590–601. https://doi.org/10.1108/09615530610669120.

[208] Bejan A, Kraus AD. heat transfer handbook.pdf 2003:1480. https://doi.org/10.1111/1467-8551.12120.

[209] Mikron Instrument Company. Table of Emissivity of Various Surfaces. TRANSMETRA Haltec GmbH 2018:1–10. http://www-eng.lbl.gov/~dw/projects/DW4229_LHC_detector_analysis/calculations/emissivity2.pdf.

[210] Murr LE, Martinez E, Hernandez J, Collins S, Amato KN, Gaytan SM, et al. Microstructures and properties of 17-4 PH stainless steel fabricated by selective laser melting. J Mater Res Technol 2012;1:167–77. https://doi.org/10.1016/S2238-7854(12)70029-7.

[211] Gu H, Gong H, Pal D, Rafi K, Starr T, Stucker B. Influences of Energy Density on Porosity and Microstructure of Selective Laser Melted 17-4PH Stainless Steel. 2013 Solid Free. Fabr. Symp., 2013, p. 474–89.

[212] Rafi HK, Pal D, Patil N, Starr TL, Stucker BE. Microstructure and Mechanical Behavior of 17-4 Precipitation Hardenable Steel Processed by Selective Laser Melting. J Mater Eng Perform 2014;23:4421–8. https://doi.org/10.1007/s11665-014-1226-y.

[213] Yadollahi A, Shamsaei N, Thompson SM, Elwany A, Bian L. Effects of building orientation and heat treatment on fatigue behavior of selective laser melted 17-4 PH stainless steel. Int J Fatigue 2017;94:218–35. https://doi.org/10.1016/j.ijfatigue.2016.03.014.

[214] Averyanova M, Cicala E, Bertrand P, Grevey D. Experimental design approach to optimize selective laser melting of martensitic 17-4 PH powder: part I – single laser tracks and first layer. Rapid Prototyp J 2012;18:28–37. https://doi.org/10.1108/13552541211193476.

[215] LeBrun T, Nakamoto T, Horikawa K, Kobayashi H. Effect of retained austenite on subsequent thermal processing and resultant mechanical properties of selective laser melted 17–4 PH stainless steel. Mater Des 2015;81:44–53. https://doi.org/10.1016/j.matdes.2015.05.026.

[216] LeBrun T, Nakamoto T, Horikawa K, Kobayashi H. Effect of retained austenite on

subsequent thermal processing and resultant mechanical properties of selective laser melted 17-4 PH stainless steel. Mater Des 2015;81:44–53. https://doi.org/10.1016/j.matdes.2015.05.026.

[217] Murr LE, Martinez E, Hernandez J, Collins S, Amato KN, Gaytan SM, et al. Microstructures and Properties of 17-4 PH Stainless Steel Fabricated by Selective Laser Melting 2012;1:167–77.

[218] Rubenchik AM, King WE, Wu S. Scaling laws for the additive manufacturing. J Mater Process Technol 2018. https://doi.org/10.1016/j.jmatprotec.2018.02.034.

[219] Chandrasekhar S. Hydrodynamic and hydromagnetic stability. Courier Corporation; 2013.

[220] Rombouts M, Froyen L, Gusarov A V., Bentefour EH, Glorieux C. Light extinction in metallic powder beds: Correlation with powder structure. J Appl Phys 2005;98. https://doi.org/10.1063/1.1948509.

[221] Mahmoodkhani Y, Ali U, Imani Shahabad S, Rani Kasinathan A, Esmaeilizadeh R, Keshavarzkermani A, et al. On the measurement of effective powder layer thickness in laser powder-bed fusion additive manufacturing of metals. Prog Addit Manuf 2019;4:109–16. https://doi.org/10.1007/s40964-018-0064-0.

[222] Wang XC, Laoui T, Bonse J, Kruth JP, Lauwers B, Froyen L. Direct Selective Laser Sintering of Hard Metal Powders: Experimental Study and Simulation. Int J Adv Manuf Technol 2002;19:351–7. https://doi.org/10.1007/s001700200024.

[223] Siddique S, Imran M, Wycisk E, Emmelmann C, Walther F. Influence of process-induced microstructure and imperfections on mechanical properties of AlSi12 processed by selective laser melting. J Mater Process Technol 2015;221:205–13. https://doi.org/10.1016/j.jmatprotec.2015.02.023.

[224] Ashby MF, Easterling KE. THE TRANSFORMATION HARDENING OF STEEL SURFACES BY LASER BEAMS-I . STEELS 1984;32.

[225] Ueda Y, Yuan MG. Prediction of Residual Stresses in Butt Welded Plates Using Inherent Strains. J Eng Mater Technol 1993;115:417. https://doi.org/10.1115/1.2904240.

[226] Deng D, Murakawa H. Prediction of welding distortion and residual stress in a thin plate butt-welded joint. Comput Mater Sci 2008;43:353–65. https://doi.org/10.1016/j.commatsci.2007.12.006.

[227] Mura T. Micromechanics of defects in solids. Springer Science & Business Media; 2013.

[228] Abbo AJ. Finite element algorithms for elastoplasticity and consolidation. University of Newcastle, 2005.

[229] Eshelby JDD. The Determination of the Elastic Field of an Ellipsoidal Inclusion, and Related Problems. Proc R Soc Lond A 1957;241:376–96.

[230] Weinberger CR, Cai W, Barnett DM. Elasticity of Microscopic Structures. Lect Notes 2005.

[231] Sönnerlind H. Singularities in Finite Element Models: Dealing with Red Spots. Comsol Forum 2015. https://www.comsol.com/blogs/singularities-in-finite-element-models-dealing-with-red-spots/.

[232] Payne LE, Lekhnitskii SG. Theory of Elasticity of an Anistropic Elastic Body. vol. 18. Holden-day; 1964. https://doi.org/10.2307/2003327.
[233] Bendsøe MP, Sigmund O. Material interpolation schemes in topology optimization. Arch Appl Mech 1999;69:635–54. https://doi.org/10.1007/s004190050248.
[234] Chen Q, Liang X, Hayduke D, Liu J, Cheng L, Oskin J, et al. An Inherent Strain Based Multiscale Modeling Framework for Simulating Part-scale Residual Deformation for Direct Metal Laser Sintering. Addit Manuf 2019. https://doi.org/10.1016/j.addma.2019.05.021.
[235] Sigmund O. A 99 line topology optimization code written in matlab. Struct Multidiscip Optim 2001;21:120–7. https://doi.org/10.1007/s001580050176.
[236] Svanberg K. The method of moving asymptotes—a new method for structural optimization. Int J Numer Methods Eng 1987;24:359–73. https://doi.org/10.1002/nme.1620240207.
[237] SHARCNET. Cluster graham.sharcnet.ca 2019. https://www.sharcnet.ca/my/systems/show/114.
[238] Etter T, Kunze K, Geiger F, Meidani H. Reduction in mechanical anisotropy through high temperature heat treatment of Hastelloy X processed by Selective Laser Melting (SLM). IOP Conf Ser Mater Sci Eng 2015;82. https://doi.org/10.1088/1757-899X/82/1/012097.
[239] Wen JF, Liu Y, Srivastava A, Benzerga AA, Tu ST, Needleman A. Environmentally enhanced creep crack growth by grain boundary cavitation under cyclic loading. Acta Mater 2018;153:136–46. https://doi.org/10.1016/j.actamat.2018.04.034.
[240] Sigmund O, Petersson J. Numerical instabilities in topology optimization: A survey on procedures dealing with checkerboards, mesh-dependencies and local minima. Struct Optim 1998;16:68–75. https://doi.org/10.1007/BF01214002.
[241] Kuo YH, Cheng CC, Lin YS, San CH. Support structure design in additive manufacturing based on topology optimization. Struct Multidiscip Optim 2018;57:183–95. https://doi.org/10.1007/s00158-017-1743-z.
[242] Lazarov BS, Wang F. Maximum length scale in density based topology optimization. Comput Methods Appl Mech Eng 2017;318:826–44. https://doi.org/10.1016/j.cma.2017.02.018.
[243] Benham PP, Armstrong CG, Crawford RJ. Mechanics of engineering meterials. Addison-Wesley; 1996.
[244] Neira Arce A. Thermal Modeling and Simulation of Electron Beam Melting for Rapid Prototyping on Ti6Al4V Alloys. North Carolina State University, 2012.
[245] Yang Y. TEMPERATURE-DEPENDENT THERMOELASTIC ANALYSIS OF MULTIDIMENSIONAL FUNCTIONALLY GRADED MATERIALS. University of Pittsburgh, 2015.
[246] Valencia JJ, Quested PN. Thermophysical Properties. ASM Hadbook, Vol 15 Cast 2011;15:468–81. https://doi.org/10.1361/asmhba0005240.

Appendix A. Temperature-Dependent Material Properties

Table A.1. Material properties of 316 stainless steel based on [21]**.**

Temperature [K]	300	1000	1700	2000	3000
Density [kg/m3]	7900	7710	7430	7140	6740
Heat capacity [J/(kg·K)]	434	498	521	531	600
Thermal conductivity [W/(m·K)]	13.96	24.96	35.95	18.97	22.25
Latent heat [GJ/m^3]	2.18				

Table A.2. Material properties of mild steel based on [226]**.**

Temperature [K]	300	1000	1700	1773	3000				
Density [kg/m3]	7900	7750	7600	7500	7500				
Temperature [K]	304.1	677.7	969.2	1023	1122.1	1673.9	1727.7	1773	3000
Heat capacity [J/(kg·K)]	426	555.3	893.3	1189.5	850	747.4	1200	1000	1000
Temperature [K]	273	672	873	1071.1	1577.7	1671.1	1722.0	1773	3000
Thermal conduct. [W/(m·K)]	54.2	47.4	38.2	26.3	28.4	31.8	100	100	100

Table A.3. Material properties of Ti-6Al-4V.

Temp. [K]	Young's Modulus.[GPa] [78]	CTE [10^-6/K] [78]	Flow Modulus. [GPa] [78]	Emissivity [79]
296	125	8.78	0.7	0.121
533	110	9.83	2.2	0.2
589	100	10.01	2.2	0.208
700	100	10.71	2.2	0.25
755	80	11.10	1.9	0.3
811	74	11.22	1.9	0.39
923	55	11.68	1.9	0.575
1073	27	12.21	2	0.595
1098	20	12.29	2	0.6
1123	5	12.37	2	0.6
1773	5	12.37	2	0.6
1923	5	12.37	2	0.405
2879	5	12.37	2	0.395
Specific heat capacity [J/(kg·K)] [244]	$C_p = 540.58 + 1.02\times10^{-1}(T-273) + 1.35\times10^{-4}(T-273)^2 - 6.5\times10^{-8}(T-273)^3$			
Thermal conduct. [W/(m·K)] [245,246]	$k = 1.1 + 0.017T$ $T < 1268K$ $k_s = -0.797 + 18.2\times10^{-3}T - 2.0\times10^{-6}T^2$ $1268K \le T < 1923K$ $k_l = 33.4$ $T = 1923K$ $k_l = 34.6$ $T = 1973K$			
Density [kg/m3] [244] [246]	$d_{solid} = 4.42 - 0.154(T-298)$ $298K < T < 1923K$ $d_{liquid} = 3.920 - 0.68(T-1923)$ $1923K < T < 2273K$			
Poisson's ratio [245]	$v = 0.289 + 3.2\times10^{-5}T$			
Yield stress [MPa] [245]	$\sigma_y = 1252 - 0.8486T$ $T \le 1400K$ $\sigma_y = 316 - 0.18T$ $T > 1400K$			
Latent heat of fusion GJ/m^3	1.65			

Appendix B. The Analytical Residual Stress Model in Section 8.5.4

At each moment, there are two equilibria to be obeyed, the force equilibrium and the moment equilibrium, as shown in Eq.(B.1).

$$\begin{aligned} \int \sigma_x(z)dz = 0 \\ \int \sigma_x(z)zdz = 0 \end{aligned} \tag{B.1}$$

where σ_x is the stress in the *x*-direction. The continuity of the deformation is assumed over the combined equilibrated body so that a linear strain profile can be described as,

$$\varepsilon_x(z) = az + b \tag{B.2}$$

where *a* and *b* are coefficient to be derived, and *z* is the coordinate in the z-direction. Suppose *m* represents the ratio of the substrate stiffness E_b to the part's stiffness E_p, and *n* is the ratio of Young's modulus between the support E_s and the printed part. In addition, the width ratio between the width of the substrate w_b and the width of the part w_p can also be merged into *m*, and similarly, support's width w_s and w_p into *n*, as illustrated in Eq.(B.2),

$$\begin{aligned} m &= \frac{w_b E_b}{w_p E_p} \\ n &= \frac{w_s E_s}{w_p E_p} \end{aligned} \tag{B.3}$$

The equilibria in Eq.(B.2) can then be expressed as follows,

$$\begin{aligned} &\int_0^{h_b} m(az+b)E_p w_p dz + \int_{h_b}^{h_b+h_s} n(az+b)E_p w_p dz + \int_{h_b+h_s}^{h_b+h_s+h_p-l}(az+b)E_p w_p dz + \int_{h_b+h_s+h_p-l}^{h_b+h_s+h_p}(az+b)\bar{\sigma}E_p w_p dz = 0 \\ &\int_0^{h_b} m(az+b)E_p w_p z dz + \int_{h_b}^{h_b+h_s} n(az+b)E_p w_p dz + \int_{h_b+h_s}^{h_b+h_s+h_p-l}(az+b)E_p w_p z dz + \int_{h_b+h_s+h_p-l}^{h_b+h_s+h_p}(az+b)\bar{\sigma}E_p w_p z dz = 0 \end{aligned} \tag{B.4}$$

where *l* is the layer thickness, $\bar{\sigma}$ is the ratio between yield stress σ and the part's stiffness E_p. From Eq.(B.4), the parameters *a* and *b* can be obtained as follows,

$$a = \frac{a_{num}}{a_{den}}$$

$$\begin{aligned}
a_{num} &= -6\bar{\sigma}l\left(mh_b^2 + nh_s^2 + h_p^2 + 2mh_bh_s + 2mh_bh_p + 2nh_sh_p - mh_bl - nh_sl - h_pl\right) \\
a_{den} &= m^2h_b^4 + n^2h_s^4 + h_p^4 + l^4 + 4mnh_b^3h_s + 4mnh_bh_s^3 + 4mh_b^3h_p + 4mh_bh_p^3 - 4mh_b^3l \\
&\quad - 4mh_bl^3 + 4nh_s^3h_p + 4nh_sh_p^3 - 4nh_s^3l - 4nh_sl^3 - 4h_p^3l - 4h_pl^3 \\
&\quad + 6mnh_b^2h_s^2 + 6mh_b^2h_p^2 + 6mh_b^2l^2 + 6nh_s^2h_p^2 + 6nh_s^2l^2 + 6h_p^2l^2 \\
&\quad + 12mh_b^2h_sh_p + 12mh_bh_s^2h_p + 12mh_bh_sh_p^2 - 12mh_b^2h_sl - 12mh_bh_s^2l + 12mh_bh_sl^2 \\
&\quad - 12mh_b^2h_pl + 12mh_bh_pl^2 - 12mh_bh_p^2l - 12nh_s^2h_pl + 12nh_sh_pl^2 - 12nh_sh_p^2l \\
&\quad - 24mh_bh_sh_pl
\end{aligned} \tag{B.5}$$

$$b = \frac{b_{num}}{b_{den}}$$

$$\begin{aligned}
b_{num} &= \bar{\sigma}l\left(2mh_b^3 + 2nh_s^3 + 2h_p^3 + l^3 - 3mh_b^2l - 3nh_s^2l + 6h_bh_p^2 + 6h_sh_p^2 + 6mh_b^2h_s\right. \\
&\quad \left. + 6nh_bh_s^2 + 6mh_b^2h_p + 6nh_s^2h_p + 6nh_s^2h_p - 6nh_bh_sl - 6h_bh_pl - 6h_sh_pl + 12nh_bh_sh_p\right) \\
b_{den} &= m^2h_b^4 + n^2h_s^4 + h_p^4 + l^4 + 4mnh_b^3h_s + 4mnh_bh_s^3 + 4mh_b^3h_p + 4mh_bh_p^3 - 4mh_b^3l \\
&\quad - 4mh_bl^3 + 4nh_s^3h_p + 4nh_sh_p^3 - 4nh_s^3l - 4nh_sl^3 - 4h_p^3l - 4h_pl^3 \\
&\quad + 6mnh_b^2h_s^2 + 6mh_b^2h_p^2 + 6mh_b^2l^2 + 6nh_s^2h_p^2 + 6nh_s^2l^2 + 6h_p^2l^2 \\
&\quad + 12mh_b^2h_sh_p + 12mh_bh_s^2h_p + 12mh_bh_sh_p^2 - 12mh_b^2h_sl - 12mh_bh_s^2l + 12mh_bh_sl^2 \\
&\quad - 12mh_b^2h_pl + 12mh_bh_pl^2 - 12mh_bh_p^2l - 12nh_s^2h_pl + 12nh_sh_pl^2 - 12nh_sh_p^2l \\
&\quad - 24mh_bh_sh_pl
\end{aligned} \tag{B.6}$$

By substituting *a* and *b* in (B.5) and (B.6) into (B.2), the strain distribution can be derived. Then the approximated residual stress can be derived easily by multiplying the strain with Young's modulus of the material used.